NMR Techniques for Measuring Transport Phenomena in Microporous Materials

Department of Chemical Engineering and Biotechnology

University of Cambridge

Mohamed Iman Ainte

Fitzwilliam College

A thesis submitted for the degree of Doctor of Philosophy

June 2017

Preface

This dissertation is the result of my own work and includes nothing which is the outcome of work done in collaboration except as declared in the Preface and specified in the text. It is not substantially the same as any that I have submitted, or, is being concurrently submitted for a degree or diploma or other qualification at the University of Cambridge or any other University or similar institution except as declared in the Preface and specified in the text. I further state that no substantial part of my dissertation has already been submitted, or, is being concurrently submitted for any such degree, diploma or other qualification at the University of Cambridge or any other University or similar institution except as declared in the Preface and specified in the text. The work was carried out in the Department of Chemical Engineering and Biotechnology at the University of Cambridge. This thesis contains not more than 60,000 words.

Acknowledgements

I would like to thank my supervisors Prof. Lynn Gladden, Dr Mick Mantle, Dr Andy York and Dr Iain Hitchcock. They have all been instrumental in providing support and guidance throughout my time in Cambridge and at the Johnson Matthey Technology Centre. It truly has been a privilege to develop under their tutelage and I am very grateful that they have given me the opportunity to join the Magnetic Resonance Research Centre (MRRC). I would like to give a special acknowledgement to Mick for dedicating many long hours to solving countless magnet related problems and aiding with the interpretation of PFG NMR data. I would also like to thank Dr Andy Sederman for providing help with NMR troubleshooting, PFG NMR data analysis and for offering his invaluable expertise on multiple occasions. I greatly appreciate their positive and friendly attitude towards me throughout my studies and for always keeping their doors open. I am also extremely grateful for the funding that I have received from the Engineering and Physical Sciences Research Council (EPSRC) and from Johnson Matthey.

I would like to thank Adam, Adeline, Jordan and Tom Partridge for willingly proof-reading parts of my thesis and for providing many helpful suggestions. I would also like to acknowledge Pierre and Rittick for providing sanity checks and useful discussions into a whole host of topics over these last few years. For that I am very grateful and I wish you all the best.

My heartfelt thanks go to all the other people who have inspired and encouraged me along the way. I would like to thank my good friends Mohamady and Hadi for always looking out for my interests and for their excellent company. I look forward to seeing you both more often. I would like to express my gratitude towards Tom Blythe for his friendship throughout my time in Cambridge. His help with analysing NMR data in the first few months of my PhD and many insightful discussions ever since have always left me richer for the experience and for that I am truly grateful. I am thankful to Jules and Yunan for their valued friendship and for always making time for me. I look forward to seeing you both more regularly and to re-commencing our European road trips. I would also like to acknowledge Alex for his friendship and his keen interest in Somali culture. I wish you and Diana all the best and I look forward to meeting your family in Buenaventura. I am also thankful to Andi, Chris and Kaspars for their shared enthusiasm for a wide range of sports.

I would also like to thank my niece and nephew, Sumaya and Yusuf, for always giving me an added reason for looking forward to coming home, and my sister Muna for her support and encouragement. Lastly, special thanks are due to my parents their support and patience, which dates back to long before I moved to Cambridge. This thesis is dedicated to them.

Name: Mohamed Iman Ainte
Title: NMR Techniques for Measuring Transport Phenomena in Microporous Materials

Abstract

The primary aim of this thesis is to investigate and quantify the self-diffusion processes of gaseous molecules adsorbed in industrially relevant microporous zeolite materials using Pulsed Field Gradient Nuclear Magnetic Resonance (PFG NMR). The main body of this work involves the use of weakly adsorbing hydrocarbon gases (CH_4, C_2H_6 and C_3H_8) adsorbed in a large pore β-zeolite structure. This thesis describes the development of a solely PFG NMR based technique for measuring the molecular displacements of these species at varying length-scales. This enabled the characterisation of self-diffusion regimes across zeolite beds and within individual zeolite crystallites. The characterisation of self-diffusion processes within single zeolite crystallites was critical with respect to accounting for quantitative discrepancies reported in the literature between PFG NMR and alternative measurement techniques. This approach also revealed that the transitions in the Gaussian probability distributions of the molecular displacements in the aforementioned self-diffusion regimes could be recorded by varying the experimental time-scale for observing molecular motion. This technique was extended to characterise the self-diffusion processes of the aforementioned hydrocarbons in small (≤ 1 μm) and large (≥ 15 μm) zeolite crystallites to investigate the dependence of this technique on zeolite geometry. It was found that the self-diffusion coefficients within single crystallites were in good agreement with one another, despite their differing crystallite geometries. This technique was subsequently used to study the self-diffusion behaviour of two-component hydrocarbon gaseous mixtures with differing sorption properties co-adsorbed in β-zeolite. Excellent chemical shift resolution was obtained for chemically similar species using NMR spectroscopy, relaxometry and diffusometry without the use of Magic Angle Spinning (MAS). This connoted that conventional PFG NMR is capable of precisely characterising individual species in real world multi-component systems.

This thesis also describes the self-diffusion of ammonia in small pore chabazite structures, which are typically used in Selective Catalytic Reduction (SCR) processes. It was found that the self-diffusion coefficient of this strongly adsorbing species increased with molecular loading up to a certain point. This peculiar behaviour implied a strong concentration and inter-molecular dependence within the zeolite structure.

Lastly, the techniques which were developed at high magnetic field strengths (300 MHz) were transferred to a lower field strength (43 MHz) benchtop spectrometer at the Johnson Matthey Technology Centre (JMTC). This describes the first characterisation of mass transport behaviour of weakly interacting sorbates in zeolites using a portable spectrometer. This presents an excellent opportunity for future off-line molecular displacement measurements to be made for complex and real-world systems in a matter of minutes.

Collaborative publications

Zhu, Q., Moggridge, G.D., Ainte, M., Mantle, M.D., Gladden, L.F., D'Agostino, C., (2016). Adsorption of pyridine from aqueous solutions by polymeric adsorbents MN200 and MN500. Part 1: Adsorption performance and PFG NMR studies. Chem. Eng. Journ. 306: 67-76.

Zhu, Q., D'Agostino, C., Ainte, M., Mantle, M.D., Gladden, L.F., Ortona, O., Paduano, L., Ciccarelli, D., Moggridge, G.D., (2016). Prediction of mutual diffusion coefficients in binary liquid systems with one self-associating component from viscosity data and intra-diffusion coefficients at infinite dilution. Chem. Eng. Sci. 147: 118-127.

Table of contents

Nomenclature

$\boldsymbol{B}_0$	Static magnetic field vector [T]
$\boldsymbol{B}_1$	Applied transverse magnetic field [T]
BEA	Beta zeolite framework [-]
b	b-factor [s m^{-2}]
CHA	Chabazite framework [-]
c	Concentration [mol m^{-3}]
D	Intrinsic, unrestricted diffusion coefficient [m^2 s^{-1}]
D_0	Corrected diffusion coefficient [m^2 s^{-1}]
D_1'	Diffusion coefficient of molecules in region one [m^2 s^{-1}]
D_2'	Diffusion coefficient of molecules in region two [m^2 s^{-1}]
$D_{1,2}'$	Diffusion coefficient from region one to two [m^2 s^{-1}]
$D_{2,1}'$	Diffusion coefficient from region two to one [m^2 s^{-1}]
D_{AB}	Fickian diffusion coefficient [m^2 s^{-1}]
D_{eff}	Effective diffusion coefficient [m^2 s^{-1}]
D_{inter}	Inter-crystalline diffusion coefficient [m^2 s^{-1}]
D_{intra}	Intra-crystalline diffusion coefficient [m^2 s^{-1}]
D_k	Knudsen diffusion coefficient [m^2 s^{-1}]
$D_{long-range}$	Long-range diffusion coefficient [m^2 s^{-1}]
d	Diameter of the diffusing species [m]
d_{inter}	Effective pore diameter of the inter-particle space [m]

E	Zeeman interaction energy [J]
eQ	Electric quadrupolar moment [C m]
FWHM, Δv	Full width at half maximum [Hz]
f	Magnetic field gradient with a negative amplitude [T m^{-1}]
G_0	Background gradient [T m^{-1}]
g	Magnetic field gradient with a positive amplitude [T m^{-1}]
h	Planck's constant [J s]
I	Spin quantum number [-]
J_{AB}	Rate of transfer of species A per unit area (Molar flux) [mol m^{-2} s^{-1}]
K	Adsorption equilibrium constant [-]
k_B	Boltzmann's constant [J K^{-1}]
$\boldsymbol{M}$	Net magnetisation or bulk magnetic moment [T]
M_A	Molecular weight [g mol^{-1}]
$M_{x,y}$	Magnetisation in the x-y plane [T]
M_z	Magnetisation along the z-axis [T]
m	Magnetic quantum number [-]
m	Mass of the diffusing species [g]
m_g	Adsorbed mass [g]
m_{wz}	Molecular weight of zeolite [g mol^{-1}]
m_z	Mass of zeolite [g]
N_A	Avogadro's number [mol^{-1}]
NO_x	Nitrous oxide gases [-]
n	Number of molecules [-]

$\boldsymbol{P}$	Angular momentum [J s]
P	Adsorbed pressure [bar]
p^0	Reference pressure [bar]
p_i	Conditional probability that a molecule moves from a given region [-]
p_1'	Population of molecules in region one [-]
p_2'	Population of molecules in region two [-]
p_1	Manifold pressure [bar]
p_2	NMR tube pressure [bar]
p_{gas}	Gas phase population [-]
p_i	Partial pressure of component i [bar]
q	Dynamic reciprocal space vector [m^{-1}]
R	Gas constant [J mol^{-1} K^{-1}]
R_1	Longitudinal relaxation rate [s^{-1}]
$\langle (\boldsymbol{r'} - \boldsymbol{r})^2 \rangle$	Root mean squared displacement in three spatial dimensions [m]
r	Distance travelled by spins between gradient pulses [m]
r	Radius of diffusing species [m]
r.f	Radiofrequency [-]
r_{pore}	Pore radius [m]
S/S_0	Normalised signal intensity in a PFG NMR experiment [-]
SNR	Signal-to-Noise Ratio [-]
S_{gas}	Gas phase signal [a.u.]
S_{bed}	Signal from zeolite bed [a.u.]

T	Longitudinal storage time interval in a PFG NMR experiment [s]
T_1	Spin-lattice (longitudinal) relaxation time constant [s]
T_2	Spin-spin (transverse) relaxation time constant [s]
T_2'	Reversible spin-spin relaxation time constant [s]
T_2^*	Total apparent spin-spin relaxation time constant [s]
T_q	Quadrupolar relaxation time constant [s]
T_R	Recycle time [s]
t_d	Delay time between 180° and 90° pulses in T_1-T_2 pulse sequence [s]
t_{pulse}	Duration of r.f. pulse [s]
v	Thermal velocity [m s^{-1}]
v_1	Manifold volume [m^3]
v_2	NMR tube volume [m^3]
v_b	Total volume occupied by zeolite powder in NMR tube [m^3]
v_m	Monolayer volume [m^3]
v_z	Zeolite bed volume [m^3]
$\langle (z' - z)^2 \rangle$	Root mean squared displacement in the z-direction [m]

Greek letters

γ	Gyromagnetic ratio [rad T^{-1} s^{-1}]
Δ	Observation time in a PFG NMR experiment [s]
δ	Duration of pulsed field gradient in a PFG NMR experiment [s]
δ_1	Delay time which precedes a gradient pulse in a PFG NMR experiment [s]
δ_2	Delay time which follows a gradient pulse in a PFG NMR experiment [s]

δ_{ppm}	Chemical shift [ppm]
ε	Zeolite bed solid fraction [-]
λ	Mean free diffusion pathway length-scale [m]
λ_{gas}	Diffusion pathway for the bulk gas phase [m]
$\boldsymbol{\mu}$	Magnetic moment [J T^{-1}]
μ_i^0	Chemical potential of component i at a reference state [J mol^{-1}]
μ_i	Chemical potential of component i [J mol^{-1}]
σ	Collision diameter [m]
τ_1	Residence time of the molecules in region one [s]
τ_2	Residence time of the molecules in region two [s]
τ_i	Mean residence time of the molecules [s]
ϕ	Void fraction of zeolite bed [-]
Ψ	Normalised echo attenuation [-]
Ω	Lennard-Jones interaction integral [a.u.]
ω_0	Larmor frequency [rad s^{-1}]

Chapter 1

Introduction

1.1. Introduction to porous materials in industrial chemical engineering and catalysis

Over 80% of industrial processes utilise heterogeneous catalysis (Bravo-Suarez *et al*. 2013). Diffusion plays a critical role in such processes as it is often the rate limiting step in determining product formation and distribution, as illustrated in figure 1.1. Therefore, understanding the molecular dynamics of industrially relevant catalytic systems is paramount with respect to optimising catalytic efficacy. The applicability of heterogeneous catalysts for certain industrial processes is governed by the process operating conditions, the phase, size and surface interactions of the feedstock material(s) with the solid catalyst material. Heterogeneous catalyst materials are typically on the nanometre scale in pore size and are hence classified as nano-porous materials.
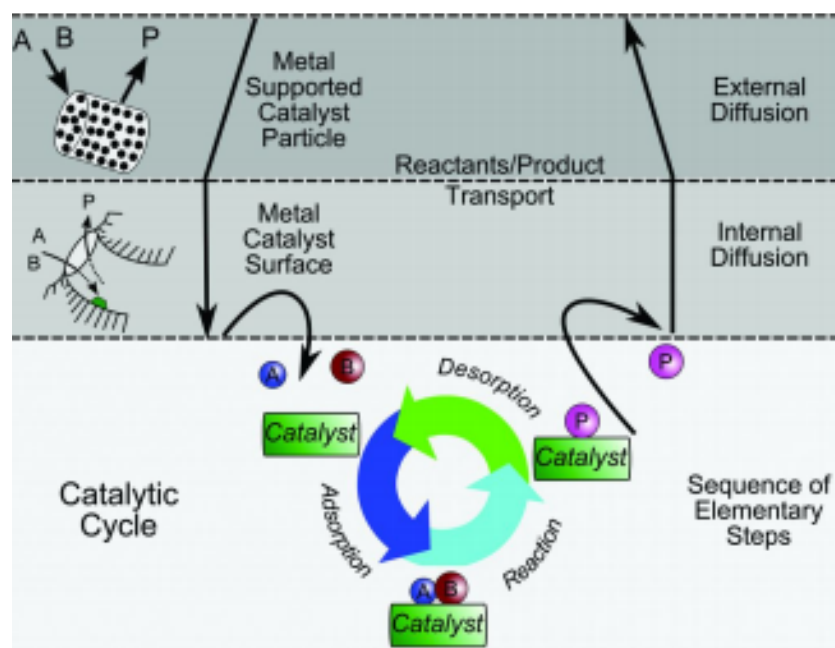
Figure 1.1: Representation of the steps involved in a typical heterogeneous catalysis cycle (Bravo-Suarez *et al*. 2013).

The International Union of Pure and Applied Chemistry (IUPAC) further sub-categorises nano-porous materials into three groups based on their pore size as elucidated in figure 1.2: microporous, mesoporous and macroporous (Sing *et al*. 1984). These materials are ideal candidates for industrial catalytic processes, either as support or catalyst materials, due to their pore structures and large geometric volumes. These properties enable vast quantities of feedstock to be converted into specific and desirable products. Macro-porous materials are typically used in applications which involve the formation of large and/or aromatic compounds such as Friedel-Crafts alkylation processes (Chiu *et al*. 2004). Recent advances in regenerative medicine have also shown that macroporous materials are excellent candidates as scaffold materials in tissue engineering, as large pore hierarchies promote healthy tissue development (Han *et al*. 2013).
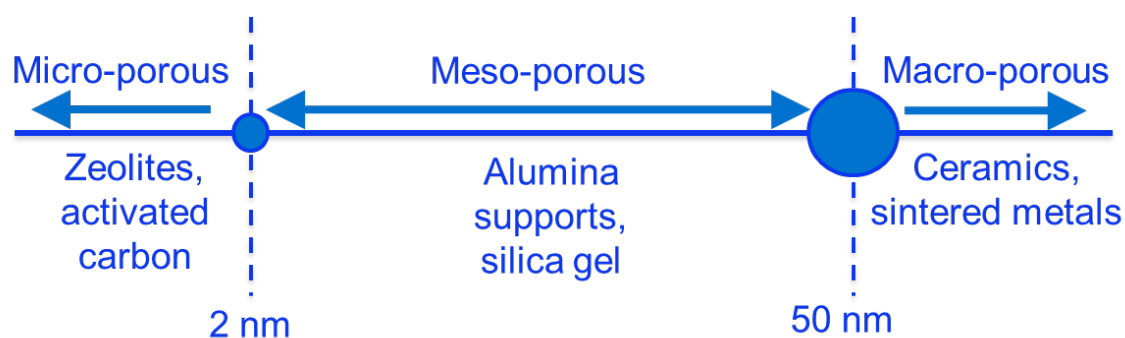
Figure 1.2: Categories of nano-porous materials and some examples.

Mesoporous and microporous materials are typically used in industrial processes which involve the formation of smaller hydrocarbon molecules. Microporous zeolite materials are particularly adept at performing such tasks due to their geometric structure and thermal stability, in which the latter is a fundamental porous material characteristic. This is because industrial operations typically occur at elevated temperatures and pressures. Microporous zeolites are often referred to as "molecular sieves" as they possess a "shape-selective" quality. This implies that the geometry of the zeolite may guide the formation of certain products, whilst inhibiting the formation of undesirable intermediates and/or by-products (Rollmann 1977). An example of this is typified by the Methanol-to-Olefin (MTO) process, which has emerged as a highly efficient technique which is capable of producing high yields of light olefins and light aliphatic compounds. These products have a significant market demand across a range of industries throughout the world, such as the energy, plastics and fine chemicals industries (Yue *et al*. 2012). The MTO process typically uses a microporous Silica-Alumina-Phosphorous material of a particular pore size (such as SAPO-34), which is introduced in chapter 7. Alternatively, a Zeolite Socony Mobil-5 (ZSM-5) material which possesses a pentasil ring structure with a Mordenite Framework Inverted (MFI) framework is used (Yarulina *et al*. 2016). Both materials possess pore windows which are less than 5.5 Å in diameter, which are connected to larger cages and intersecting channels respectively, possessing large pore volumes which exceed 0.17 $cm^3 g^{-1}$ (Krishna 2012). Therefore, light olefins and light aliphatic components may pass through the channels of the materials, since they do not exceed 4.9 Å in diameter (Krishna 2012). Figure 1.3 shows that the aforementioned desired products are formed in conjunction with large(r) cyclic and aromatic compounds which amass in the pore cavities, which is often referred to as a "hydrocarbon pool" (Tian *et al*. 2015). However, the desorption

of these compounds is minimised due to the restrictive size of the pore windows. Although this is to the detriment of the overall efficiency of the zeolites, as the accumulation of larger molecules in the pore network ultimately results in catalyst deactivation *via* coking (Chen *et al*. 2012).
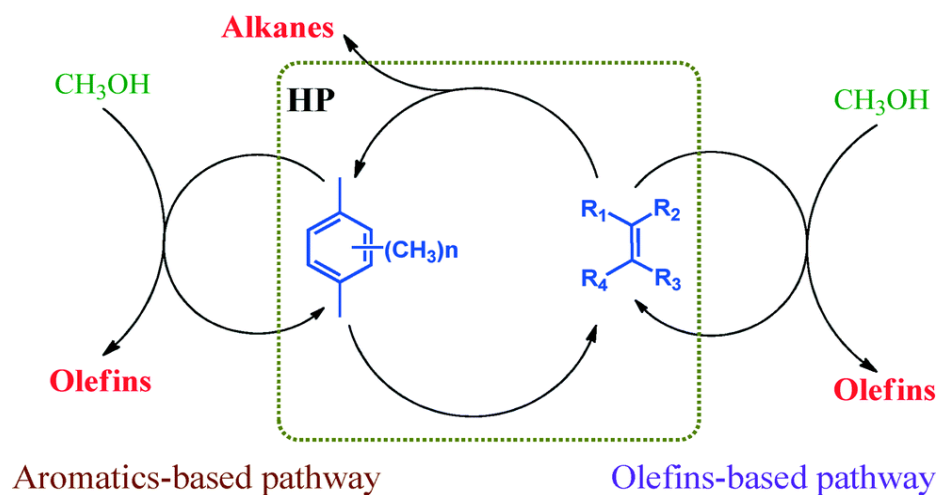
Figure 1.3: Simplified representation of an industrial MTO process (Wang *et al*. 2014).

Some of the microporous zeolite structures of interest to Johnson Matthey are β-zeolite and chabazite, which are introduced in chapters 5 and 7 respectively and these are the focus of the work in this thesis. Both materials are used in Selective Catalytic Reduction (SCR) processes which utilise ammonia (*via* urea). This process converts noxious nitrogen oxide gases (NO_x), which are formed in the combustion chamber of an engine, into benign and atmospherically friendly products, as shown by the schematic in figure 1.4.
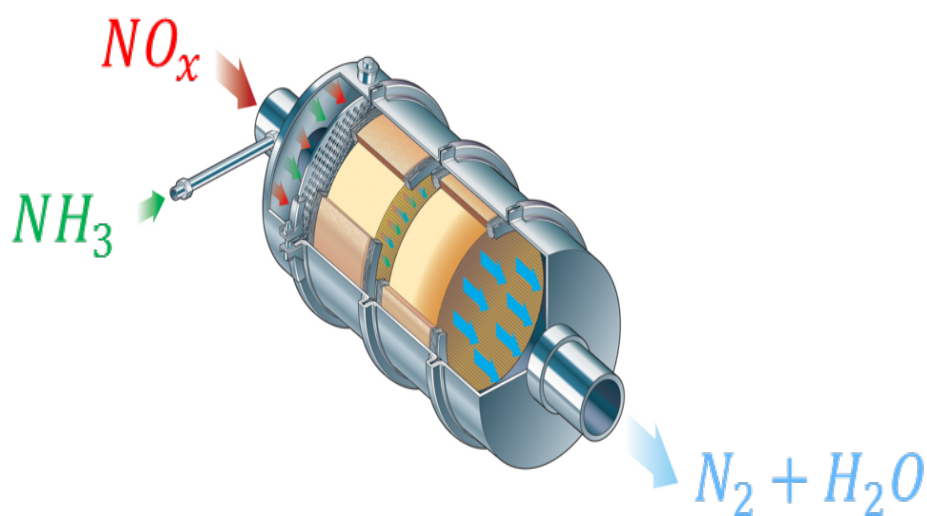
Figure 1.4: Representation of an SCR process in a catalytic converter (Copyright Johnson Matthey Plc 2007).

SCR processes occur in power plant operations, catalytic converters (which are found in conventional diesel engines in automotive vehicles) and other pollution sources. Combustion in diesel engines occurs under lean conditions in the presence of excess oxygen, and injected urea (which is converted to ammonia in the exhaust) acts as a reducing agent and its role may be summarised by the following equations (Arnarson *et al.* 2017):

$$4NH_3 + 4NO + O_2 \rightarrow 4N_2 + 6H_2O \qquad\qquad 1.1$$

$$4NH_3 + 2NO + 2NO_2 \rightarrow 4N_2 + 6H_2O \qquad\qquad 1.2$$
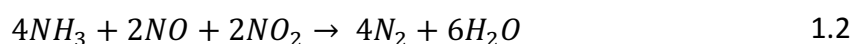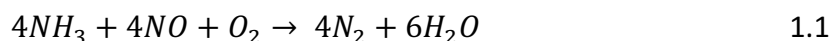
SCR catalyst systems can enable more than 99% of nitrogen oxide products to be eliminated and, in combination with other catalyst components, can simultaneously eradicate unburnt hydrocarbons and carbon monoxide (DiGiulio *et al.* 2014). Figure 1.5 shows some examples of modern day sources of pollution, the majority of which arise due to combustion processes.
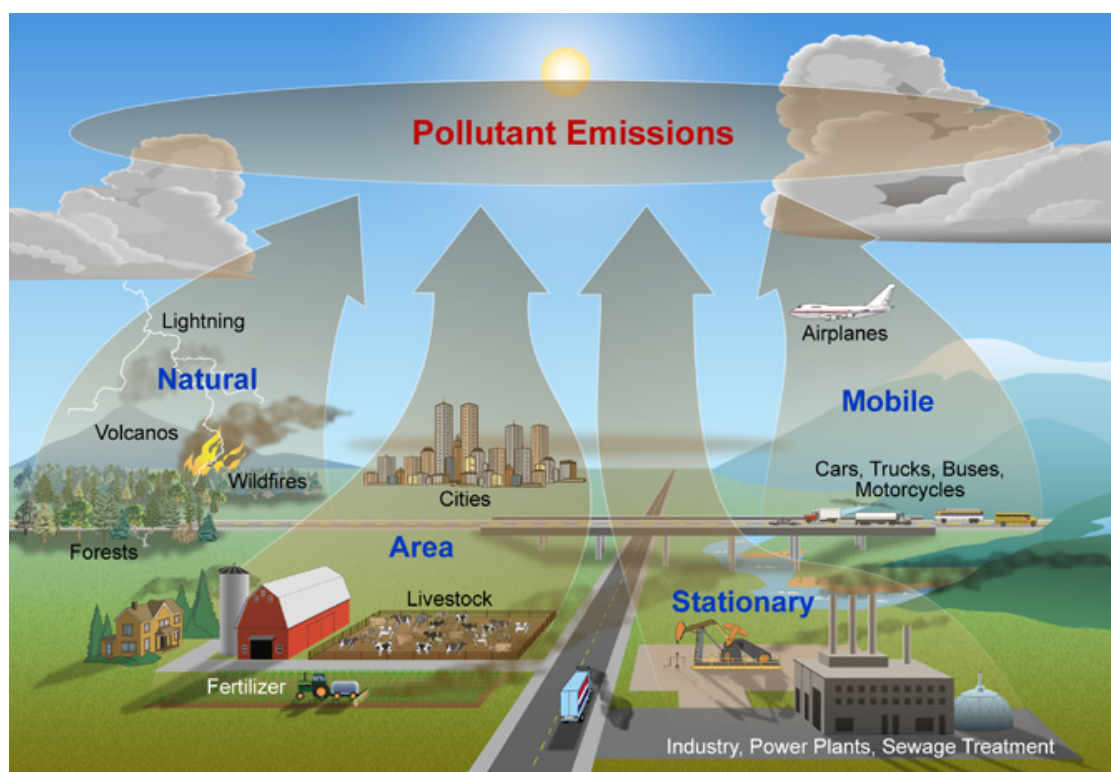
Figure 1.5: Sources of modern day pollution (U.S. Department of the Interior 2017).

Optimising the efficacy of microporous zeolites by comprehensively characterising the molecular dynamics processes of the molecules involved in SCR is therefore of considerable environmental importance. The challenges faced with respect to measuring molecular displacements using conventional experimental techniques are discussed in chapters 3 - 7.

Studying the molecular transport behaviour of the molecules central to the SCR zeolites is one of the aims of this thesis and therefore ammonia is used in some studies, which will be discussed further in chapter 7. However, NO_x is substituted with materials which have similar surface interactions and kinetic properties for safety reasons, which will be discussed further in chapter 4, and also because it does not contain protons.

1.2. Scope of thesis

Pulsed Field Gradient Nuclear Magnetic Resonance (PFG NMR) is a powerful technique which has emerged over the past few decades to characterise the diffusion behaviour of molecules in bulk and under restricted conditions (Kärger and Ruthven 1992). The aim of this thesis is to use conventional and modified PFG NMR protocols to study the diffusion of gaseous and adsorbed phase species in microporous chabazite (CHA) and β-zeolite (BEA) frameworks. The particular focus is on the characterisation of the different diffusion regimes which typically exist in packed, microporous zeolite beds. NMR spectroscopy and relaxometry are used to aid with extracting the parameters of interest from a molecular transport perspective. Subsequently, the work is extended to study the adsorption and diffusion behaviour of hydrocarbon species co-adsorbed in these zeolite materials. Additionally, the aim of this thesis is to improve insights into the large disparities reported in the literature for the self-diffusion coefficients of molecules adsorbed in microporous zeolites characterised using alternative measurement techniques.

One of the many advantages of working with an industrial collaborator (Johnson Matthey) included benefiting from their industrial expertise with respect to performing complete porous material characterisation. This included conducting gas sorption isotherm studies, Scanning Electron Microscopy (SEM), X-Ray Diffraction (XRD) and X-ray Photoelectron Spectroscopy (XPS) techniques. These characterisation methods were carried out prior to the PFG NMR experiments. Another advantage included the use of a 43 MHz benchtop NMR spectrometer, which enables the techniques developed at a higher magnetic field strength to be transferred to study the diffusion of the aforementioned molecules of interest. This gives room for providing Johnson Matthey

with an in-house PFG NMR method for characterising transport in (micro) porous media. The advantages of using a benchtop NMR spectrometer to perform such characterisations will be discussed in chapter 8.

1.3. Outline of chapters

Chapter 1 provides background information into the different classifications of porous materials and their typical applications. The aims of the thesis are stated and the rationalisation for using PFG NMR to achieve these aims is outlined.

Chapter 2 is an introduction to the theory and principles of NMR relevant to the work presented in this thesis.

Chapter 3 is a literature survey of the various types of diffusion processes which are typically found in porous materials and the techniques used to characterise them. Comparisons are drawn between the different techniques, in addition to detailing their respective strengths and weaknesses. A summary table of literature self-diffusion coefficients, obtained using PFG NMR, reported in the literature is also included.

Chapter 4 describes the methods which are used to prepare the gaseous and adsorbed phase samples prior PFG NMR analysis. Attempts to improve the Signal-to-Noise Ratios (SNRs) of NMR measurements performed using conventional diffusometry protocols are also outlined.

Chapter 5 concerns the development of a solely PFG NMR based method capable of characterising the diffusion regimes of gaseous and liquid phase molecules in large pore β-zeolite structures at varying molecular displacement length-scales. Comparisons are also made with β-zeolite materials which differ in crystallite size.

Chapter 6 builds on the methods established in chapter 5 to perform PFG NMR of two-component gaseous mixtures with varying sorption properties co-adsorbed in β-zeolite. ^{1}H-^{2}H NMR relaxometry is also performed using protonated and deuterated guest molecules to compare the relaxation time constants of gaseous and liquid phase isotopes.

Chapter 7 details the use of small pore chabazite structures to observe the molecular dynamics of weakly and strongly adsorbing molecules as a function of molecular loading and temperature.

Chapter 8 assesses the suitability of using conventional PFG NMR techniques at 43 MHz to measure the molecular displacements of the systems introduced in chapters 5 and 6.

Chapter 9 presents the main conclusions of this thesis and gives a brief outlook on potential areas of future research.

1.4. References

Arnarson, L., Falsig, H., Rasmussen, S.B., Lauritsen, J.V., Moses, P.G., (2017). A complete reaction mechanism for standard and fast selective catalytic reduction of nitrogen oxides on low coverage VO_x/TiO_2 (001) catalysts. J. Catal. 346: 188-197.

Bravo-Suarez, J.J., Chaudhari, R.V., Subramaniam, B., (2013). *Novel materials for catalysis and fuels processing. Design of heterogeneous catalysts for fuels and chemicals processing: an overview.* American Chemical Society.

Chen, D., Moljord, K., Holmen, A., (2012). A methanol to olefins review: Diffusion, coke formation and deactivation on SAPO type catalysts. Micropor. Mesopor. Mater. 164: 239-250.

Chiu, J.J., Pine, D.J., Bishop, S.T., Chmelka, B.F., (2003). Friedel-Crafts alkylation properties of aluminosilica SBA-15 meso/macroporous monoliths and mesoporous powders. J. Catal. 221: 400-412.

DiGiulio, C.D., Pihl, J.A., Parks II, J.E., Amiridis, M.D., Toops, T.J., (2014). Passive-ammonia selective catalytic reduction (SCR): Understanding NH_3 formation over close-coupled three way catalysts (TWC). Catal. Today. 231: 33:45.

Han, L.H., Lai, J.H., Yu, S., Yang, F., (2013). Dynamic tissue engineering scaffolds with stimuli-responsive macroporosity formation. Biomat. 34: 4251-5258.

Johnson Matthey, Automotive catalyst technologies. (2007). Ammonia-SCR system. [ONLINE] Available at: http://ect.jmcatalysts.com/catalyst-technologies-johnson-matthey/ammonia-scr-systems-johnson-matthey. [Accessed 21 March 2017].

Kärger, J., Ruthven, D., (1992). *Diffusion in zeolites and other microporous solids*. Wiley & Sons.

Krishna, R., (2012). Diffusion in porous crystalline materials. Chem. Soc. Rev. 41: 3099-3118.

National Park Service, U.S. Department of the Interior. (2017). Sources of Air Pollution. [ONLINE] Available at: https://www.nature.nps.gov/air/aqbasics/sources.cfm. [Accessed 21 March 2017].

Rollmann, L.D., (1977). Systematics of shape selectivity in common zeolites. J. Catal. 47: 113-121.

Sing, K.S.W., Everett, D.H., Haul, R.A.W., Moscou, L., Pierotti, R.A., Rouquérol, J., Siemieniewska, T., (1984). Reporting physisorption data for gas/solid systems. Pure. Appl. Chem. 57: 603-619.

Tian, P., Wei, Y., Ye, M., Liu, Z., (2015). Methanol to Olefins (MTO): from fundamentals to commercialisation. ACS Catal. 5: 1922-1938.

Yarulina, I., Goetze, J., Gücüyener, C., van Thiel, L., Dikhtiarenko, A, Ruiz-Martinez, J., Weckhuysen, B.M., Gascon, J., Kapetijn, F., (2016). Methanol-to-olefins process over zeolite catalysts with DDR topology: effect of composition and structural defects on catalytic performance. Catal. Sci. Technol. 6: 2663-2678.

Wang, C.M., Wang, Y.D., Xie, Z.K., (2014). Verification of the dual cycle mechanism for methanol-to-olefin conversion in HSAPO-34: a methylbenzene-based cycle from DFT calculations. Catal. Sci. Technol. 4: 2631-2638.

Yue, H., Zhao, Y., Ma, X., Gong, J., (2012). Ethylene glycol: properties, synthesis and applications. Chem. Soc. Rev. 41: 4218-4244.

Chapter 2

Nuclear Magnetic Resonance theory

2.1. Introduction

Nuclear magnetic Resonance was developed in the 1940s to initially study the chemical compositions of samples (Bloch 1946; Purcell 1946). NMR was subsequently advanced in the 1970s (Lauterbur 1973; Mansfield 1976) into a non-invasive imaging technique known as Magnetic Resonance Imaging (MRI) and is widely recognised as one of the most powerful tools in diagnostic radiology. MRI and NMR techniques have since been extended to non-invasively study transient and steady-state systems in situ (Gladden 1994). NMR has emerged as a potent and versatile technique for characterising a wide range of industrially relevant systems, as it can be used to accurately study chemical compositions, environments, spatial positions and molecular motion, or any combination of these. Many excellent texts which discuss these magnetic resonance subjects are widely available (Fukushima and Roeder 1981; Callaghan 1993; Levitt 2001) and some of the basic principles which are relevant to the work in this thesis are discussed in this chapter.

2.2. Nuclear spin

NMR is a phenomenon which is underpinned by the quantum mechanical properties of atomic nuclei, which are assumed to behave as though they are spinning about an axis, which is referred to as nuclear spin. The magnetic moment of a nucleus, $\boldsymbol{\mu}$, is related to its angular momentum, $\boldsymbol{P}$, by:

$$\boldsymbol{\mu} = \gamma \boldsymbol{P}$$
2.1

where γ is the gyromagnetic ratio, which is a property of the nucleus under observation. For ^{1}H, γ is 2.68×10^8 rad s^{-1} T^{-1} and for ^{2}H, γ is 4.11×10^7 rad s^{-1} T^{-1}. The magnitude of the spin angular momentum is quantised and may be expressed as:

$$\boldsymbol{P} = \frac{h}{2\pi}\sqrt{I(I+1)}$$
2.2

where I is the spin quantum number and h is Planck's constant, 6.63×10^{-34} J s. Each nucleus possesses a unique value of I and its associated nuclear spin may take up $2I + 1$ levels, which is dictated by the magnetic quantum number, m, and may take the values $-I$, $-I + 1$, ….,$I - 1$, I. In the absence of a magnetic field, spin states are said to be degenerate. Nuclei with an even number of protons and neutrons will have a value of I which is equal to 0 and are subsequently rendered NMR inactive, as they lack magnetic properties. Nuclei with an odd mass number will have half integer values of I, whereas nuclei with odd atomic numbers and even mass numbers will have integer values. Therefore, spin 1 nuclei such as ^{2}H may take up three spin states by either absorbing or emitting energy, with the magnetic quantum number, m, equal to - 1, 0 or 1, giving two energy transitions when the spins are not degenerate. Spin ½ nuclei such as ^{1}H are able to take up two spin states, with m equal to - ½ or + ½, giving one energy transition when the spins are not degenerate.

Placing a sample which possesses a spin ½ nucleus in an external, static magnetic field, $\boldsymbol{B}_0$, results in the z-component either aligning in a parallel or anti-parallel orientation to the magnetic field. As such, the energy states of spin ½ nuclei are interchangeably referred to as parallel and anti-parallel states or α- and β-states respectively, with the parallel or α-states possessing a lower energy. An example of the possible energy levels for a spin ½ nucleus is shown in figure 2.1. Placing nuclei in external, static magnetic fields lifts the degeneracy of the assumed energy levels. The interaction energy, E, between the magnetic moment and the external magnetic field is known as the Zeeman interaction and may be expressed as:

$$E = -m\frac{h}{2\pi}\gamma \boldsymbol{B}_0$$
2.3

The (external) energy which is required to induce a transition between the α- and β- energy states is given by:

$$\Delta E = \pm\, h\nu = \pm\, \frac{h}{2\pi}\gamma \boldsymbol{B}_0 \qquad\qquad 2.4$$

$$\boldsymbol{B}_0 \neq 0$$

High energy, β, state: $m = +\frac{1}{2}$

$$\Delta E = \frac{h}{2\pi}\gamma B_0$$

Low energy, α, state: $m = -\frac{1}{2}$

$$\boldsymbol{B}_0 = 0$$

$$\boldsymbol{B}_0 \neq 0$$
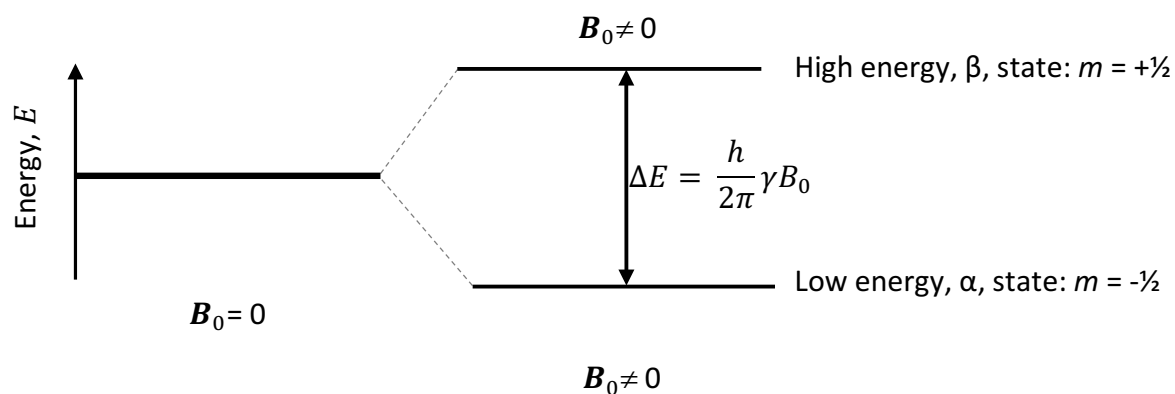
Figure 2.1: Energy level diagram for a spin ½ nucleus.

The frequency of electromagnetic radiation which is required to achieve such transitions is expressed as:

$$\nu = \frac{\gamma \boldsymbol{B}_0}{2\pi} \qquad\qquad 2.5$$

The electromagnetic frequency may also be expressed as an angular frequency, which is known as the Larmor frequency:

$$\omega_0 = \gamma \boldsymbol{B}_0 \qquad\qquad 2.6$$

The populations of the α- and β-energy states when placed in a static magnetic field at thermal equilibrium may be expressed using a Boltzmann distribution:

$$\frac{N_\beta}{N_\alpha} = exp\left(-\frac{\Delta E}{k_B T}\right) \qquad\qquad 2.7$$

There is a slight preponderance of spins in the lower energy state at room temperature. For highly sensitive nuclei such as ^{1}H, the ratio of the α- to the β-energy states is 1.00005. This

disparity in the energy states results in a net magnetisation, M, which at equilibrium will be aligned in the direction of the applied magnetic field, with the net magnetisation in the transverse (x-y) plane equal to zero. The excess number of spins in the α-state may be represented as a number of magnetic moments distributed randomly around a precessional cone, as illustrated in figure 2.2. Therefore, the whole spin ensemble may be represented by a bulk magnetisation vector, M.
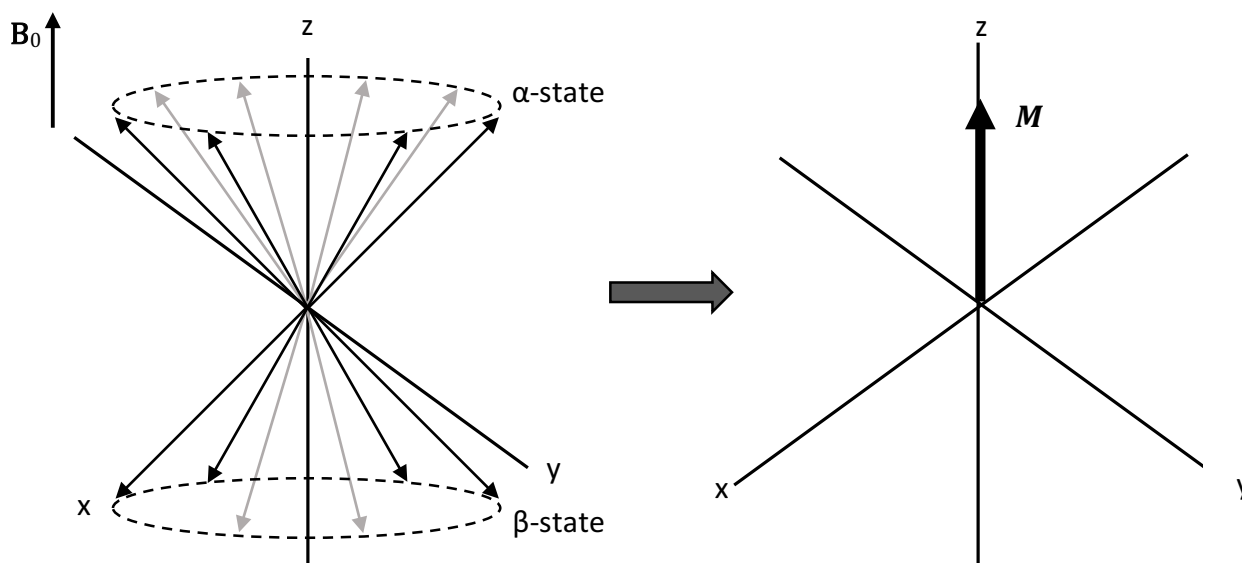
Figure 2.2: Representation of the magnetisation vector model.

2.3. Spin excitation and the rotating frame of reference

The NMR experiment is based on the excitation of individual nuclear spins (and thus effectively the bulk magnetisation vector, M) from thermal equilibrium and subsequently detecting their eventual return to equilibrium. In a typical NMR experiment, a cryogenically cooled, superconducting magnet is the source of B_0. Applying a magnetic field, B_1, which oscillates at the Larmor frequency provides the energy required to achieve magnetic resonance. This field is perpendicular to the static magnetic field and results in the generation of a radiofrequency (r.f.) signal. The application of B_1 fields in the form of short, typically for a few microseconds, pulses of electromagnetic radiation enables the magnetisation vector to be manipulated. Whilst by convention r.f. pulses are applied about the x-direction, they can

be applied in any direction in the transverse plane by altering their phase with respect to one another.

Consequently, the magnetisation vector, $\boldsymbol{M}$, tips away from thermal equilibrium and eventually, *via* unrestricted precession at ω_0, returns to its equilibrium position. This process induces an oscillating current in the r.f. coil, which is detected as an NMR signal. The oscillating signal in the time domain is known as a Free Induction Decay (FID) and upon Fourier transformation, yields a frequency domain NMR spectrum. The interaction between the spin ensemble in the static magnetic field, $\boldsymbol{B}_0$, and the oscillating field, $\boldsymbol{B}_1$, may be described using the rotating frame of reference and classical mechanics. The magnetic moment may be related to an aligning torque and is expressed as:

$$\frac{d\boldsymbol{M}}{dt} = \gamma \boldsymbol{M} \times \boldsymbol{B} \qquad\qquad 2.8$$

The solution to equation 2.8 in which $\boldsymbol{B}$ is a magnetic field, which for a given amplitude of $\boldsymbol{B}_0$ yields a precession of the magnetisation at the Larmor frequency: $\omega_0 = \gamma \boldsymbol{B}_0$ (Lauterbur 1973). Applying a transverse magnetic field, $\boldsymbol{B}_1$, oscillating at ω_0 results in the simultaneous precession of the magnetisation vector about $\boldsymbol{B}_1$. The amplitude of the induced field is significantly lower than $\boldsymbol{B}_0$, and therefore precession about $\boldsymbol{B}_1$ is much slower than that about $\boldsymbol{B}_0$. The complex motion of $\boldsymbol{M}$ about $\boldsymbol{B}_0$ and $\boldsymbol{B}_1$ which arises due to the interaction of the two magnetic fields is referred to as nutation and is often simplified using a rotating frame of reference as an example. The rotating frame of reference rotates around the $\boldsymbol{B}_0$ field at the Larmor frequency. The angle, θ, by which the magnetisation vector rotates is dependent on the time for which the r.f. pulse is applied, t_{pulse}, and is given by:

$$\theta = \omega_1 t_{pulse} \qquad\qquad 2.9$$

The pulse duration is inversely proportional to the range of Larmor frequencies that it excites. Typically in NMR, the r.f. pulses will be chosen to have a wide excitation band width so that the spin manipulation is equal for all Larmor frequencies present in the sample. Such a pulse is referred to as a non-selective or "hard" excitation and typically has a duration of a few microseconds and is rectangular in shape. In some applications, it is beneficial to excite only

a narrow frequency range, for example, in a slice selective or chemically selective experiment. In these cases, "soft" pulses of much longer duration and consequently lower amplitude are used. The application of a 90° pulse rotates the magnetisation vector from its equilibrium position into the transverse plane, whilst a 180° pulse rotates it into the negative z-axis. This is shown in figure 2.3.
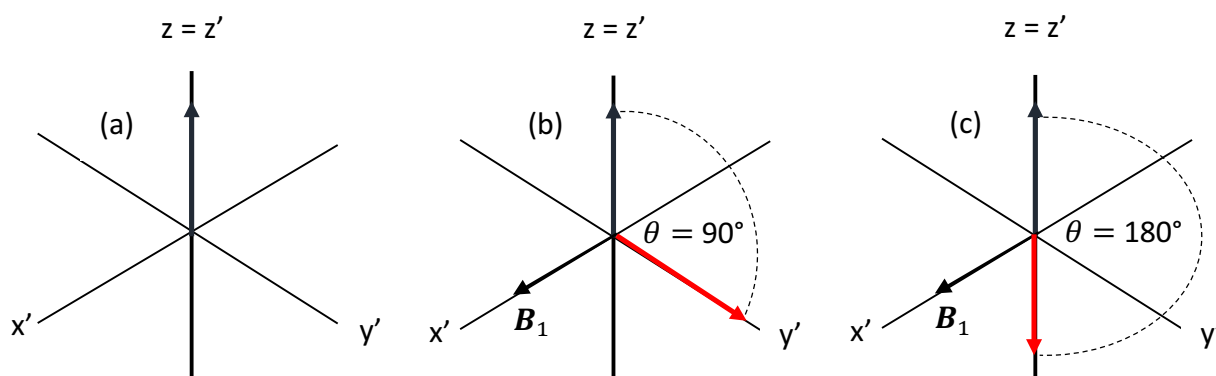
Figure 2.3: Representation of the effect of applying the B_1 field on the magnetisation vector in the rotating frame: (a) at equilibrium, (b) following the application of a 90° r.f. pulse and (c) following the application of a 180° r.f. pulse. x', y' and z' indicate that the coordinate system is represented in the rotating frame.

The rotating frame of reference, in which a B_1 magnetic field possesses a given frequency, demonstrates that the effective field which is aligned with the direction of the constant B_0 field is equal to: $B_0 - \omega/\gamma$.

The application of an r.f. pulse which is on resonance, in which $\omega = \omega_0$, results in rotation about the applied B_1 field only, in which there is no z-component in the magnetic field. However, the application of an off resonance r.f. field causes the rotating frame magnetisation to possess a residual component in the z-direction, resulting in the magnetisation to precess about an effective magnetic field gradient, which is the vector sum of $B_0 - \omega/\gamma$ and B_1.
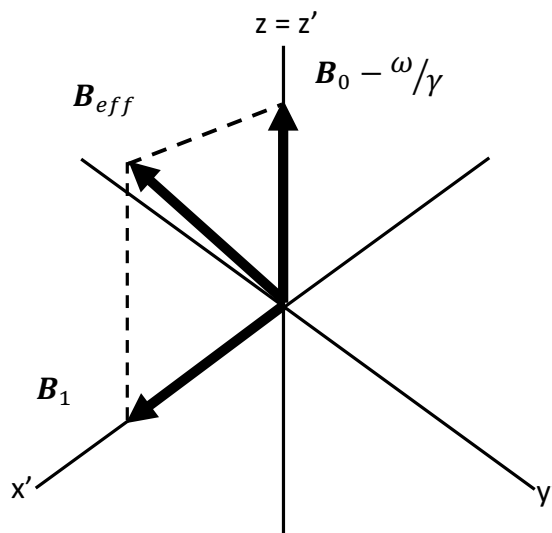
Figure 2.4: Effective magnetic field in the rotating frame of reference.

2.4. NMR relaxation

The application of a resonant r.f. excitation results in the perturbation of a spin system from its equilibrium position. Relaxation describes the precessional motion whereby the magnetisation vector emits excess energy and eventually returns to its equilibrium position. A brief description of the two main types of relaxation, which are known as spin-lattice relaxation and spin-spin relaxation, are outlined in this chapter. A more in-depth overview may be found in Pines and Slichter (1955) and Abragam (1961).

2.4.1. Spin-lattice relaxation

Spin-lattice is the process whereby following an excitation pulse, the magnetisation vector returns to its equilibrium position along the z-direction, *i.e.* parallel to the static, homogeneous field. This symbolises the exchange of energy which is absorbed as a result of the excitation pulse. Spin-lattice relaxation is also referred to as longitudinal relaxation, T_1 relaxation or signal recovery. According to Bloch theory of NMR, the restoration of the magnetisation along the z-direction, undergoing T_1 relaxation only, to equilibrium is expressed as follows:

$$\frac{dM_z}{dt} = -\frac{(M_z - M_0)}{T_1}$$
$$2.10$$

Using initial conditions of M_z ($t = 0$) = -M_z (0), the solution to the differential equation is:

$$M_z(t) = M_z(0)\,exp\left(-\frac{t}{T_1}\right) + M_0\left[1 - exp\left(-\frac{t}{T_1}\right)\right]$$
$$2.11$$

where $M_z(0)$ is the longitudinal magnetisation at $t = 0$. The T_1 relaxation time constant represents the time needed for M_z to change by 63%, and is dependent on the molecular structure and the lattice structure. It may also be affected by a number of factors such as temperature and viscosity, and tends to range from milliseconds to tens of seconds. The addition of paramagnetic species (e.g. Gd^{3+}, Mn^{2+}) to samples may significantly reduce T_1, by a process which is referred to as doping. The T_1 time constants reported in this thesis are measured using an inversion recovery pulse sequence, as shown in figure 2.5, although there are a number of alternative methods which may be used (Fukushima and Roeder 1981).
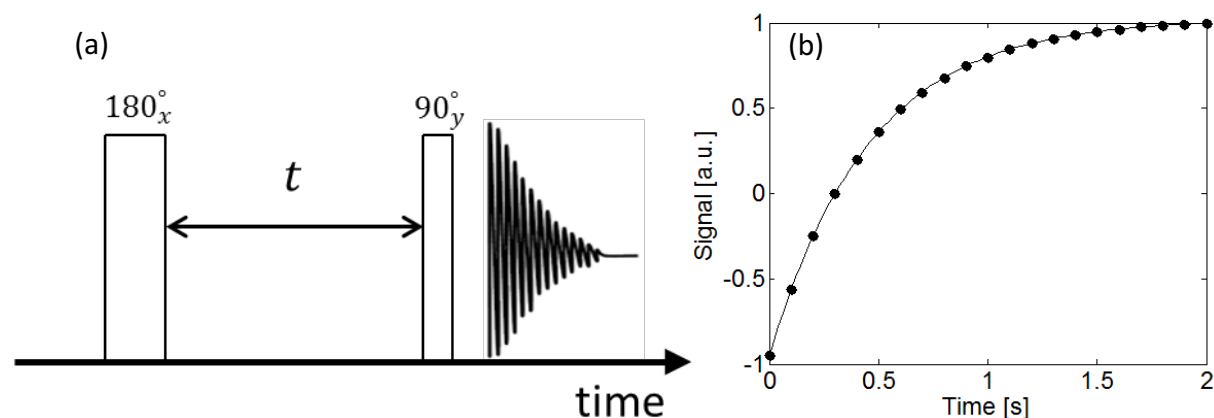
Figure 2.5: (a) T_1 inversion recovery pulse sequence and (b) T_1 inversion recovery plot. The solid line is a fit of the data (black dots) to equation 2.12.

From thermal equilibrium, the application of a 180_x° pulse causes the magnetisation vector to flip onto the negative z-axis by a process known as inversion. From this point, the magnetisation vector begins to recover along the longitudinal axis. Following a variable delay time, t, a 90_y° pulse is applied to place the magnetisation vector in the transverse plane, since the return to equilibrium cannot be detected along the z-axis. A recycle time of approximately $5 \times T_1$ is typically used, which results in a recovery of more than 99% of the magnetisation.

Plotting the z-component of the magnetisation vector as a function of t enables the determination of the T_1 time constant by fitting to the following function:

$$M_z(t) = M_z(0)\left[1 - 2exp\left(-\frac{t}{T_1}\right)\right]$$
(2.12)

2.4.2. Spin-spin relaxation

Spin-spin relaxation is an irreversible process whereby the individual nuclear spins lose phase coherence with one another in the x-y plane following the application of a $90°$r.f. excitation pulse. This governs the period of time over which a signal may be observed in an NMR experiment, as the superposition of spins with an equal and opposite phase negate one another. This results in an exponential decrease in the observed signal intensity, which may be described by the T_2 time constant. Unlike spin-lattice relaxation, this process does not result in surplus energy being removed from the spin system. Rather, an increase in the entropy of the spin system is observed due to a loss in phase coherence. Spin-spin relaxation is also referred to as transverse or T_2 relaxation, although it is not the sole source of spin relaxation in the transverse plane. It widely established that $T_2 \leq T_1$ in all instances (Callaghan 1993). The evolution of the magnetisation in the transverse plane is expressed by:

$$\frac{dM_{x,y}}{dt} = -\frac{M_{x,y}}{T_2}$$
(2.13)

The solution to this differential equation is:

$$M_{x,y}(t) = M_{x,y}(0)\exp\left(-\frac{t}{T_2}\right)$$
(2.14)

T_2 is commonly measured using either a Hahn echo (Hahn 1950) or Carr-Purcell-Meiboom-Gill (CPMG) (Carr and Purcell 1954; Meiboom and Gill 1959) pulse sequence, as shown in figure 2.6. Both techniques are based on the concept known as a spin echo. The former involves the application of a 90° pulse followed by a 180° pulse after a time, τ. The latter involves the application of a series of refocusing 180° pulses after the initial 90° excitation pulse, with shorter time delays. The advantage of the CPMG pulse sequence over the Hahn echo pulse sequence is that it refocuses the spins which are no longer in phase with one

another due to heterogeneities in the local magnetic field, i.e. a loss of phase coherence. This results in a reduced contribution from factors which have a detrimental impact on signal longevity, such as molecular diffusion. The dashed line corresponds to the end of a simple spin echo sequence. The time from the initial excitation pulse to the centre point of the echo is referred to as the echo time, T_E.
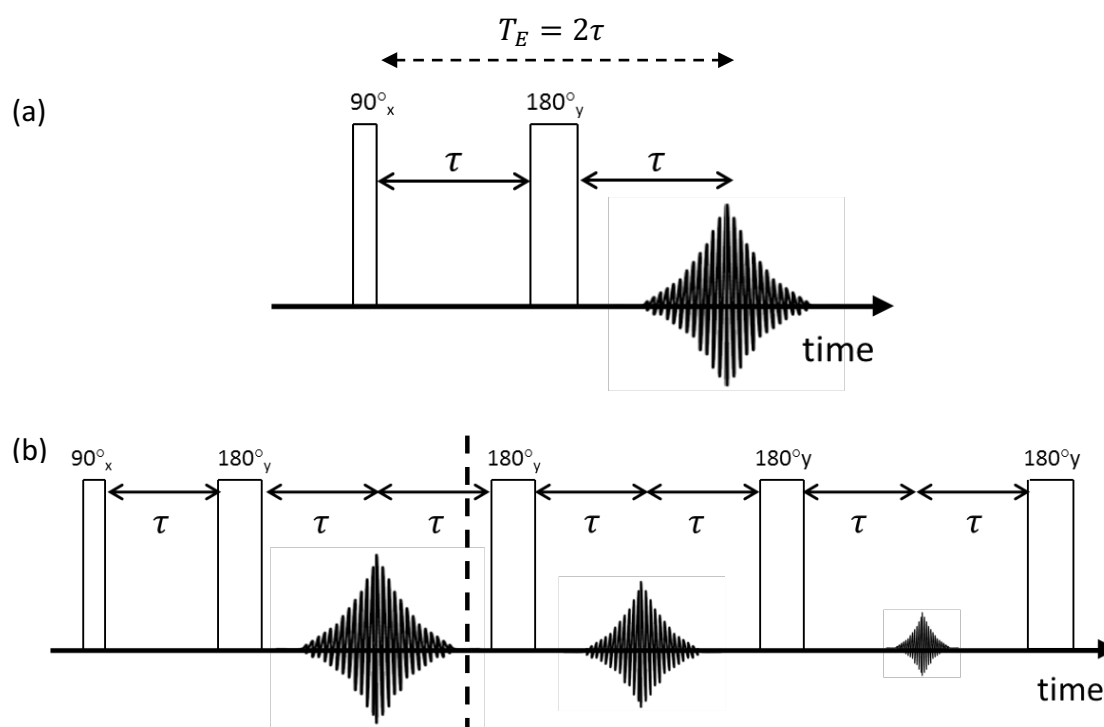
Figure 2.6: (a) Hahn echo and (b) CPMG pulse sequences.

2.4.3. Apparent transverse relaxation

Relaxation in the transverse plane may also be induced by inhomogeneity in the constant $\boldsymbol{B}_0$ field. Small local variations in the magnetic field (referred to as internal/background gradients) may arise as a result of hardware imperfections or due to magnetic susceptibility differences at phase boundaries within samples. Field inhomogeneities may be minimised by adjusting the shape of the magnetic field, by a process known as shimming. Variations in the magnetic field of $\Delta\boldsymbol{B}_0$ between two points in the spin system results in differences in the local Larmor frequency which may be described as follows:

$$\Delta\omega = \gamma\Delta\boldsymbol{B}_0 \qquad\qquad 2.15$$

Therefore, these variations in magnetic field results in spin ensembles precessing at varying rates. This subsequently leads to a dephasing of the magnetisation and transverse relaxation occurs, which is denoted by a time constant, T_2'. In the absence of diffusion or random motion, this is a reversible process, whereby the application of a 180° pulse refocuses any dephased spins. Thus, the total apparent transverse relaxation, T_2^*, is given by the sum of the irreversible and reversible transverse relaxation processes respectively:

$$\frac{1}{T_2^*} = \frac{1}{T_2} + \frac{1}{T_2'} \qquad\qquad 2.16$$

T_2^* relaxation processes therefore govern the attenuation of the time domain FID and may typically be described by an exponential function. As shown in figure 2.7, frequency domain NMR spectra are typically Lorentzian in shape, which is broadened by T_2^* relaxation. The T_2^* relaxation time constant may be calculated from the full width half maximum (FWHM) of the peak, Δv, *via*:

$$T_2^* = \frac{1}{\pi \Delta v} \qquad\qquad 2.17$$

For homogeneous systems such as liquids (with a single resonance frequency), T_2^* will approach the T_2 of the liquid. In heterogeneous systems, such fluids confined in porous media, phase boundaries which exist give rise to small magnetic field gradients which lead to differences in magnetic susceptibilities. This yields local field heterogeneities and broad linewidths, and thus $T_2 \neq T_2^*$.
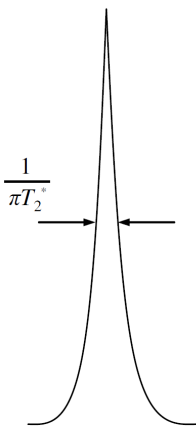
Figure 2.7: Fourier transform of the real part of an FID.

2.4.4. Relaxation time constants and correlation time

Spin-lattice and spin-spin relaxation are caused by fluctuating local magnetic fields which cause nuclei to flip between their available spin states. In the case of spin-lattice relaxation, the rate of this process is dependent on the probability that the local fields have a component which oscillates at the resonance frequency, ω_0.

The local field varies from one spin to another and therefore the precession frequency is slightly different for each spin. The consequence of this is that the precession frequencies of the individual moments will be out of step with one another. The main cause of these fluctuations in local magnetic fields at a nucleus is rotational motion of the molecule, referred to as molecular tumbling motion. The characteristic time for this motion may be defined as the rotational correlation time, τ_c. This corresponds to the average time required for a molecule to undergo a rotation of one radian from its starting position. According to the Bloembergen-Purcell-Pound (BPP) theory of relaxation, both T_1 and T_2 relaxation constants will be dependent on τ_c as follows (Bloembergen *et al*. 1948):

$$\frac{1}{T_1} = K \left[\frac{\tau_c}{1 + \omega_0^2 \tau_c^2} + \frac{4\tau_c}{1 + 4\omega_0^2 \tau_c^2} \right] \qquad 2.18$$

$$\frac{1}{T_2} = \frac{K}{2} \left[3\tau_c + \frac{5\tau_c}{1 + \omega_0^2 \tau_c^2} + \frac{2\tau_c}{1 + 4\omega_0^2 \tau_c^2} \right] \qquad 2.19$$

where K is a constant and ω_0 is the Larmor frequency. The dependence of T_1 and T_2 on τ_c is qualitatively shown in figure 2.8.
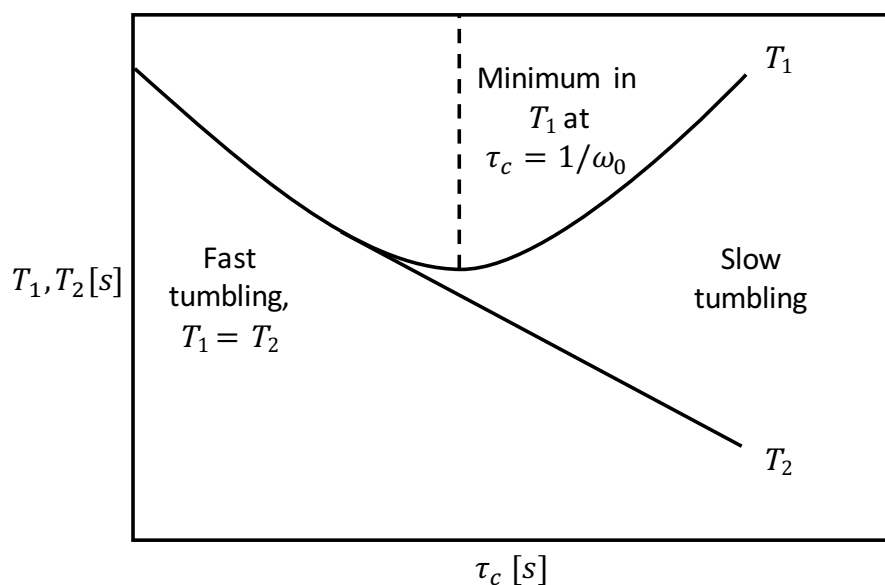
Figure 2.8: Relationship between τ_c and T_1 and T_2 according to BPP theory. At short τ_c, the molecular tumbling is fast and $T_1 = T_2$. As τ_c increases, *i.e.* molecular mobility decreases, T_1 and T_2 begin to diverge (adapted from Bloembergen *et al.* 1948).

The dependence of T_1 on τ_c shows a minimum, which separates the fast tumbling region from the slow tumbling region. This minimum is observed due to the manner in which the spin system interacts with surrounding environment. This interaction may be thought of as an exchange of energy between the magnetic energy of the spins and the energy of thermal motion of the surrounding environment. The energy exchange process will be the most efficient when τ_c^{-1} matches ω_0 (such that $\omega_0 \tau_c = 1$).

The T_2 relaxation constant decreases as τ_c increases, since dipolar interactions contribute to enhancing the spin-spin relaxation rate. It can be seen that in the fast tumbling region, both T_1 and T_2 are approximately equal to one another and have a similar dependence on τ_c. As molecular mobility decreases, their values diverge and T_1 may become much larger than T_2 (Levitt 2001).

2.4.5. Two-dimensional T_1-T_2 measurements

The T_1 and T_2 NMR relaxometry pulse sequences introduced in sections 2.4.2 and 2.4.3 may be considered as one-dimensional experiments, whereby the signal recovery and decay respectively are recorded as a function of time. However, it is possible to combine both pulse sequences as to conduct both experiments in two dimensions, whereby the signals are recorded as a function of two independent time variables and Laplace inversions are

performed in each dimension (Song *et al.* 2002; Hürlimann *et al.* 2002). Figure 2.9 shows an example of a 2D T_1-T_2 pulse sequence, whereby the inversion recovery and CPMG pulse sequences are combined. The time delay between the initial 180° and 90° pulses, t_d, may be varied, which thus makes the signal sensitive to T_1. Altering the number of echoes in the CPMG train results in a dependence on T_2. This pulse sequence may be used with a conventional CPMG set-up, or as a one-shot CPMG sequence, whereby the latter is preferable as it involves a shorter experimental timeframe.
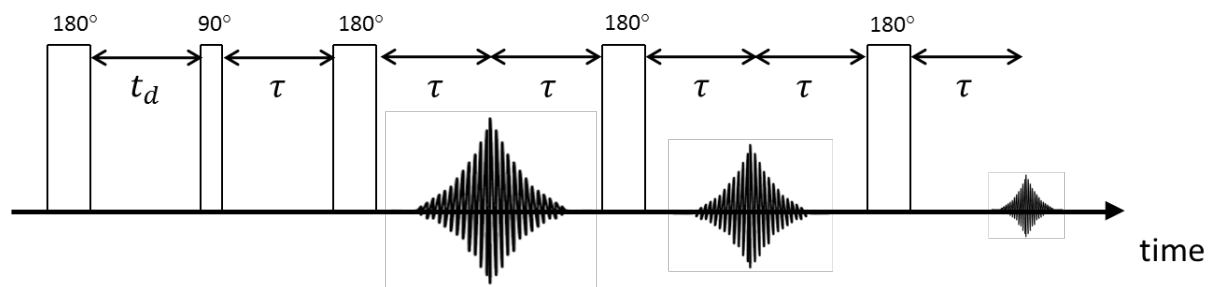
Figure 2.9: T_1-T_2 pulse sequence. T_1 is encoded by inversion recovery and T_2 by a CPMG train of echoes.

Figure 2.10 shows an example of a typical T_1-T_2 plot, which illustrates that a distribution of T_1 and T_2 values is obtained for the entire spin ensemble. However, only the average value, which is given by the point of maximum signal intensity on the correlation plot, will be considered for all T_1-T_2 correlation plots shown in this thesis.
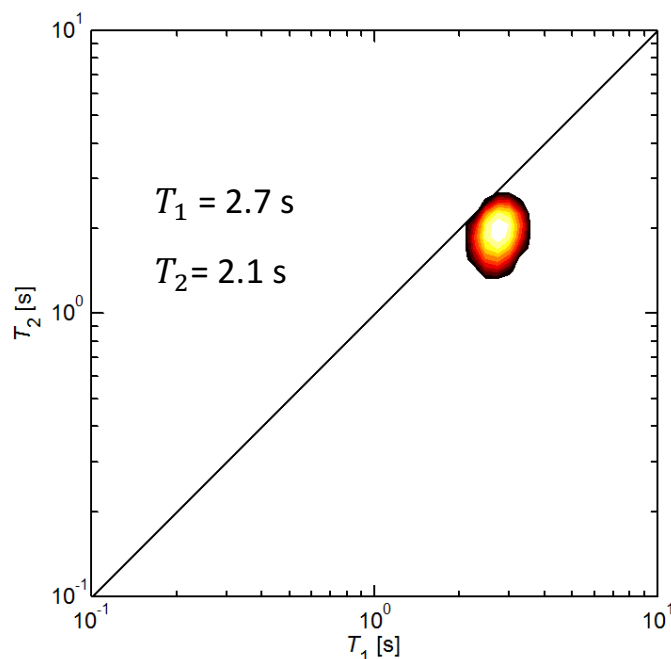
Figure 2.10: T_1-T_2 correlation plot of water at 20 °C at a ^{1}H resonance frequency of 400 MHz. The diagonal line corresponds to the points at which T_1 is equal to T_2.

2.4.6. Relaxation mechanisms

Whilst the relaxation processes described in sections 2.4.1, 2.4.2 and 2.4.3 occur in all NMR active species, the mechanisms which govern these processes vary from sample to sample, depending on the size, spin number(s) and spatial orientation(s) of molecules. The different types of relaxation mechanisms are not discussed in detail in this thesis but the interested reader is forwarded to Mason (1987) and Jameson (1991). Only a brief description of the types of mechanisms which typically occur in the systems studied in this thesis is given.

The predominant relaxation mechanism for spin ½ nuclei, provided that the γ is sufficiently large, is by dipole-dipole interactions between neighbouring spins which undergo random motion, as they tumble and collide with one another. It may be approximated in terms of average values of ω and a correlation time during which the local magnetic field is preserved. Subsequently, relaxation occurs at: $\omega_0 = \gamma B_0$. NMR probe molecules such as water follow this relaxation mechanism, whereby $T_1 \approx T_2$ in pure systems.

The principal mechanism for small molecules with a spin quantum number of ½, particularly those that are in the gas phase, is by spin rotation. Such nuclei experience magnetic fields due to the differential rotation of charges in the molecular frame and fluctuations of these fields,

in similar fashion to collisions, induces relaxation. In contrast to dipole-dipole interactions, increases in the spin rotation rates are observed with an increase in temperature and decreases in viscosity and pressure. NMR probe molecules such as CH_4 follow this relaxation mechanism (Mason 1987).

For nuclei with a spin quantum number which exceeds ½, the quadrupolar relaxation mechanism governs relaxation. Such nuclei possess an ellipsoidal distribution of charge and an electric quadrupole moment: eQ. Electric field gradients exist due to asymmetry in local charge distributions caused by the presence of adjacent electrons and nuclei. Changes in local electric field gradients caused by molecular motion induces transition(s) between the different spin quantum states, which subsequently causes spin relaxation. Additionally, placing quadrupolar nuclei in magnetic fields, whereby nuclear spin ensembles are aligned with the direction of the field, results in the nuclear magnetic energy levels being dependent on both $\boldsymbol{B}_0$ and the electric field gradient. Nuclei such as ^{2}H, ^{14}N and ^{17}O follow this relaxation mechanism and it has been shown that high resolution NMR spectroscopy is possible for these weak quadrupolar nuclei provided that the electronic environment is sufficiently symmetric. However, line broadening is often observed in certain systems, which subsequently has a detrimental impact on the ability to chemically resolve two or more species. In bulk systems, the quadrupolar relaxation time, T_q, determines the linewidth of NMR spectra, and $T_q (= T_1 \approx T_2)$ (Mason 1987).

2.5. NMR spectroscopy

2.5.1. Chemical shift

Regardless of the homogeneity of the applied $\boldsymbol{B}_0$, local electronic environments govern the magnetic field experienced by a nucleus. Chemical shift arises due to shielding of a nucleus by neighbouring electrons. This shielding effect therefore alters the magnetic field experienced by a nucleus and subsequently changes its resonance frequency. The term chemical shift is thus used to describe this change in resonance frequency and is dependent

on $\boldsymbol{B}_0$. Reference molecules such as Tetra Methyl Silane (TMS) are typically used to observe such changes in ^{1}H, ^{13}C and ^{29}Si systems.

Chemical shifts are often used to gain insights into the structures of molecules as it is determined by the chemical environment(s) which are present in a molecule. It is defined as the difference between the resonance frequency of the nucleus of interest, v_n, and that of TMS, v_{TMS}, in units of parts per million (ppm):

$$\delta_{ppm} = \frac{v_n - v_{TMS}}{v_{TMS}} \times 10^6$$

2.20

2.5.2. ^{1}H and ^{2}H NMR

The ^{1}H nucleus is the most widely used nucleus in NMR spectroscopy due to its high natural abundance (99.98%) and high NMR sensitivity. Qualitative information regarding (bio)-chemical samples may be inferred from the number of NMR resonances in the system, which corresponds to the number of environments present. Quantitative information may be obtained using the relaxation corrected peak intensities and/or peak areas of NMR resonances, whereby examples will be shown in chapter 4, as this directly corresponds to the number of protons present in a sample.

The ^{2}H nucleus in contrast to the ^{1}H nucleus is less commonly used due to a significantly poorer natural abundance in comparison (0.015%). Nevertheless, ^{2}H NMR has proved to be a particularly useful tool in applications such as solid-state NMR, signal suppression and the characterisation of transport in porous media at variable temperatures (Duer 2001; Sattler and Fesik 1996; Gonçalves *et al*. 1995). An example where comparisons are made between ^{1}H and ^{2}H relaxometry will be shown in chapter 6.

2.6. Pulsed Field Gradient (PFG) NMR

PFG NMR is a powerful technique for the characterisation of molecular transport processes in bulk and restricted conditions (Kärger and Ruthven 1992; Callaghan 1993). PFG NMR techniques enable spin ensembles to be labelled with respect to their position

via the application of pulsed magnetic field gradients. Figure 2.11 illustrates the principles involved in a PFG NMR experiment, using a sample tube filled with water as an example. A 90° excitation pulse perturbs the bulk magnetisation from thermal equilibrium and rotates the magnetisation into the transverse plane. Subsequently, the application of a phase encoding gradient imparts a phase shift to the spins, and a phase decoding gradient reverses this effect. In instances where there is no motion, the spins are completely rewound and the spins revert to their initial position and no signal attenuation is observed. In instances where there is motion, the phase decoding gradient does not completely rewind the spins and those spins which have moved to a new position have a net phase shift. Subsequently, the net phase shift is recorded for random motion. This net phase offset results in the contribution of an individual spin to the gradient echo being reduced and therefore signal attenuation is observed. Hence, signal attenuation is related to the motion of spins in a sample.
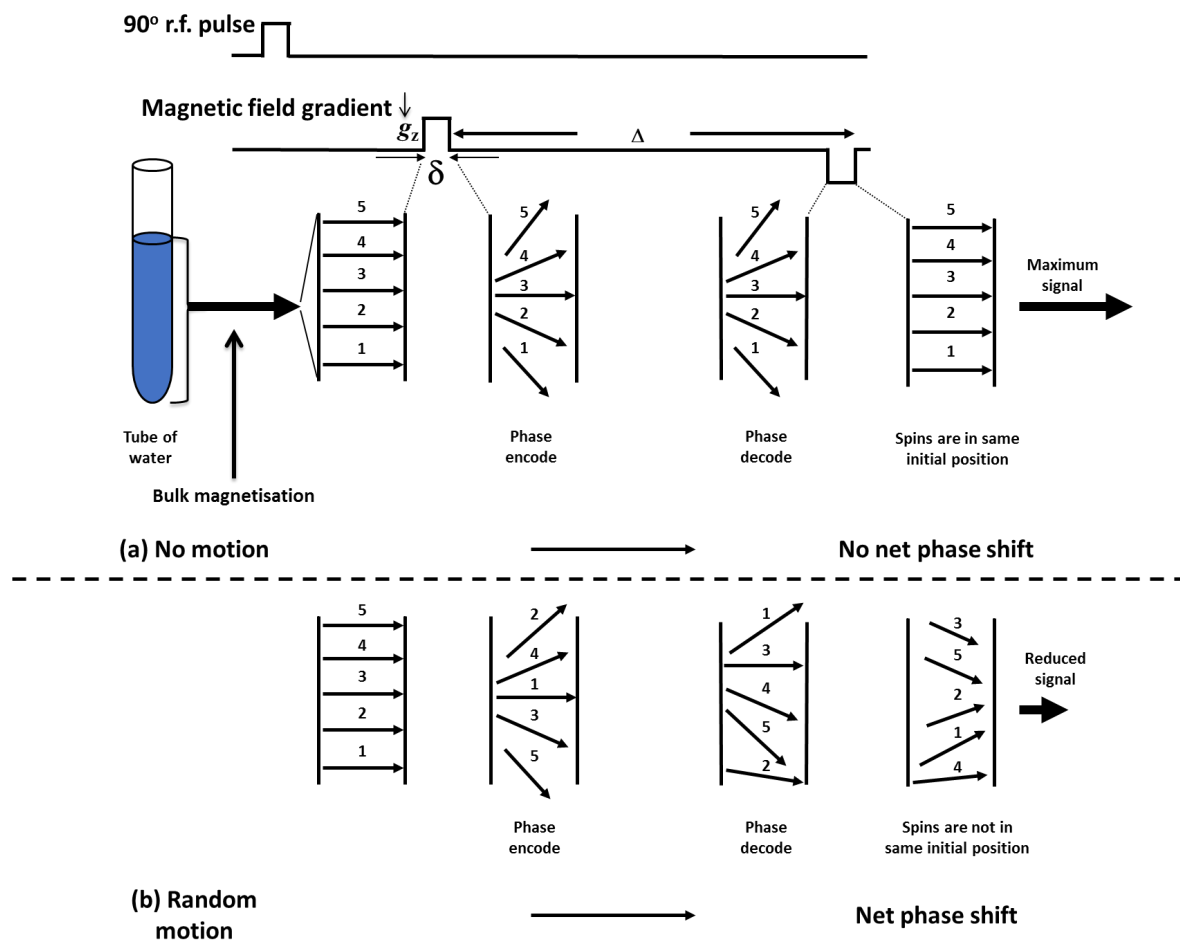
Figure 2.11: Principles involved in PFG NMR. The dotted line separates instances where (a) there is no motion and (b) where random motion occurs.

This procedure is repeated with increasing pulsed field gradient amplitudes. The acquired time domain signal decay from an NMR experiment is Fourier transformed to yield a frequency domain spectrum. Therefore, the signal attenuation may be tracked by plotting the peak intensities or areas against the gradient strength. Figure 2.12 shows an example of the typical Gaussian exponential decay curve that is obtained by plotting the attenuating peak area against increasing gradient strength, using a sample of pure water as an example. The significance of a Gaussian exponential decay in a PFG NMR experiment will be discussed in chapter 3.
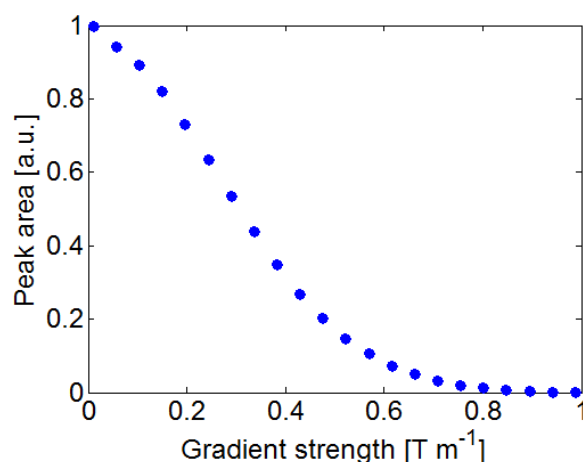
Figure 2.12: Typical single component Gaussian signal decay of molecular displacements as a function of gradient strength from a PFG NMR experiment.

The Stejskal-Tanner equation may be used to correlate the attenuation in signal to the self-diffusion coefficient of a species:

$$\frac{S}{S_0} = \ exp\left[-\gamma^2\delta^2 g^2 D \left(\Delta - \frac{\delta}{3}\right)\right] = \exp\left(-bD\right) \qquad\qquad 2.21$$

where δ is the duration of the pulsed magnetic field gradient, γ is the gyromagnetic ratio, g is the amplitude of the pulsed magnetic field gradient and Δ is the time frame in between the gradient pulses and may be referred to as an "observation time", "diffusion time" or "contrast time". The $\gamma^2\delta^2 g^2\left(\Delta - \delta/3\right)$ variables are referred to as a "b-factor" in this thesis for convenience. The gradient strength is typically varied, whilst the observation time and gradient pulse duration are kept constant, to ensure that the system is subject to the same degree of T_1 and T_2 relaxation at all b-factor points.

Complications with respect to data interpretation which may arise in the form of non-linear semi-log plots are discussed in more detail in chapter 3.

To obtain the self-diffusion coefficient, the signal attenuation is typically plotted on a semi-log scale against either the square of the gradient or against the b-factor. As illustrated in figure 2.13, using bulk water at 25°C as an example, the self-diffusion coefficient may then be obtained from the slope of the straight line. This type of plot is hereafter referred to as an echo attenuation plot. Examples and typical causes of non-linear echo attenuation plots which arise due to a non-Gaussian probability distribution of molecular displacements will be discussed in chapter 3.
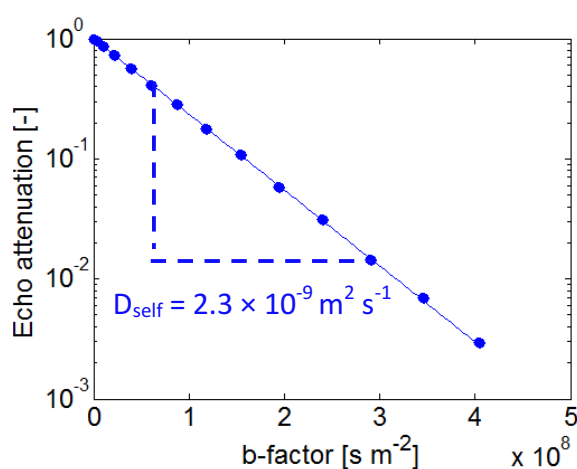
Figure 2.13: Typical echo attenuation plot of bulk water at 25 °C. The solid line is a fit of the data (blue dots) to the Stejskal-Tanner equation to give the self-diffusion coefficient.

A reciprocal space vector known as q-space is commonly used to illustrate that spatial position(s) may be traversed in time or gradient strength in a PFG NMR experiment and is defined as:

$$q = \frac{\gamma \delta g}{2\pi}$$

2.22

Echo attenuation plots may also be generated by plotting the signal attenuation against the q-space vector, dependent or independent of time.

2.6.1. Pulsed Gradient Spin Echo (PGSE)

The simplest pulse sequence that is used in PFG NMR is the PGSE pulse sequence, developed by Stejskal and Tanner. It is a combination of the spin echo pulse sequence shown in figure 2.6 and the pulse field gradient method described in section 2.6. This pulse sequence involves applying the phase encoding gradients either side of the 180° refocusing pulse, as illustrated in figure 2.14.
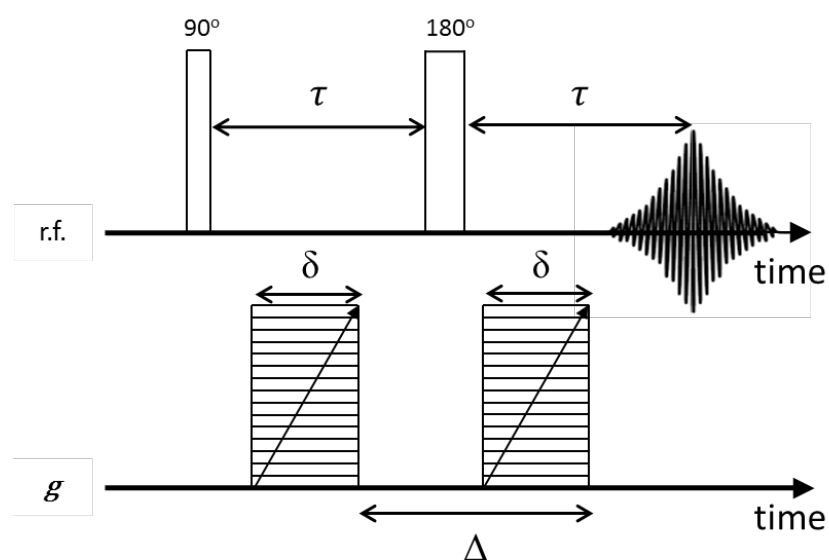
Figure 2.14: PGSE pulse sequence.

The observation time in PGSE sequences is limited by the T_2 relaxation constant of the system under investigation. Therefore, this pulse sequence is ideally suited to systems such as bulk liquids and gases, which typically possess T_2 relaxation times of the order of seconds and tens of milliseconds respectively.

2.6.2. Pulsed Gradient Stimulated Echo (PGStE)

The determination of self-diffusion coefficients using PGSE pulse sequences are limited by the loss of phase coherences due to transverse relaxation processes. The advantage of using a PGStE sequence over a PGSE is that magnetisation is stored along the longitudinal axis during the time interval T, where it is only subject to T_1 relaxation. Since T_1 relaxation is generally a slower process than T_2 relaxation, the magnetisation may be preserved for a longer period of time and subsequently molecular displacements may be probed over longer length scales. A representation of the PGStE pulse sequence is shown in figure 2.15.
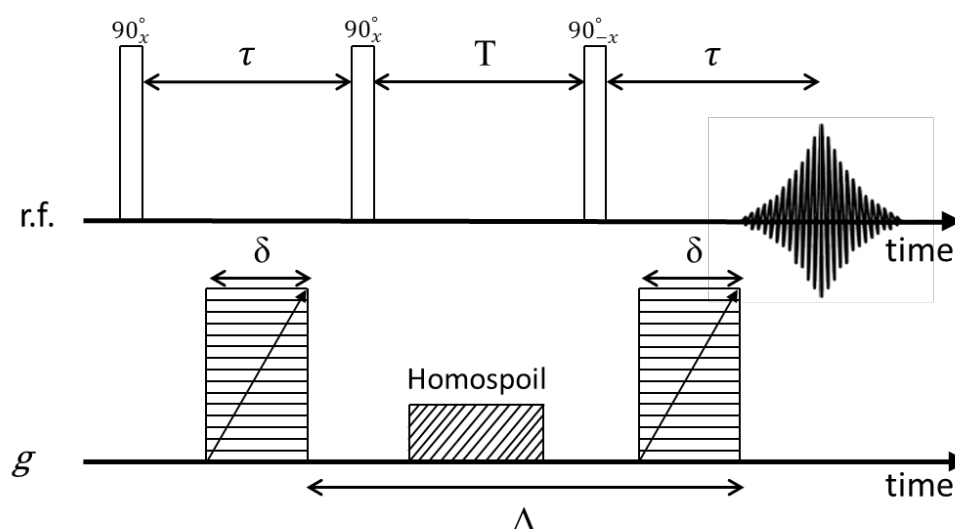
Figure 2.15: PGStE pulse sequence.

The principles that are involved in the formation of a stimulated echo are similar to that of a spin echo formation. The initial 90° pulse rotates the magnetisation into the transverse plane. Subsequently, it is possible to phase encode the sample by applying a linear magnetic field gradient. After a time interval, τ, magnetisation possesses x- and y-components and the second 90° pulse stores the y-component along the -z-axis for a duration, T. The use of a homospoil gradient enables residual magnetisation in the transverse plane to be eliminated, to prevent the formation of unwanted echoes, as each 90° pulse is capable of forming an FID and any two 90° pulses can form a spin echo. The final 90° pulse returns the magnetisation into the transverse plane, whereby the second magnetic field gradient is applied and the spins are decoded. As with the PGSE sequence, a short echo time is desirable as to minimise the amount of signal lost due to T_2 relaxation processes during the τ intervals.

2.6.3. Alternating Pulsed Gradient Stimulated Echo (APGStE)

The application of bipolar pulsed field gradients to eliminate the contribution from the cross term between the applied and background gradient has been evaluated in the literature (Karlicek and Low 1980). Their pulse sequence also acknowledges the role of spin echoes to reduce the effect of background gradients. Subsequently, a pulse sequence which is based on a stimulated echo, whereby the phase encoding interval is divided into a spin echo dephasing and rephasing section with bipolar gradients was developed (Cotts 1989). The use of the bipolar gradients also enables the cumulative addition of the desired dephasing in the phase encoding period.

Background gradients arise due to differences in the magnetic susceptibilities of the porous material and guest molecule under investigation. The presence of strong background gradients in heterogeneous systems gives rise to transverse relaxation contributions which influences the value of the self-diffusion coefficient. The APGStE pulse sequence tackles the issue of transverse relaxation processes occurring during the τ intervals of the PGStE pulse sequence. The insertion of the 180° pulse preserves the signal to ensure that spins which have dephased due to transverse relaxation are refocused. A representation of this pulse sequence which is not drawn to scale, as the T region is longer than the individual τ regions, is shown figure in 2.16. Ignoring the effects of background gradients and flow, the b-factor for this pulse sequence is given by:

$$b - factor = \gamma^2 \delta^2 g^2 \left(4\Delta - 2\tau - \frac{2\delta}{3} \right) \qquad \qquad 2.23$$
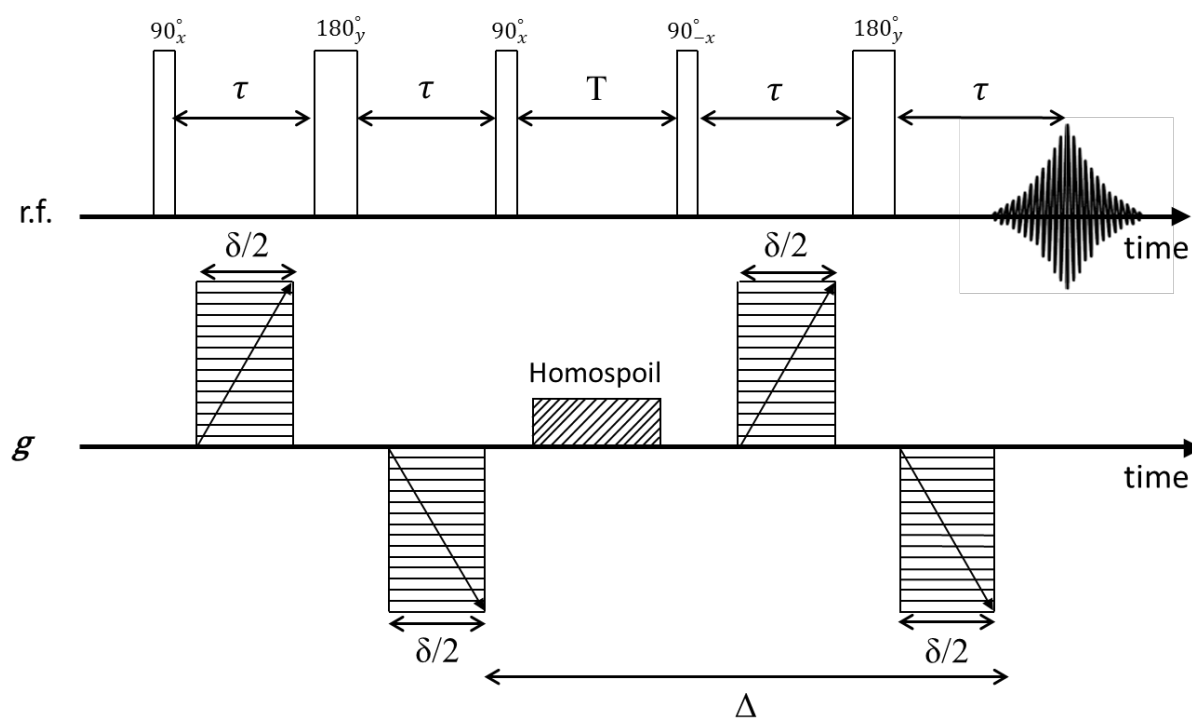
Figure 2.16: APGStE pulse sequence.

where τ corresponds to the time interval from initial spin excitation to the initial 180°.

2.7. References

Abragam, A., (1961). *Principles of Nuclear Magnetism*. Clarendon Press.

Bloch, F., Hansen, W.W., Packard, M., (1946). Nuclear Induction. Phys. Rev. 69: 127.

Bloembergen, N., Purcell, E.M., Pound, R.V., (1948). Relaxation effects in nuclear magnetic resonance absorption. Phys. Rev. 73(7): 679-715.

Bloembergen, N., Purcell, E.M., Pound, R.V., (1948). Relaxation effects in nuclear magnetic resonance absorption. Phys. Rev. 94: 630-638.

Callaghan, P., (1993). *Principles of nuclear magnetic resonance microscopy*. Clarendon Press.

Carr, H.Y., Purcell, E.M., (1954). Effects of diffusion of free precession in nuclear magnetic resonance experiments. Phys. Rev. 94(3): 630-638.

Cotts, R.M., Hoch, M.J.R., Sun, T., Markert, J.T., (1989). Pulsed field stimulated echo methods for improved NMR diffusion measurements in heterogeneous systems. J. Magn. Reson. 83: 252-266.

Duer, M.J., (2001). *Solid state NMR spectroscopy: principles and applications*. Wiley-Blackwell.

Fukushima, E., Roeder, S.B.W., (1981). *Experimental Pulse NMR. A nuts and bolts approach*. Addison-Wesley.

Gladden, L.F., (1994). Nuclear-Magnetic-Resonance in Chemical-Engineering - Principles and Applications. Chem. Eng. Sci. 49: 3339-3408.

Gonçalves, J. A., Portsmouth, R.L., Alexander, P., Gladden, L.F., (1995). Intercage and intracage transport of aromatics in zeolites NaY, HY and USY studied by ^{2}H NMR. J. Phys. Chem. 99: 3317-3325.

Hahn, E.L., (1950). Spin echoes. Phys. Rev. 80(4): 580-594.

Hürlimann, M.D., Venkataramanan, L., Flaum, C., (2002). The diffusion-spin relaxation time distribution function as an experimental probe to characterise fluid mixtures in porous media. J. Chem. Phys. 117: 10223.

Hürlimann, M.D., Venkataramanan, L., (2002). Quantitative measurement of two-dimensional distribution functions of diffusion and relaxation in grossly inhomogeneous fields. J. Magn. Reson. 157: 31.

Jameson, C. J., (1991). Gas-phase NMR spectroscopy. Chem. Rev. 91: 1375-1395.

Kärger, J., Ruthven, D., (1992). *Diffusion in zeolites and other microporous solids*. Wiley & Sons.

Karlicek, R.F., Lowe, I.J., (1980). A modified pulsed gradient technique for measuring diffusion in the presence of large background gradients. J. Magn. Reson. 37: 75-91.

Lauterbur, P. C., (1973). Image formation by induced local interactions: Examples employing nuclear magnetic resonance. Nature 242: 190-191.

Mansfield, P., (1976). Proton Spin Imaging by Nuclear Magnetic Resonance. Contemp. Phys. 17: 553.

Mason, J., (1987). *Multinuclear NMR*. Plenum Press.

Meiboom, S., Gill, D., (1959). Modified spin echo method for measuring nuclear relaxation times. Rev. Sci. Instrum. 29(8): 688.

Levitt, M. H., (2001). *Spin dynamics: Basics of Nuclear Magnetic Resonance*. John Wiley & Sons.

Pines, D., Slichter, P.C., (1955). Relaxation Times in Magnetic Resonance. Phys. Rev. 100: 1014.

Purcell, E. M., Torrey, H.C., Pound, R.V., (1946). Resonance absorption by nuclear magnetic moments in a solid. Phys. Rev. 69: 37.

Sattler, M., Fesik, S.W., (1996). Use of deuterium labelling in NMR: overcoming a sizeable problem. Structure. 4(11): 1245-1249.

Song, Y.Q., Venkataramanan, L., Hürlimann, M.D., Flaum, M., Frulla, P., Straley, C., (2002). T_1 T_2 correlation spectra obtained using a fast two-dimensional Laplace inversion. J. Magn. Reson. 154: 261.

Chapter 3

Literature review of molecular displacement processes and measurement techniques

3.1. Introduction

The aim of this chapter is to introduce the concepts that are involved in characterising the self-diffusion behaviour of molecules adsorbed in porous materials which are relevant to this thesis. A brief history of the discovery of random molecular motion and its association with self-diffusion coefficients is presented. The various types of diffusion regimes which are of relevance to the bulk and adsorbed phase (gaseous) systems used in this thesis are also introduced. A literature survey is included to summarise the industrially relevant methods that are typically used to characterise transport behaviour in microporous materials. Large discrepancies are reported in the literature between the self-diffusion coefficients from PFG NMR and those from alternative techniques. Therefore, a discussion of the comparisons in the time- and length-scales between these measurement techniques is presented. Lastly, a literature summary table of PFG NMR self-diffusion coefficients of systems which are relevant to this thesis is also included.

Many excellent texts which discuss these diffusion processes are widely available (Crank 1975; Bird *et al.* 2007; Cussler 2009; Callaghan 2011) and some of the basic principles which are relevant to the work in this thesis are discussed in this chapter.

3.2. Gas phase diffusion in porous media

The porous materials of interest in this thesis are microporous zeolites, specifically chabazite and β-zeolite, as they are used in Selective Catalytic Reduction (SCR) processes. Gas phase guest molecules will be used to study the molecular dynamics behaviour in the aforementioned porous materials, as industrial processes such as SCR occur in the gas phase. However, as mentioned in chapter 1, section 1.1, NO_x will be replaced with CH_4 as both gases possess similar transport and adsorption properties in large pore zeolites (McDaniel *et al*. 1996).

In nano-porous materials, the dominating diffusion mechanism and the rate of mobility of adsorbed gaseous molecules is dependent on the geometry of the host porous material (provided that the gas pressure is significantly lower than the saturation pressure).

Large pore structures such as macro-porous materials promote molecule-molecule interactions, and thus molecular diffusion is the dominant mechanism.

With decreasing pore size, the number of collisions with the pore wall increases, until the pore size becomes smaller than the mean free path of the gas molecules. The mean free path is the average distance that a molecule travels between two collisions. Once this occurs, Knudsen diffusion is the dominant mechanism and molecular mobility in mesoporous materials is governed by the size of the pore. This concept was originally presented by Martin Knudsen in 1909 as a means of characterising molecular flow with respect to the mean free path available for molecular transport (Knudsen 1909). Figure 3.1 shows a simple representation of this behaviour. The Knudsen diffusion coefficient, D_k, can be calculated *via*:

$$D_k = \frac{2r_{pore}}{3} \sqrt{\frac{8RT}{\pi M_A}} \qquad 3.1$$

where r_{pore} is the pore radius, R is the gas constant, T is the temperature and M_A is the molecular weight of the diffusion molecule.
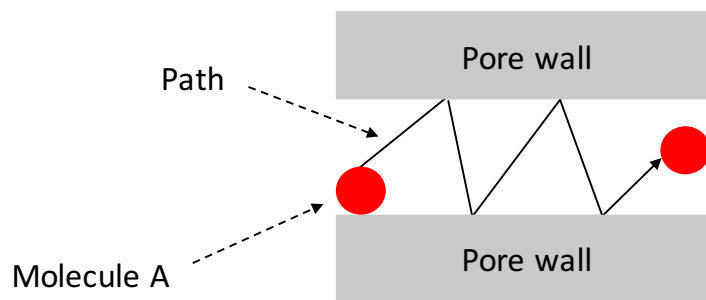
Figure 3.1: Representation of Knudsen diffusion in a narrow pore system.

In systems where the pore sizes are even smaller, such as microporous materials, the molecules continuously interact with the walls. The dominant mechanism in such instances is referred to as configurational diffusion. Configurational diffusion mechanisms are typically observed in one-dimensional zeolite structures, such as mordenite, which are comparable in size and shape to the diffusing molecules (Schuring 2002). In this mechanism, the molecules travel in "single-file" as they are unable to pass one another in narrow pore structures. However, since the zeolites used in this thesis were three-dimensional structures, configurational diffusion will not be discussed further.

Figure 3.2 illustrates the typical diffusion mechanisms, orders of magnitude of diffusivity and the requisite activation energies of molecules confined in nano-porous materials, as a function of pore diameter.
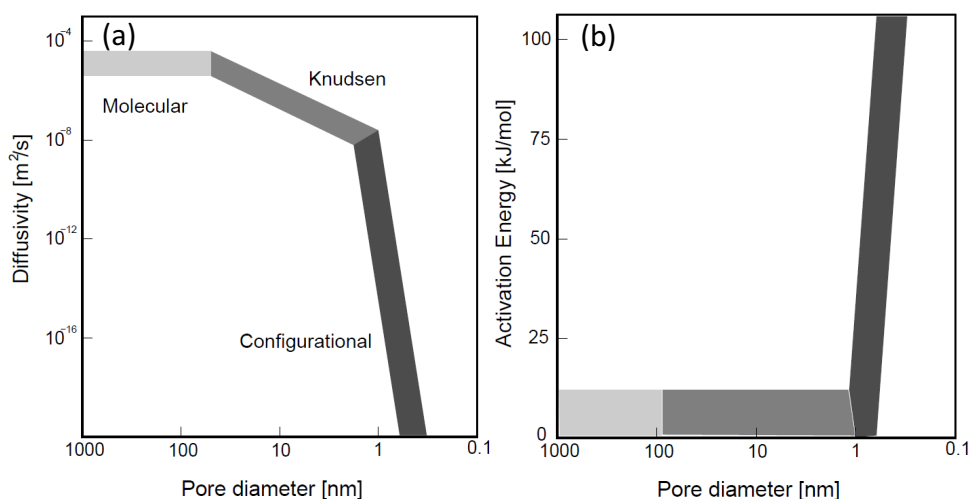
Figure 3.2: Illustration of (a) the types of diffusion mechanisms and typical orders of magnitude of diffusion coefficients and (b) requisite activation energies for molecular mobility as a function of pore size (Schuring 2002).

3.3. Types of diffusion in bulk and porous systems

3.3.1. Fickian diffusion

The mathematical equation of heat conduction which was developed by Joseph Fourier (1822) was adopted by Adolf Fick (1855) to mathematically model random molecular motion. The diffusion coefficient arising from this model is used to characterise the rate of molecular transport of a species. This characterises a phenomenon known as Fickian diffusion, and is often referred to as mutual or binary diffusion. Fickian diffusion describes the isotropic process in which the presence of a concentration gradient enables molecular transport to and from regions with differing chemical environments. Although, from a thermodynamic perspective, it is the presence of a chemical potential gradient which enables transport. Using Fick's laws of diffusion, it is possible to relate the net rate of transport to concentration gradients. Starting with Fick's 1st law of diffusion, a binary system of species A and B has a net molecular transport rate of:

$$J_{AB} = -D_{AB} \frac{dc_i}{dx}$$

3.2

Where J_{AB} is the rate of transfer per unit area (molar flux), c is the concentration of the diffusing species and x is the spatial dimension across the concentration gradient profile. Since by definition the transport process from region A to region B and vice versa is a mutual process, the diffusion coefficients to and from region A and B are equal to one another: $D_{AB} = D_{BA}$. The negative sign arises due to diffusion occurring in the direction which is opposite to that of increasing concentration. Figure 3.3 shows an example of the net movement of molecules from a high concentration region to a low concentration region, upon which equilibrium is eventually established.
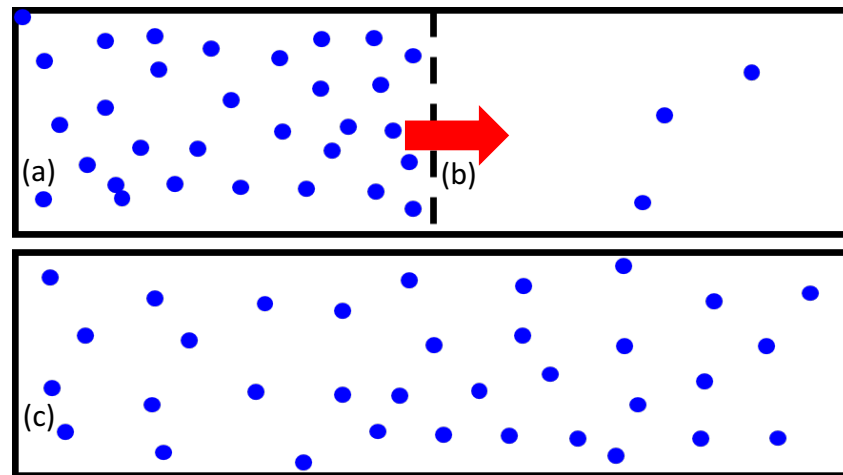
Figure 3.3: Movement of molecules from (a) a high concentration region to (b) a low concentration region separated by a permeable barrier and (c) upon complete mixing, eventual equilibrium is established across both regions.

The rate of time dependent molecular transport is characterised by Fick's 2nd law of diffusion and is given by:

$$\frac{\partial c}{\partial t} = D \frac{\partial^2 c}{\partial x^2} \qquad\qquad 3.3$$

This equation is only suitable for one-dimensional diffusion (*i.e.* if there is only a concentration gradient along the x-axis, in this example). Complications which arise due to multi-directional diffusion are briefly discussed in section 3.4.3.

The concentration profile of a substance may also be tracked using labelled atoms. This process is referred to as tracer diffusion and describes the spontaneous mixing of molecules due to the presence of a concentration gradient. Tracer diffusion is often probed using isotopic tracers and by observing their concentration profile as a function of time. This process therefore occurs under non-equilibrium conditions. Whilst there is no overall concentration gradient of the unlabelled species, there exists an initial concentration gradient of the labelled species. As such, this flux of labelled molecules may be determined using Fick's laws of diffusion.

3.3.2. Corrected diffusion

The equations in section 3.3.1 which characterise Fickian diffusion assume that the driving force for molecular transport is the concentration of species A. However, the true driving force is the chemical potential gradient. For an ideal gas component i, the chemical potential, μ_i, is given by:

$$\mu_i = \mu_i^0 + RT \ln \frac{p_i}{p^0} \qquad\qquad 3.4$$

where μ_i^0 is the chemical potential at a reference state, R is the ideal gas constant, T is the temperature, p_i is the partial pressure of component i and p^0 is the reference pressure.

The main assumption of equation 3.4 is that the equilibrium vapour phase behaves as an ideal gas. This equation is also applicable for non-gas phase species, since equilibrium vapour pressures give an accurate representation of a species' thermodynamic behaviour. Therefore, the relationship between the Fickian diffusion coefficient and the corrected diffusion coefficient, D_0, is obtained by modification by a thermodynamic correction factor and is given by:

$$D = D_0 \frac{\partial \ln p_i}{\partial \ln c_i} = D_0 \frac{c_i}{p_i} \frac{\partial p_i}{\partial c_i} \qquad\qquad 3.5$$

where c_i is the concentration of component i. In systems where adsorption in porous materials occurs, c_i may be replaced with q_i which is the adsorbed phase loading. By applying this thermodynamic correction, the concentration dependence of Fickian diffusion is accounted for. At low concentrations, the thermodynamic factor tends to one and thus the Fickian diffusivity approaches the corrected diffusivity (Conner and Fraissard 2003).

3.3.3. Self-diffusion

Self-diffusion describes the process whereby molecular transport of molecules occurs at equilibrium, in the absence of a chemical potential gradient (Einstein 1905). In section 3.3.1, Fickian diffusion was introduced, whereby the presence of a chemical potential gradient

results in molecular motion which eventually reaches a concentration equilibrium. Once equilibrium is established, self-diffusion occurs due to a spontaneous mixing of molecules induced by intermolecular collisions. This occurs due to a phenomenon known as Brownian motion, which is the nexus between the random motion of particles and temperature.

The origin of random motion dates back to the 19th century, whereby Ludwig Boltzmann theorised that the effect of temperature was apparent in the random motion of atoms and particles. Boltzmann proposed that for every independent molecular motion, there exists an equal distribution of kinetic energy proportional to temperature. A century prior to Boltzmann's proposal, Daniel Bernoulli applied Newtonian mechanics to describe the concept of gas pressure in terms of particles colliding with a solid wall. Boltzmann subsequently applied his proposed principle by taking statistical averages to explain the gas laws, as well as the laws of thermodynamics. This led to a significant amount of scepticism and ridicule from his contemporaries at a time when theoretical physics was in its infancy, ultimately leading to Boltzmann's suicide. The most notable objections came from Ernst Mach and Wilhelm Ostwald as they were fundamentally opposed to acknowledging the existence of atoms and molecules. This was despite the fact that in the early 19th century, John Dalton had proposed the existence of molecules and particles in volumes of gases. The detractors presented their cynicism by drawing comparisons between the laws of mechanics and thermodynamics. They suggested that since the laws of mechanics are reversible, the expectation would be that heat would flow from a colder temperature to a hotter temperature, if the theory was in fact reasonable. Boltzmann responded by explaining that whilst such behaviour would not be impossible, it would not be probable since a large number of molecules would be involved in this process. As such, molecules would be characterised en masse and would thus follow conventional thermodynamic behaviour. However, recent studies have shown that a reversal of this expected trend is indeed possible in systems with a small number of molecules (Wang *et al*. 2002). Boltzmann's statistical mechanics are widely considered as one of the fundamentals of modern physics. The constant of proportionality for equipartition, Boltzmann's constant, is thus named as an homage to its pioneer.

The controversy surrounding Boltzmann's proposal regarding the random motion of molecules was ultimately settled in 1905 by Albert Einstein, whose work based on Brownian motion vindicated Boltzmann. This phenomenon was reported in 1827 by the botanist Robert

Brown, upon observing the random migration of pollen grains in a solution of water through an optical microscope. This migration process is referred to as a "random walk" as the molecules, under unrestricted conditions, do not have a preferred direction of motion. Einstein subsequently theorised that whilst the pollen grains were large enough to be seen through a microscope, they were sufficiently small as to succumb to the influence of the random thermal motion of the surrounding water molecules. Further, Jean Perrin's experimental work on Brownian motion in 1909 proved the existence of atoms by the preparation of various liquid phase samples which differed in composition. Perrin maintained that if molecules were indeed real, the particles in a mixture such as an emulsion should not all sink to the bottom and should instead distribute themselves throughout the liquid (Perrin 1909). It was at this point, after Boltzmann's suicide, that the scientific community universally accepted the existence of atoms and unanimously agreed with Boltzmann's work.

Supported by Brown's observations, Einstein numerically showed that random molecular displacements may be expressed as a probability density, which follows Fick's laws of diffusion. This corresponds to the probability of a molecule moving in a given direction. Hence, this probability varies in the same manner as a particle concentration function with respect to time. Assuming motion in the z-direction, at time t_0, the position of the molecule is z_0. The probability of finding a molecule between position z_1 and $z_1 + dz_1$ does not depend on the position of the particle before t_0. This is referred to as a Markovian process and therefore it is possible to calculate the probability of various displacement paths in a stepwise manner. The time dependent solution of this probability density is obtained by a Dirac delta function and enables this function to be expressed in terms of a molecular displacement length. This expression is referred to as a Root Mean Squared Displacement ($RMSD$), which describes the distance that a molecule travels in a given timeframe. In a PFG NMR experiment, this timeframe is equal to the observation time, Δ, specified in the pulse sequence. The $RMSD$ is given by the Einstein relation:

$$\langle (z' - z)^2 \rangle = \sqrt{2D\Delta} \qquad\qquad 3.6$$

where z' is the final position of the molecules, z is the initial position and D is the self-diffusion coefficient. Equation 3.6 corresponds to an isotropic molecular displacement

process in a single spatial dimension. The supposition used by the Dirac delta function is that the solution to the probability density for self-diffusion follows a Gaussian probability distribution. The time dependence of this function is illustrated in figure 3.4, in which an increase in time results in the preservation of the continuous Gaussian distribution of molecular displacements. At sufficiently large times, it is possible to observe molecular displacement behaviour which deviates from this Gaussian profile. Examples of such trends will be shown in chapter 5 to highlight the differences in typical PFG NMR data for Gaussian and non-Gaussian probability distributions.
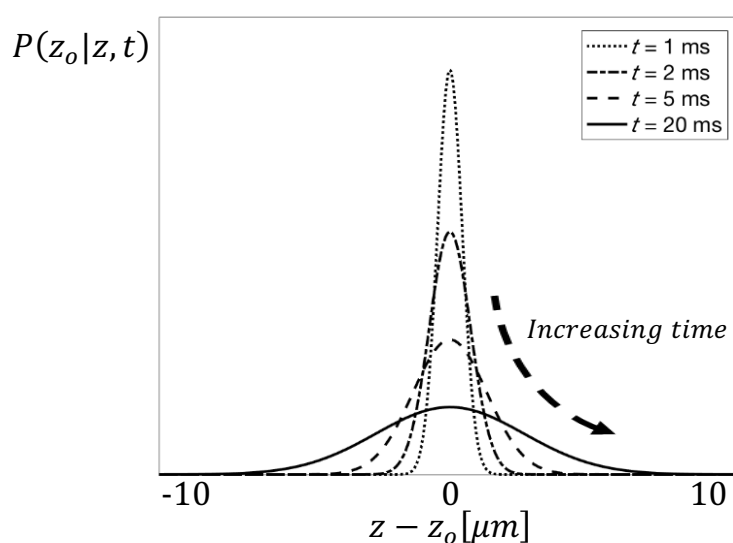
Figure 3.4: Behaviour of the conditional probability for an ensemble of molecules undergoing Brownian motion where the successive Gaussians correspond to successively increasing time (adapted from Sørland 2014).

Hence, a PFG NMR experiment does not measure a self-diffusion coefficient. Rather, it measures a stochastic molecular displacement based on the aforementioned conditional probability, by labelling the initial and final positions (and thus the net phase shift) of NMR active nuclei. If a Gaussian distribution is observed with respect to the signal attenuation, the (normalised) signal decay is proportional to the self-diffusion coefficient. As mentioned in chapter 2, the acquired time domain signal decay from an NMR experiment is Fourier transformed to yield a frequency domain spectrum. The Fourier transform of a Gaussian function is also a Gaussian function. Therefore, in a PFG NMR experiment the Gaussian probability distribution of the molecular displacements is preserved.

With respect to fluids confined in porous materials, $RMSD$s which are smaller than the porous material's geometry result in motion which is uncorrelated from one molecule to another (Neuman 1974). It has been shown that the molecular displacements of molecules confined in porous media measured in a PFG NMR experiment can undergo a probability distribution change, as a function of the experimental observation time (Sen 2004). This phenomenon is referred to as the Gaussian phase approximation. At short observation times, a negligible number of spins interact with the surface of the porous material and thus it is assumed that they do not contribute to the observed net phase shift during a PFG NMR experiment. Therefore, the displacement pathways for each particle are uncorrelated from one another and the motion of the molecules follows a random walk model, resulting in the molecular displacements following a Gaussian probability distribution. As the observation time increases and the molecular displacements approach the porous material's geometric size, molecular motion transitions to a correlated profile, and hence follows a non-Gaussian distribution, whereby a porous material's structure significantly influences molecular displacement pathways. This is typically present in the form of curvature in an echo attenuation plot, giving rise to the presence of multiple diffusion coefficients. However, further increasing the displacement length, by selecting large observation times, enables the molecules to successively exit and re-enter multiple particles, which effects a molecular displacement averaging across a packed bed. Thus, each individual spin experiences the bulk, inter-particle region at multiple times, albeit momentarily for each given point. This averaging effect results in an enhanced weighting toward unrestricted diffusion behaviour. Therefore, at random points in these comparably spacious regions in a packed bed of particles it is assumed that spatial displacements of each spin can be treated as an independent "jump". Hence, this once again satisfies the criteria for random motion, and reverts to an uncorrelated motion profile with a Gaussian displacement distribution (Grebenkov 2007).

For molecular displacements in the x, y and z-dimensions, as is the case with diffusion anisotropy in 3D zeolite structures, the molecular displacement is given by:

$$\langle (\boldsymbol{r'} - \boldsymbol{r})^2 \rangle = \sqrt{6D\Delta} \qquad\qquad 3.7$$

However, all $RMSD$s quoted in this thesis were calculated using equation 3.6, since all PFG

NMR measurements were performed in the z-direction. The significance of equation 3.6 in the characterisation of displacements length-scales and diffusion regimes will be discussed in section 3.6, as it is central to a PFG NMR measurement.

Contrary to Fickian diffusion, self-diffusion processes are not associated with a net flux. Additionally, in two-component systems where the diffusing species are inherently different to one another, the self-diffusion coefficients of both species are not equal to one another. The self-diffusion coefficients of two-component mixtures can be precisely characterised using PFG NMR, and will be described in chapter 6.

Further, the self-diffusion coefficient is related to the viscosity and geometry of the diffusing species according to the Stokes-Einstein relationship:

$$D = \frac{k_B T}{c \eta r} \qquad\qquad 3.8$$

where k_B is Boltzmann's constant, T is the temperature, η is the shear viscosity and r is the hydrodynamic radius of the molecule. The constant, c, is dependent on the boundary conditions of the system and is equal to 6π for no-slip and 4π for slip conditions.

3.4. Origins of curvature in echo attenuation plots in PFG NMR

As shown in chapter 2, figure 2.13, plotting the (semi-) log of the echo attenuation *vs*. the "b-factor" typically produces a straight line for single component systems such as bulk water. Non-linearity in (semi-) log echo attenuation plots occurs when molecules in the system under investigation are travelling at different length-scales over the same period in time. More mobile molecules lead to longer displacement length-scales whereas slower molecules result in shorter displacement length-scales. This therefore results in a non-Gaussian distribution of molecular displacements, which yields a curved echo attenuation plot. Therefore, each linear part of the plot, which corresponds to the portion of molecular displacements with a Gaussian distribution, is evaluated separately. The self-diffusion coefficients, D_i, from a non-linear echo attenuation plot may be obtained by fitting the curve to a multi-component exponential model (Kärger and Pfeifer 1988):

$$\Psi = \sum_{i=n}^{n} p_i \, exp(-bD_i) \qquad\qquad 3.9$$

where Ψ is the normalised signal attenuation, p_i is the population of component i and b is the b-factor. Some examples which lead to non-linear echo attenuation plots are listed in this section.

3.4.1. Multi-component systems

One of the simplest explanations for the manifestation of curvature is due to the presence of multiple species which possess different self-diffusion coefficients due to differences in their molecular weights (and thermal velocities). An example of an echo attenuation curve for a two-component mixture of ethane and benzene confined in zeolite NaX is shown in the literature (Pampel *et al*. 2006). The PFG NMR data were fitted to equation 3.9 to obtain two separate self-diffusion coefficients. It was found that ethane was the faster component (D_{self} = 3.3 × 10^{-10} m^2 s^{-1}) and thus its signal attenuated more quickly in comparison to benzene which was less mobile (D_{self} = 0.9 × 10^{-10} m^2 s^{-1}) and attenuated more slowly.

3.4.2. Chemical exchange

Chemical exchange may be a source of curvature in aqueous systems that are capable of forming hydrogen bonds, particularly ionic and acidic liquids. "Proton conduction" may occur in such systems which results in anomalously fast self-diffusion due to intra- and inter-molecular transport processes. The former involves the addition of water to the aqueous solution, which facilitates the rapid formation of hydrogen bonds between the water molecules and the ionic or acidic liquid. In such instances, curvature would be expected by virtue of having more than one molecule present. Further, the self-diffusion coefficient of the ionic or acidic liquid would be faster than one would anticipate due to the rapid exchange of protons (Vilčiauskas *et al*. 2012). The latter involves polar and/or acidic liquids that are confined in highly acidic porous materials forming hydrogen bonds with surface silanol groups and/or Brønsted acid sites. This may also result in a transfer of protons through the hydrogen bonding network. Proton movement of the order of micrometres for water confined in a highly acidic polymer structure has been reported in the literature in such systems, with self-

diffusion coefficients ranging from 0.05 - 5 × 10^{-10} m^2 s^{-1} over a temperature range of 223 - 323 K. This may therefore act as a significant contribution in systems which involve molecular displacements over short length-scales, such as polar liquids confined in acidic microporous materials (Ogawa *et al*. 2014).

3.4.3. Adsorption and capillary condensation

Adsorption and capillary condensation are common sources of multi-phase behaviour in heterogeneous catalysis and diffusion processes. The presence of gas and liquid phase molecules in pore structures results in two distinct molecular displacement regions with differing self-diffusion coefficients. This occurs because liquids are less mobile than gases as they possess a larger molecular weight.

The extent to which a molecule adsorbs onto a pore surface is dependent on both the surface properties of the porous material and the guest molecule. Hydrophilic surfaces favour the adsorption of polar molecules, whereas hydrophobic surfaces have an affinity towards non-polar molecules. However, it is possible for gas and liquid phase molecules to co-exist in the pore geometry. For example, some molecules may adsorb onto the pore surface and are therefore in the liquid phase, whereas some molecules may occupy the spaces in between the adsorption sites and are therefore present in the vapour phase. This effect is particularly appreciable in *operando* PFG NMR studies of heterogeneous processes which occur at elevated temperatures and pressures. The NMR signal from the vapour phase molecules is typically lower than their adsorbed phase counterparts for equivalent concentrations, for reasons which will be described in chapter 4. However, it is possible to detect and differentiate between the two phases, as their molecular transport and NMR relaxation properties are significantly different from one another. Hence, two-component self-diffusion behaviour may be observed in PFG NMR experiments, which gives rise to curvature in echo attenuation plots. An example of this is shown in the literature for the diffusion of 1-octene in 1 wt % Pd/θ-Al$_2$O$_3$ catalyst trilobes. The self-diffusion coefficients, 1 × 10^{-9} m^2 s^{-1} and 2 × 10^{-11} m^2 s^{-1}, in this system were attributed to the bulk pore and pore surface regions respectively (Weber *et al*. 2010).

Multi-phase behaviour in microporous zeolite materials is generally not observed as the pore windows are not large enough to co-host multiple molecules of more than one state of matter. However, capillary condensation may occur at considerably high pressures provided that the pore sizes are small enough to stimulate inter-molecular interactions (Climent *et al*. 1991).

3.4.4. Hierarchical pore structures

An inhomogeneity in the macroscopic pore structure of porous materials gives rise to a range of pore sizes. Consider the diffusion of a molecule with a critical diameter of 0.6 nm in a hierarchical pore system with micropore and mesopore diameters of 0.7 nm and 20 nm respectively. Molecules in the micropores are restricted to a greater extent and small molecular displacements may be observed. In comparison, molecules confined in the mesopores are constrained to a lesser degree and therefore larger molecular displacements may be observed. Hence, two separate self-diffusion coefficients may be obtained corresponding to the two different geometric regions (Schneider *et al*. 2016). Many real-world zeolites, particularly β-zeolite, involve a range of micropore and mesopore size distributions as it is not always possible to control the exact geometric dimensions of the final pore structure at the material synthesis stage (Camblor *et al*. 2008).

3.4.5. Diffusion and molecular exchange in two regions

In systems in which diffusion occurs in two regions with differing self-diffusivities, molecular exchange may occur between the two physical regions at equilibrium. When applied to gaseous systems confined in microporous zeolites, these two regions correspond to the internal and external crystalline regions of the zeolite structure (Kärger *et al*. 1988). In fast exchange cases at equilibrium, the internal crystalline self-diffusion coefficient is weighted towards the (faster) external crystalline self-diffusion coefficient and hence the echo attenuation plot is (nominally) linear. Therefore, a PFG NMR experiment cannot distinguish between the self-diffusion coefficients corresponding to the molecules in the two regions in such instances and an average diffusivity is quoted. This is because the observation time, Δ, is significantly longer than the exchange time between the two regions.

However, in slow and intermediate exchange regimes at equilibrium, discernible and simultaneous exchange environments exist. In such instances, the curved echo attenuation plot corresponds to the molecules in the internal and external crystalline regions. Molecular mobility in the external crystalline region is faster than in the internal crystalline region, as it is larger in size and therefore less restrictive. Figure 3.5 shows an example of *n*-hexane diffusing in mesoporous MCM-41 particles. The self-diffusion coefficients, 4×10^{-6} m^2 s^{-1} and 6×10^{-10} m^2 s^{-1}, in this system were attributed to the external and internal MCM-41 particle regions respectively. These diffusion coefficients are weighted by the population of molecules present in both regions. The external and internal populations of the *n*-hexane molecules in this system were reported as 0.85% and 99.15% respectively (Hansen *et al*. 1998).
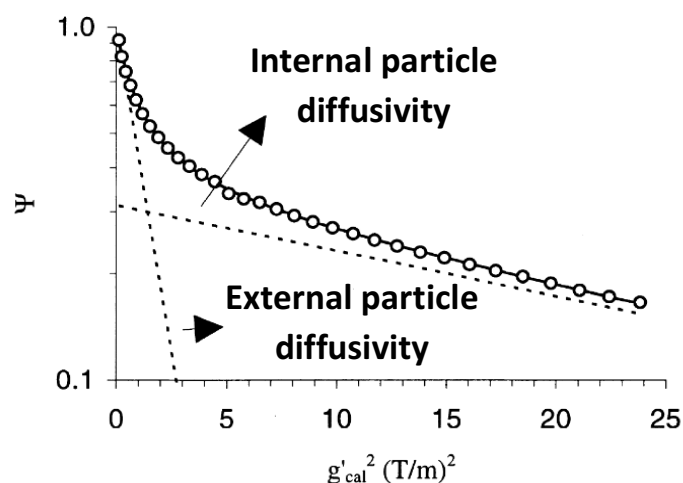
Figure 3.5: Non-linear echo attenuation plot showing exchange behaviour of n-hexane in MCM-41 between the internal and external particle regions. The solid line is a fit of the data (black circles) to equations 3.10 - 3.14 (Hansen *et al* 1998).

Varying the observation time in PFG NMR experiments plays a critical role in observing molecular exchange in large crystallite zeolite systems. Short observation times enable the characterisation of molecules in the intra-crystalline region, as the $RMSD$ of molecules may be limited to a single crystallite in certain cases. Increasing the observation time, which subsequently increases the $RMSD$ of the guest molecule, enables molecules to travel through the permeable zeolite structure. Consequently, the signal from the molecules in the inter-crystalline region may be detected. It is thus assumed that at equilibrium, molecules simultaneously travel to and from the two regions.

Fitting a simple bi-exponential model, such as equation 3.9, to this type of curve would not be suitable as it does not account for the exchange process. It has been shown that a numerical model which incorporates PFG NMR parameters may be used to characterise the self-diffusion coefficients between the inter- and intra-crystalline regions. This model (hereafter referred to as the Kärger model) uses equation 3.9 as a platform and incorporates additional parameters which approximate the populations and residence times of the molecules in both regions (Kärger *et al.* 1988). The Kärger model also estimates the probabilities of molecules moving to and from differing zeolite regions, based on the aforementioned residence times and the permeability of the zeolite. The expressions to determine these parameters are given by equations 3.10 - 3.14:

$$\Psi = p'_1 exp(-bD'_1) + p'_2 exp(-bD'_2)$$
<div align="right">3.10</div>

where

$$D'_{2,1} = \frac{1}{2}\left\{ D_1 + D_2 + \frac{1}{\gamma^2\delta^2 g^2}\left(\frac{1}{\tau_1} + \frac{1}{\tau_2}\right) \right.$$

<div align="right">3.11</div>

$$\left. \pm \left[\left(D_2 - D_1 + \frac{1}{\gamma^2\delta^2 g^2}\left(\frac{1}{\tau_2} - \frac{1}{\tau_1}\right)\right)^2 + \frac{4}{\gamma^2\delta^2 g^2\tau_1\tau_2}\right]^{1/2} \right\}$$

$$p'_2 = \frac{1}{D'_2 - D'_1}(p_1 D_1 + p_2 D_2 - D'_1),$$
<div align="right">3.12</div>

$$p'_1 = 1 - p'_2,$$
<div align="right">3.13</div>

$$p_i = \frac{\tau_i}{\tau_1 + \tau_2}$$
<div align="right">3.14</div>

where $D'_{2,1}$ is the self-diffusion coefficient from region two to one, D_1 and D_2 are the self-diffusion coefficients of the molecules in region one and region two respectively, τ_1 and τ_2

are the residence times of the molecules in region one and region two respectively, p_2' is the population of molecules in region two, p_1' is the population of molecules in region one, p_i is the conditional probability that a molecule moves from a given region and τ_i is the mean residence time of the molecules.

3.5. Self-diffusion of gases

The thermal conductivities of dilute monoatomic gases may be characterised using the kinetic theory of gases. A key assumption for this concept involves treating the diffusing species as rigid, spherical particles which are non-attracting. The thermal velocity, v, of the diffusing species may be calculated as follows:

$$v = \sqrt{\frac{8k_BT}{\pi m}}$$

<div align="right">3.15</div>

where m is the mass of the diffusing species. The thermal velocity is typically modified by a length-scale, λ, which is a function of the mean free diffusion pathway, and the pore geometry in some heterogeneous systems. For the former, it is given by:

$$\lambda = \frac{1}{\sqrt{2}\pi d^2 N_A P}$$

<div align="right">3.16</div>

where d is the diameter of the diffusing species and N_A is Avogadro's number and P is the gas pressure. The self-diffusion coefficient may therefore be obtained by the following expression:

$$D = \frac{1}{3}v\lambda$$

<div align="right">3.17</div>

With the aid of equations 3.15, 3.16 and 3.17, in conjunction to the wall collision frequency of the diffusing species (shown in appendix A8), the self-diffusion approximation may be extended to systems which involve more than one species. The self-diffusion coefficients of

multicomponent gaseous mixtures of comparable sizes may also be calculated using the Chapman-Enskog approximation and is given by (Chapman and Cowling 1970):

$$D = \frac{0.00186T^{3/2} \left(1/M_A + 1/M_B\right)^{1/2}}{p\sigma_{1,2}^2 \Omega} \qquad 3.18$$

where D is the self-diffusion coefficient, T is the temperature, M_A and M_b are the molecular weights of species A and B, p is the pressure, σ is the collision diameter and Ω is a dimensionless Lennard-Jones interaction integral.

The importance of chemical kinetics with respect to the characterisation of diffusion regimes in zeolite structures will be discussed in chapter 5.

3.6. Self-diffusion regimes in microporous zeolites

It is possible to observe more than one self-diffusion process in heterogeneous systems involving molecular transport and adsorption. However, the focus of this thesis is on the characterisation of self-diffusion behaviour in microporous zeolites. With this in mind, the main types of self-diffusion regimes that are observed are discussed in this section.

Figure 3.6 shows an example of the three regimes that are pertinent to the characterisation of molecular displacements in zeolites using PFG NMR.
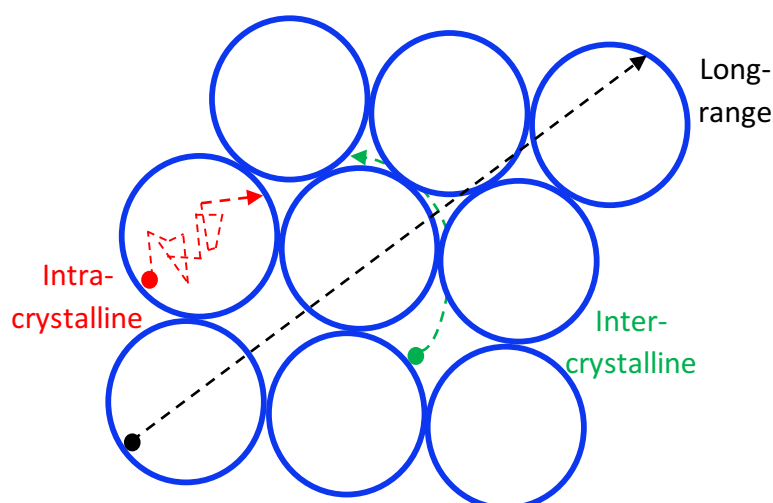
Figure 3.6: Representation the typical self-diffusion regimes observed in microporous zeolite crystallites (adapted from McDaniel *et al*. 1996).

3.6.1. Intra-crystalline self-diffusion

The characterisation of intra-crystalline diffusion regimes is of paramount interest from an academic and industrial perspective. This is because it typically offers an accurate reflection of molecular displacements in single crystallites which are unblemished by contributions from external framework species, surface topology and void spaces. Diffusion processes are often the rate limiting step in industrial processes which involve heterogeneous catalysis and may lead to catalytic deactivation in certain instances. Therefore, characterising this diffusion regime enables the performance of industrial zeolite materials to be investigated, as deactivation processes such as coking typically occurs within the crystallite's pore structure (Guisnet and Magnoux 1989). This diffusion regime may be observed by probing short displacement length-scales using gas or liquid phase molecules, in small and large pore microporous zeolites with large crystallites.

3.6.2. Inter-crystalline self-diffusion

Conversely, the characterisation of inter-crystalline diffusion regimes is enabled by using more mobile species or by increasing the PFG NMR observation time to probe longer length-scales. Whilst intra- and inter-crystalline diffusion processes occur simultaneously in real time, it is possible to eliminate the signal from the former as molecules residing in both regimes possess different relaxation properties (Hansen *et al*. 1998). This will be discussed further in chapter 5, as the inter-crystalline region plays an important part in the characterisation of the intra-crystalline self-diffusion coefficient.

3.6.3. Long-range self-diffusion

Lastly, further increasing the molecular displacement length to enable molecules to experience multiple intra- and inter-crystalline regions results in the manifestation a long-range diffusion regime. In such instances, the diffusion regime represents an average across a zeolite bed and is expressed as (McDaniel *et al*. 1996):

$$D_{long-range} = p_{inter}D_{inter} + p_{intra}D_{intra} \qquad 3.19$$

Long-range diffusion is unavoidable in many zeolite systems, such as those which involve gas phase guest molecules adsorbed in medium or large pore zeolites which have small crystallite sizes. This is because these molecules typically possess $RMSD$s which may exceed 100 μm. Zeolite crystals are synthesised *via* a crystallisation process which occurs at elevated temperatures and pressures in an autoclave. The formation of crystallite sizes exceeding 100 μm is particularly challenging, as the prohibitively long timespans involved often result in a compromise in the material's structural integrity. Additionally, the twinning of zeolite crystallites, which is an unwanted yet probable result, may occur during the crystallisation process. This gives rise to significant void spaces, which increases the overall inter-crystalline space, contributing to the long-range diffusion as more molecules are able to occupy this space. Therefore, long-range diffusion regimes are acknowledged and accounted for in the literature when characterising self-diffusion in zeolite systems. The long-range diffusion regime is at the heart of reported conflicts in the literature when drawing comparisons between molecular displacements measured using PFG NMR and alternative techniques. This will be discussed further in section 3.8.

3.6.4. Unrestricted diffusion in microporous materials

Literature studies have also shown that it is possible to describe unrestricted molecular motion in heterogeneous systems using an approximation model based on the geometry of the porous material. This is referred to as Mitra's short-time approximation model (Mitra *et al*. 1993). By extrapolating the observation time to t = 0, the intrinsic, unrestricted diffusion coefficient, D, may be calculated from the effective self-diffusion coefficient, D_{eff}, obtained from the PFG NMR experiment (Beckert *et al*. 2013):

$$D_{eff}(t) = D - \frac{4}{3\sqrt{\pi}R}D^{3/2}\sqrt{t}$$

3.20

where R is the radius of confinement and t is the observation time. An example in which the unrestricted diffusion coefficients of water and cations confined in LSX type zeolites are obtained using this method is summarised in table 1. This table also gives a literature summary of the self-diffusion regimes which are observed for gases and liquids confined in porous materials using PFG NMR.

3.7. Literature summary of PFG NMR self-diffusion coefficients

This section includes a brief literature summary table of the self-diffusion coefficient of various molecules confined in porous materials that are of relevance to this thesis. All reported results were obtained using PFG NMR methods.

Table 1: Summary of PFG NMR self-diffusion coefficients of fluids in porous media reported in the literature.

Guest molecule(s) and zeolite system(s)	Diffusivity $[m^2 \, s^{-1}]$	Temperature [K]	Crystallite size [μm]	Self-diffusion regime	PFG NMR parameters	Reference
Paraffins in NaX	$0.0005 - 1 \times 10^{-8}$	123 - 593	50	Intra	Δ = 10 ms	Kärger $et\ al$. 1980
C_4H_{10} in NaX	$0.0002 - 5 \times 10^{-7}$	173 - 333	5, 16	Long-range, inter	Δ = 50 - 200 ms	Kärger $et\ al$. 1981
C_2H_4 and C_2H_6 in NaX	$1 - 5 \times 10^{-9}$	293	60	Intra	Δ = 2 - 15 ms, δ = 0.1 - 0.6 ms, g = 0 - 280 G cm^{-1}	Hong $et\ al$. 1991
CH_4 in H-ZSM-5	7×10^{-9}	250	25	Intra	Δ = 2 - 5 ms	Kärger and Pfeifer 1991
CH_3OH in NaX	$0.02 - 7 \times 10^{-10}$	293 - 433	50, 100	Intra	Δ = 14 ms	Grenier $et\ al$. 1994
H_2O, C_3H_8, C_3H_6, C_3H_6O and C_3H_8O in NaX	$0.005 - 6 \times 10^{-7}$	200 - 500	20 - 30	Intra	Δ = 2 - 10 ms	Schwarz $et\ al$. 1995
Xe in NaX	6×10^{-10}	298	6 - 25	Intra	Δ = 2.5 - 50 ms	Bolt-Westerhoff $et\ al$. 1996

Guest molecule(s) and zeolite system(s)	Diffusivity [$m^2\ s^{-1}$]	Temperature [K]	Crystallite size [μm]	Self-diffusion regime	PFG NMR parameters	Reference
N_2 in 5A and 13X	$0.01 - 3 \times 10^{-6}$	167 - 289	1.5	Long-range	Δ = 3 ms, 2 ms	McDaniel *et al.* 1996
C_6H_{14} in porous glass[+]	$0.2 - 3 \times 10^{-9}$	303	80 - 130*	Intra*	Δ = 3 - 1500 ms δ = 0.01 - 0.03 ms	Valiullin *et al.* 1997
n-hexane in MCM-41^{+}	$0.0006 - 4 \times 10^{-6}$	298	N/A	Intra and inter	Δ = 1 - 21 ms, δ = 0.2 ms, g = 47 - 499 G cm^{-1}	Hansen *et al.* 1998
NH_3 in silicalite[+]	$0.1 - 2 \times 10^{-10}$	200 - 500	12	Intra	Δ = 1.5 - 3 ms	Jobic *et al.* 1998
C_2H_6 in ZSM-5	$4 - 7 \times 10^{-11}$	213 - 233	20	Intra	Δ = 1 - 9 ms, δ = 0.2 ms, g = 0 - 700 G cm^{-1}	Gjerdåker *et al.* 1999
H_2O in polystyrene[+] and glass spheres[+]	$1 - 2 \times 10^{-9}$	298	30*	Long-range, inter	Δ = 125, 800 ms δ = 0.25 ms g = 0 - 960 G cm	Seland *et al.* 2000
CH_4 and C_4H_{10} in ZSM-5 and silicalite[+] respectively	$0.1 - 7 \times 10^{-9}$	123 - 383	25 - 100	Intra	Δ = 2 - 35 ms δ = 0.2 ms g = 10 - 2400 G cm^{-1}	Vasenkov *et al.* 2001

Guest molecule(s) and zeolite system(s)	Diffusivity [$m^2\ s^{-1}$]	Temperature [K]	Crystallite size [µm]	Self-diffusion regime	PFG NMR parameters	Reference
H_2O in silicalite[+]	2×10^{-9}	298, 393	30	Intra	Δ = 0.8 - 2 ms δ = 0.26 ms	Bussai *et al* 2002
H_2O in NaCaA	$0.01 - 5 \times 10^{-10}$	298 - 573	0.25 - 4	Intra	Δ = 5 - 20 ms, δ = 0.4 - 1 ms, g = 0 - 3200 G cm^{-1}	Paoli *et al*. 2002
C_2H_6 in NaX	$0.1 - 7 \times 10^{-7}$	193 - 368	20 - 30	Long-range, inter	Δ = 20 - 100 ms δ = 0.05 - 0.16 ms g = 0 - 270 G cm^{-1}	Vasenkov *et al*. 2003
Octane in USY	$0.4 - 9 \times 10^{-11}$	173 - 298	3	Intra	Δ = 10 ms	Kortunov *et al*. 2005
n-butane in silicalite[+]	3×10^{-10}	293	-	Intra	Δ = 30 ms, δ = 2 ms	Pampel *et al*. 2005
Propane in silica gel[+]	2×10^{-9}	301	335*	Intra	Δ = 3.6 ms δ = 0.5 ms g = 0 - 125 G cm^{-1}	Hedin *et al*. 2006
n-alkanes in MFI structures	$0.0001 - 6 \times 10^{-8}$	298 - 453	> 30	Intra	Δ = 3 - 20 ms	Jobic *et al*. 2006

Guest molecule(s) and zeolite system(s)	Diffusivity $[m^2 s^{-1}]$	Temperature [K]	Crystallite size [μm]	Self-diffusion regime	PFG NMR parameters	Reference
C_2H_4, C_2H_6, H_2O and C_6H_6 in NaX	$0.9 - 3 \times 10^{-10}$	-	50	Intra	Δ = 10 ms	Pampel *et al*. 2006
C_3H_6 in ITQ-29, CaA and NaCaA	$0.5 - 8 \times 10^{-13}$	301	3	Intra	Δ = 69 - 500 ms δ = 1.5 ms g = 10 - 1160 G cm^{-1}	Hedin *et al*. 2007
CH_4 and C_2H_6 in NaCaA	$0.08 - 2 \times 10^{-9}$	223 - 373	5 and 35	Intra	Δ = 1 - 30 ms	Krutyeva *et al.* 2007
C_4H_{10} - C_8H_{20} in NaX	$0.06 - 2 \times 10^{-9}$	298	80 - 100	Intra	Δ = 6 - 12 ms, δ = 0.2 ms, g = 0 - 1200 G cm^{-1}	Adem *et al.* 2008
CH_4, C_2H_6, C_2H_4, C_3H_6 in Si-CHA, Si-LTA and ZSM-58	$0.005 - 140 \times 10^{-8}$	301	3, 4 and 5	Intra	Δ = 2 - 15 ms, g = 0 - 1200 G cm^{-1}	Hedin *et al*. 2008
$C_{10}H_{22}$ and $C_{17}H_{36}$ in meso-porous aluminosilicates[+]	$0.0001 - 2 \times 10^{-8}$	173 - 296	10,000*	Intra	Δ = 20 ms	Krutyeva *et al*. 2009
CH_4 in LTA	5×10^{-10}	298	30	Intra	Δ = 5 - 800 ms	Binder *et al*. 2011
C_2H_4 and C_2H_6 in SAPO-34^{+}	$0.6 - 2 \times 10^{-11}$	295 - 353	20 - 30	Intra	Δ = 10 - 40 ms	Dai *et al*. 2012
C_2H_6 and C_6H_{12} in NaCaA	$0.01 - 2 \times 10^{-10}$	163 - 333	11	Intra	Δ = 5 - 80 ms	Mehlhorn *et al*. 2012

Guest molecule(s) and zeolite system(s)	Diffusivity [$m^2\ s^{-1}$]	Temperature [K]	Crystallite size [µm]	Self-diffusion regime	PFG NMR parameters	Reference
H_2O and ^7Li in LSX	$0.1 - 2 \times 10^{-10}$	298 and 373	3 - 10	Long-range, unrestricted	Δ = 1.2 – 150 ms, δ = 0.5 - 1.5 ms	Beckert *et al.* 2013
H_2O and ^7Li in LSX	$0.2 - 3 \times 10^{-10}$	373	10	Long-range, unrestricted	Δ = 10 ms, 100 ms, δ = 1 ms, g = 5 - 50 G cm^{-1}	Freude *et al.* 2013
H_2O in NaMSX and 4A[+]	$0.06 - 3 \times 10^{-10}$	260 - 353	-	Intra	Δ = 3 - 30 ms	Mehlhorn *et al.* 2014

+These porous materials are not classified as zeolites.

*Refers to the mean particle diameter.

3.8. Comparison of diffusion characterisation techniques

From an academic and industrial perspective, one of the main aims of this thesis was the development of solely PFG NMR based methods which are capable of characterising self-diffusion regimes. The aim is to then transfer these methods to the Johnson Matthey Technology Centre (JMTC) to enable self-diffusion characterisations of real world samples to be performed in an industrial setting.

There exists a wide range of measurement techniques which have been used to perform similar characterisations. Figure 3.7 illustrates the metrological advancements of the last century with respect to the characterisation of diffusion in porous materials. The techniques of interest to the JMTC are PFG NMR and Quasi Elastic Neutron Scattering (QENS). Further, molecular Dynamics (MD) simulations are widely used in the literature to predict molecular displacements in microporous materials. These computational practices are also used at JMTC to validate experimental data obtained from the aforementioned techniques of interest.
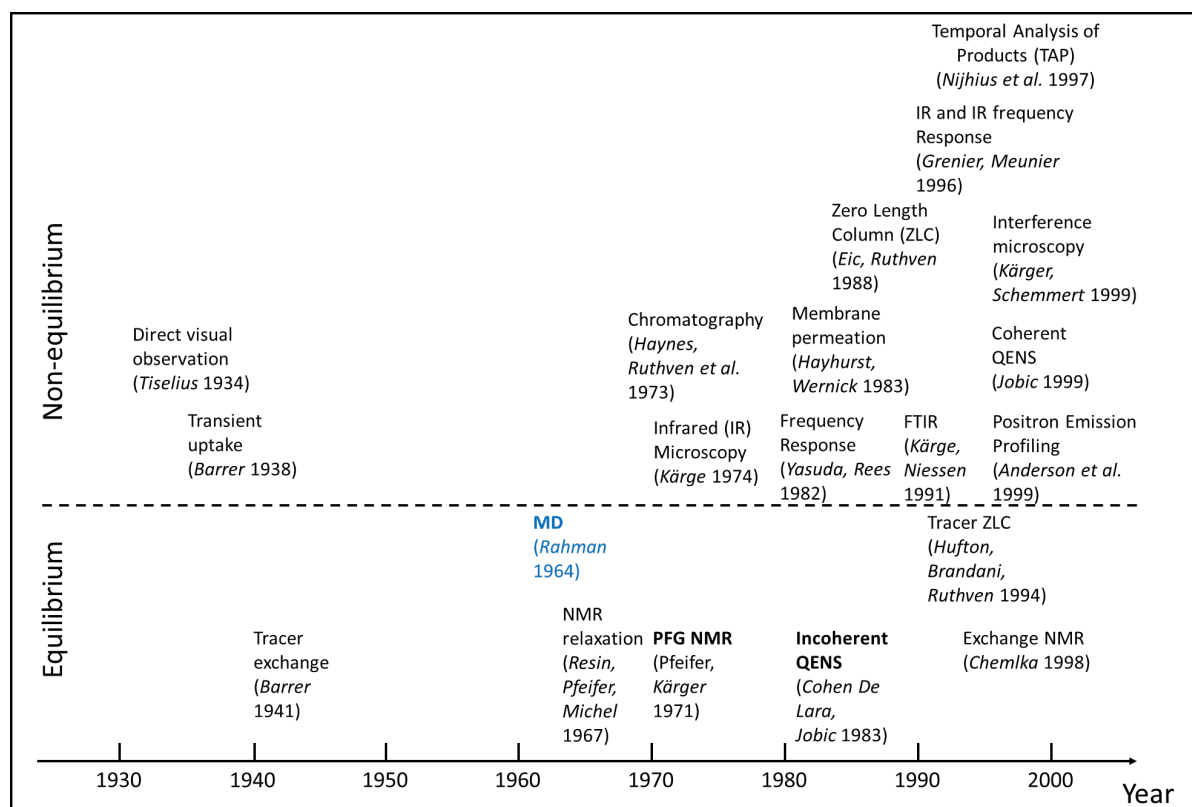
Figure 3.7: Historical overview of developed techniques which characterise a range of diffusion processes and their founders in brackets. The full references are included in the references list (adapted from Conner and Fraissard 2003).

Large differences are reported in the literature between the self-diffusion coefficients obtained using PFG NMR, QENS and MD for molecules adsorbed in zeolites (Conner and Fraissard 2003). Another aim of this thesis is to account for the discrepancies in the reported self-diffusion coefficients using these methods, as it has a direct impact on the analysis of mass transport data relevant to the JMTC. Figure 3.8 shows the typical differences observed in the self-diffusion coefficients of n-alkanes in silicalite, which were obtained using the techniques of interest under comparable conditions.
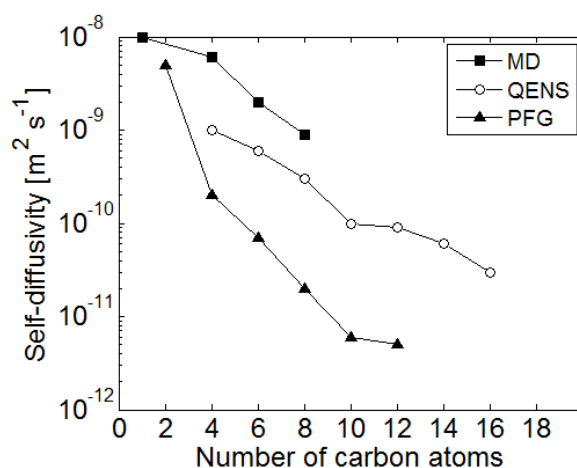
Figure 3.8: Comparison of self-diffusion coefficients of n-alkanes in silicalite characterised at 300 K using techniques relevant to JMTC (re-plotted from Conner and Fraissard 2003).

This disparity was attributed to the length-scales over which the measurements and simulations are made, which stems from the large differences in the observation times involved in each technique. The observation times of PFG NMR measurements typically ranges from a few milliseconds to several seconds and is limited by the T_1 relaxation constant of the molecule of interest. However, the observation times in QENS and MD are significantly shorter, ranging from picoseconds to nanoseconds and are limited by hardware and computing capabilities respectively (Jobic and Theodorou 2007). The consequence of this is linked to equation 3.6, Einstein's relation, which is critical for the interpretation of probing various molecular displacement length-scales in zeolite geometries. The longer observation time-scales in PFG NMR result in the probing of displacement length-scales ranging from microns to millimetres. Typical industrial processes which utilise zeolites involve crystallite sizes which range from hundreds of nanometres to a few microns in diameter (Tonetto *et al*. 2004). The diameters of zeolite crystallites that are used in research applications are typically of the order of microns. Therefore, guest molecules can typically experience several

crystallites during a typical PFG NMR experiment, which results in the characterisation of a long-range diffusion regime. Molecular displacements in long-range diffusion regimes are more susceptible to defects, extra-framework ions and Brønsted acid sites in the zeolite crystallite, which can lead to an additional resistance barrier to diffusion (O'Malley 2015).

However, the shorter time-scales typically used in QENS and MD probe significantly shorter displacement length-scales, ranging from angstrom to nanometres. As such, molecular displacements are limited to single zeolite crystals, which thus describes an intra-crystalline diffusion regime. Therefore, large variations are observed in the self-diffusion coefficients between the various techniques due to the characterisation of significantly different diffusion regimes. Figure 3.9 illustrates the typical differences in time-, length-scales and the range of self-diffusion coefficients characterised using the different techniques. The Zero Length Column (ZLC) method, which is a non-equilibrium technique, is also included as this is of interest to different research groups within Johnson Matthey. Additionally, it is often used as a comparison with equilibrium techniques such as PFG NMR (Ruthven and Brandani 2000; Silva and Rodrigues 2015). Table 2 gives a brief description along with the advantages and disadvantages associated with each technique.

Table 2: Summary of diffusion characterisation techniques relevant to the JMTC.

Technique	Description	Advantages/Disadvantages (+/-)
Pulsed Field Gradient (PFG) NMR	Excitation radiofrequency pulse tips magnetisation away from equilibrium. Gradient pulse labels position of spins and imparts a net phase shift. Second gradient pulse labels new position of spins and reverses the effect of the first. Motion during this time is recorded. Increasing the gradient amplitudes enables the net phase shift and signal attenuation to be tracked, which allows the deduction of the self-diffusion coefficient.	**+** Well established, non-destructive method. **+** Capable of measuring large molecular displacements up to millimetres by selecting a range of observation times. This enables the characterisation of a number of self-diffusion regimes in microporous structures. **-** Signal and measurable range of molecular displacements are limited by transverse relaxation processes. **-** Full signal attenuation of strongly adsorbing species may require large gradient strengths that are not within measurement capabilities. **-** Presence of paramagnetic and industrially relevant additives, e.g. Cu^{2+}, further hinders NMR relaxation processes.

Zero-length column (ZLC)	Sorbate molecule is adsorbed onto zeolite bed *via* a carrier system and is allowed to reach equilibrium. The desorption rate is measured when the carrier system is switched to a non-adsorbing feed. The effluent stream concentration is subsequently recorded with respect to time.	**+** Experiment can be conducted at high and industrially relevant temperatures. **-** Not possible to accurately characterise the diffusion of weakly adsorbing species due similarities in response curves of diffusion and non-linear equilibrium processes. **-** Lengthy desorption response times. **-** Desorption curves of macro- and micro-porous materials show similar concentration profiles, which generates ambiguous data.
Quasi Elastic Neutron Scattering (QENS)	Porous material is subjected to a neutron beam and differences in the energy of incident and scattered neutrons are analysed as a function of neutron momentum transfer. This data is subsequently used to fit displacement vectors to models which characterise self-diffusion processes.	**+** Short observation times, of the order of picoseconds, enables the characterisation of intra-crystalline self-diffusion coefficients of industrially sized (nanometres to microns) microporous materials. **-** Access to neutron beam is extremely scarce due to high operating costs: ≈ £14,000/day. **-** Lengthy experimental timeframes and elaborate sample preparation. Also requires prior analysis of a (blank) reference sample.
Molecular Dynamics (MD)	Predicts time-dependent molecular displacements using Newtonian equations of motion. Correlates this motion to self-diffusivity using Einstein's relation (eq. 3.7).	**+** The selection of short observation items enables comparisons to be made with QENS. **-** Computationally intensive process which requires several days to run a simulation at a fixed temperature and pressure. **-** Longer observation times (> nanoseconds) to probe larger molecular displacements, as to draw comparisons with PFG NMR, cannot be selected due to processing power limitations of modern day computers.
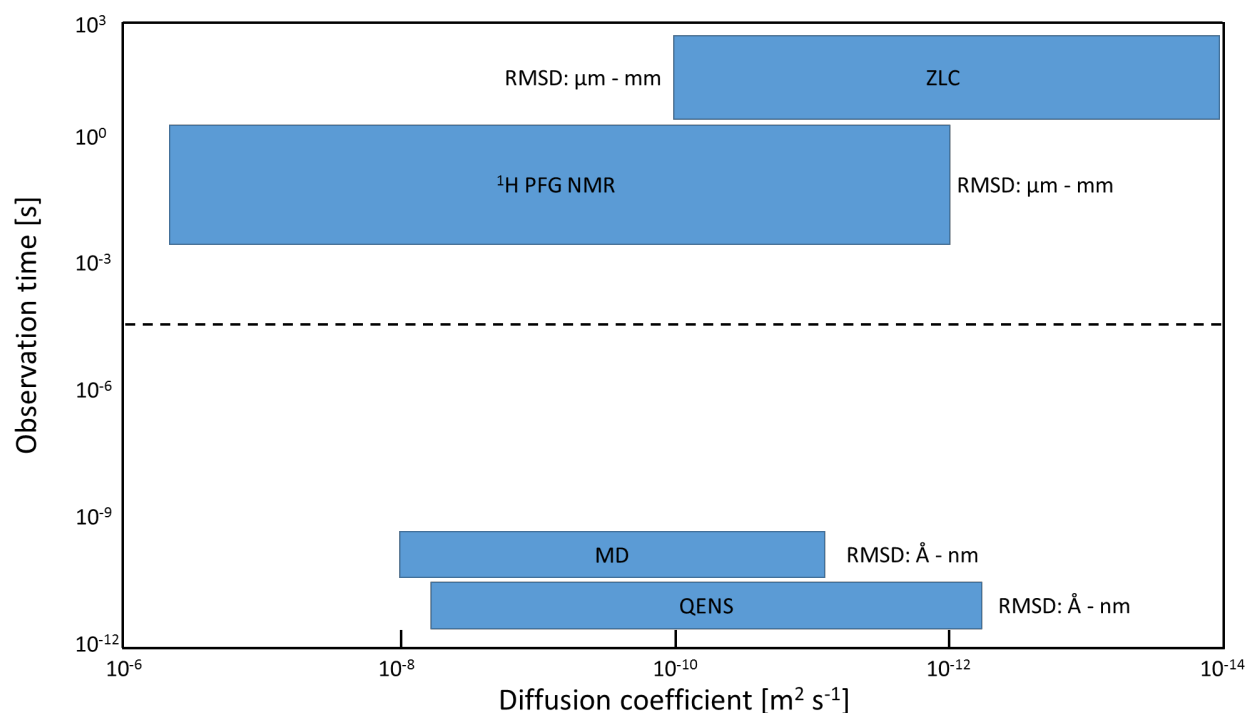
Figure 3.9: Typical range of diffusion coefficients probed by various diffusion characterisation techniques and associated observation time-scales for diffusion.

Regarding figure 3.8, the self-diffusion coefficients simulated using MD are significantly higher than those obtained using PFG NMR and QENS, as many simulation studies are conducted with infinite dilution assumptions, resulting in the removal of all sorbate-sorbate interactions. This results in a faster diffusivity of sorbate molecules through the zeolite channels, which subsequently increases the self-diffusion coefficients. Since these interactions cannot be removed experimentally, the self-diffusion coefficients obtained using PFG NMR and QENS are generally lower than those from MD simulations (O'Malley 2015).

The variations in the self-diffusion coefficients of mobile (e.g. gas phase) and less mobile (e.g. liquid phase) molecules confined in zeolites which are obtained using PFG NMR and QENS have differing interpretations (Jobic *et al* 2006). On the one hand, highly mobile sorbates in PFG NMR experiments possess large $RMSDs$. Consequently, they are prone to interacting with the crystallite structure and may potentially cross over into a long-range diffusion regime due to the long(er) observation times associated with this technique. This results in a faster self-diffusion coefficient in comparison to QENS, as molecules frequently experience the inter-crystalline space, which subjects the molecules to a reduced degree of restriction. The void fraction in between the zeolite crystallites has a considerable impact on the extent to

which the inter-crystalline region contributes to the overall signal. The significance of this will be discussed in further detail in chapter 5.

The self-diffusion coefficients of the less mobile sorbate molecules obtained using PFG NMR are typically lower than those from QENS. This is because such molecules are more susceptible to adsorb onto the surface of the zeolite and are therefore more likely to be influenced by the aforementioned crystallite defects and extra-framework ions, which therefore adds to the molecular transport resistance (Jobic *et al*. 2006).

The observation time in PFG NMR experiments cannot be reduced below a few milliseconds due to hardware limitations. Therefore, to draw comparisons between intra-diffusion regimes using PFG NMR and alternative techniques, certain measures are taken in order to prevent the *RMSDs* from approaching the crystallite size of the zeolite. These include the use of large zeolite crystals, to increase the window for observing intra-crystalline diffusion, and the use of low experimental temperatures and high sorbate pressures, to obtain lower self-diffusion coefficients (Kärger *et al*. 1980; Hong *et al*. 1991; Jobic *et al*. 1998; Mehlhorn *et al*. 2012).

There exists a lack of experimental literature data for the self-diffusion of gas and liquid phase molecules adsorbed in β-zeolite using PFG NMR. Therefore, comparisons are made with an alternative large pore zeolite in this thesis, which will be discussed further in chapter 5. However, β-zeolite has been used in the literature to characterise the diffusion processes of propane and isobutane in small (< 1 μm) crystallites using the Tapered Element Oscillating Microbalance (TEOM) method. This section outlines a brief summary of the method and the reported findings in the aforementioned literature study.

3.8.1. Literature results for propane and isobutane diffusion in beta zeolite using a TEOM

The TEOM technique was originally developed to quantify particulate concentrations in gas phase systems (Patashnick and Rupprecht 1991). However, it has since been extended to measure and study equilibrium adsorption isotherms (Zhu *et al*. 1998; Giaya and Thompson 2002), the kinetics of coking (Liu *et al*. 1997; Petkovic and Larsen 1999; Chen *et al*. 2000) and the influence of coke on catalytic activity and selectivity (Chen *et al*. 1996a, 1997, 1999a; Liu *et al*. 1997b; Petkovic and Larsen 2000; van Donk *et al*. 2002).

The technique involves flowing gaseous sorbate molecules over the instrument, which has a tapered element that secures the sample in between layers of quartz wool, which subsequently contacts the solid sample in a packed bed. The top of the tapered element is secured such that the entire element can oscillate in a clamped-free manner. The oscillation frequency of the tapered element increases when the mass of the solid sample decreases, and *vice versa*. The oscillating frequency is recorded, along with the initial oscillating frequency at the beginning of the experiment. The change in mass is then recorded by a microbalance between two time points, 0 and 1, using the following equation:

$$\Delta m = K \left[\frac{1}{f_1^2} - \frac{1}{f_0^2} \right]$$

3.21

where Δm is the change in mass, K is the spring constant of the tapered element, f_0 is the oscillating frequency at time 0 and f_1 is the oscillating frequency at time 1. The change in mass, at equilibrium, is then recorded as a function of time and subsequently gas pressure to obtain a gas sorption isotherm. A more detailed introduction of the TEOM technique is given in the literature (Zhu 2001). Figure 3.10 shows an example of a typical experimental setup.
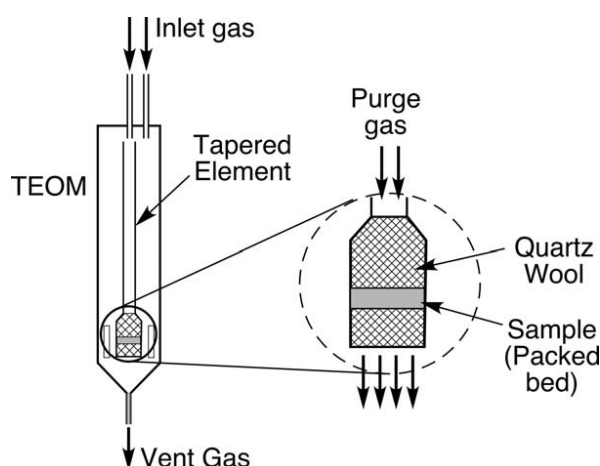
Figure 3.10: Schematic diagram of a TEOM instrument (Gong *et al*. 2010).

It has been shown that the quantity adsorbed by a zeolite sample may be correlated to an intra-crystalline diffusion coefficient *via* (Kärger and Ruthven 1992):

$$D_{intra} = \frac{D_0}{1 - \frac{q}{q_s}}$$ 3.22

where D_0 is the corrected diffusivity (which was introduced in section 3.3.2), q is the concentration in the adsorbed phase and q_s is the saturation concentration in the adsorbed phase. It has been demonstrated that the intra-crystalline diffusion coefficients of propane in β-zeolite range from 1 - 3 $\times$ 10^{-8} m^2 s^{-1} over a temperature range of 303 - 348 K and a loading of up to 0.06 g/g of β-zeolite. The intra-crystalline diffusion coefficients of isobutane in β-zeolite range from 1 - 4 $\times$ 10^{-8} m^2 s^{-1} over a temperature range of 323 - 398 K and a loading of up to 0.08 g/g of β-zeolite (Gong *et al*. 2010).

3.9. Conclusions

This chapter introduced the different types of diffusion processes typically observed in bulk and adsorbed phase systems. An introduction into the history of observed molecular displacements and its association with self-diffusivity was given. Examples of potential causes of curvature in PFG NMR echo attenuation plots were shown, to aid with the interpretation of diffusometry data which will be presented in this thesis. Lastly, the different self-diffusion regimes that are typically observed in zeolite systems were discussed, with comparisons drawn between alternative molecular displacement characterisation techniques of interest to the JMTC. Discrepancies in the literature with respect to the dissimilar reported self-diffusion coefficients for these techniques were discussed, as the differences in experimental time- and length-scales were identified as the source of this disparity.

3.10. References

Adem, Z., Guenneau, F., Springel-Huet, M.A., Gédéon, A., (2008). PFG NMR investigation of hydrocarbon diffusion in large NaX zeolite crystals: Effect of internal field gradients on diffusion data. Micropor. Mesopor. Mater. 114: 337-342.

Anderson, B.G., van Santen, R.A., de Jong, A.M., (1999). Positrons as *in situ* probes of transient phenomena. Top. Catal. 8: 125-131.

Barrer, R.M., (1938). The sorption of polar and non-polar gases by zeolites. Proc. Roy. Soc. A. 167: 392–420.

Barrer, R.M., (1941). Migration in crystal lattices. Trans. Faraday Soc. 37: 590–599.

Beckert, S., Stallmach, F., Toufar, H., Freude, D., Kärger, J., Haase, J., (2013). Tracing water and cation diffusion in hydrated zeolites of type Li-LSX by pulsed field gradient NMR. J. Phys. Chem. C. 117: 24866-24872.

Binder, T., Adem, Z., Krause, C.B., Krutyeva, M., Huang, A., Caro, J., Kärger, J., (2011). Micropor. Mesopor. Mater. 146: 151-157.

Bird, R.B., Stewart, W.E., Lightfoot, E.N., (2007). *Transport phenomena*. John Wiley & Sons.

Bolt-Westerhoff, J.A., Datema, K.P., Nowak, A.K., Stallmach, Kärger, J., (1996). PFG NMR tracer exchange measurements of xenon in zeolites. Magn. Reson. Im. 14: 967-969.

Bourdin, V., Grenier, Ph., Meunier, F., Sun, L.M., (1996). Thermal frequency response method for the study of mass-transfer kinetics in adsorbents. AIChE J. 42: 700–712.

Brown, R., (1829). A brief account of microscopical observations made in the months of June, July and August, 1827, on the particles contained in the pollen of plants; and on the general existence of active molecules in organic and inorganic bodies. Phil. Mag. 4:16.

Bussai, C., Vasenkov, S., Liu, H., Böhlmann, W., Fritzsche, S., Hannongbua, S., Haberlandt, R., Kärger, J., (2002). On the diffusion of water in silicalite-1: MD simulations using ab initio fitted potential and PFG NMR measurements. Appl. Catal. A. 232: 59-66.

Callaghan, P.T., (2011). *Translational dynamics & magnetic resonance*. Oxford University Press.

Camblor, M.A., Corma, A., Valencia, S., (2008). Characterization of nanocrystalline zeolite beta. Microporous Mesoporous Mater. 25: 59-74.

Chapman, S., Cowling, T.G., (1970). *The mathematical theory of non-uniform gases*. Cambridge University Press.

Chen, D., Grønvold, A., Rebo, H.P., Moljord, K., Holmen, A., (1996a). Catalyst deactivation studied by conventional and oscillating microbalance reactors. Appl. Catal. A: Gen. 137:L1-L8.

Chen, D., Rebo, H.P., Moljord, K., Holmen, A., (1997). Influence of coke deposition on selectivity in zeolite catalysis. Ind. Eng. Chem. Res. 36: 3473-3479.

Chen, D., Rebo, H.P., Fuglerud, T., Holmen, A., (1999a). The effect of crystal size of SAPO-34 on the selectivity and deactivation of the MTO reaction. Micropor. Mesopor. Mater. 29: 191-203.

Chen, D., Rebo, H.P., Grønvold, A., Moljord, K., Holmen, A., (2000). Methanol conversion to light olefins over SAPO-34: kinetic modelling of coke formation. Micropor. Mesopor. Mater. 35-36: 121-135.

Climent, M.J., Corma, A., García, H., (1991). Zeolites as catalysts in organic reactions: condensation of aldehydes with benzene derivatives. J. Catal. 130: 138-146.

Cohen de Lara, E., Kahn, R., Mezei, F. (1983). Determination of the intracrystalline diffusion-coefficient of methane in A-zeolites by means of neutron spin-echo experiments. J. Chem. Soc. Faraday Trans. I 79: 1911–1920.

Conner, W.C., Fraissard, J., (2003). *Fluid transport in nanoporous materials*. NATO science series. Springer publishing.

Crank, J., (1975). *The mathematics of diffusion*. Oxford Science publications.

Cussler, E.L., (2009). *Diffusion. Mass transfer in fluid systems.* Cambridge University Press.

Dai, W., Scheibe, M., Li, N., Guan, N., Hunger, M., (2012). Effect of the Methanol-to-Olefin conversion on the PFG NMR self-diffusivities of ethane and ethene in large crystalline SAPO-34. J. Phys. Chem. C. 116: 2469-2476.

Eic, M., Ruthven D.M., (1988). A new experimental technique for the measurement of intracrystalline diffusivity. Zeolites 8: 40–45.

Einstein, A., (1905). On the movement of small particles suspended in a stationary liquid demanded by the molecular-kinetic theory of heat. Annln. Phys. 17: 549.

Favre, D.E., Schaefer, D.J., Auerbach, S.M., Chmelka, B.F., (1998). Direct measurement of intercage hopping in strongly adsorbing guest zeolite systems. Phys. Rev. Lett. 81: 5852-5855.

Fick, A., (1855). Ueber diffusion. Annln Phys. 170: 59-86.

Fourier, J.B., (1822). Theorie analytique de la chaleur. English translation by A. Freeman, (1955). Dover Publications.

Freude, D., Beckert, S., Stallmach, F., Kurzhals, R., Täschner, D., Toufar, H., Kärger, J., Haase, J., (2013). Ion and water mobility in hydrated Li-LSX zeolite studied by ^{1}H, ^{6}Li and ^{7}Li NMR spectroscopy and diffusometry. Micropor. Mesopor. Mater. 172: 174-181.

Giaya, A., Thompson, R.W., (2002). Single component gas phase adsorption and desorption studies using a tapered element oscillating microbalance. Micropor. Mesopor. Mater. 55: 265-274.

Gjerdåker, L., Sørland, G.H., Aksnes, W., (1999). Application of the short diffusion time model to diffusion measurements by NMR in microporous crystallites. Micropor. Mesopor. Mater. 32: 305-310.

Gong, K., Subramaniam, B., Ramachandran ,P.A., Hutchenson, K.W., (2010). Tapered Element Oscillating Microbalance (TEOM) studies of isobutane, n-butane and propane sorption in β- and Y-zeolites. AIChE. 56(5): 1285-1296.

Grenier, P., Meunier, F., Gray, P.G., (1994). Diffusion of methanol in NaX crystals: Comparison of i.r., ZLC, and PFG NMR measurements. Zeolites. 14: 242-249.

Guisnet, M., Magnoux, P., (1989). Coking and deactivation of zeolites: influence of the pore structure. Appl. Catal. 54: 1-27

Hansen, E.W., Courivaud, F., Karlsson, A., Kolboe, S., Stöcker, M., (1998). Effect of pore dimension and pore surface hydrophobicity on the diffusion of *n*-hexane confined in

mesoporous MCM-41 probed by NMR – a preliminary investigation. Micropor. Mesopor. Mater. 22: 309-320.

Haynes, H.W., Sarma, P.N., (1974). Application of gas chromatography to measurements of diffusion in zeolites. Adv. Chem. 133: 205–217.

Hedin, N., DeMartin, G.J., Reyes, S.C., (2006). Automated sample preparation station for studying self-diffusion in porous solids with NMR spectroscopy. Rev. Sci. Instrum. 77(035114):1-5.

Hedin, N., DeMartin, G.J., Strohmaier, K.G., Reyes, S.C., (2007). PFG NMR self-diffusion of propylene in ITQ-29, CaA and NaCaA: Window size and cation effects. Micropor. Mesopor. Mater. 98: 182-188.

Hedin, N., DeMartin, G.J., Roth, W.J., Strohmaier, K.G., Reyes, S.C., (2008). PFG NMR self-diffusion of small hydrocarbons in high silica DDR, CHA and LTA structures. Micropor. Mesopor. Mater. 109: 327-334.

Hong, U., Kärger, J., Kramer, R., Pfeifer, H., Seiffert, G., Muller, U., Unger, K.K., Lück, H.B., Ito, T., (1991). PFG NMR study of diffusion anisotropy in oriented ZSM-5 type zeolite crystallites.

Hong, U., Kärger, J., Pfeifer, H., (1991). Selective two-component self-diffusion measurement of adsorbed molecules by pulsed field gradient Fourier transform NMR. J. Am. Chem. Soc. 13: 4812-4815.

Jobic, H., Ernst, H., Heink, W., Kärger, J., Tuel, A., Bée, M., (1998). Diffusion of ammonia in silicalite studied by QENS and PFG NMR. Micropor. Mesopor. Mater. 26: 67-75.

Jobic, H., Kärger, J., Bée, M., (1999). Simultaneous measurement of self- and transport diffusivities in zeolites. Phys. Rev. Lett. 82: 4260–4263.

Jobic, H., (2000). Diffusion of linear and branched alkanes in ZSM-5. A quasi-elastic neutron scattering study. J. Mol. Catal. A: Chem., 158: 135–142.

Jobic, H., Schmidt, W., Krause, C.B., Kärger, J., (2006). PFG NMR and QENS diffusion study of *n*-alkane homologues in MFI-type zeolites. Micropor. Mesopor. Mater. 90: 299-306.

Jobic, H., Theodorou, D.N., (2007). Quasi-elastic neutron scattering and molecular dynamics simulation as complementary techniques for studying diffusion in zeolites. Micropor. Mesopor. Mater. 102: 21-50.

Kärge, H.G., Klose, K., (1974). IR-spectroscopic study of pyridine diffusion in zeolites at high temperatures. Ber. Bunsen. Ges. Phys. Chem. 78: 1263.

Kärge, H.G., Nießen, W., (1991). A new method for the study of diffusion and counter-diffusion in zeolites. Catal. Today. 8: 451-465.

Kärger, J., (1971). Der Einfluß der Zweibereichdiffusion auf die Spinechodämpfung unter Berücksichtigung der Relaxation bei Messungen mit der Methode der gepulsten Feldgradienten. Annln. Phys. 482: 107-109.

Kärger, J., Pfeifer, H., Rauscher, M., Walter, A., (1980). Self-diffusion of n-paraffins in NaX zeolite. J.C.S. Faraday I. 76:771-737.

Kärger, J., Kočirik, M., Zikanová, A., (1981). Molecular transport through assemblages of microporous particles. J. Coll. Interf. Sci. 84: 240-249.

Kärger, J., Heink, W., (1983). The propagator representation of molecular transport in microporous crystallites. J. Magn. Reson. 51: 1-7.

Kärger, J., Pfeifer, H., Rauscher, M., Walter, A., (1980). Self-diffusion of *n*-paraffins in NaX zeolite. J.C.S. Faraday I. 76: 717-737.

Kärger, J., Pfeifer, H., Heink, W., (1988). Principles and applications of self-diffusion measurements by nuclear magnetic resonance. Adv. Magn. Reson. 12: 1-89.

Kärger, J., Pfeifer, H., (1991). Nuclear magnetic resonance measurement of mass transfer in molecular sieve crystallites. J.C.S. Faraday. 87: 1989-1996.

Knudsen, M., (1909). Die Gesetze der Molekularströmung und der inneren Reibungsströmung der Gase durch Röhren. Annln Phys. 333: 75-130.

Kortunov, P., Vasenkov, S., Kärger, J., Valiullin, R., Gottschalk, P., Fé Elía, M., Perez, M., Stöcker, M., Drescher, B., McElhiney, G., Berger, C., Gläser, R., Weitkamp, J., (2005). The role of mesopores in intracrystalline transport in USY zeolite: PFG NMR diffusion study on various length scales. J. Am. Chem. Soc. 127: 13055-13059.

Krutyeva, M., Vasenkov, S., Yang, X., Caro, J., Kärger, J., (2007). Surface barriers on nanoporous particles: A new method of their quantification by PFG NMR. Micropor. Mesopor. Mater. 104: 89-96.

Krutyeva, M., Grinberg, F., Kärger, J., Chorro, C., Donzel, N., Jones, D.J., (2009). Study of the diffusion of liquids and their binary mixtures in mesoporous aluminosilicates under freezing conditions. Micropor. Mesopor. Mater. 120:104-108.

Liu, K., Fung, S.C., Ho, T.C., Rumschitzki, D.S., (1997a). Kinetics of catalyst coking in heptane reforming over Pt-Re/Al$_2$O$_3$. Ind. Eng. Chem. Res. 36: 3264-3274.

Liu, K., Fung, S.C., Ho, T.C., Rumschitzki, D.S., (1997b). Identification of coke precursors in heptane reforming with a multioutlet fixed-bed reactor and a novel vibrational microbalance. J. Catal. 169: 455-468.

McDaniel, P.L., Coe, C.G., Kärger, J., Moyer, J.D., (1996). Direct observation of N$_2$ self-diffusion in zeolitic adsorbents using ^{15}N PFG NMR. J. Phys. Chem. 100: 16263-16267.

Mehlhorn, D., Valiullin, R., Kärger, J., Cho, K., Ryoo, R., (2012). Exploring the hierarchy of transport phenomena in hierarchical pore systems by NMR diffusion measurement. Micropor. Mesopor. Mater. 164:273-279.

Mehlhorn, D., Valiullin, R., Kärger, J., Schumann, K., Brandt, A., Unger, B., (2014). Transport enhancement in binderless zeolite X- and A-type molecular sieves by PFG NMR diffusometry. Micropor. Mesopor. Mater. 188: 126-132.

Mitra, P., Sen, P.N., Schwartz, L.M., (1993). Short-time behaviour of the diffusion coefficient as a geometrical probe of porous media. Phys. Rev. B. 47: 8565-8574.

Nijhuis, T.A., van den Broeke, L.J.P., van de Graad, J.M., Kapeteijn, F., Makkee, M., Moulijn, J.A., (1997). Bridging the gap between macroscopic and NMR diffusivities. Chem. Eng. Technol. 52: 3401-3404.

Ogawa., T., Kamiguchi, K., Tamaki, T., Imai, H., Yamaguchi, T., (2014). Anal. Chem. 86: 9362-9366.

O'malley, A.J., (2015). Hydrocarbon dynamics in microporous catalysts. PhD thesis, University College London.

Pampel, A., Fernandez, M., Freude, D., Kärger, J., (2005). New options for measuring molecular diffusion in zeolites by MAS PFG NMR. Chem. Phys. Lett. 407: 53-57.

Pampel, A., Engelke, F., Galvosas, P., Krause, C., Stallmach, F., Michel, D., Kärger, J., (2006). Selective multi-component diffusion measurement in zeolites by pulsed field gradient NMR. Micropor. Mesopor. Mater. 90: 271-277.

Paoli, H., Méthivier, A., Jobic, H., Krause, C., Pfeifer, H., Stallmach, F., Kärger, J., (2002). Comparative QENS and PFG NMR diffusion studies of water in zeolite NaCaA. Micropor. Mesopor. Mater. 55: 147-158.

Paravar, A., Hayhurst, D.T., (1984). *Direct measurement of diffusivity for butane across a single large silicalite crystal*. In Proc. 6th Int. Zeolite Conf., Reno 1983. Guildford Press.

Patashnick, H., Rupprecht, E.G., (1991). Continuous PM-10 measurements using the tapered element oscillating microbalance. J. Air. Waste Manage. 41: 1079-1083.

Perrin, J.B., (1909). Mouvement Brownien et realite moleculaire. Ann. de. Chim. et. de. Phys. Huitieme serie. Tome XVIII. 5:113.

Petkovic, L.M., Larsen, G., (1999). Oligomerisation of *n*-butenes on the surface of a ferrierite catalyst: real-time monitoring in a packed bed reactor during isomerisation to isobutene. Ind. Eng. Chem. Res. 38: 1822-1829.

Petkovic, L.M., Larsen, G., (2000). Linear butenes from isobutene over H-ferrierite: *in situ* studies using an oscillating balance reactor. J. Catal. 191: 1-11.

Rahman, A., (1964). Correlations in the motion of atoms in liquid argon. Phys. Rev. 136: 2A. A405-A411.

Resing, H.A., Thompson, J.H., (1967). NMR relaxation in adsorbed molecules. V SF_6 on Faujasite – dipolar coupling of fluorine nuclei to ferric-ion impurities. J. Phys. Chem. 46: 2876–2880.

Resing, H.A., Thompson, J.H., (1967). NMR relaxation in adsorbed molecules. V SF_6 on Faujasite – dipolar coupling of fluorine nuclei to ferric-ion impurities. J. Phys. Chem. 46: 2876–2880.

Ruthven, D.M., Loughlin, K.F., Derrah, R.I., (1973). Sorption and diffusion of light hydrocarbons and other simple nonpolar molecules in type A zeolites. *Molecular sieves – Advances in chemistry*. American Chemical Society.

Ruthven, D.M., Brandani, S., (2000). *Measurement of diffusion in porous solids by ZLC methods*. Elsevier.

Schaefer, D.J., Favre, D.E., Wilhelm, M., Weigel, S.J., Chmelka, B.F., (1997). J. Am. Chem. Soc. 119: 9252-9267.

Schemmert, U., Kärger, J., Weitkamp, J., (1999). Interference microscopy as a technique for directly measuring intracrystalline transport diffusion in zeolites. Microporous Mesoporous Mater. 32: 101–110.

Schneider, D., Mehlhorn, D., Zeigermann, P., Kärger, J., Valiullin, R., (2016). Transport properties of hierarchical micro-mesoporous materials. Chem. Soc. Rev. 45: 3467.

Schumacher, R.R., Anderson, B.G., Noordhoek, N.J. (2000). Tracer-exchange experiments with positron emission profiling: diffusion in zeolites. Microporous Mesoporous Mater. 35–36: 315–326.

Seland, J.G., Sørland, G.H., Zick, K., Hafskjold, B., (2000). Diffusion measurements at long observation times in the presence of spatially variable internal magnetic field gradients. J. Magn. Reson. 146:14-19.

Silva, J.A.C., Rodrigues, A.E., (2015). Limitations of the Zero-Length Column technique to measure diffusional time constants in microporous adsorbents. Chem. Eng. Technol. 38: 2335-2339.

Schuring, D., (2002). Diffusion in zeolites: towards a microscopic understanding. PhD thesis, Technische Universiteit Eindhoven.

Schwarz, H.B., Ernst, H., Ernst, S., Kärger, J., Röser, T., Snurr, R.Q., Weitkamp, J., (1995). NMR study of intrinsic diffusion and reaction in CsNaX type zeolites. Appl. Catal. A. 130: 227-241.

Sørland, G.H., (2014). *Dynamic Pulsed Field Gradient NMR*. Springer.

Tiselius, A.W.K., (1934). The diffusion of water in zeolite crystals. An article on the question of absorbed molecule mobility. Z. Phys. Chem. A 169: 425–458.

Tonetto, G., Atias, J., de Lasa, H., (2004). FCC catalysts with different zeolite crystallite sizes: acidity, structural properties and reactivity. Applied Catal. A. 270: 9-25.

Valiullin, R.R., Skirda, V.D., Stapf, S., Kimmich, R., (1997). Molecular exchange processes in partially filled porous glass as seen with NMR diffusometry. Phys. Rev. E. 55(3): 2664-2671.

van den Begin, N., Rees, L.V.C., Caro, J., Bülow, M., (1988). Fast adsorption-desorption kinetics of hydrocarbons in silicalite-1 by the single-step frequency response method. Zeolites. Micropor. Mesopor. Mater. 9: 287-292.

van Donk, S., Broersma, A., Gijzeman, O.L.J., van Bokhoven, J.A., Bitter, J.H., de Jong, K.P., (2002). Combined diffusion, adsorption, and reaction studies of *n*-hexane hydroisomerisation over Pt/H-mordenite in an oscillating microbalance. J. Catal. 204: 272-280.

Vasenkov, S., Böhlmann, W., Galvosas, P., Geier, O., Liu, H., Kärger, J., (2001). PFG NMR study of diffusion in MFI-type zeolites: Evidence of the existence of intracrystalline transport barriers. J. Phys. Chem. B. 105: 5922-5927.

Vasenkov, S., Geier, O., Kärger, J., (2003). Gas diffusion in zeolite beds: PFG NMR evidence for different tortuosity factors in the Knudsen and bulk regimes. Eur. Phys. J. E. 12(s01):s35-s38.

Vilčiauskas, L., Tuckerman, M.E., Bester, G., Paddison, S.J., Kreuer, K.D., (2012). The mechanism of proton conduction in phosphoric acid. Nat. Chem. 4: 461-466.

Wang, G.M., Sevick, E.M., Mittag, E., Searles, D.J., Evans, D.J., (2002). Experimental demonstration of violations of the second law of thermodynamics for small systems and short time scales. Phys. Rev. Lett. 89: 050601.

Weber, D., (2009). Magnetic resonance studies of diffusion and adsorption in catalysts. PhD thesis, University of Cambridge.

Yasuda, Y., (1982). Determination of vapour diffusion coefficients in zeolites by the frequency-response method. J. Phys. Chem. 86: 1913-1917.

Zhu, W., van de Graaf, J.M., van der Broeke, L.J.P., Kapeteijn, F., Moulijn, J.A., (1998). TEOM: a unique technique for measuring adsorption properties. Light alkanes in silicalite-1. Ind. Eng. Chem. Res. 37: 1934-1942.

Zhu, W., (2001). Adsorption and diffusion in microporous materials: an experimental study with the TEOM. Delft University of Technology, PhD thesis.

Chapter 4

PFG NMR pulse sequence modifications and vacuum line calibrations

4.1. Introduction

The aim of this chapter is to set the scene prior to performing Pulsed Field Gradient Nuclear Magnetic Resonance (PFG NMR) experiments, whereby appropriate methods for sample preparation, data acquisition and analysis are outlined.

The first section of this chapter describes the sample preparation techniques which are performed on a vacuum manifold. The calibration procedures for all samples prepared on the vacuum manifold are described. Ideal gas and Boyle's law behaviour are assumed for all gaseous guest molecules used in this thesis.

The latter section of this chapter details the use of a modified Alternating Pulsed Gradient Stimulated Echo (APGStE) pulse sequence in comparison to its well-established, unedited counterpart. The changes made in the modified sequence include the use of shorter echo times and unequal pulsed gradient amplitudes. The rationales for these proposed changes are to improve Signal-to-Noise Ratios (SNRs) and to reduce PFG NMR artefacts for calculating diffusion coefficients in PFG NMR diffusometry experiments. The applicability of the

accompanying equation for this unconventional pulse sequence is briefly discussed and examples where typical improvements in SNRs are observed are also given.

4.2. Background

As mentioned in chapter 2, stimulated echoes with bipolar gradients in PFG NMR diffusometry pulse sequences are particularly adept at removing background gradient contributions in heterogeneous systems, where enhanced magnetic susceptibility effects result in relaxation weighted signal losses and spectral line broadening (Cotts *et al*. 1989). Such PFG NMR protocols also have the added advantage of enabling magnetisation storage for a prolonged period of time in the longitudinal plane, whereby this particular benefit is capitalised upon, with respect to the samples discussed in chapter 5. However, the occurrence of molecular displacements may also act as a source of such artefacts which add to the inhomogeneity of the system and hinder measurement accuracy, as cross-term magnetisation between the applied gradient and the background gradients may not be adequately subdued using conventional, well established methods (Sun *et al*. 2003). Figure 4.1 shows the conventional APGStE pulse sequence which is used as a platform for increasing the SNRs of heterogeneous systems.
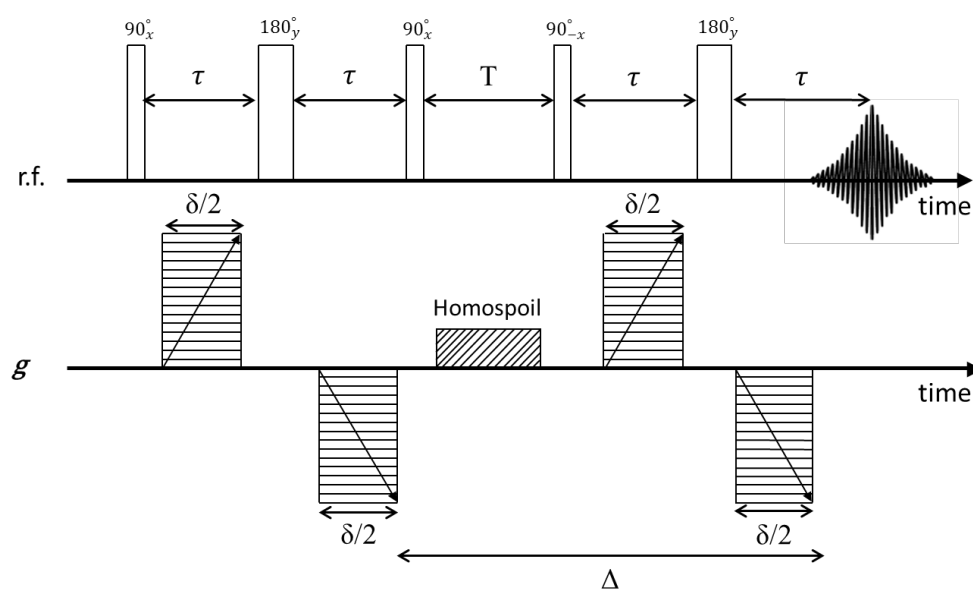

Figure 4.1: Conventional APGStE pulse sequence with bipolar gradients.

Conventional PFG NMR diffusometry involving zeolite systems for the most part suffer from poor SNRs and short T_2 relaxation times. In such instances, whereby these prohibitive limitations become increasingly evident with decreasing pore size, the benefits which come with the removal of background signal(s) are often an experimental pre-requisite (Sørland *et al*. 2007). Modifications have been typically proposed in the literature which aim to minimise the influence of background gradients on experimentally applied gradients during the phase encoding and decoding intervals, which yielded promising results for a range of heterogeneous systems (Sørland *et al*. 2002). Brief examples of such changes are introduced in this chapter, in comparison to conventional APGStE techniques, using guest molecules with varying T_2 relaxation times.

4.3. Chemicals and zeolites

Table 1 lists the purity and origin of all materials used in this thesis. All materials were used as received. All adsorbed phase spectra obtained from pulse acquisition experiments were referenced to anhydrous Tetra Methyl Silane (TMS).

Table 1: Summary of materials used in this thesis.

Material	Purity (%)	Origin
CH_4	99	BOC
C_2H_6	99.99	Air Liquide
C_3H_8	99.99	BOC
NH_3	99.99	Argo International Speciality Products
Tetra Methyl Silane (TMS)	99.5	Sigma Aldrich
15 µm β-zeolite	-	Tosoh Corporation *via* Johnson Matthey, United Kingdom
0.3 and 0.5 µm β-zeolite	-	Clariant, Germany

4.4. Vacuum line calibrations

To ensure that the guest molecules of interest to this thesis were adsorbed by moisture free zeolites without impurities, a vacuum line was used to prepare all samples used in the PFG NMR experiments outlined in this thesis. A representation of the vacuum manifold used is shown in figure 4.2 with each volume region outlined. The volume of each region was determined by separately filling each region with distilled water at 20 °C (with a density of 998 kg m^{-3}) and by using the recorded mass of the water. The calibration bulb was used to calibrate the pressure gauge, of which an example will be shown in appendix A1.

$$V_{total} = V_1 + V_2 + V_3 + V_4 + V_5 = 211 \text{ mL}$$

$V_1 = 143$ mL

$V_2 = 50$ mL

$V_3 = 7$ mL

$V_4 = 2$ mL

$V_5 = 9$ mL

Vacuum line manifold sealed tube expansion ratio = 72

To vacuum pump

Pressure indicator

PI

Valve 5

Valve 1

Valve 6

Gas feed

Valve 2

Valve 3

Valve 4

Calibration bulb

5 mm o.d. tube with zeolite powder

5 mm o.d. tube with liquid
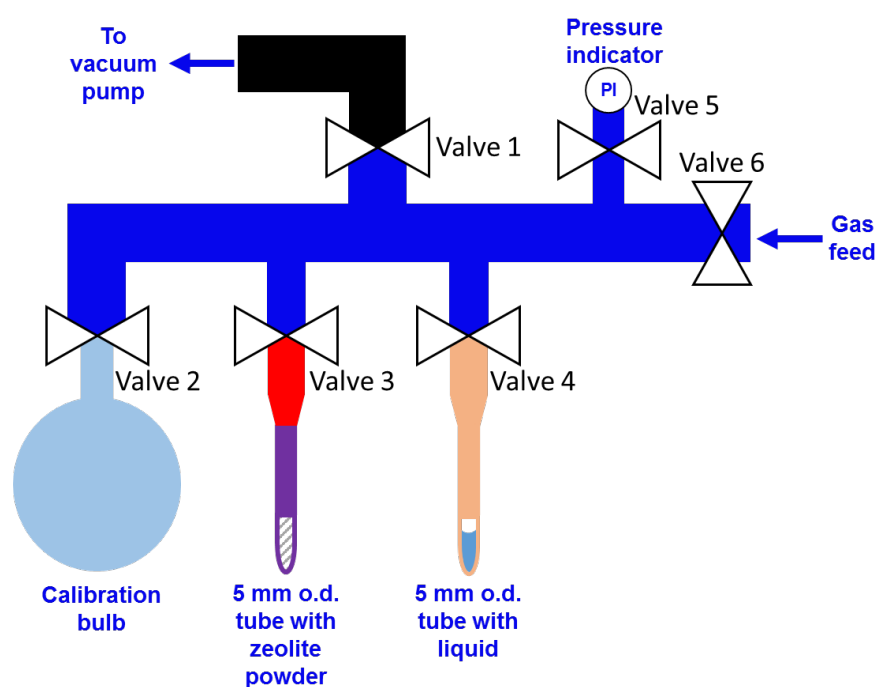
Figure 4.2: Vacuum line representation.

All gaseous molecules used in this study (CH_4, C_2H_6, C_3H_8 and NH_3) were treated as ideal gases which follow Boyle's law. The pressure gauge was independently calibrated, initially with air and subsequently with the aforementioned gases, to determine the suitability of these assumptions and the precision of the pressure indicator fitted to the manifold.

4.4.1. Sample preparation

4.4.1.1. Gas phase hydrocarbon dosing

The zeolite samples were prepared in a similar manner to the conventional method detailed in the literature (Kärger and Ruthven 1992), with the only significant difference being the reduced 'degassing' timeframe for β-zeolite, which will be discussed further in chapter 5. The steps involved in the gas phase sample preparation procedure are detailed in this section.

- In each instance, 0.09 ± 0.001 g of the zeolite powder was introduced into a custom made 5 mm o.d. borosilicate tube, corresponding to a bed height of approximately 12 mm. Glass wool was then inserted and placed near the top of the tube to prevent the powder from being carried into the turbopump once it was switched on.

- The tube had a 14 mm diameter ground glass B14 cone attached at the top, which enabled it to be connected to the vacuum line. Subsequently, ultra-high vacuum grease was used to ensure a secure seal between the cone and the vacuum line connection. All valves were initially closed, except for valve number 5. Valve number 1 was then opened to evacuate the manifold to a pressure less than 10^{-6} mbar.

- Subsequently, valve number 3 was carefully opened and the zeolite sample was heated to 573 K, at a rate of 50 K/min, and held at a pressure less than 10^{-6} mbar for varying timeframes. Self-steaming effects across the zeolite bed were not observed under these conditions.

- Valve number 1 was then closed and the sample was subsequently cooled down to room temperature and was exposed to a known pressure of the guest molecules, by opening valve number 6. The guest molecules were introduced to the zeolite bed at room temperature.

- Lastly, valve number 3 was closed and liquid nitrogen was used to confine the guest molecules to the zeolite bed region, and the NMR tube was then hermetically flame sealed using a propane blowtorch. The sealed tube was subsequently kept at room temperature for 30 minutes to allow the molecules to equilibrate in the zeolite bed. An equilibration time of 30 minutes was selected as there were no discernible differences in the signal intensities and peak areas in a pulse acquisition experiment

for a sample which was left to equilibrate for 30 minutes and one which was left for 24 hours.

In order to quantify the gas phase loadings in the zeolite samples used in this study, an NMR based calibration was performed, which will be described in section 4.5.2. The same method was applied to determine the quantity of gas above the zeolite bed, since this signal could be detected in a conventional pulse acquisition experiment, as it was under pressure in a sealed tube with a finite volume.

4.4.1.2. Liquid phase hydrocarbon dosing

- The hydrocarbon liquid guest molecules were dosed onto the zeolite bed using a "freeze-pump-thaw" method detailed in the literature (Jobic *et al*. 2005). A tube filled with approximately 20 cm^3 of the liquid of interest was attached to the adjacent entry point on the vacuum line, as shown in figure 4.2.

- Subsequently, the liquids were frozen by immersing the tubes in liquid nitrogen. The frozen liquid was then exposed to the vacuum pump by opening valve number 4, to remove any impurities and moisture from within and above the sample.

- The liquid nitrogen supply was isolated from the tube and once the hydrocarbon liquid began to melt, valve number 4 was closed.

- Subsequently, valve number 1 was closed, at which point valve number 4 was re-opened, to establish a vapour pressure equilibrium in the manifold. Valve number 4 was eventually closed once the vapour pressure recorded by the pressure gauge remained constant. The vapour pressure was used to determine the molecular loading.

- Lastly, the tube containing the evacuated zeolite powder was immersed in liquid nitrogen and valve number 3 was opened to expose the zeolite bed to the vapour rich manifold. Due to the large temperature differential of the zeolite sample (77 K) and the vacuum manifold (298 K), all the hydrocarbon vapour molecules entered the zeolite bed. The pressure of the manifold displayed by the pressure gauge reduced to zero in each instance, upon which valve number 3 was closed and the tube was flame sealed.

Upon flame sealing the tube, the signal above the zeolite was not detectable in the NMR experiments, therefore it was assumed that the quantity recorded by the pressure gauge corresponded to the quantity adsorbed by the zeolite bed. The recorded vapour pressures of the hydrocarbon liquids were in good agreement with the physical properties at room temperature. Additionally, a reduction in vapour pressure was recorded with increasing chain length.

The 5 mm sample tubes that were used were able to withstand a pressure of 2 bar. Therefore, low adsorption pressures were selected to ensure that great care was taken to prepare the samples in a safe and controlled manner, as the ratio of the volume of the vacuum manifold to the volume of the tube is approximately 72:1.

4.5. NMR Experimental

4.5.1. ^{1}H NMR parameters

All NMR calibration experiments were performed using a Bruker BioSpin DMX spectrometer operating at a ^{1}H resonance frequency of 300.13 MHz with a 5 mm radiofrequency (r.f.) coil fitted to a Pulse Field Gradient probe head, which was placed inside a cryo-magnet. Figure 4.3 shows the 5 mm ^{1}H saddle r.f. coil that was used in all gas phase and adsorbed phase NMR experiments. All measurements were taken at 294 K, with a precision of ± 1 K using a Bruker BVT-3000 temperature control unit. Conventional T_1 inversion recovery and T_2 Carr-Purcell-Meiboom-Gill (CPMG) relaxation experiments were performed with 16 increases in delays ranging from 0.001 s to 32 s and 0.001 s to 0.5 ms respectively. Single component T_1 and T_2 values were obtained in each instance for each individual gas, with a coefficient of determination (R^2) that exceeded 0.98.

Pulse acquisition experiments were conducted using a 1D Hahn echo pulse sequence, with the echo time set to 2.5 ms for all CH_4 samples and 0.5 ms for all C_2H_6, C_3H_8, NH_3 and liquid phase samples. A recycle time, T_R, ranging from 0.5 - 14 s was used, corresponding to (a minimum of) 5 × T_1 for each sample used in each NMR experiment, which enabled a 99.3% recovery of the magnetisation. 512 scans were used to acquire each spectrum, with a receiver

gain of 512. All quoted sample pressures in this thesis are absolute pressures. Each experiment was repeated three times and the standard deviation of all three experiments was calculated and subsequently used in the error propagation calculations, which will be shown in appendix A5.
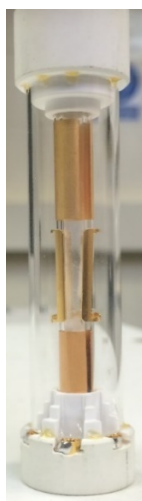
Figure 4.3: 5 mm ^{1}H saddle r.f. coil used in this study. Figure is not to scale.

4.5.2. Gas phase NMR signal-pressure calibrations

4.5.2.1. Preparation of the calibration tubes

This section outlines the steps which are involved in the preparation a range of empty (*i.e.* without a zeolite) calibration tubes using the vacuum manifold, prior to the NMR analysis:

- A known pressure, and hence a known volume, of gas was introduced into the (evacuated) vacuum manifold. The absolute pressure was recorded by a gas independent ASG2 NW16 Edwards Active strain gauge supplied by Edwards Vacuum.

- The gas was then introduced from the manifold into an empty 5 mm o.d. tube. The pressure was recorded and the tube was subsequently isolated from the manifold by closing the connecting valve, in order to keep the pressure in the tube constant.

- Subsequently, the tube was immersed in liquid nitrogen and flame sealed. This was then repeated with different pressures, with separate empty tubes. All tubes were flame sealed at nominally the same height.

This method was used to prepare calibration tubes for all the gaseous guest molecules discussed in chapters 5, 6, 7 and 8: methane, ethane, propane and ammonia. The pressure range selected for the hydrocarbon gases was 5 - 500 mbar and 250 - 1000 mbar for ammonia.

4.5.2.2. NMR analysis of the calibration tubes

The calibration tubes were placed in the r.f. coil in the magnet and a 1D Hahn echo experiment was conducted. The same pulse sequence delay times, dwell times, shim gradient settings, receiver gains and number of scans were used for each sample tube for each individual gaseous molecule studied. This ensured that an accurate comparison was obtained between the different sample tubes containing the different gas pressures.

In order to use the NMR signals in a quantitative manner, the frequency domain spectra were relaxation corrected. This was achieved by conducting each spectrum acquisition experiment with a minimum recycle time of $5 \times T_1$, to recover 99.3% of the magnetisation, and by accounting for the amount of signal lost due to T_2 relaxation by conducting a T_2 CPMG experiment and correcting each spectrum in the following manner:

$$Relaxtion\ corrected\ NMR\ signal = \frac{Uncorrected\ NMR\ signal}{exp^{-\left(\frac{2t}{2T}\right)}} \qquad 4.1$$

where t is half-the-echo-time [s] and T is a time constant from the exponential fitting model [s]. The relaxation corrected signals from each sealed tube are then plotted as a function of known tube pressure and a linear relationship is observed for all bulk gas phase samples used. Figure 4.4 shows a calibration plot of the NMR signals *vs*. the known pressures of the gases used in this thesis: CH_4, C_2H_6, C_3H_8 and NH_3.
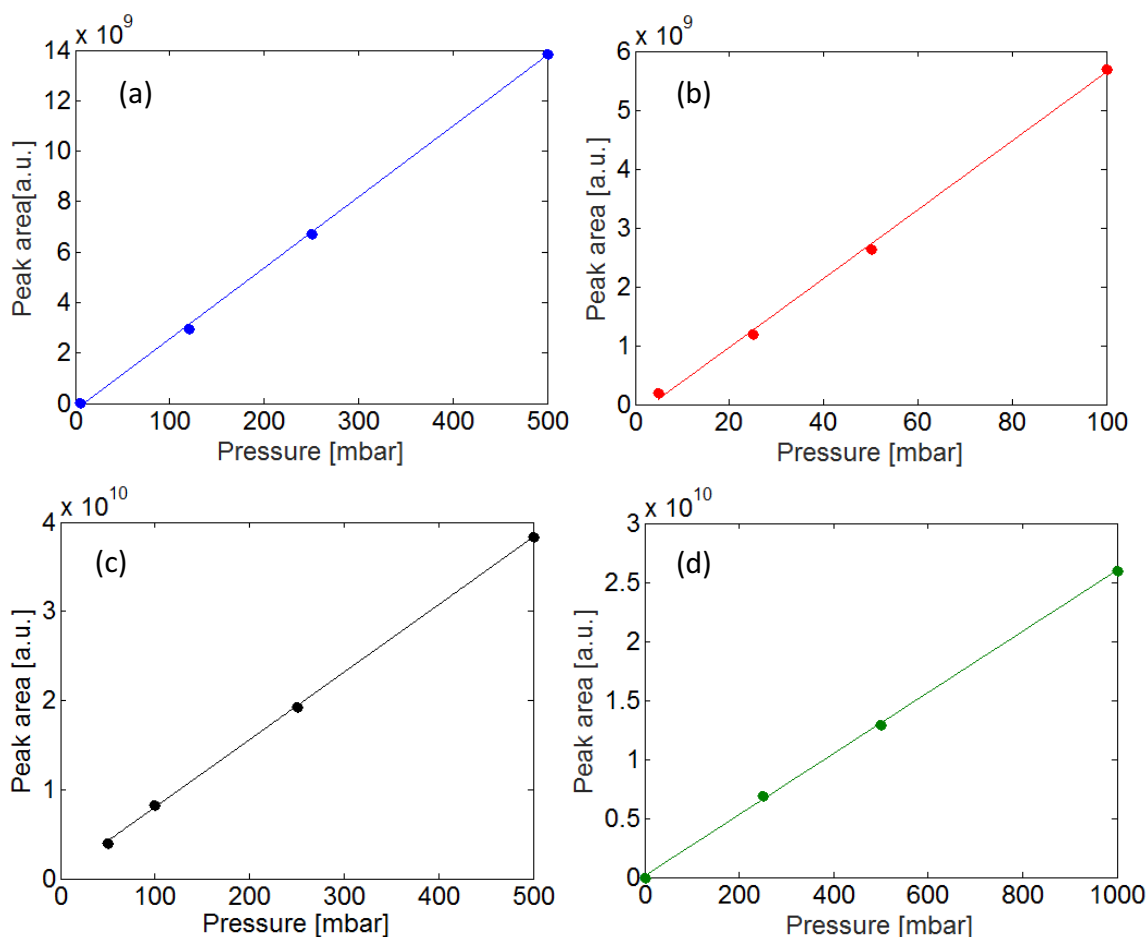
Figure 4.4: Bulk gas NMR calibration plots showing relaxation corrected signal *vs*. tube pressure for (a) CH_4, (b) C_2H_6, (c) C_3H_8 and (d) NH_3.

The calibration plots were used to determine the pressures of the adsorbed and gas phase regions in and above the zeolite bed in the sealed tubes, which were prepared using the method described in section 4.4.1.

4.5.3. Adsorbed and gas phase molecular loading calculation

The relaxation corrected ^{1}H signals from both the adsorbed phase and gas phase above the zeolite bed were acquired using the same pulse sequences and experimental parameters as those used to generate the calibration plots. For the analysis of the adsorbed phase, it was possible to ensure that only the zeolite bed was detected by the active region of the r.f. coil by securing the tube in a fixed position using a rubber o-ring, with a diameter larger than the diameter of the orifice of the coil. Moving the tube down to the bottom of the coil, by removing the o-ring, enabled analysis of the gas phase above the bed. This is illustrated in figure 4.5.
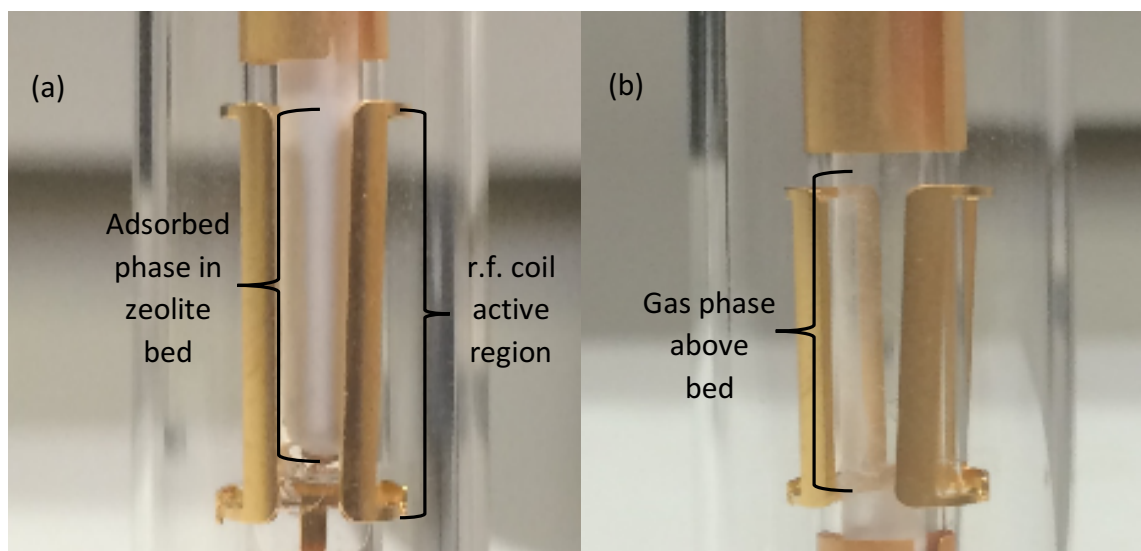
Figure 4.5: Representation of the: (a) adsorbed phase in the zeolite bed and (b) gas phase above the bed positioned in the active region of the r.f. coil.

As shown in figure 4.6, the (relaxation corrected) adsorbed phase signals are typically much larger (and broader) than their gas phase counterparts above the bed. This is due to the zeolite possessing a large pore volume (0.27 cm^3 g^{-1}), which provides a large adsorption capacity. Therefore, a significantly larger number of molecules may be held in the zeolite bed compared to the gas phase. Typical spectral linewidths for the adsorbed phase and gas phase regions above the bed are 75 Hz and 26 Hz respectively.
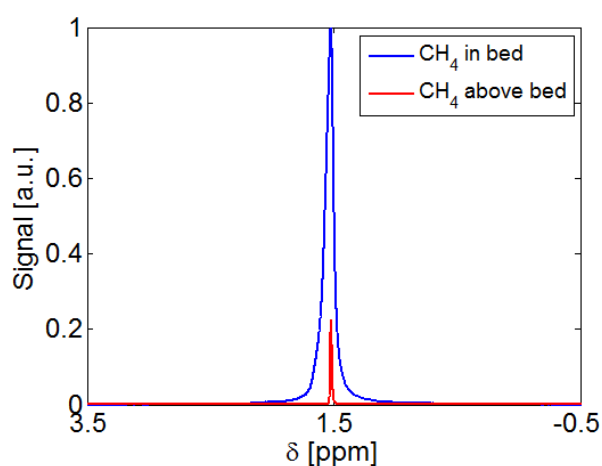
Figure 4.6: ^{1}H pulse acquisition comparison of typical adsorbed and gas phase signals.

The relaxation corrected signal intensities were used to determine the pressures for each region by:

a. **Gas phase above the zeolite bed:** Plotting the signal intensities of each species on their respective calibration plots and determining the corresponding pressure.

b. **Adsorbed phase:** Fitting the signal intensities to the straight line equation of the calibration plots. Since these signal intensities were significantly greater than their gas phase counterparts by at least an order of magnitude, the signals were extrapolated to their corresponding pressures.

The pressures in the adsorbed phase regions were determined from the calibration plots and were subsequently converted to the number of adsorbed moles. A summary of the steps involved in determining the molecular loadings in the zeolite beds is illustrated by figure 4.7, with a sample calculation included in appendix A2. The adsorbed quantities are tabulated in the subsequent chapters in which their respective host systems are introduced.
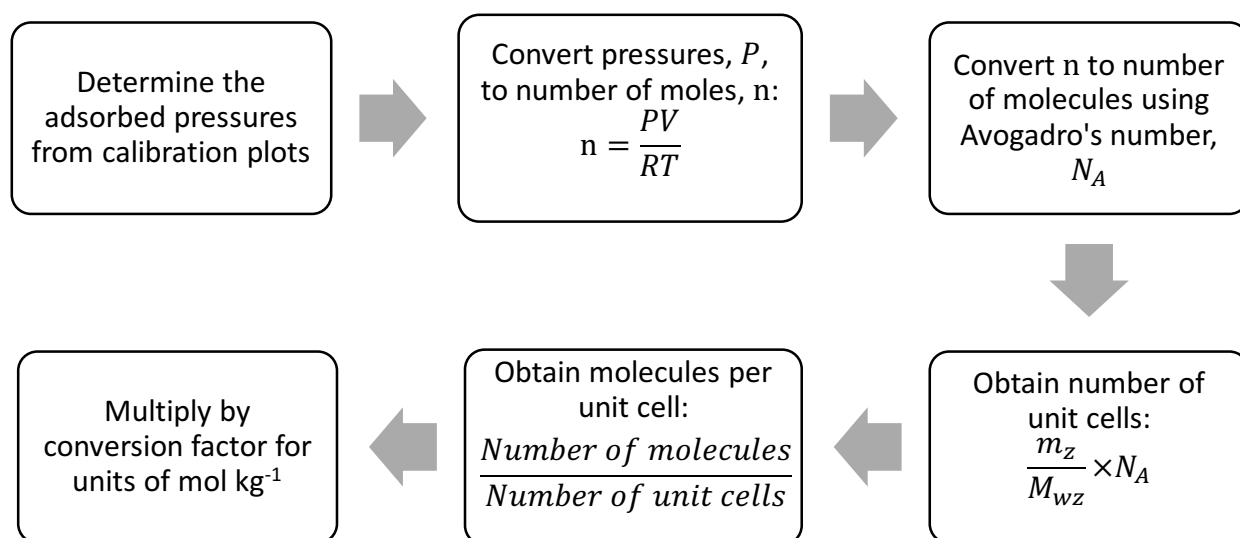
Figure 4.7: Flowchart of steps involved for calculating guest molecule loadings from NMR calibrations.

where m_z and M_{wz} are the mass and molecular weight of the zeolite respectively. The number of molecules per unit cell were multiplied by a conversion factor of 0.26 and 0.23 for BEA and chabazite frameworks respectively. This converted the units to mol kg^{-1}, to enable comparisons to be made with loadings determined using alternative techniques, which will be described in chapter 5 (Krishna 2012).

4.6. PFG NMR pulse sequence modifications

As mentioned in chapters 2 and 3, guest molecules adsorbed in porous materials suffer from poor SNRs due to short T_2 and T_2^* relaxation times which decrease with increasing levels of confinement (such as decreasing pore size). Using conventional APGStE PFG NMR methods to obtain self-diffusion coefficients in such systems relies on the use of gradient pulse durations, δ, and observation times, Δ, which are of the order of milliseconds in conjunction with large gradient amplitudes in order to achieve sufficient signal attenuation. Additionally, delay times (that are also of the order of milliseconds) are incorporated in conventional PFG NMR pulse sequences as a rule of thumb to protect the experimental hardware. Examples include the rate at which the (shaped) pulsed gradients are ramped up to the maximum amplitudes, and the delay times which immediately follow the application of the pulsed gradients, as to allow enough time for any eddy currents which may have formed to dissipate. The nature of the conventional APGStE pulse sequence and the position of these delay times, as shown by the time intervals labelled τ in figure 4.1, results in losses in signal due to T_2 relaxation processes. Whilst the presence of 180° r.f. pulses refocuses dephased spins, increases in these delay times lengthen the echo time of the pulse sequence and in instances where T_2 relaxation times are excessively short, this is not desirable.

The proposed changes that were made to the conventional APGStE pulse sequence were initially two-fold and served different purposes:

i.   The use of shorter delay times in the modified sequence to reduce the total echo time of the pulse sequence by approximately 700 μs.

ii.   The application of asymmetric bipolar gradient pulses to provide additional homospoiling to reduce artefacts for calculating the self-diffusion coefficient.

A level of asymmetry was initially introduced by effecting both changes, as the former involved reducing the delay time which immediately preceded the gradient pulses, δ_1, whereas the delay time which immediately followed the application of the gradient pulses, δ_2, was not shortened. This was purely the case as a precautionary measure, since the maximum gradient strength of the PFG probe's gradient set (10 T m^{-1}) was used in all experiments introduced in chapter 7. Therefore, δ_1 did not exceed 50 μs, whereas δ_2 was not reduced to below 200 μs in each experiment. The implication of using delay times which were

91

not symmetrical either side of the gradient pulses resulted in the requirement of equation 4.4, which is a modified version of the "Stejskal-Tanner equation" to fit to the PFG NMR data obtained in each diffusometry experiment. It has been shown that a cross-magnetisation term between the applied gradient, g, and the background gradient, G_0, may have a prominent effect in such instances and thus an additional term must be taken into account in the equation due to this contribution (Sørland *et al.* 1997):

$$\Psi = \sum_{i=n}^{n} p_i \, exp\left(-D_i\gamma^2 \left[-D_i\delta^2 \left(\Delta + \frac{3}{2}\tau - \frac{\delta}{3}\right)g^2\right] + \left(\Delta + \tau - \frac{\delta}{3}\right)f^2(\Delta + \tau)gf\right.$$
$$\left. + \delta(\delta_1 - \delta_2)\tau(f + g)G_0 + \frac{4}{3}\tau^3 G_0{}^2\right)$$

4.2

where Ψ is the echo attenuation [a.u.], γ is the ^{1}H gyromagnetic ratio [rad s^{-1} T^{-1}], g is the gradient strength with an amplitude ratio of 1 [T m^{-1}], f is the gradient strength with an amplitude ratio of 0.8 [T m^{-1}], δ is the gradient pulse width [s], G_0 is the constant background gradient which is present in the sample [T m^{-1}] and Δ is the effective observation time [s]. Whilst only a section of the modified pulse sequence is shown in figures 4.8 and 4.9 (the first three r.f. pulses and only one pair of bipolar gradients), the same changes were made to the delay times preceding the second set of bipolar gradients:
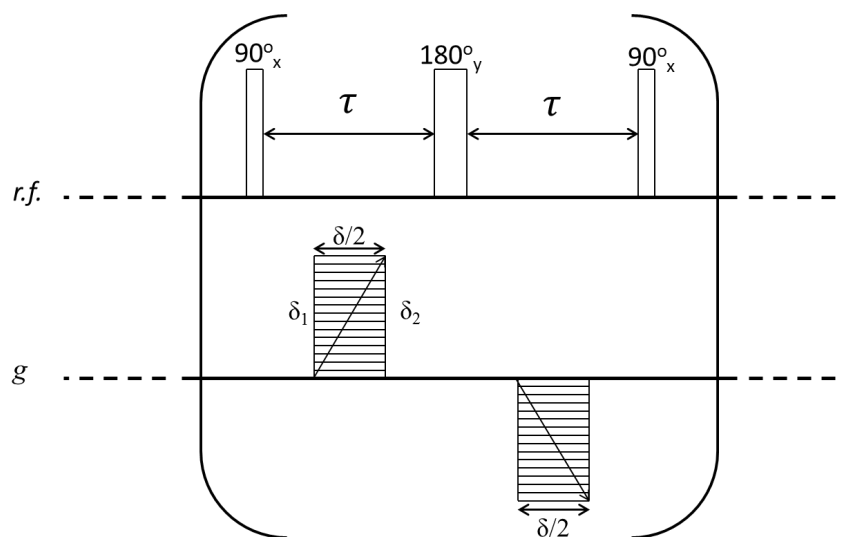
Figure 4.8: Section of the conventional APGStE pulse sequence. Both gradients are equal to one another in amplitude, and $\delta_1 = \delta_2$.
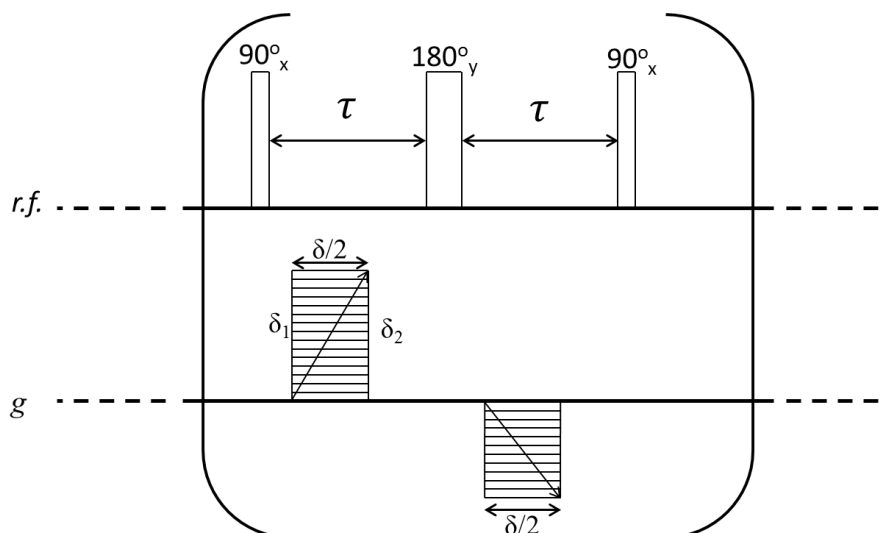
Figure 4.9: Section of the modified APGStE pulse sequence. Both gradients are not equal to one another in amplitude, and $\delta_1 \neq \delta_2$.

Regarding the first alteration, the reductions made in the overall echo time resulted in signal enhancement due to reduced T_2 weighting. Figure 4.10 shows a spectral comparison between the two pulse sequences for two different samples with differing T_2 relaxation times: (i) CH$_4$ adsorbed in β-zeolite and (ii) C$_2$H$_6$ adsorbed in β-zeolite. These samples were selected to highlight the influences of T_2 relaxation times on signal loss.
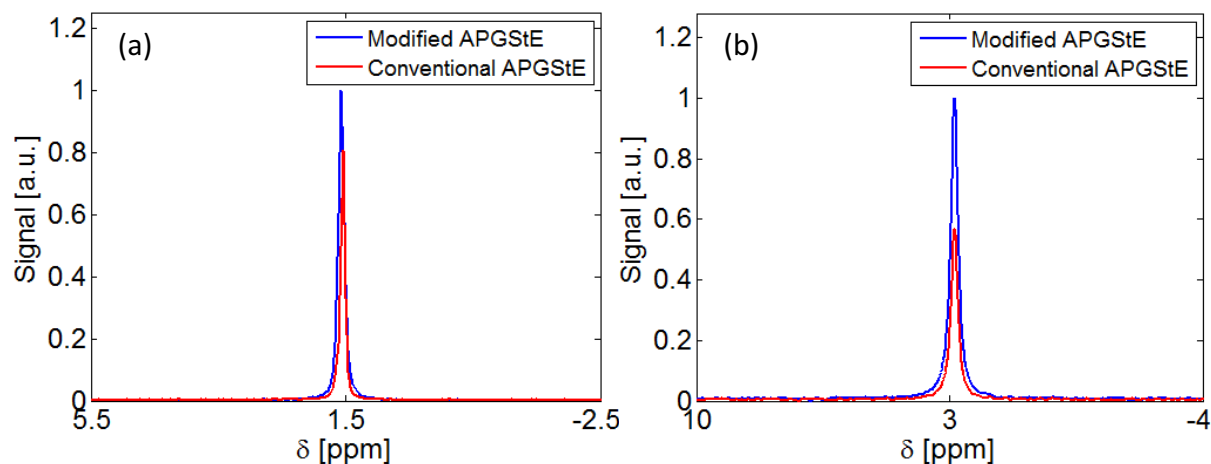
Figure 4.10: Comparison of the modified and conventional APGStE pulse sequences for (a) methane and (b) ethane adsorbed in β-zeolite.

The echo times are 2.3 ms and 1.6 ms for the conventional and modified pulse sequences respectively. The benefits of the reduced echo time in the latter are accentuated in samples which suffer from short T_2 relaxation times, as the total magnetisation is preserved to a

greater extent. The T_2 relaxation times of methane and ethane adsorbed in β-zeolite are 9 and 4 ms respectively, and thus the proportion of T_2 weighted signal loss induced by transverse relaxation processes vary for both species and may be determined *via*:

$$T_2 \, Weighting = \, exp\left(-\frac{2T}{T_2}\right) \qquad 4.3$$

where $2T$ is the sum of the delay times which contribute to the echo time of the APGStE pulse sequence.

The second alteration to the pulse sequence involves the application of asymmetric bipolar gradients, where the positive gradient amplitudes are larger than the negative gradient amplitudes. It has been shown that the use of unequal bipolar gradients, with a net positive gradient amplitude, offers the benefit of eliminating the requirement of a homospoil gradient to suppress background gradients and eliminate residual magnetisation in the transverse plane, since these positive gradients are applied during the transverse magnetisation storage intervals shortly after the 90° r.f. pulses, and prior to the application of the 180° pulses (Sørland *et al.* 1997; Sun *et al.* 2003). Incorporating such changes into conventional PFG NMR pulse sequences has therefore been highly recommended in the literature to study the diffusion of molecules adsorbed in microporous materials such as zeolites. Avoiding the use of large homospoil gradients during the longitudinal storage interval also by-passes the prospect of placing the experimental hardware under duress at high gradient amplitudes. Additionally, doing so is particularly beneficial as large homospoil gradients are often the source of unwanted coherence, which is more apparent in low SNR systems (Sørland 2014).

In order to illustrate this effect, a flame sealed sample of 0.34 mol kg^{-1} of methane adsorbed in β-zeolite was used. No discernible differences were observed by varying the positive-negative gradient amplitudes from ratio of 1:1 to an amplitude ratio of 1.25:1. It has been suggested that the length of the gradient pulse duration, as well as the SNR of the sample, has a significant impact on the efficacy of ^{1}H background signal removal. The former could not be further reduced or significantly increased beyond 0.25 ms, in a bid to observe such noticeable differences due to hardware limitations and the adsorbed phase samples possessing short T_2 relaxation times respectively. Literature studies which report significant improvements in background signal removal were conducted using bulk water, with a

gradient pulse duration of 3 ms, whereby the T_2 relaxation time was of the order of seconds (Sun *et al.* 2003). No discernible improvements were observed by incorporating these changes in bipolar gradient amplitudes, with respect to the SNRs, removal of background gradients and signal attenuation. Therefore, the minutiae of observing any differences in phase coherences and any associated changes in applied gradient integrals due to differences in pulse areas between asymmetric, bipolar pulses are not discussed. The interested reader is forwarded to the work of Sørland 2014. However, significant reductions in signal attenuation and SNRs were observed by further increasing the imbalance in bipolar amplitudes, below an amplitude ratio of 1.43:1, as shown in figure 4.11. Similar trends were observed in the chabazite frameworks, with methane and ethane as guest molecules. Therefore, the amplitude ratio was set to 1:1 and the data from all PFG NMR experiments in this thesis were fitted to equation 4.1 with this in mind.
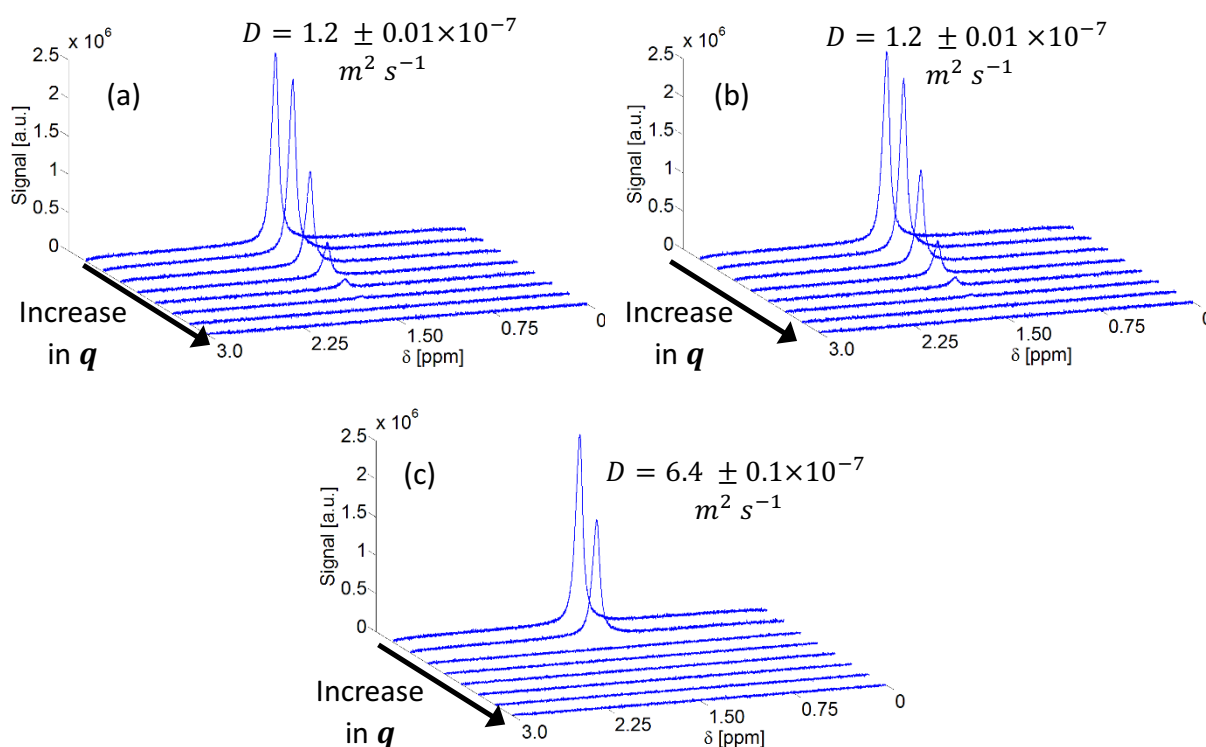
Figure 4.11: Spectral attenuation comparison from a PFG NMR diffusometry experiment using positive-negative bipolar gradient amplitude ratios of (a) 1:1, (b) 1.25:1 and (c) 1.43:1. Identical PFG NMR parameters are used: δ = 0.25 ms, Δ = 100 ms and g = 0.001 - 0.36 T m^{-1}.

4.7. Conclusions

A calibrated vacuum line was used to prepare all zeolite samples outlined in this thesis, using well established methods discussed in the literature. A modified APGStE pulse sequence was used in each diffusometry experiment of the adsorbed phase region in the sealed tube. Reductions were made to the total echo times to reduce the proportion of signal lost due to transverse relaxation processes. Improvements were seen in all systems compared to the conventional pulse sequence, whereby increases in SNR and signal attenuation were more apparent with increasingly short T_2 relaxation times. These proposed changes were not made to any bulk gas/liquid phase measurements discussed in this thesis by virtue of such molecules possessing sufficiently long T_2 relaxation times as to enable conventional pulse sequences to adequately determine self-diffusion coefficients with excellent SNRs.

4.8. References

Charnell, J.F., (1971). Gel growth of large crystals of sodium A and sodium X zeolites. J. Cryst. Growth. 8: 291-294.

Cotts, R.M., Hoch, M.J.R., Sun, T., Markert, J.T., (1989). Pulsed field stimulated echo methods for improved NMR diffusion measurements in heterogeneous systems. J. Magn. Reson. 83: 252-266.

Gribov, E.N., Cocina, D., Spoto, G., Bordiga, S., Ricchiardi, G., Zecchina, A., (2006). Vibrational and thermodynamics properties of Ar, N_2, O_2, H_2, and CO adsorbed and condensed into (H, Na)—Y zeolite cages as studied by variable temperature IR spectroscopy. Phys. Chem. Chem. Phys. 8: 1186-1196.

Kärger, J., Ruthven, D., (1992). *Diffusion in zeolites and other microporous solids*. Wiley & Sons.

Krishna, R., (2012). Diffusion in porous crystalline materials. Chem. Soc. Rev. 41: 3099-3118.

Sørland, G.H., Aksnes, D., (2002). Artefacts and pitfalls in diffusion measurements by NMR. Magn. Reson. Chem. 40: S139-S146.

Sørland, G.H., Djurhuus, K., Widerøe, Lien, R.J., Skauge, A., (2007). Absolute pore size distributions from NMR. Diffusion fundamentals. 5: 4.1-4.15.

Sørland, G.H., Hafskjold, B., Herstad, O., (1997). A Stimulated Echo Method for Diffusion Measurements in Heterogeneous Media Using Pulsed Field Gradients. J. Magn. Reson. 124: 172-176.

Sørland, G.H., (2014). *Dynamic Pulsed Field Gradient NMR*. Springer.

Stejskal, E.O., Tanner, J.E., (1965). Spin diffusion measurements: spin echoes in the presence of a time dependent field gradient. J. Chem. Phys. 42: 288-292.

Sun, P.Z., Seland, J.G., Cory, D., (2003). Background gradient suppression in pulsed gradient stimulated echo measurements. J. Magn. Reson. 161: 168-173.

Chapter 5

Single component self-diffusion of CH$_4$, C$_2$H$_6$ and C$_3$H$_8$ in large pore β-zeolite structures

5.1. Introduction

Conventional PFG NMR methods have been used in the literature to study the dynamics of both gaseous and liquid phase guest molecules in microporous zeolites to characterise self-diffusion processes at various molecular displacement lengths. Literature studies have also shown that the equation which is used to calculate the intra-diffusion coefficients (D_{intra}) of gas phase molecules adsorbed in large pore zeolites (those exceed 6 Å in pore diameter) is given by (Kärger and Ruthven 1992):

$$D_{intra} = \frac{D_{long-range} - p_{inter}D_{inter}}{p_{intra}}$$
5.1

The method outlined in the literature is indirect as it relies on gas sorption isotherms and kinetic theory approximations to determine the inter-particle population (p_{inter}) and the inter-particle diffusivity (D_{inter}) respectively. The long-range diffusion coefficient ($D_{long-range}$) can be obtained from conventional PFG NMR experiments, as the molecular displacement lengths of gases in large pore zeolites typically exceed the crystallite size of zeolites at room temperature.

The main aim of this chapter is to demonstrate a novel, solely NMR based method capable of calculating the D_{intra} of single component gas phase guest molecules confined in large pore zeolites with variable crystallite sizes. The inter-particle parameters are obtained from the PFG NMR measurements of the gas phase regions above the zeolite bed in the flame-sealed tubes, which are prepared using the method outlined in chapter 4. The PFG NMR experiments are conducted using hydrocarbon gases which are adsorbed in β-zeolite, at a temperature of 294 K. Therefore, the interpretations of the results using this technique are applicable to industrially relevant operations such as Selective Catalytic Reduction (SCR). This is because these processes occur at elevated temperature and pressures and involve molecules which are in the gas phase.

Comparisons are also made between these results and those found in the literature using Molecular Dynamics (MD) simulations. Novel results are also presented to discuss the variations in the Gaussian distributions of the aforementioned measured molecular displacements. This behaviour is illustrated *via* the transitions from linear to curved and subsequently back to linear PFG NMR echo attenuation plots. The rationalisations for not taking the subsequent two-region exchange behaviour, which the intermediate curved echo attenuation plots exhibit, are discussed in section 5.5.5.

5.1.1. Fast molecular exchange in zeolite systems

It has been shown that in cases where there is fast molecular exchange between the inter- and intra-crystalline regions, their relationship with the long-range diffusion coefficients may be described by the following expression (Kärger *et al*. 1981):

$$D_{long-range} = p_{inter}D_{inter} + p_{intra}D_{intra} \qquad 5.2$$

where p is the population and D is the diffusivity of the inter-crystalline and intra-crystalline regions. The applicability of the fast exchange scenario in a PFG NMR measurement for gaseous guest molecules in zeolites may be verified by:

i.   Calculating the $RMSD$ of the guest molecules, using Einstein's equation. If the $RMSD$ is found to substantially exceed the geometric dimensions of the crystallite, a significant averaging across zeolite beds is expected. This implies that a fast exchange regime will dominate, provided that the molecules are capable of penetrating the

surface and subsequently migrating through the permeable structure, as opposed ricocheting against the walls without leaving the crystallite (Zhao and Snurr 2009). The latter may arise if there are significant resistance barriers to diffusion on the external surface of the crystallite. In this case, this method would not be required, since intra-diffusion coefficients would be characterised directly and surface contributions may be corrected for using Mitra's short-time approximation model (Mitra *et al*. 1993).

ii.   Observing a linear echo attenuation plot with a self-diffusion coefficient which satisfies case (i). This indicates that there is a Gaussian distribution with respect to the probability distribution of the molecular displacements measured.

As it pertains to case (ii), a linear echo attenuation plot is indicative of unrestricted, uncorrelated molecular motion for a given region in a zeolite (Sørland 2014). However, this may also be observed in systems where the $RMSD$ is much smaller than the crystallite size, examples of which include the intra-diffusion of strong and weakly adsorbing gaseous guest molecules in small pores, which will be described in chapter 7. Therefore, case (i) has a critical role in determining the suitability of the fast exchange approximation, as simply using the echo attenuation plot alone can lead to misleading interpretations.

In addition, there is reason to believe that the molecules are adsorbed by the zeolite bed as shown by the hydrocarbon sorption isotherms in section 5.4.4, as a change in mass is recorded by the instrument *via* an internal microbalance. The gas sorption device is only capable of detecting changes in adsorbed pressures. Therefore, it is reasonable to assume that the molecules in the intra-crystalline region dominate the ^{1}H NMR contribution from a tube containing the section of the zeolite bed placed in the active region of the r.f. coil in the PFG NMR experiments.

5.1.2. Literature techniques for determining p_{inter} and D_{inter} using gas sorption isotherms and kinetic theory approximations

The case has been made in the literature that in most instances involving the diffusion of gases in zeolites, where the population of molecules is highly weighted towards the inter-particle region, equation 5.2 may be reduced as to exclude the intra-particle term entirely (McDaniel *et al*. 1996). Therefore, in such instances the long-range diffusion coefficient

measured in the PFG NMR experiment is proportional to the inter-particle diffusivity, D_{inter}, and is modified by the inter-particle population, p_{inter}. It has been shown that this population can be calculated using data obtained from gas sorption experiments, since, for a given pore volume, the quantity of molecules which are present in between the particles may be determined (Rittig *et al*. 2002). D_{inter} can be calculated from kinetic approximations typically used to calculate Knudsen diffusion coefficients, using the thermal velocity of the molecule under study, and is often used to validate the long-range diffusion coefficient obtained from the PFG NMR experiment (Kärger and Valiullin 2013). The following (non-NMR based) expressions are used to calculate D_{inter} (Kärger and Ruthven 1992; Rohlf 1994):

$$D_{inter} = \frac{v\lambda}{3}$$
<div style="text-align:right">5.3</div>

$$\frac{1}{\lambda} = \frac{1}{d_{inter}} + \frac{1}{\lambda_{gas}}$$
<div style="text-align:right">5.4</div>

$$\lambda_{gas} = \frac{RT}{\sqrt{2}\pi d^2 N_A P}$$
<div style="text-align:right">5.5</div>

where λ is the effective mean free diffusion pathway [m], d_{inter} is the effective pore diameter of the inter-particle space [m], λ_{gas} is the diffusion pathway for the bulk gas phase [m], R is the gas constant [J mol^{-1} K^{-1}], T is the temperature [K], d is the diameter of the diffusing species [m], N_A is Avogadro's number [mol^{-1}] and P is the pressure of the gas [J m^{-3}],

$$v = \sqrt{\left(\frac{8RT}{\pi M_A}\right)}$$
<div style="text-align:right">5.6</div>

where v is the molecule's thermal velocity [m s^{-1}], R is the gas constant [J mol^{-1} K^{-1}], T is the temperature [K] and M_A is the molecular weight of the molecule [kg mol^{-1}] Cussler (2009). As discussed in chapter 3, section 3.2, equations 5.3 and 5.6 may be used to characterise Knudsen diffusion regimes. From the SEM image shown in figure 5.2, the systems used in this thesis possess a d_{inter} which is comparable to the crystallite size of the zeolite, approximately 1×10^{-5} m. High gas pressures, up to 1.5 bar, are obtained for the samples discussed in this thesis. At a gas pressure of 1.5 bar, λ is equal to 3.80×10^{-8} m. However, since λ is significantly

smaller than d_{inter}, Knudsen diffusion is not the dominant diffusion regime and therefore, equations 5.3 - 5.6 are not used to calculate D_{inter} in this thesis. Therefore, equations 5.3 - 5.6 are only suitable for dilute gas systems (Kärger *et al*. 1981).

The argument has been made that the presence of inter-particle regions in zeolite beds are a source of added complication, as it would be simpler if this regime did not exist when solving equation 5.1. As such, gas sorption isotherms and chemical kinetics calculations described by equations 5.3, 5.4, 5.5 and 5.6 would not be required. Potential solutions, in the form of abstract concepts, have been proposed relating to the sample preparation stage, whereby upon flame sealing the NMR tubes, a centrifuge may be utilised to create a densely packed, void-free zeolite bed (Bar *et al*. 1995). However, there are concerns, from a practical and safety point of view, in terms of subjecting a potentially imperfectly sealed tube to the substantial centripetal forces required to create this desired effect. Section 5.5.3 outlines a solely PFG NMR based method which is capable of determining all the parameters in equation 5.1.

5.2. Background

Conventional β-zeolite belongs to the BEtA (BEA) framework, which has an anisotropic geometry consisting of intersecting channels: a 10-ring channel, which is 5.6 Å in diameter, and a 12-ring channel, which ranges from 7.1 - 7.3 Å in diameter (Krishna 2012).
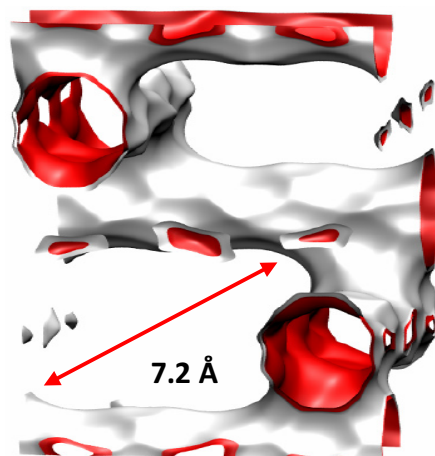

Figure 5.1: Simulated 3D structure of a BEA framework (Krishna 2012).

Large pore microporous zeolites such as β-zeolite enable the sorption of a wide range of molecules vastly differing in sizes and shapes, examples of which include linear aliphatic and cyclic aromatic compounds (Corma *et al.* 1995; Corma *et al.* 2000). Literature reports have demonstrated that β-zeolite is of particular relevance in industrial applications such as alkylation, oxidation and SCR (Corma *et al.* 2001; Delahay *et al.* 2001). It is selected for these applications due to its large pore cavity which enables the shape selective passage of cyclic and aromatic compounds. In addition to this, it has been shown to display a higher stability towards catalytic deactivation, in comparison to its large pore microporous zeolite counterparts (Primo and Garcia 2014). The Silica-to-Alumina (Si/Al) ratio of the zeolite has been shown to have a profound impact on the synthesis time of the material, whereby halving this ratio from 42 results in a doubling of the synthesis time, up to 140 hours (Mintova *et al.* 2006). As such, conventional, industrial grade β-zeolite is typically synthesised with a Si/Al ratio that is usually higher than that which most zeolites possess. In addition, the Si/Al ratio also affects the surface chemistry of the material as described in section 5.4.2. Therefore, any variations in this ratio can significantly impact the selectivity of the zeolite and the conversion of reactant materials.

5.3. Methods and materials

5.3.1. Gas and adsorbed phase PFG NMR experiments

All PFG NMR experiments were performed using a Bruker BioSpin DMX spectrometer operating at a ^{1}H resonance frequency of 300.13 MHz with a 5 mm radiofrequency (r.f.) coil fitted to a PFG probe head, which was placed inside a cryo-magnet. All measurements were taken at 294 K, with a precision of ± 1 K. In each instance, 0.090 ± 0.001 g and 0.045 ± 0.001 g of the 15 μm and the small (0.3 and 0.5 μm) β-zeolite powders were used respectively, corresponding to a bed height of approximately 12 mm in the sealed tube. The 15 μm and small β-zeolite samples possess framework densities of 1509 kg m^{-3} and 754 kg m^{-3} respectively. The modified version of the APGStE pulse sequence introduced in chapter 4, was used in each PFG NMR experiment.

Each experiment was repeated three times and the standard deviation of all three experiments was calculated and subsequently used in the error propagation calculations.

Table 1 shows a summary of the PFG NMR parameters used for the gas and adsorbed phase regions in the sealed tube.

Table 1: Summary of the PFG NMR parameters for the gas and adsorbed phase regions in the sealed tube.

PFG NMR parameters	Gas phase above bed	Adsorbed phase in bed
Observation time [ms]	4	100
Gradient strength [T m^{-1}]	0.001 - 0.7	0.001 - 1
Gradient pulse duration [ms]	0.3	0.3
Gradient ramp time [ms]	0.2	0.1
90° pulse [μs]	13	13
Recycle time [s]	15	3
Number of scans [-]	64	128
Number of points [-]	16	16

Data obtained from the PFG NMR experiments involving the single- and two-component systems, whereby the latter are introduced in chapter 6, were fitted to single and two component exponential decay models respectively, and can be expressed as (Sørland *et al.* 1997):

$$\Psi = \sum_{i=n}^{n} p_i \, exp\left[-\gamma^2 \delta^2 D_i \left(\Delta + \frac{3}{2}\tau - \frac{\delta}{3}\right)g^2\right] + \left(\Delta + \tau - \frac{\delta}{3}\right)f^2(\Delta + \tau)gf$$
$$+ \delta(\delta_1 - \delta_2)\tau(f + g)G_0 + \frac{4}{3}\tau^3 G_0{}^2$$

<div align="right">5.7</div>

where Ψ is the echo attenuation [a.u.], γ is the ^{1}H gyromagnetic ratio [rad s^{-1} T^{-1}], g is the

gradient strength with an amplitude ratio of 1:1 [T m^{-1}], f is the gradient strength with an amplitude ratio of 1:1 [T m^{-1}], δ is the gradient pulse width [s]. G_0 is the constant background gradient which is present in the sample [T m^{-1}] and Δ is the effective observation time [s]. The solid lines in the PFG plots in this chapter are fitting the data to equation 5.7. The delay times either side of the gradient pulses, δ_1 and δ_2, were set to 50 and 201.25 µs respectively, in a bid to minimise the overall echo time in the pulse sequence (Sun *et al*. 2003). Therefore, since an additional element of asymmetry in terms of the pulse sequence delay times was introduced, the cross-magnetisation term arising due to background field gradients was taken into account. The origin and purity of the materials described in this chapter were summarised in chapter 4, table 1.

5.4. Characterisation methods

5.4.1. Scanning Electron Microscopy (SEM) of zeolite materials

Figure 5.2 shows SEM images of the 15 µm β-zeolite material used in this study. The sample consists of a mixture of truncated octahedral particles with a rough surface morphology and irregular structures in the form needle shaped rods. The zeolite was used in the H-form.
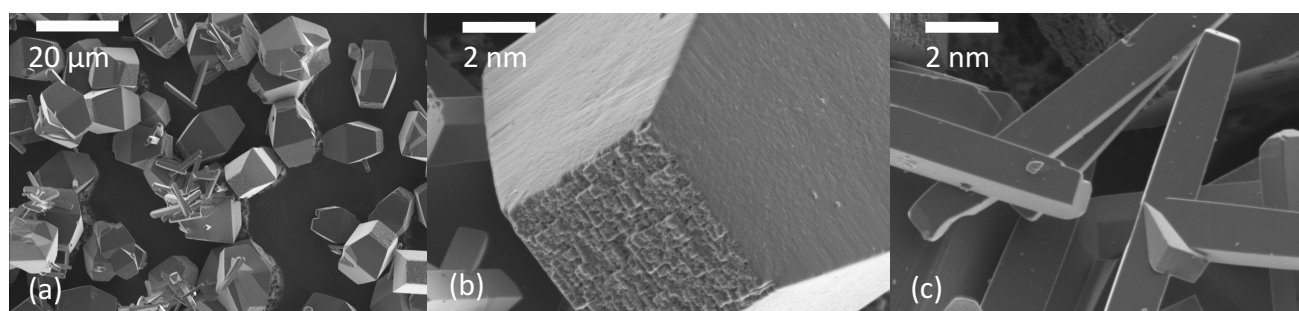
Figure 5.2: SEM image of the 15 µm β-zeolite used in this thesis: (a) Wide angle view of octahedral particles with rod shaped artefacts, (b) zoomed in view of the surface of the octahedral particles, (c) zoomed in view of rod-shaped artefacts.

The SEM of the 0.3 and 0.5 µm β-zeolite samples shown in figure 5.3 indicates that these zeolites possess particles which tend to aggregate and form particulate clusters. The zeolites were used in the H-form.
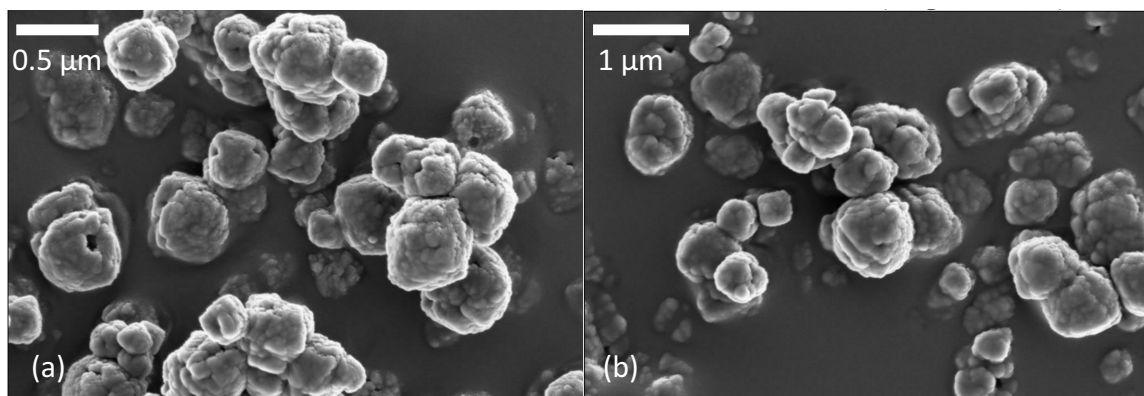
Figure 5.3: SEM image of (a) 0.3 µm and (b) 0.5 µm β-zeolite which will be discussed in section 5.5.8.

5.4.2. Removing moisture from zeolites

Elemental analysis was performed on the 15 µm β-zeolite material using X-ray Photoelectron Spectroscopy (XPS), which showed that there was a small amount of alumina present in the zeolite. A Si/Al ratio of 124 gave rise to a highly hydrophobic surface (Namba *et al*. 1985). As a result, the sample did not adsorb polar solvents as it has a poor acid site content, which is typically a pre-requisite for the adsorption of such guest molecules. However, it has previously been shown that it is possible to synthesise highly hydrophobic β-zeolites which are capable of preferentially adsorbing water and other polar molecules over hydrocarbon molecules (Corma *et al*. 2003). Figure 5.4 shows the sample pre-treatment results from an experiment conducted using a Hiden Isochema Intelligent Gravimetric Analyser (IGA) at Johnson Matthey's Technology Centre (JMTC). This instrument determines the amount of moisture lost from the sample at high temperature and low pressure.

The zeolite was heated at rate of 10 K min^{-1} and was held at 573 K and less than 1×10^{-7} mbar for 13 hours, and the mass lost corresponded to a negligible amount: less than 0.15% of the initial zeolite sample mass. As such, extensive sample preparation which involves dehydrating samples for a prolonged period of time under vacuum, prior to dosing with the desired guest molecules, was not required. No discernible differences were observed between the signal intensities and peak areas of β-zeolite in a ^{1}H NMR pulse acquisition spectra which was not evacuated and one which was evacuated for 13 hours and subsequently flame sealed. Hence, all sample tubes which contain β-zeolite experienced pre-treatment for no longer than 15

minutes, for the sole purpose of removing air, and thus moisture, from the region above the zeolite bed.
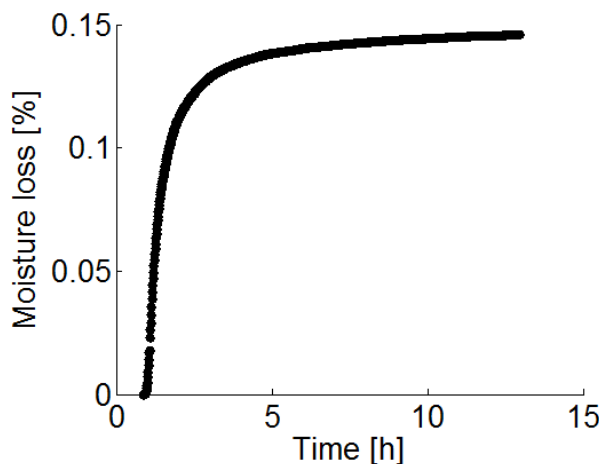
Figure 5.4: IGA dehydration profile of β-zeolite at 573 K and 9.5×10^{-8} mbar.

5.4.3. Nitrogen sorption isotherm

It has been shown that β-zeolite can often possess multiple levels of porosities (Camblor *et al*. 2008). The type I N_2 sorption isotherm shown in figure 5.5 was conducted at 77 K, at the JMTC. The vertical region which rapidly adsorbs N_2 corresponds to the micropore region and the region which gradually fills with N_2 corresponds to the mesopore region. Figure 5.5 shows that the level of mesoporosity which exists in the β-zeolite sample corresponds to less than 5% of the total porosity. Therefore, any contributions from the mesoporous region are excluded in terms of the PFG NMR data interpretation.
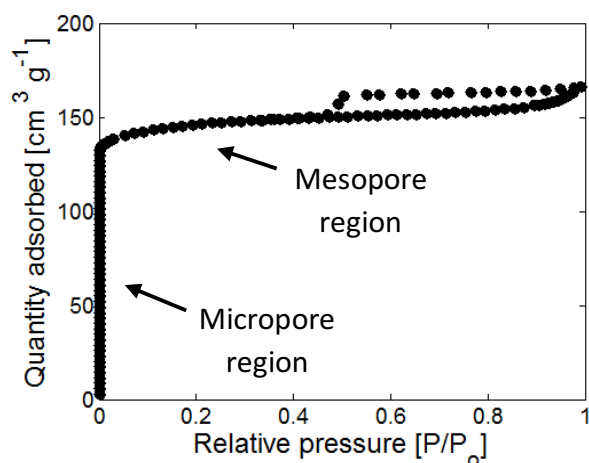
Figure 5.5: N_2 in β-zeolite adsorption-desorption isotherm at 77 K.

5.4.4. Hydrocarbon gas sorption isotherms

The methane and ethane gas sorption experiments were carried out on the IGA instrument at JMTC, using 0.09 g of β-zeolite at 294 K, and the sorption pressures used ranged from 0 to a maximum of 3.5 bar. The propane gas sorption experiment was also carried out using an IGA instrument at Hiden Isochema, United Kingdom, using 0.06 g of β-zeolite at 294 K, and the sorption pressures used ranged from 0 to 5.5 bar. These experiments were conducted in order to gain insights into the relationship between adsorption and self-diffusion with increasing hydrocarbon chain length. Large pore structures such as those in β-zeolite possess poor methane adsorption characteristics (Zhang *et al*. 2014; Li *et al*. 2015). Hence, the methane sorption experiment operated in Henry's region at the pressure range used in this thesis. As shown in figure 5.6 (a), approximately 0.02 g of methane was adsorbed per gram of zeolite. This is in stark contrast to ethane and propane, as displayed by their respective sorption curves in figure 5.6 (b) and 5.6 (c), with approximately 0.08 g of ethane and 0.1 g of propane adsorbed per gram of zeolite respectively. The methane and ethane gas sorption isotherm were extrapolated using a Langmuir model shown by equation 5.8, to the point at which the isotherms plateaued, to gauge the differences in saturation pressures for the three different hydrocarbons:

$$m_g = \frac{v_m K P}{1 + K P}$$
5.8

where m_g is the quantity of the adsorbed gas [mg], v_m is the molecular monolayer quantity [mg], K is an adsorption equilibrium constant [-] and P is the sorption pressure [Pa]. Doing so offers insights into the effects of adsorption on molecular displacements, in a bid to understand the vast disparity between the self-diffusion coefficients for single-component species with differing chain lengths in zeolites as referenced in the literature (Kärger *et al*. 1980; Conner and Fraissard 2003).
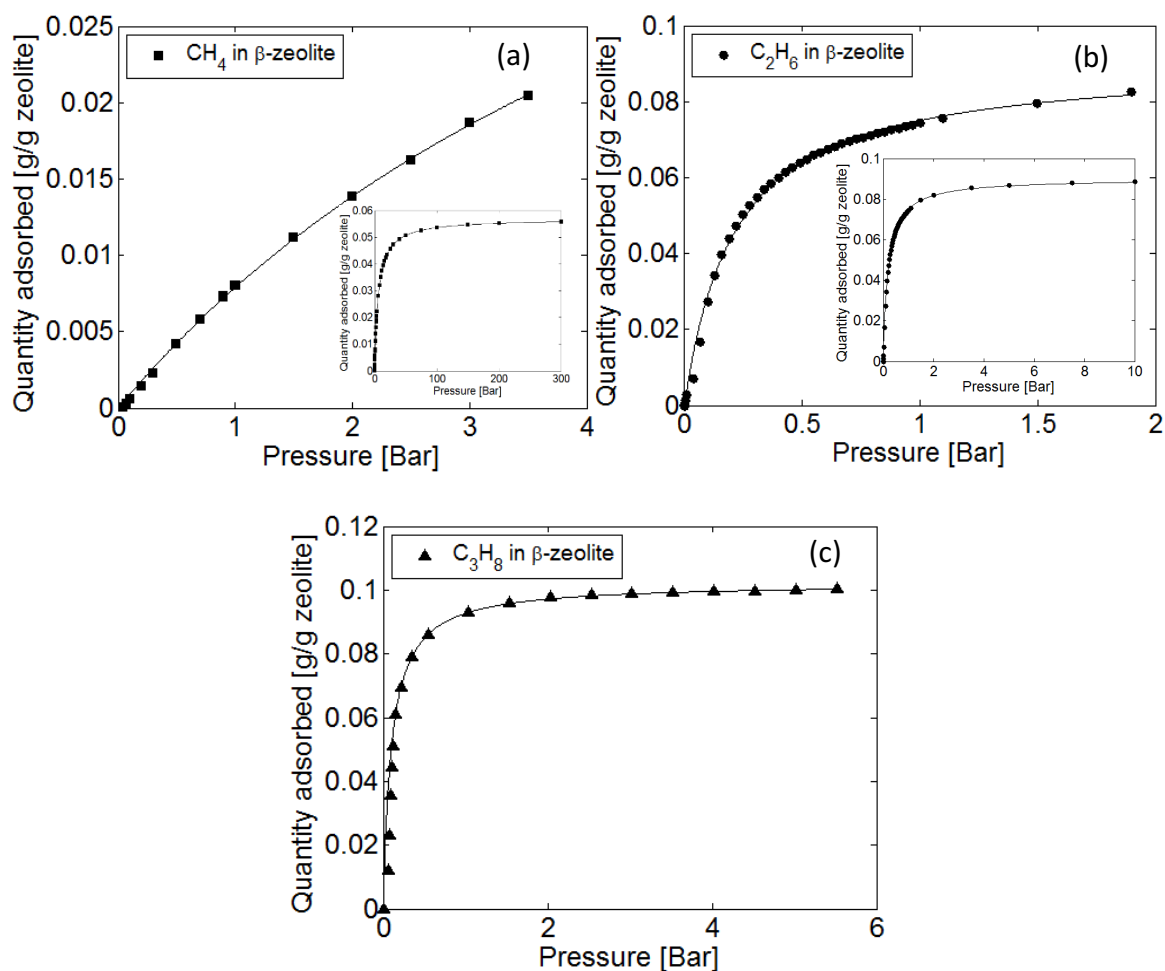
Figure 5.6: (a) CH$_4$, (b) C$_2$H$_6$ and (c) C$_3$H$_8$ sorption isotherms in β-zeolite at 294 K. Extrapolated isotherms (up to saturation) are embedded for methane and ethane.

Differences in the adsorption isotherm profiles also offer insights into different molecular displacement behaviours for binary species co-adsorbed in β-zeolite, which will be discussed further in chapter 6.

5.5. PFG NMR results and discussion

5.5.1. ^{1}H Background PFG NMR signal(s)

In each PFG NMR experiment discussed in this chapter, a single component echo attenuation profile is expected, since a single component guest molecule and a macroscopically homogeneous porous material are used. However, as shown in figure 5.7, curvature was observed during preliminary experiments involving 0.2 bar of methane adsorbed in β-zeolite.

Potential sources of this anomalous behaviour were outlined in chapter 3. Therefore, an investigation into the data was required prior to characterising the self-diffusion behaviour of the guest molecules of interest.
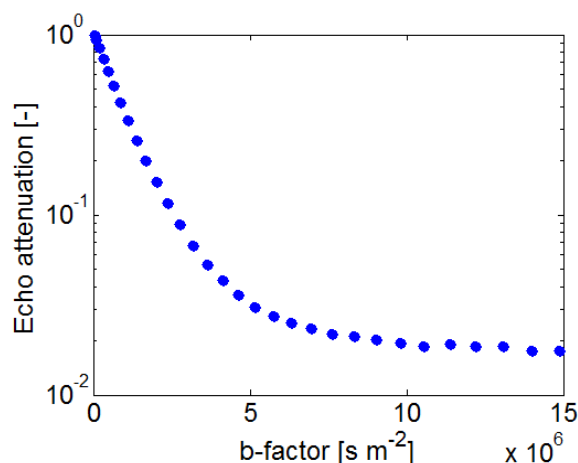
Figure 5.7: Curved ^{1}H echo attenuation plot of 0.2 bar methane adsorbed in β-zeolite.

The linear methane sorption isotherm in figure 5.6 (a) shows that it is a weakly adsorbing molecule which is assumed to be present in the pore structures in the gas phase, for the pressure range studied. This therefore ruled out the possibility of having two-phase behaviour in the zeolite cavity, which could potentially arise due to molecules adsorbing more strongly at certain active sites. The spectral attenuation of the peaks obtained from the PFG NMR experiment was observed using the both the conventional and modified APGStE pulse sequences. As shown in figure 5.8, a noisy peak, which is significantly broader than that of a guest molecule peak of interest, 1400 Hz compared to 105 Hz, was present at the higher gradient strengths.
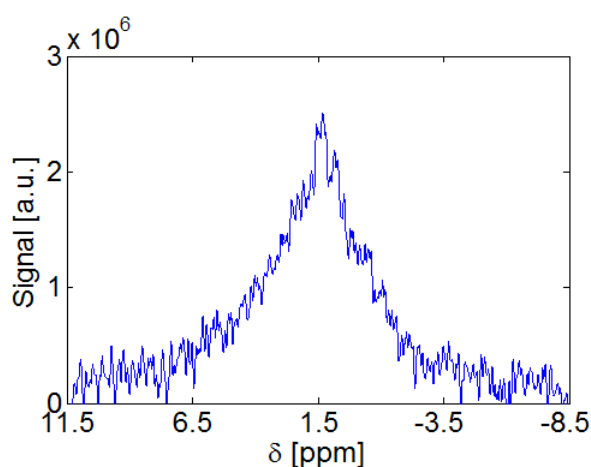
Figure 5.8: Broad ^{1}H background peak present at points furthest out in q-space.

Therefore, to track any potential attenuation of this noisy artefact, the PFG NMR experiment was repeated with 2048 scans and the gradients were increased to within 90% of the PFG probe's maximum gradient strength: 10 T m^{-1}. Consequently, this broad peak did not attenuate and was nevertheless present at the highest gradient strength. It was therefore determined that the aforementioned curvature was due to this misleading artefact. Subsequently, the mean of the last three echo attenuation points was subtracted from the total echo attenuation in all PFG NMR experiments. Consequently, linear profiles were obtained from the curved echo attenuation plots for different pressures of methane, ethane and propane, as shown in figure 5.9. An example is also illustrated which also demonstrates the lack of attenuation of the broad, background artefact, which is in stark contrast to the methane signal attenuation.
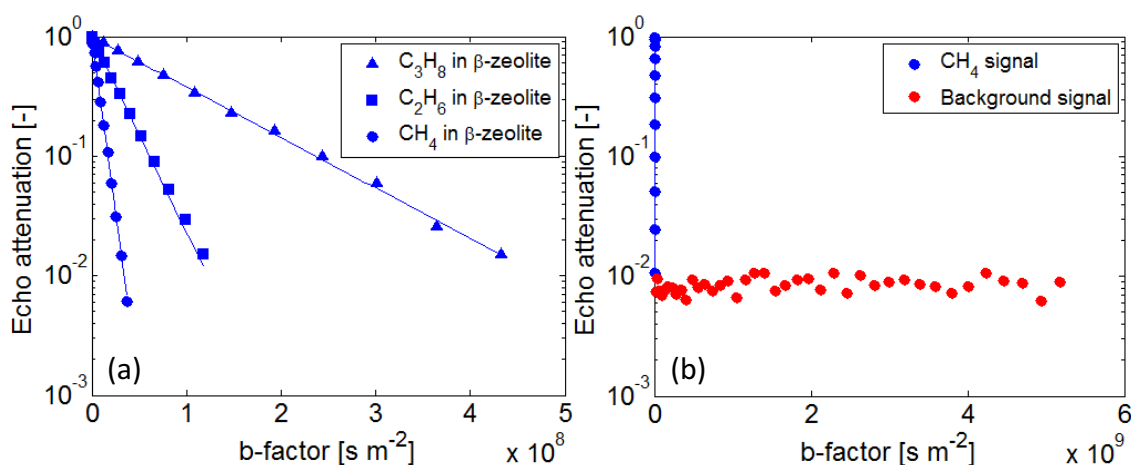
Figure 5.9: (a) Example of corrected echo attenuation plots for CH$_4$, C$_2$H$_6$ and C$_3$H$_8$ adsorbed in β-zeolite and (b) corrected echo attenuation plot alongside the echo 'attenuation' of the of the background signal using CH$_4$ adsorbed in β-zeolite as an example. The difference in the x-coordinates is a result of the different maximum gradient strengths used.

A PFG NMR experiment was conducted without a 90° excitation pulse to investigate the origin of this background artefact. No detectable signal was observed, which ruled out the possibility of the spectrometer as the source of the background artefact. Additionally, a flame sealed tube of evacuated β-zeolite, which was not dosed with any gaseous molecules, was placed inside the magnet. Similarly, no detectable signal was observed in a "pulse acquire" or PFG NMR experiment. It is therefore likely that the source of this background signal was a trace

impurity from the dosing gas cylinder. The spectral linewidth of this background peak is broader than the CH_4 peak of interest by a factor of 13, which implies that this extremely slow-moving species is not present in the gas phase.

5.5.2. Obtaining $D_{long-range}$ for single component gaseous guest molecules in β-zeolite from PFG NMR diffusometry

The determination of the long-range diffusion coefficients in the experiments involving β-zeolite exposed to gaseous molecules were performed with carefully selected experimental parameters and curve fitting methods. Figure 5.11 shows a ^{1}H spectral attenuation plot from a PFG NMR experiment, using CH_4 adsorbed in β-zeolite as an example. Remarkable chemical shift resolution with an excellent Signal-to-Noise Ratio (SNR) is obtained for β-zeolite imbibed in methane, with a typical spectral linewidth of 75 Hz. This presents the opportunity for analysing multiple gaseous species confined in zeolite systems, which will be explored in chapter 6.
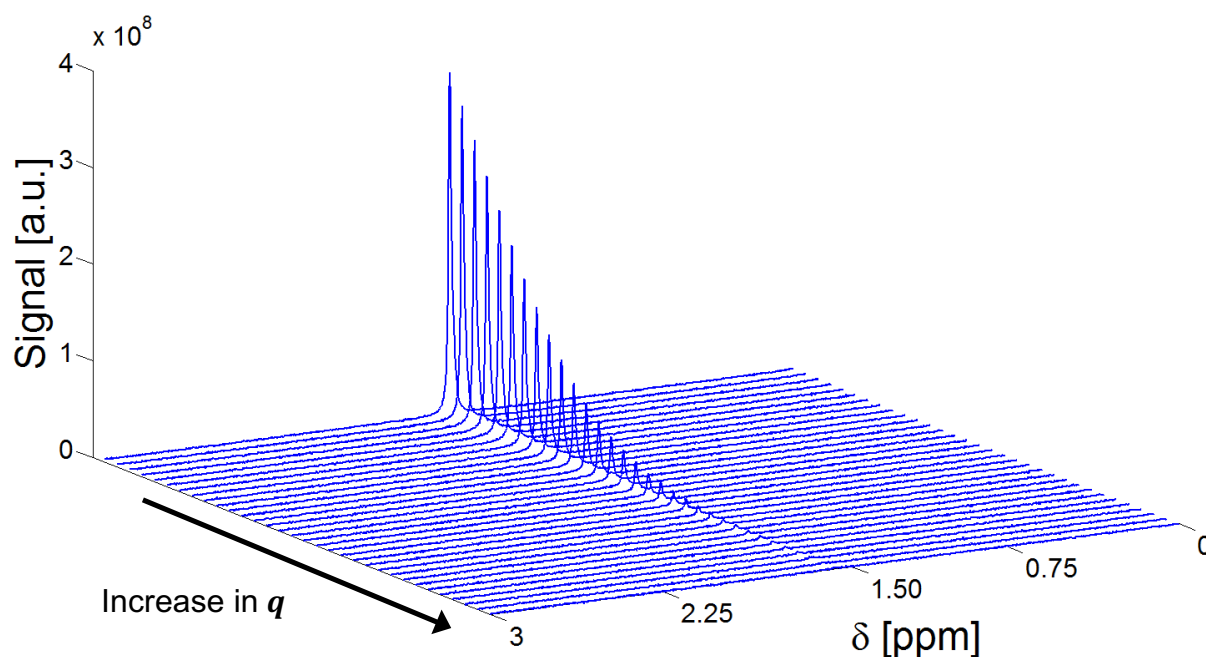
Figure 5.11: Spectral attenuation of 0.2 bar methane adsorbed in β–zeolite as a function of q-space in a PFG NMR experiment. δ = 0.25 ms, Δ = 100 ms and g = 0.001 - 0.36 T m^{-1}.

Deliberately large observation times were selected to measure molecular displacements spanning several crystallites across the zeolite bed, which resulted in the characterisation of long-range diffusion coefficients. This was carried out in a bid to prove that exceeding zeolite

crystallite sizes is not a prohibitive measure in terms of calculating intra-diffusion coefficients, and will be discussed further in section 5.5.8.

Figure 5.12 shows the echo attenuation plots for methane, ethane and propane adsorbed in β-zeolite, and a summary of the long-range diffusion coefficients as a function of loading.
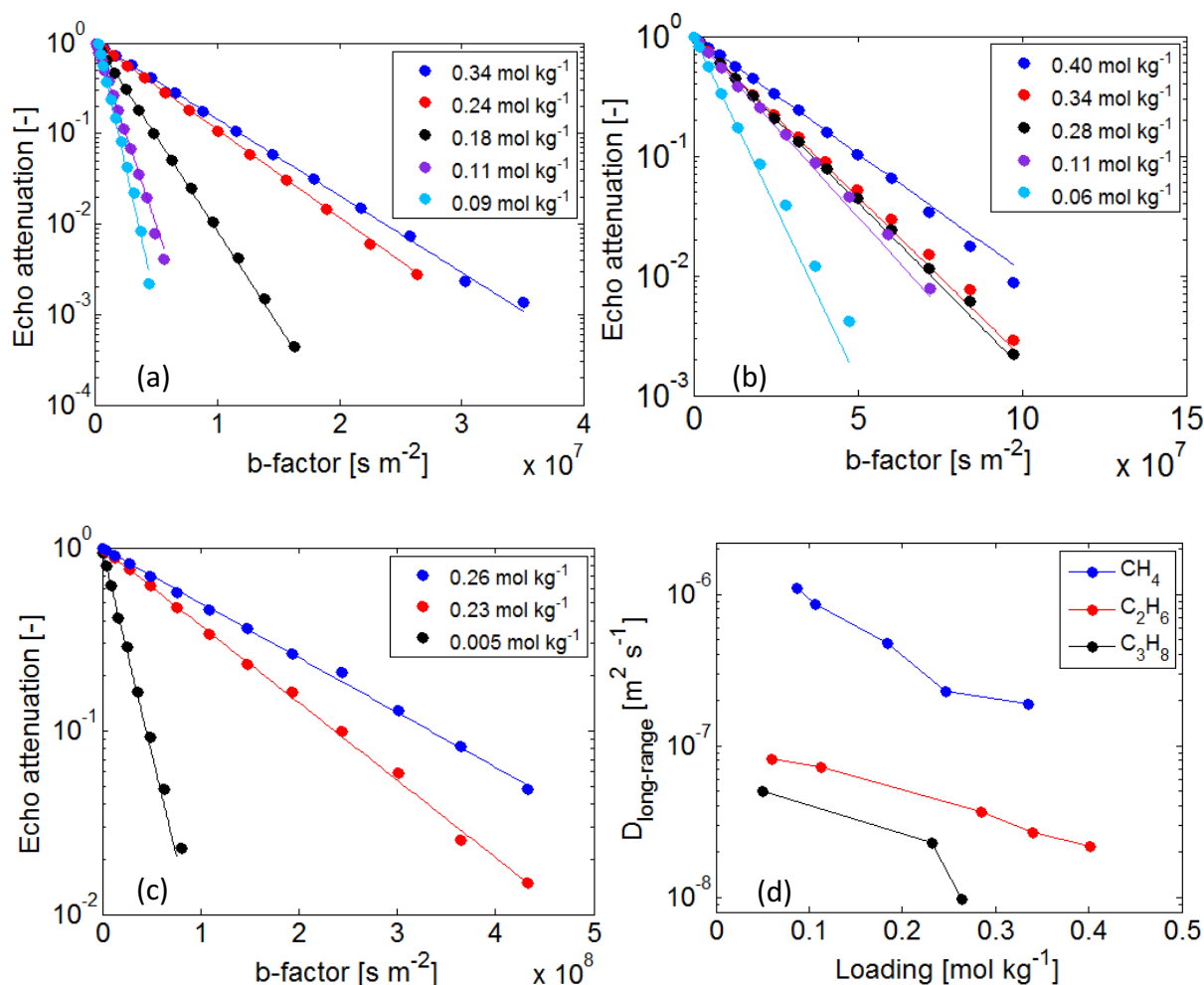
Figure 5.12: Echo attenuation plots for long-range (a) CH_4, (b) C_2H_6 and (c) C_3H_8 diffusion in β-zeolite at variable hydrocarbon loading, and (d) a summary of the long-range diffusion coefficients *vs.* loading. δ = 0.25 ms, Δ = 100 ms and g = 0.001 - 0.96 T m^{-1}. The error bars are within the size of the markers.

As the hydrocarbon loading increases, the long-range diffusion coefficient decreases. This trend is expected since the level of confinement is enhanced as the number of molecules in the system increases, resulting in increased restrictions to molecular mobility. Table 2 shows that there is a difference of at least an order of magnitude in the long-range diffusion coefficients between the three different species at higher loadings. However, at lower

loadings, this disparity is less pronounced, as contributions from the inter-particle region display increases in dominance, which results in an enhanced weighting effect on the long-range diffusion coefficient, as described by equation 5.1. Additionally, there is a reduction in the total echo attenuation with increasing hydrocarbon chain length. This is due to a stronger adsorption interaction between the guest molecules and the zeolite surface as the size (and molecular weight) of the guest molecules increases. This results in a greater degree of restrictions, as the molecules gradually begin to behave as conventional hydrocarbon liquid phase molecules confined in porous media. Table 2 shows a summary of the long-range diffusion coefficients of CH_4, C_2H_6 and C_3H_8 adsorbed in the 15 μm β-zeolite. In each instance, the $RMSD$s vastly exceed the crystallite size of the zeolite, therefore a fast exchange regime is dominant.

Table 2: Summary of the long-range diffusion coefficients of CH_4, C_2H_6 and C_3H_8 in β-zeolite. The equivalent adsorbed pressures were calculated using the method shown in figure 4.7 in chapter 4. The quantity in the adsorbed phase is equal to an equivalent pressure determined using: $PV = nRT$, in which $P \propto n$.

Species	Equivalent adsorbed pressure [mbar]	Adsorbed phase loading [mol kg^{-1}]	Long-range diffusion coefficient [m^2 s^{-1}]	RMSD [μm]
CH_4	158.88	0.087	$1.1 \pm 0.01 \times 10^{-6}$	469
	194.01	0.106	$8.7 \pm 0.01 \times 10^{-7}$	417
	335.97	0.184	$4.8 \pm 0.01 \times 10^{-7}$	310
	450.01	0.246	$2.3 \pm 0.02 \times 10^{-7}$	214
	611.65	0.335	$1.9 \pm 0.01 \times 10^{-7}$	195
C_2H_6	109.64	0.060	$8.2 \pm 0.03 \times 10^{-8}$	128
	203.85	0.112	$7.3 \pm 0.03 \times 10^{-8}$	121
	518.98	0.284	$3.7 \pm 0.01 \times 10^{-8}$	86
	621.18	0.340	$2.7 \pm 0.03 \times 10^{-8}$	73
	895.50	0.401^a	$2.2 \pm 0.01 \times 10^{-8}$	66
C_3H_8	98.70	0.050	$5.0 \pm 0.08 \times 10^{-8}$	100
	494.01	0.232	$2.3 \pm 0.03 \times 10^{-8}$	68
	561.52	0.263	$9.7 \pm 0.01 \times 10^{-9}$	44

5.5.3. PFG NMR based method for calculating D_{intra}

5.5.3.1. Determining p_{inter} and D_{inter} using PFG NMR

The novel method described in this subsection utilises the realistically unavoidable inter-particle spaces in zeolite beds. This involves re-arranging equation 5.2 to solve for the intra-diffusion coefficient:

$$D_{intra} = \frac{D_{long-range} - p_{inter}D_{inter}}{(1 - p_{inter})}$$

$$5.9$$

As mentioned in chapter 4, the gas phases above the zeolite beds are in equilibrium in the sealed tube. Since the gaseous hydrocarbon probe molecules used in this study possess poor sorption properties, it is assumed that the diffusivity of the bulk gas phase above the bed is equal to the inter-particle diffusivity. This suggests that the 'inter-particle tortuosity factor', which is the ratio of the bulk gas diffusivity to the inter-particle diffusivity, is equal to one and that molecules in the outer regions follow a path of least resistance. Therefore, it is assumed that the inter-particle diffusivity is equal to the diffusivity of the gas phase above the zeolite bed. The D_{gas} of CH_4, C_2H_6 and C_3H_8 range from 10^{-6} m^2 s^{-1} - 10^{-5} m^2 s^{-1}, in which linear echo attenuation plots are obtained in each instance, with an example of CH_4 above the β-zeolite bed shown in figure 5.13. Gas pressures ranging from 0.3 bar to 1.5 bar, were used for the samples discussed in this thesis. Therefore, it was not possible to calculate D_{inter} using equations 5.3 - 5.6, as these expressions are only suitable for dilute gas systems. $D_{inter} \approx D_{gas}$ is regarded as an acceptable assumption for fast exchange systems in the literature (McDaniel *et al*. 1996). [1]

---

[1] A sensitivity analysis of D_{intra} to the tortuosity is presented in table 4 in section 5.5.4.
It is noted that the tortuosity is a universal scaling parameter in fluid transport processes.
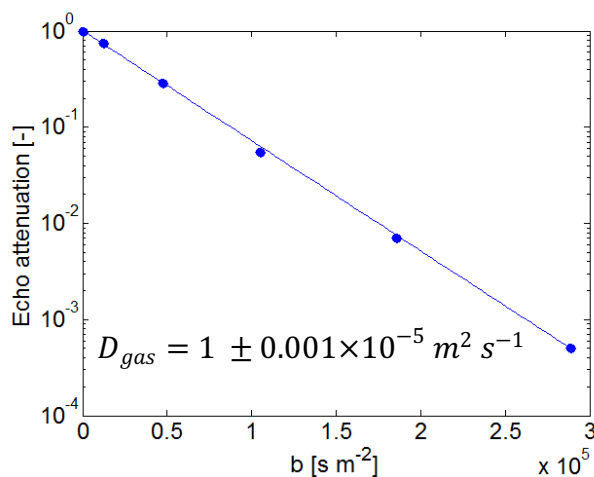
Figure 5.13: Echo attenuation plot of the gas phase region above the zeolite bed using 0.25 bar CH$_4$ as an example. δ = 0.25 ms, Δ = 4 ms and g = 0.001 - 0.2 T m^{-1}.

The areas of the relaxation corrected spectra for both the adsorbed and the gas phase above the bed were used to obtain the zeolite bed (which is the sum of the adsorbed and inter-particle signal) and bulk gas populations, p_{bed} and p_{gas} respectively, in the sealed tube. This is shown by equations 5.10, 5.11 and 5.12. As mentioned in section 5.3.1, 0.09 g of the 15 μm β-zeolite powder was used in each sample tube. The β-zeolite framework possesses a skeletal density of 1509 kg m^{-3} and this enabled the volume occupied by the zeolite bed, v_z, to be calculated for each sample. By measuring the zeolite bed height in the 5 mm o.d. sealed tube, which has a total wall thickness of 1.5 mm, using a Vernier calliper, the total, bulk volume, v_b, which is occupied by the zeolite powder was calculated. A bed height of 12 mm was recorded in each instance. Subsequently, the solid fraction, ε, was calculated by taking a ratio of these two volumes, and this enabled the void fraction, ϕ, to be calculated, as the sum of these fractions is equal to one:

$$\phi = 1 - \varepsilon \qquad\qquad 5.10$$

The inter-particle gas population in the zeolite bed was then obtained by multiplying the gas population above the bed by the void fraction of the zeolite bed:

$$p_{inter} = p_{gas} \times \phi \qquad\qquad 5.11$$

with

$$p_{gas} = \frac{S_{gas}}{S_{bed}} \qquad\qquad 5.12$$

where S_{gas} is the relaxation corrected signal of the gas phase above the bed and S_{bed} is the sum of the relaxation corrected signals of the adsorbed and inter-particle regions. This procedure is summarised by the flowchart in figure 5.14 and in appendix A4.
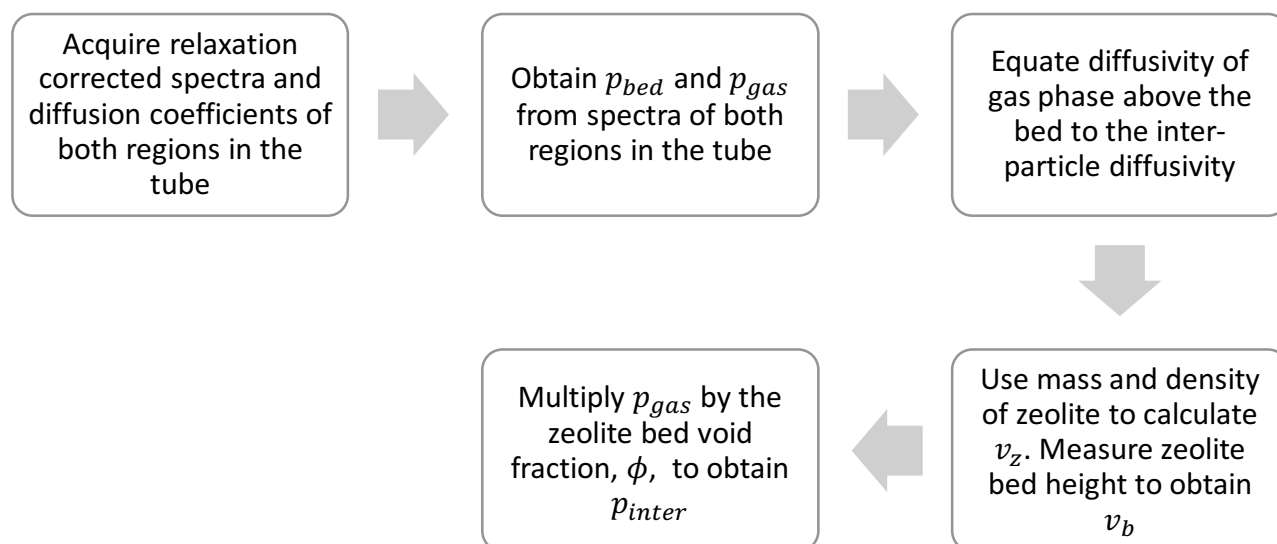
Figure 5.14: Flowchart of steps involved for calculating intra-diffusion coefficients solely from PFG NMR measurements.

The proposed method is a purely (PFG) NMR based method, capable of determining all the parameters outlined in equation 5.1 and requires no additional experimental techniques. This, to the author's knowledge, has not been demonstrated in the literature. The intra-diffusion coefficients of methane and ethane in β-zeolite were determined in the same manner, and are summarised as a function of loading in figure 5.15 and table 3.
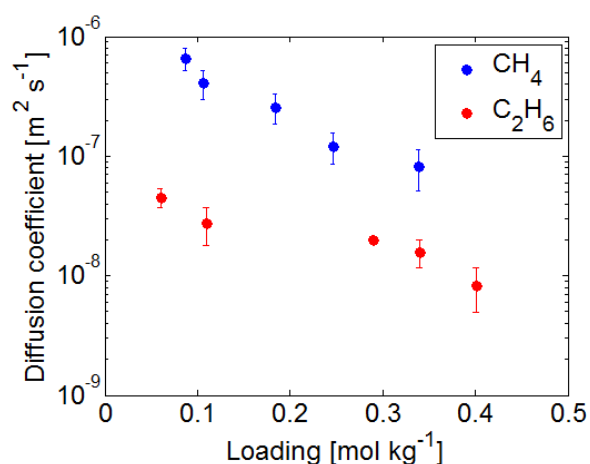
Figure 5.15: Summary of intra-diffusion coefficients of CH$_4$ and C$_2$H$_6$ in adsorbed β-zeolite. Error bars are calculated from an error propagation method described in appendix A5.

Table 3: Summary of equivalent adsorbed pressures, molecular loadings and calculated intra-diffusion coefficients of methane and ethane adsorbed in β-zeolite.

Species	Equivalent adsorbed pressure [mbar]	Adsorbed phase loading [mol kg^{-1}]	Intra-diffusion coefficient [m^2 s^{-1}]	RMSD [μm]
CH$_4$	158.88	0.087	$6.6 \pm 0.21 \times 10^{-7}$	363
	194.01	0.106	$4.1 \pm 0.27 \times 10^{-7}$	286
	335.97	0.184	$2.6 \pm 0.29 \times 10^{-7}$	228
	450.01	0.246	$9.3 \pm 0.29 \times 10^{-8}$	136
	611.65	0.335	$8.2 \pm 0.38 \times 10^{-8}$	128
C$_2$H$_6$	109.64	0.060	$4.5 \pm 0.19 \times 10^{-8}$	95
	203.85	0.112	$2.7 \pm 0.35 \times 10^{-8}$	73
	518.98	0.284	$2.0 \pm 0.03 \times 10^{-8}$	63
	621.18	0.340	$1.6 \pm 0.26 \times 10^{-8}$	57
	895.50	0.401^a	$8.2 \pm 0.40 \times 10^{-9}$	41

a. *corresponds to 1.5 molecules per cavity*

Similar to the long-range diffusion coefficients, a decrease in the intra-diffusion coefficients is observed with increasing loading, for both guest molecules. As expected, all D_{intras} are smaller than $D_{long-range}$. These differences are less noticeable at lower hydrocarbon loadings, where the two diffusion regimes are of the same order of magnitude. This can be explained by an enhanced weighting effect on the long-range diffusivity by the inter-particle region at lower loadings, since faster long-range diffusion coefficients in this region result in a larger *RMSD* across the zeolite bed, which in turn increases the intra-diffusivity as governed by equation 5.2.

5.5.4. Comments on error analysis

The calculation of the intra-diffusion coefficients relied on both the measurement and calculation of several parameters. As such, the error propagation associated with each

approximation is significantly larger than that associated with each PFG NMR measurement, which is typically less than 3%, determined by repeating each measurement 3 times. The errors for the calculated intra-diffusion coefficients are less than or equal to 30% for all methane and ethane samples. These errors were calculated by taking the partial derivatives of the addition and multiplication terms in equation 5.2, using Wolfram Mathematica. A sample calculation is included in appendix A5.

The stronger the sorption properties of the guest molecules, the lower the proportion of molecules present in both the inter-particle and in the gas phase regions above the zeolite bed. As such, this technique will not be ideal for strongly adsorbing gaseous guest molecules. However, this is not a deterrent since a strongly adsorbing species confined in a zeolite possesses a diffusion coefficient which is sufficiently slow as to qualify as an intra-diffusion coefficient. This is because its associated $RMSD$ at room temperature typically does not exceed the zeolite crystallite size, even in industrial grade zeolites. Therefore, this technique will not be required when the $RMSD$ is less than the crystallite size, since the parameter of interest can be characterised directly using PFG NMR.

The largest source of error in the calculation of the intra-diffusion coefficient method was from the zeolite bed height, which was measured using a Vernier calliper. However, the assumed tortuosity also had an impact on the intra-diffusivity. Table 4 shows a brief sensitivity analysis of the method to these parameters and their impact on the overall error, using CH_4 and C_2H_6 adsorbed in β-zeolite as examples. The values highlighted in bold correspond to the original values used in this thesis. The non-bold values were manually varied to determine the impact of these parameters on D_{intra}.

Table 4: Sensitivity of the D_{intra} calculation method to the parameters associated with equation 5.2 using (a) CH$_4$ and (b) C$_2$H$_6$ adsorbed in a 15 μm β-zeolite as examples. Values in bold correspond to original values used in this thesis. Non-bold values correspond to variation of the original values.

(a)	τ [-]	D_{intra} for CH$_4$ [m^2 s^{-1}]	Error [%]	(b)	τ [-]	D_{intra} for C$_2$H$_6$ [m^2 s^{-1}]	Error [%]
	1	**4.1×10^{-7}**	**27**		**1**	**4.5×10^{-8}**	**19**
	2	6.5×10^{-7}	17		2	6.4×10^{-8}	13
	3	7.3×10^{-7}	15		3	7.0×10^{-8}	12
	4	7.7×10^{-7}	15		4	7.3×10^{-8}	12

Zeolite bed height [mm]	D_{intra} for CH$_4$ [m^2 s^{-1}]	Error [%]		Zeolite bed height [mm]	D_{intra} for C$_2$H$_6$ [m^2 s^{-1}]	Error [%]
12	**4.1×10^{-7}**	**27**		**12**	**4.5×10^{-8}**	**19**
8	9.6×10^{-7}	17		8	8.8×10^{-8}	14
10	6.3×10^{-7}	21		10	6.3×10^{-8}	16
14	2.5×10^{-7}	35		14	3.3×10^{-8}	22

As mentioned in section 5.1.2, literature studies have reported that in instances where the population of molecules is highly weighted towards the inter-particle region, equation 5.2 may be reduced to exclude the intra-particle term entirely (McDaniel *et al*. 1996). In such instances, p_{inter} and D_{inter} are obtained from gas sorption isotherms and kinetic theory respectively. Table 5 shows a comparison between the long-range diffusion coefficients obtained using PFG NMR and those calculated from the product of the inter-particle parameters. The aim of this is to confirm the suitability of using this assumption with the adsorbed phase systems discussed in this thesis, in instances where PFG NMR and intra-crystalline characterisations may not available to the researcher.

Table 5: Comparison of long-range diffusion coefficients obtained from PFG NMR and the literature method, *via* gas sorption isotherms and kinetic theory approximations. An example is shown for single component CH_4 and C_2H_6 adsorbed in a 15 μm β-zeolite powder.

Species	Adsorbed phase loading [mol kg^{-1}]	$D_{long-range}$ from PFG NMR [m^2 s^{-1}]	$D_{long-range} = p_{inter}D_{inter}$ [m^2 s^{-1}]
CH_4	0.106	$8.7 \pm 0.01 \times 10^{-7}$	4.7×10^{-8}
C_2H_6	0.060	$8.2 \pm 0.03 \times 10^{-8}$	3.6×10^{-8}

The long-range diffusion coefficients which include and exclude the intra-crystalline region are in poor agreement with one another. This therefore highlights that the intra-crystalline region has a significant contribution and must be accounted for in PFG NMR and alternative experimental applications which involve these guest molecules and zeolite materials.

5.5.5. Variable observation time PFG NMR

In order to observe both intra- and long-range diffusion regimes within the same system, a guest molecule (with a sufficiently long T_1 relaxation constant) which travels less than 15 μm at short observation times and greater than 15 μm at longer times is required. This would also enable the subsequent slow exchange regimes to be probed. Figure 5.16 shows that it was possible to conduct an experiment involving 0.26 mol kg^{-1} propane adsorbed in a large pore 15 μm β-zeolite bed to observe the transitions in molecular displacement probability distributions discussed in chapter 3. This enabled the characterisation of non-exchanging and various exchanging diffusion regimes.

The observation time was initially set to 3 ms, which yielded a linear echo attenuation plot, with a diffusion coefficient of $2.4 \times 10^{-9}\,m^2\,s^{-1}$. The resulting $RMSD$ of 4 μm illustrates that the molecular displacement is significantly smaller than the zeolite's crystallite size and is interpreted as an intra-diffusion coefficient. The observation time was subsequently increased to 8, 20 and 30 ms respectively. Consequently, changes in the shapes of the echo attenuation profiles are observed due to developing curvature, which implies that there is a level of molecular exchange taking place between the inner and outer crystallite regions. The effects of exchange behaviour are not investigated in this thesis, since it is assumed that any

molecules which are present in the external crystallite regions behave as bulk gases. As such, they possess relaxation and diffusive properties which are likely to be different to those belonging to the molecules inside the crystallites. Since near identical relaxation properties are a pre-requisite for studying exchange behaviour, the well-established equations to characterise such behaviour are not applicable:

"… Thus, a correction for nuclear relaxation during the diffusion period cannot be applied…"

"…Furthermore, the a priori assumption of an exponential lifetime distribution makes Kärger's approach unsuitable for the study of more complex systems." (Valiullin et al. 1997).

As such, the curved echo attenuation plots were not fitted to equation 5.7 and the characterisation of exchange behaviour and the interpretation of the associated numerical results are not in the scope of this thesis.

By further increasing the observation time to 100 ms, the echo attenuation curve reverts to a linear profile, with a long-range diffusion coefficient of $2.3 \times 10^{-8}\, \mathrm{m^2\, s^{-1}}$ with a resulting $RMSD$ of 68 μm. This transition from a Gaussian, to non-Gaussian and subsequently back to a Gaussian probability distribution of measured molecular displacements indicates the absence and presence of both slow and fast exchange diffusive behaviour. Therefore, the assumptions made with respect to molecules adsorbing onto the surface and subsequently migrating across the crystallite bed, as opposed to reflecting off the inner zeolite surface and being prevented from exiting the crystallite, are valid. This provides proof for the existence of two-region molecular exchange in the system described in this thesis. Table 6 shows a summary of the limiting self-diffusion coefficients of propane in β-zeolite at the different observation times.
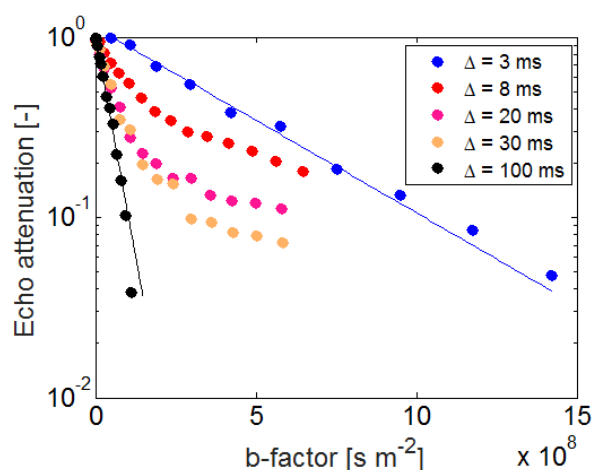
Figure 5.16: Variable observation time PFG NMR of 0.26 mol kg^{-1} propane adsorbed in β-zeolite to characterise non-exchanging and various exchanging diffusion regimes. δ = 0.25 - 1 ms, Δ = 100 ms and g = 0.001 - 2.06 T m^{-1}.

Table 6: Summary of the self-diffusion coefficients of 0.26 mol kg^{-1} propane adsorbed in a 15 μm β-zeolite at different observation times.

Observation time [ms]	Self-diffusion coefficient [m^2 s^{-1}]	RMSD [μm]	Self-diffusion regime
3	2.4 × 10^{-9}	4	Intra
8	-	-	Exchange
20	-	-	Exchange
30	-	-	Exchange
100	2.3 × 10^{-8}	68	Long-range

5.5.6. Comparisons with PFG NMR literature studies

At appropriate loadings, both the long-range and intra-diffusion coefficients reported in this study may be compared with data found in the literature, characterised using macroscopic techniques, as well as simulation studies.

There exists a dearth of experimental literature data for the self-diffusion of gas and liquid phase molecules adsorbed in β-zeolite obtained using PFG NMR. Therefore, comparisons are made with an alternative large pore (7.4 Å) NaX zeolite with a faujasite framework, using both the long-range and intra-diffusion coefficients of ethane and propane respectively. However, this zeolite material possesses a uniform cage structure which may not necessarily deal with preferential diffusion pathways, unlike the zeolite framework discussed in this chapter, which has intersecting channels of slightly differing sizes (Krishna 2012).

The long-range diffusion of ethane in NaX outlined by Vasenkov *et al*. (2003) was characterised at variable temperature on a 400 MHz spectrometer, using a conventional APGStE pulse sequence and involved a gradient pulse width and observation time ranging from 0.05 - 0.16 ms and 20 - 100 ms respectively. The mass of the powder used was 300 mg, the NaX crystallite size ranged from 20 - 30 μm and the samples were dehydrated on a vacuum line at 573 K for 20 hours. Subsequently, 50 mbar of ethane was adsorbed onto the zeolite, which was left to reach equilibrium for 4 hours. The sample was then sealed and separated from the vacuum line and the quantity adsorbed remained constant during this process, although the details of this step are not specified. This was then repeated using 80 mbar of ethane as the adsorption pressure. Figure 5.17 shows a comparison between the experimental results reported in this thesis and those found in the literature.
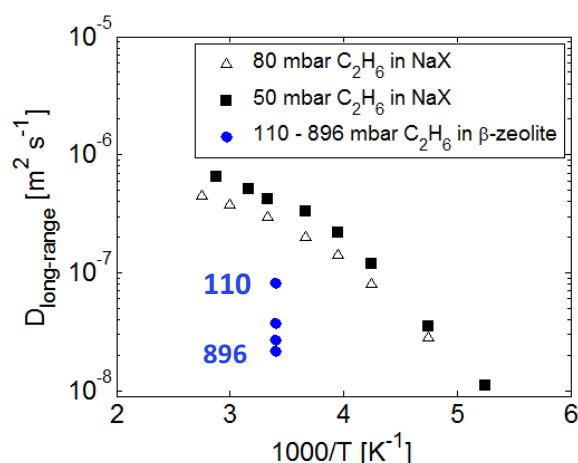

Figure 5.17: Comparison of literature PFG NMR data from ethane adsorbed in NaX at variable temperature and pressure with PFG NMR data reported in this thesis from ethane adsorbed in β-zeolite at fixed temperature and variable pressure (re-plotted from Vasenkov *et al* 2003).

The long-range diffusion coefficients reported in the literature are higher than those reported in this thesis, since a lower molecular loading and a slightly larger pore structure are used. Once these disparities are considered, the results are in reasonable agreement between zeolite structures with similar pore sizes.

However, by evaluating the diffusion of ethane in this same NaX zeolite, Pampel *et al.* (2006) studied and reported an intra-diffusion coefficient of 4.6×10^{-9} m^2 s^{-1} at a loading of 1.5 molecules per cavity. The adsorption of ethane in NaX crystallites, with a diameter of 50 μm, was obtained using a sample preparation method similar to that described in chapter 4. Using an APGStE pulse sequence, the specified observation time of 10 ms resulted in an RMSD of 10 μm, which was considerably smaller than the crystallite size. This result was in reasonable agreement with the intra-diffusion coefficient (8.2×10^{-9} m^2 s^{-1}) of ethane adsorbed in β-zeolite reported in this study, (shown in table 3), at an identical molecular loading per zeolite cavity.

Similarly, the intra-diffusion coefficient of propane adsorbed in NaX was reported by Schwarz *et al.* (1995) as 6.0×10^{-10} m^2 s^{-1}, at a loading which was 50% higher than the highest loading reported in this thesis. This is also in good agreement with the intra-diffusion obtained from the variable observation time experiment shown in figure 5.16 (2.4×10^{-9} m^2 s^{-1}), which characterises an intra-diffusion coefficient directly at an observation time of 3 ms.

5.5.7. Comparing PFG NMR with MD simulations

As described in chapter 3, significant disparities are observed when self-diffusion coefficients obtained using PFG NMR, QENS and MD simulation studies are compared. Currently unpublished MD simulation data generated by the Rajamani Krishna group at the University of Amsterdam, Netherlands, showed a minimal decrease in the self-diffusion coefficients of methane adsorbed in BEA as a function of loading (Krishna 2014, private communication). Similar trends were reported for propane adsorbed in the same framework. The apparent lack of variation is more evident when only simulated motion in the z-direction is considered, with a decrease of 10% observed from a loading of 0.2 - 0.8 mol kg^{-1}, as demonstrated in figure 5.18. This seems counter intuitive, in the sense that whilst the guest molecules used as a comparison possess poor sorption properties, confinement is nonetheless expected to govern

motion, with respect to hindering molecular displacements in an Angstrom sized unit cell. Therefore, a change in loading is expected to have a marked effect on the intra-diffusivity, as well as the long-range diffusivity, even though the latter may be weighted by the faster, inter-particle diffusivity. The intra-diffusion coefficients and long-range diffusion coefficients calculated and obtained respectively using PFG NMR show a plausible decrease in diffusivity as a function of loading, as one would expect in fluids confined in porous media (Herden *et al*. 1992).
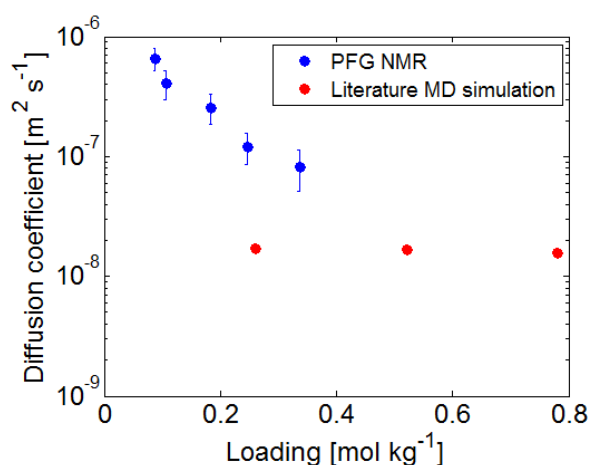
Figure 5.18: Comparison of PFG NMR intra-diffusion coefficients of CH_4 in β-zeolite with its simulated MD counterpart.

With respect to motion in the 3D cage structures of zeolites, it was also reported by Krishna *et al*. that the self-diffusion coefficients simulated in the x, y and z dimensions were significantly different from one another, varying by up to a factor of 4. This unusually large disparity was not anticipated and is yet to be accounted for. Whilst it is evident that β-zeolite is an anisotropic material, and thus small differences in the diffusivities in the three dimensions are anticipated due slight differences in orthogonal geometries, a difference of a factor of 4 is significantly larger than expected.

The PFG NMR data published by Vasenkov *et al*. (2003) showed a similar trend to the experimental results presented in this thesis, in that a decrease in the long-range diffusion coefficient of ethane in a large pore zeolite as a function of loading was observed. Therefore, the criticisms levelled at the validity of MD simulations arising from the differences in the length-scales probed when compared to the longer timescales of a PFG NMR experiment are relevant for this argument. The use of a simulated observation time of the order of picoseconds, which results in a molecular displacement of the order of angstroms -

nanometres, gives an indication of how far and fast molecules can move in that specified time/length-scale. However, it is not a representative scenario of a real-world system, since effects which are typically observed in small and large pore zeolites are overlooked entirely Clark *et al.* (1999). These include particle-particle collisions, surface contributions and the prospect of preferential diffusion pathways of guest molecules. Sorbate molecules, regardless of the strength of their sorption properties, interacting with zeolite surfaces are susceptible to confinement effects whereby molecules either adsorb or ricochet against the solid surface. Guest molecules interacting with surfaces are ubiquitous in real-world industrial reactions and operations. This is due to the large *RMSD*s and small unit cell dimensions involved in such applications. Additionally, variations in temperatures and product distributions typically result in the formation of molecules with differing surface interactions. Therefore, the specified time scale of the simulation could be sufficiently short such that the aforementioned effects are not experienced at all by the guest molecules. The most significant limitation of MD simulation studies is that the observation time cannot be lengthened sufficiently such that the molecules experience zeolite surface layers to account for this, due to hardware limitations of the simulating computer. Therefore, it is not suitable to make meaningful, direct comparisons with PFG NMR. The procedure typically used to simulate this data is currently a computationally intensive process which can take several days to run, with a simulated observation time of the order of picoseconds, at a fixed temperature and molecular loading.

In summary, it is not sensible to exclude the effects of surface contributions when assigning intra-diffusion coefficients to molecules confined in porous media, particularly zeolites, which possess some of the smallest pore geometries in materials typically used as catalysts and support materials (Cheung and Hedin 2014). However, PFG NMR does take this into account and is therefore capable of characterising industrially relevant molecular displacements, despite its limitations. On the one hand, long observation timescales are problematic with respect to limiting molecular displacements to single zeolite crystallites and therefore inter-particle contributions are consequently introduced. On the other hand, guest molecule interactions with zeolite surfaces are an accurate, real world representation of the way in which fluids behave in porous materials. Therefore, one of the advantage of PFG NMR is that its versatility enables intra-diffusion coefficients to be calculated from long-range diffusion regimes which involve significant surface interactions. This strengthens the case that it is a

robust technique which is capable of characterising the vast majority of cases of gaseous transport phenomena in porous materials.

5.5.8. Comparison of crystallite sizes

Typical industrial operations which utilise zeolites involve crystallite sizes which range from hundreds of nanometres to a few microns. This is the case since smaller crystallites are much simpler, and much quicker, to synthesise as they are produced in a continuous process on a production line (Tonetto *et al*. 2004). The zeolite powders are typically used in fluidised beds, whilst they may also be pelletised, with a mechanical press and often with the aid of a binder, in alternative operations for a variety of reasons. These include ensuring an easy manner of retrieving the zeolite for regeneration once it is deactivated post reaction. However, the primary reason is to prevent significant pressure drops over zeolite beds, since the industrial operations in which these materials are used, outlined in section 5.2, occur at elevated temperatures and pressures. Therefore, using zeolites as powders, which have significantly larger surface areas than pellets, is not preferable in certain industrial applications, from a process intensification perspective.

However, for research applications, the use of zeolite powders as opposed to pellets, is of critical importance, as it is vital that molecular dynamics are characterised when the level of confinement of the porous medium is the sole source of resistance to diffusion. It has been shown that the use of binders and other additives to form pellets and aggregate zeolite materials can have a significant impact on a zeolite's transport properties and therefore results in an inaccurate characterisation of a guest molecule's transport phenomena (Mehlhorn *et al*. 2014). Large crystallites are typically synthesised in a batch process at high temperatures and pressures using an autoclave, as described by the Charnell method (Kärger and Ruthven 1992).

The research grade 15 μm β-zeolite crystallites used in this thesis are compared with industrial grade β-zeolite with a crystallite size of 0.5 μm and 0.3 μm. Using 0.2 mol kg^{-1} of methane as the gaseous guest molecule, the long-range diffusion coefficients are in good agreement with one another. Figure 5.19 shows a comparison between the echo attenuation plots of the different crystallite samples.
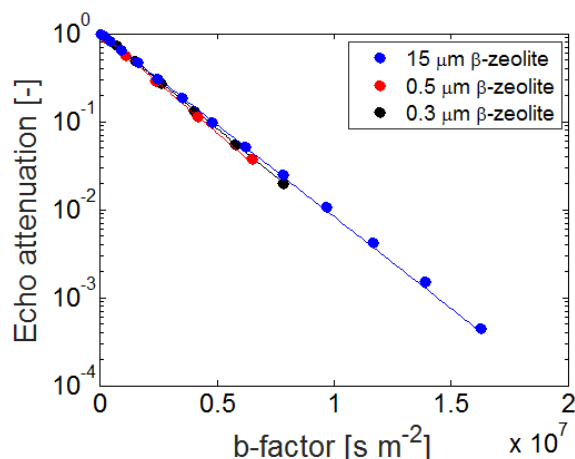
Figure 5.19: Comparison of long-range diffusion coefficients of CH_4 in various β-zeolite crystallites. Loading is 0.2 mol kg^{-1} in each instance. δ = 0.25 ms, Δ = 100 ms and g = 0.001 - 0.36 T m^{-1}.

The intra-diffusion coefficients of methane are also in good agreement with one another, as shown in figure 5.20. This trend is anticipated, since the guest molecules are expected to behave similarly in the confined geometry of a zeolite channel which possesses the same pore size, anisotropic geometry and similar surface chemistries, as shown by elemental XPS analysis studies performed at JMTC. The long-range and intra-diffusion coefficients in the three different crystallite sizes are summarised in table 7.
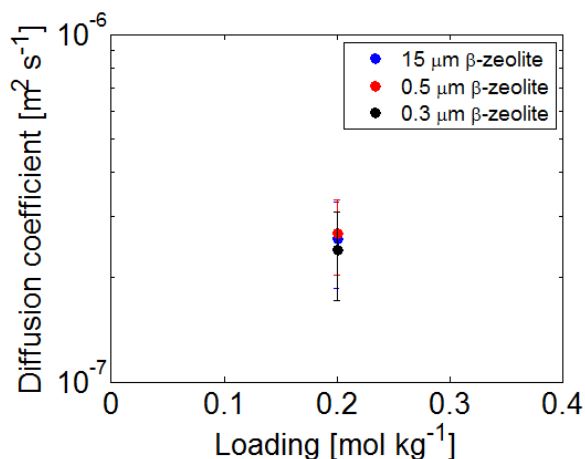
Figure 5.20: Summary of intra-diffusion coefficients of CH_4 in various β-zeolite crystallite sizes. Loading is 0.2 mol kg^{-1} in each instance.

It has been shown in the literature that a range of zeolite crystallites may be used to characterise intra-diffusion coefficients (Kärger *et al*. 1980). However, the results elucidated in this sub-section are obtained using the solely PFG NMR based method described in section 5.5.3. Direct comparisons between intra-diffusion coefficients of identical guest molecules in

different crystallite sizes are made with measured molecular displacements in a fast exchange regime.

Table 7: Summary of molecular loadings, long-range and intra-diffusion coefficients of methane adsorbed in β-zeolites with variable crystallites.

Crystallite size [μm]	Adsorbed phase loading [mol kg^{-1}]	Long-range diffusion coefficient [m^2 s^{-1}]	Intra-diffusion coefficient [m^2 s^{-1}]	Intra RMSD [μm]
15	0.2	$4.8 \pm 0.020 \times 10^{-7}$	$2.6 \pm 0.29 \times 10^{-7}$	228
0.5	0.2	$5.2 \pm 0.002 \times 10^{-7}$	$2.7 \pm 0.24 \times 10^{-7}$	232
0.3	0.2	$5.0 \pm 0.002 \times 10^{-7}$	$2.4 \pm 0.29 \times 10^{-7}$	219

5.5.9. PFG NMR of β-zeolite imbibed in hydrocarbon liquid phase guest molecules

The self-diffusion behaviour of liquid phase guest molecules in the 15 μm β-zeolite is studied to compare the echo attenuation profiles with those obtained from their gas phase counterparts adsorbed in the 15 μm β-zeolite. By preparing the samples in the same manner as described in chapter 4, the 15 μm β-zeolite samples were separately dosed with 0.004, 0.002 and 0.002 mol kg^{-1} of liquid phase octane, nonane and decane respectively (supplied by Sigma Aldrich). Linear chained liquid phase hydrocarbons were selected due to their simplicity with respect to self-diffusion coefficients varying as a function of chain length, and due to the limitations of the zeolite's hydrophobic surface.

As shown in figure 5.21, linear echo attenuation profiles are obtained for each hydrocarbon guest molecule, which implies a Gaussian distribution of measured molecular displacements in the PFG NMR experiments. As is the case with the 15 μm β-zeolite sample which contains 0.26 mol kg^{-1} of propane with an observation time of 3 ms, described in section 5.5.5, this is due to measured molecular displacements that are much smaller than the zeolite crystallite size.
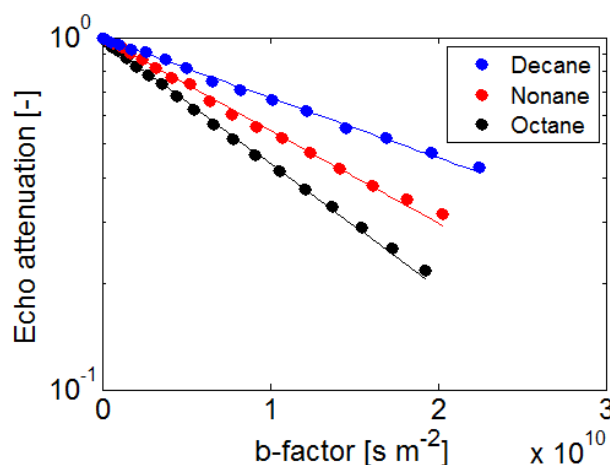
Figure 5.21: Intra-diffusion echo attenuation plots of 15 µm β-zeolite imbibed separately in 0.004 mol kg^{-1} octane, 0.002 mol kg^{-1} nonane and 0.002 mol kg^{-1} decane. δ = 1 ms, Δ = 20 ms and g = 0.05 - 8.2 T m^{-1}.

As summarised in table 8, the *RMSD*s from the intra-diffusion coefficients are all less than 2 µm. Therefore, the use of all three liquid phase guest molecules enables intra-diffusion coefficients to be characterised directly from the fit of the PFG NMR experiments, without utilising the method outlined in section 5.5.3. Therefore, molecular displacements exceeding geometric dimensions of zeolites is typically a gas phase problem, since liquids are slowed down by enhanced adsorption and guest molecule geometry by comparison, and molecular mobility may therefore be confined to single zeolite crystallites. This makes the study of gaseous guest molecules in both small and large crystallites a prudent venture. This is because elevated temperatures and pressures which are used in industrial processes involving zeolites which are of interest to Johnson Matthey typically result in reactant and product molecules existing in the gas phase.

Table 8: Summary of intra-diffusion coefficients of octane, nonane and decane adsorbed in β-zeolite and root mean squared displacements.

Hydrocarbon guest molecule	Intra-diffusion coefficient [m^2 s^{-1}]	RMSD [µm]
C_8H_{18}	$8.3 \pm 0.02 \times 10^{-11}$	1.8
C_9H_{20}	$6.2 \pm 0.03 \times 10^{-11}$	1.6
$C_{10}H_{22}$	$3.8 \pm 0.03 \times 10^{-11}$	1.2

5.6. Conclusions

A solely PFG NMR based method was demonstrated to calculate the single component intra-diffusion coefficients of light aliphatic molecules adsorbed in a 15 μm β-zeolite bed from long-range diffusion coefficients, which are unavoidably obtained using such conventional measurements. Comparisons were made to experimental literature results obtained using PFG NMR and the results were in good agreement. However, the comparisons made to MD simulations were not in good agreement and large deviations in the self-diffusion coefficients were observed as a function of molecular loading due to the differences in experimental and simulated time and length-scales of both techniques.

By conducting a variable observation time experiment, it was possible to characterise non-exchanging, slow and fast exchanging regimes using 0.26 mol kg^{-1} propane adsorbed in β-zeolite. Molecular exchange behaviour using the established Kärger model was not used due to significant differences in the relaxation properties of the inter- and intra-crystalline regions of the zeolite bed.

"Research grade" β-zeolite was compared with "industrial grade" β-zeolite to observe differences in diffusion regimes and to test the validity of the solely NMR based method to calculate intra-diffusion coefficients in real world systems. The long-range diffusion coefficients and the intra-diffusion coefficients of both grades of material were in good agreement with another.

Lastly, liquid phase molecules were adsorbed in the large pore "research grade" β-zeolite, which enabled intra-diffusion coefficients to be characterised directly from a conventional PFG NMR experiment, as the associated molecular displacements did not exceed the size of the zeolite crystallite. Subsequently, linear echo attenuation plots were obtained with single intra-diffusion coefficients for each species.

5.7. References

Bar, N.K., Kärger, J., Krause, C., Schmitz, W., Seiffert, G., (1995). Pitfalls in PFG NMR self-diffusion measurements with powder samples. J. Magn. Reson. Ser. A. 113: 278-280.

Bell, A., (1994). *NMR Techniques in Catalysis.* CRC Press.

Camblor, M.A., Corma, A., Valencia, S., (2008). Characterization of nanocrystalline zeolite beta. Microporous Mesoporous Mater. 25: 59-74.

Cheung, O., Hedin, N., (2014). Zeolites and related sorbents with narrow pores for CO_2 separation from flue gas. RSC Adv. 4: 14480-14494.

Clark, L.A., Ye, G.T., Gupta, A., Hall, L.L., Snurr, R.Q., (1999). Diffusion mechanisms of normal alkanes in faujasite zeolites. J. Chem. Phys. 111: 1209-1222.

Corma, A., Gonzàlez-Alfaro, V., Orchillés, A.V., (1995). Catalytic cracking of alkanes on MCM-22 zeolite. Comparison with ZSM-5 and beta zeolite and its possibility as an FCC cracking additive. Appl. Catal., A. 129: 203-215.

Corma, A., Melo, F.V., Mendioroz, S., Fierro, J.L.G., (2000). *12th International Congress on Catalysis.* Elsevier.

Corma, A., Nemeth, L.T., Renz, M., Valencia, S., (2001). Sn-zeolite beta as a heterogeneous chemoselective catalyst for Baeyer-Villiger oxidations. Nature. 412: 423-425.

Corma, A., (2003). State of the art and future challenges of zeolites as catalysts. J. Catal. 216: 298-312.

Cussler, E.L., (2009). *Diffusion. Mass transfer in fluid systems.* Cambridge University Press.

Delahay, G., Mauvezin, M., Coz, B., Kieger, S., (2001). Selective catalytic reduction of nitrous oxide by ammonia on iron zeolite beta catalysts in an oxygen rich atmosphere: effect of iron contents. J. Catal. 202: 156-162.

Grebenkov, D.S., (2007). NMR survey of reflected Brownian motion. Rev. Mod. Phys. 79: 1077-1137.

Herden, H., Kärger, J., Pfeifer, H., Kube, C., Schöllner, R., (1992). PFG NMR study of self-diffusion of low carbon chain length paraffins in carbonaceous adsorbents. J. Colloid Interface Sci. 152: 281-283.

Kärger, J., Pfeifer, H., Rauscher, M., Walter, A., (1980). Self-diffusion of n-paraffins in NaX zeolite. J. Chem. Soc. Faraday. Trans. 1. 76: 717-737.

Kärger, J., Kočiřik, M., Zikánová, A., (1981). Molecular transport through assemblages of microporous particles. J. Colloid Interface Sci. 84: 240-249.

Kärger, J., Ruthven, D., (1992). *Diffusion in zeolites and other microporous solids*. Wiley & Sons.

Kärger, J., Valiullin, R., (2013). Mass transfer in mesoporous materials; the benefit of microscopic diffusion measurement. Chem. Soc. Rev. 42: 4172-4197.

Krishna, R., (2012). Diffusion in porous crystalline materials. Chem. Soc. Rev. 41: 3099-3118.

Li, S., Zong, Z., Zhou, S.J., Huang, Y., Song, Z., Feng, X., Zhou, R., Meyer, H.S., Yu, M., Carreon, M.A., (2015). SAPO-34 membranes for N_2/CH_4 separation: Preparation, characterisation, separation performance and economic evaluation. J. Membr. Sci. 487: 141-151.

McDaniel, P.L., Coe, C.G., Kärger, J., Moyer, J.D., (1996). Direct observation of N_2 self-diffusion in zeolitic adsorbents using ^{15}N PFG NMR. J. Phys. Chem. 100: 16263-16267.

Mehlhorn, D., Valiullin, R., Kärger, J., Schumann, K., Brandt, A., Unger, B., (2014). Transport enhancement in binderless zeolite-X and A-type molecular sieves revealed by PFG NMR diffusometry. Microporous Mesoporous Mater. 188: 126-132.

Mintova, S., Valtech, V., Onfroy, T., Marichal, C., Knözinger, H., Bein, T., (2006). Variation of the Si/Al ratio in nanosized zeolite beta crystals. Microporous Mesoporous Mater. 90: 237-245.

Mitra, P., Sen, P.N., Schwartz, L.M., (1993). Short-time behaviour of the diffusion coefficient as a geometrical probe of porous media. Phys. Rev. B. 47: 8565-8574.

Neuman, C.H., (1974). Spin echo of spins diffusion in a bounded medium. J. Chem. Phys. 60: 4508-4511.

Namba, S., Hosonuma, N., Yashima, T., (1981). Catalytic Application of Hydrophobic Properties of High-Silica Zeolites. J. Catal. 72: 16-20.

Pampel, A., Engelke, F., Galvosas, P., Krause, C., Stallmach, F., Michel, D., Kärger, J., (2006). Selective multi-component diffusion measurements in zeolites by pulsed field gradient NMR. Microporous Mesoporous Mater. 90: 271-277.

Primo, A., Garcia, H., (2014). Zeolites as catalysts in oil refining. Chem. Soc. Rev. 43: 7548-7561.

Rittig, F., Coe, C.G., Zielinski, J.M., (2002). Predicting gas transport in formed zeolite adsorbents from NMR studies. J. Am. Chem. Soc. 124: 5264-5265.

Rohlf, J.W., (1994). *Modern physics from A to Z^0.* Wiley.

Schwarz, H.B., Ernst, H., Ernst, S., Kärger, J., Röser, T., Snurr, R.Q., Weitkamp, J., (1995). NMR studies of intrinsic diffusion and reaction in CsNaX type zeolites. Appl. Catal. A. 130: 227-241.

Sen, P.N., (2004). Time-dependent diffusion coefficient as a probe of geometry. Concepts Magn. Reson. A. 23A: 1-21.

Sørland, G.H., Hafskjold, B., Herstad, O., (1997). A Stimulated Echo Method for Diffusion Measurements in Heterogeneous Media Using Pulsed Field Gradients. J. Magn. Reson. 124: 172-176.

Sørland, G.H., (2014). *Dynamic Pulsed Field Gradient NMR*. Springer.

Sun, P.Z., Seland, J.G., Cory, D., (2003). Background gradient suppression in pulsed gradient stimulated echo measurements. J. Magn. Reson. 161: 168-173.

Tonetto, G., Atias, J., de Lasa, H., (2004). FCC catalysts with different zeolite crystallite sizes: acidity, structural properties and reactivity. Applied Catal. A. 270: 9-25.

Valiullin, R.R., Skirda, V.D., Stapf, S., Kimmich, R., (1997). Molecular exchange processes in partially filled porous glass as seen with NMR diffusometry. Phys. Rev. E. 55 (3): 2664-2671.

Vasenkov, S., Geier, O., Kärger, J., (2003). Gas diffusion in zeolite beds: PFG NMR evidence for different tortuosity factors in the Knudsen and bulk regimes. Eur. Phys. J. E. 12: 35-38.

Weber, D., Sederman, A.J., Mantle, M.D., Mitchell, J., Gladden, L.F., (2009). Surface diffusion in porous catalysts. Phys. Chem. Chem. Phys. 12:2619-2624.

Zhang, J., Burke, N., Zhang, S., Liu, K., Pervukhina, M., (2014). Thermodynamic analysis of molecular simulations of CO_2 and CH_4 adsorption in FAU zeolites. Chem. Eng. Sci. 113: 54-61.

Zhao, Q., Snurr, R.Q., (2009). Self-diffusion studies of binary mixtures in NaX zeolites using pulsed field gradient NMR and a Maxwell-Stefan Model. J. Phys. Chem. A. 113: 3904-3910.

Chapter 6

Binary NMR spectroscopy, relaxometry and diffusometry in microporous and mesoporous materials

6.1. Introduction

The first section of this chapter details the use of PFG NMR techniques to perform NMR spectroscopy, relaxometry and diffusometry of two-component (binary) gaseous mixtures in the adsorbed and bulk gas phase. The two-component systems studied are methane-ethane and methane-propane mixtures co-adsorbed in a 15 μm β-zeolite bed (introduced in the previous chapter) and the gas phase above the bed. The aim of this section is to demonstrate the characterisation of binary diffusion for molecules co-adsorbed in microporous zeolites systems using PFG NMR. In addition, it is shown that chemical shift resolution is possible in binary methane-ethane systems. Conventional measurements suffer from prohibitive magnetic susceptibility and line broadening effects and are typically incapable of elucidating such effects (Sørland 2014). Examples of chemical shift resolution for both gaseous and adsorbed phase molecules are shown for binary methane-ethane systems, whereby it is also possible to characterise the diffusion and relaxation properties of the individual species. The intra-diffusion coefficients of the methane-ethane systems are obtained using the method introduced in chapter 5, whereby long-range diffusion regimes are dominant in most instances. Long-range diffusion coefficients for methane-propane systems co-adsorbed in β-zeolite are also presented. However, it is not possible to calculate any associated intra-

diffusion coefficients or to obtain sufficient chemical shift resolution of methane and propane in the adsorbed phase due to excessive spectral line broadening.

The final section of this thesis briefly deals with binary, ^{1}H-^{2}H NMR to compare the relaxation times of these (spin-half and quadrupolar) nuclei, which adhere to different relaxation mechanisms. The main aim of this section is to conduct relaxometry experiments to observe improvements in the T_2 relaxation times of deuterated molecules in comparison to their protonated isotopes, which are of interest to Johnson Matthey. This will enable better Signal-to-Noise Ratios (SNRs) to be obtained in a sensible timeframe in future ^{2}H PFG NMR experiments. Longer T_2 relaxation time constants also enable increases in signal attenuation to be observed in future diffusometry experiments. This is because the echo times of PFG NMR pulse sequence can be lengthened, which will allow longer gradient pulse durations to be selected. This is of particular relevance to systems involving ammonia strongly adsorbed in small pore chabazite structures, which will be discussed further in chapter 7.

6.2. Background

Conventional industrial operations which rely on the use of microporous materials in chemical reactions, separation and drying processes often involve the presence of multiple phases and species in the porous network. Therefore, the ability to characterise the molecular dynamics of such environments is particularly pertinent with respect to improving insights into the chemical kinetics and longevity of porous materials in real world applications. It is extremely difficult to analyse the fluid behaviour of multiphase systems in porous media due to limitations of the sorbate molecules used in this study and in the experimental hardware. Nonetheless, PFG NMR is a powerful tool which is capable of investigating the transport behaviour of methane-ethane and methane-propane mixtures with remarkable accuracy.

The use of PFG NMR to chemically resolve different environments and diffusion coefficients of multi-component systems has been widely discussed in the literature (Snurr and Kärger 1997; Acosta *et al*. 2006). Chemical shift resolution is possible in bulk gas and liquid phase systems, since the T_2^* relaxation time constants of such environments are sufficiently long: up to 2.5 milliseconds, as spectral linewidths of 20 Hz are attainable. This therefore enables peak

separation of chemically similar molecules. Diffusion Ordered Spectroscopy (DOSY) has been used in such instances, whereby the signals emanating from mixtures of molecules which differ in size may be separated based on their self-diffusion coefficients to generate a diffusion domain of DOSY spectra (Morris and Johnson 1992; Morris and Barjat 1997). Such techniques have been shown to act as powerful characterisation tools in complex multicomponent mixtures, although the caveat for accurately utilising this method in most instances is dependent on well-shimmed, narrow spectral linewidths. Glass wool is typically inserted in sample tubes containing such mixtures, which successfully combats the effects of convection which is a relevant problem in elevated temperature measurements of bulk liquids. However, this has been shown to have a sufficiently detrimental impact which prohibits the use of such spectroscopic methods to chemically resolve complex mixtures of liquids, due to enhanced spectral line broadening (Swan *et al*. 2015).

The enhanced line broadening observed due to significant magnetic susceptibility effects typically prevents the observation of such chemical shift resolution in heterogeneous systems, such as fluids adsorbed in zeolites, using conventional PFG NMR. Spectral linewidths of gaseous guest molecules in such confined conditions may exceed 1000 Hz, which will be discussed further in chapter 7. This therefore results in significant peak overlap, thereby preventing the differentiation of varying chemical environments, in a spectroscopic sense. However, it is possible to obtain separate self-diffusion coefficients and relaxation parameters for chemically diverse components using conventional PFG NMR measurements despite this obstacle, as shown in section 6.4, and as demonstrated in the literature, for up to eight co-adsorbed species (Stilbs 1987). As proposed in the literature and as shown in figure 6.1, Magic Angle Spinning (MAS) has been employed to reduce spectral linewidths and to remove line broadening artefacts (Pampel *et al*. 2005). However, it was not possible to replicate such experiments as it pertains to the work discussed in this thesis, due to the scarcity of available combined MAS PFG NMR hardware.
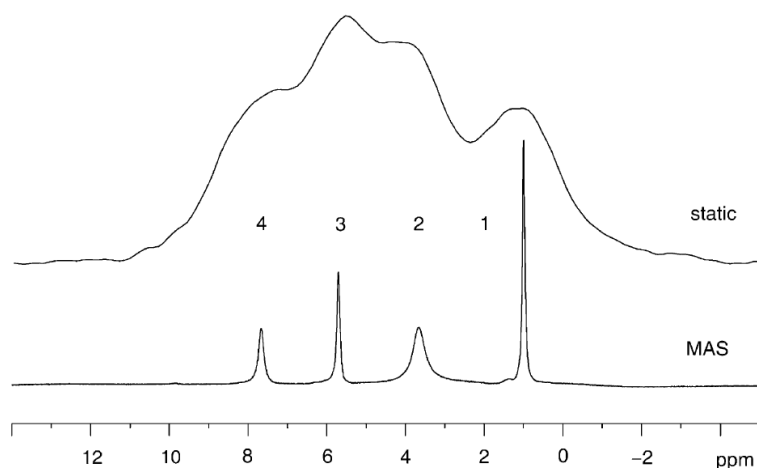
Figure 6.1: ^{1}H NMR spectra of variable pressure ethane (1, 3), water (2) and benzene (4) adsorbed in zeolite NaX at 400 MHz (static) and with MAS (Pampel *et al*. 2006).

Chapter 4 showed the modifications that were made to the Alternating Pulsed Gradient Stimulated Echo (APGStE) pulse sequence to achieve an improvement in the SNRs of PFG NMR measurements of molecules confined in zeolite systems, where this is a significant issue. Whilst such improvements were observed, reducing the delay times in the PFG NMR pulse sequence placed hardware instruments under strain because of the high maximum gradient strength required to achieve adequate signal attenuation. Additionally, limitations were also present with respect to increasing observation times to obtain increased signal attenuations, which will be discussed further in chapter 7. Therefore, the ideal scenario is to conduct experiments with systems which possess long T_1 and T_2 relaxation times, thereby allowing longer observation and echo times to be selected in the pulse sequence respectively, to prevent relaxation times from significantly hindering diffusometry. The manner in which non spin-half (quadrupolar) nuclei may be used to observe such improvements, as well as improvements in experimental time frames of which examples are shown in section 6.5, has also been described in the literature. This is because line broadening and relaxation time constants typically scales with magnetic susceptibility, for identical relaxation mechanisms (Callaghan 1993).

6.3. Methods and materials

6.3.1. Gas and adsorbed phase PFG NMR experiments

All PFG NMR experiments were performed using a Bruker BioSpin DMX spectrometer operating at a ^{1}H resonance frequency of 300.13 MHz with a 5 mm radiofrequency (r.f.) coil fitted to a PFG probe head, which was placed inside a cryo-magnet. All measurements were taken at 294 K, with a precision of ± 1 K. In each instance, 0.05g and 0.09 g of the 11 μm chabazite and 15 μm β-zeolite powder was used respectively. The modified version of the APGStE pulse sequence introduced in chapter 4, was used in each PFG NMR experiment. All error bars were obtained from the standard deviation of three repeats on the same sample. All relaxometry experiments were conducted using a 2D T_1-T_2 pulse sequence, with an echo time of 1 ms and a maximum inversion time delay of 5 s, with 16 points in the time delay lists. 16 and 8 scans were used in the protonated and deuterated experiments respectively. Table 1 shows a summary of the PFG NMR parameters used for the gas phase and adsorbed phase regions in the sealed tube.

Table 1: Summary of the PFG NMR parameters for the gas and adsorbed phase regions in the sealed tube.

PFG NMR parameters	Gas phase above bed	Adsorbed phase in bed
Observation time [ms]	4	100
Gradient strength [T m^{-1}]	0.001 - 0.7	0.001 - 6.2
Gradient pulse duration [ms]	0.3	0.3
Gradient ramp time [ms]	0.2	0.1
90° pulse [μs]	13	12
Recycle time [s]	15	2
Number of scans [-]	64	128
Number of points [-]	16	16

Data obtained from the PFG NMR experiments discussed in this chapter were fitted to the single component exponential decay model introduced in chapter 4 and can be expressed as (Sørland *et al.* 1997):

$$\Psi = \sum_{i=n}^{n} p_i \, exp\left[-\gamma^2\delta^2 D_i\left(\Delta + \frac{3}{2}\tau - \frac{\delta}{3}\right)g^2\right] + \left(\Delta + \tau - \frac{\delta}{3}\right)f^2(\Delta + \tau)gf$$
$$+ \delta(\delta_1 - \delta_2)\tau(f + g)G_0 + \frac{4}{3}\tau^3 G_0{}^2$$

6.1

where Ψ is the echo attenuation [a.u.], γ is the ^{1}H gyromagnetic ratio [rad s^{-1} T^{-1}], g is the gradient strength with an amplitude ratio of 1 [T m^{-1}], f is the gradient strength with an amplitude ratio of 1 [T m^{-1}], δ is the gradient pulse width [s], G_0 is the constant, background gradient which is present in the sample [T m^{-1}] and Δ is the observation time [s]. The solid lines in the PFG plots in this chapter are fitting the data to equation 6.1. As mentioned in the previous chapter, the delay times either side of the gradient pulses, δ_1 and δ_2, were set to 50 and 201.25 µs respectively, in a bid to minimise the overall echo time in the pulse sequence (Sun *et al.* 2003). The echo times of the PFG NMR experiments discussed in this chapter did not exceed 3 ms. Since an additional element of asymmetry in terms of the pulse sequence delay times was introduced, the cross-magnetisation term arising due to background field gradients was considered. By running a PFG NMR experiment, a persistent background signal was observed in the sample. Therefore, similar to the data in chapter 5, the mean of the last three points was subtracted from the total echo attenuation to account for this.

6.3.2. Gas and liquid phase relaxometry experiments

Table 2 shows a summary of the parameters used in the relaxometry experiments shown in section 6.5.

Table 2: Summary of the parameters used in the T_1-T_2 experiments.

Relaxometry parameters	Value
Maximum inversion time [s]	4
Echo time [ms]	1
Number of echoes [-]	128
90° pulse duration [μs]	8
Recycle time [s]	4
Number of scans [-]	16
Number of points [-]	16

6.3.3. Chemicals and zeolites

The purity and origin of the materials used are shown in table 3. Each sample was used as received.

Table 3: Summary of materials used in this discussed in this chapter.

Material	Purity (%)	Origin
CH_4	99	BOC
CD_4	99	Sigma Aldrich
C_2H_6	99.99	Air Liquide
C_3H_8	99.99	BOC
H_2O	99.99	Sigma Aldrich
D_2O	99.99	Sigma Aldrich
Tetra Methyl Silane (TMS)	99.5	Sigma Aldrich
15 μm β-zeolite	-	Tosoh Corporation *via* Johnson Matthey, United Kingdom
11 μm chabazite	-	Johnson Matthey, United Kingdom
γ-alumina pellets, 20 nm pore size	-	Johnson Matthey, United Kingdom

6.3.4. Sample preparation

All gaseous guest molecules were adsorbed onto the zeolite powders using the sample preparation method outlined in chapter 4, and the loadings were determined using the procedure outlined therein. In the case of the co-adsorbed species, the weaker sorption molecule was the first to be adsorbed into the zeolite bed. Differences in the number of protons in all binary systems were accounted for in order to make a meaningful comparison between molecules with varying numbers of protons. All ethane and propane signals were multiplied by 4/6 and 4/8 respectively. The pressures and corresponding loadings of the gaseous guest molecules discussed in this chapter are summarised in tables 5 and 6, which also include a summary of each associated long-range and intra-diffusion coefficient, where applicable. The water guest molecules adsorbed on the mesoporous γ-alumina pellets were prepared by submerging the pellets in water for a period of 24 hours. The pellets were subsequently dried using paper towels to remove excess moisture on the surface of the pellets and transferred to a 5 mm NMR tube, which was capped and sealed with Parafilm[®] M.

6.4. PFG NMR results and discussion

6.4.1. Binary ^{1}H methane-ethane relaxation and diffusion above and in β-zeolite beds

As shown in figure 6.2, chemical shift resolution was possible for the gas phase binary methane-ethane systems above the zeolite beds, since the T_2^* relaxation times were of the order of several milliseconds for both species. As such, each peak was integrated separately in the relaxometry and diffusometry experiments and individual T_1 and T_2 relaxation times were obtained.
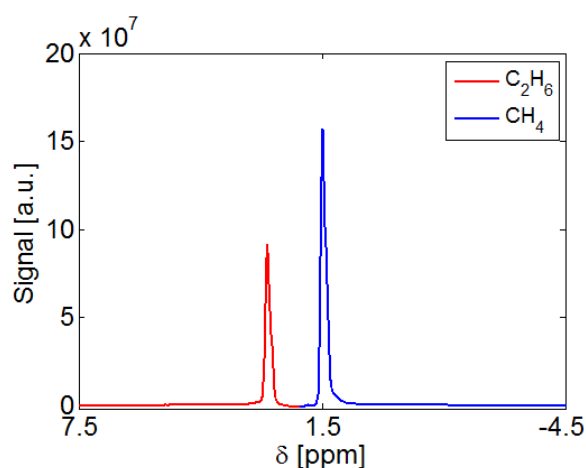
Figure 6.2: Binary ^{1}H spectrum of 0.54 bar CH_4 and 0.25 bar C_2H_6 above a β-zeolite bed.

Additionally, two self-diffusion coefficients, 2.6×10^{-6} m^2 s^{-1} and 1.8×10^{-6} m^2 s^{-1}, corresponding to methane and ethane respectively, were obtained from the PFG NMR experiment. Figure 6.3 shows the echo attenuation plot for each species.
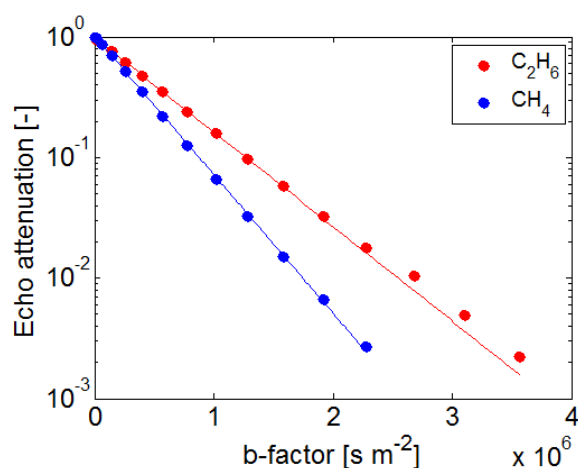

Figure 6.3: Echo attenuation plot of binary 0.54 bar CH_4 and 0.25 bar C_2H_6 above β-zeolite bed.

$δ$ = 0.25 ms, $Δ$ = 4 ms and g = 0.001 - 0.40 T m^{-1}.

Table 4 – Summary of typical relaxation times and self-diffusion coefficients of gas phase methane-ethane.

Binary sample	T_1 [ms]	T_2 [ms]	D [m^2 s^{-1}]
CH_4	144 ± 1	36 ± 1	2.6 ± 0.01 × 10^{-6}
C_2H_6	567 ± 3	46 ± 1	1.8 ± 0.40 × 10^{-6}

As mentioned in section 6.2, the ability to chemically resolve two different, albeit similar, species has been illustrated in the literature for both gaseous and liquid phase probe

molecules using DOSY. Methane and ethane were selected for investigating two-component transport in microporous materials due to their narrow peak linewidths in the bulk gas phase, 26 Hz and 20 Hz respectively, in the hope of obtaining a similar degree of peak separation in heterogeneous systems. The linewidths of liquid phase hydrocarbon guest molecules such as octane adsorbed in β-zeolite typically exceed 1000 Hz on a 300 MHz NMR spectrometer. This is due to an enhancement in adsorption and therefore magnetic susceptibility effects in comparison to gas phase hydrocarbons adsorbed in β-zeolite, which therefore prevents unique species identification. The same conundrum applies to small pore systems, whereby considerably enhanced levels of confinement results in (increasingly) significant background gradient effects. This therefore results in short T_2^* relaxation times which prohibitively broaden the peak widths of the species under investigation to a similar extent, for both gaseous and liquid phase guest molecules alike.

It was possible to chemically resolve binary methane-ethane samples co-adsorbed in β-zeolite, in both the pulse acquire, relaxometry and diffusometry experiments. Figure 6.4 shows that chemical shift resolution was possible for pressures of 0.17 bar and 0.04 bar methane and ethane co-adsorbed in β-zeolite respectively. The gas sorption isotherms shown in chapter 5 enabled a rough estimation to be made with respect to selecting appropriate sorption pressures during the sample preparation stage. In each instance, a methane pressure which sufficiently exceeded that of ethane was selected in order to prevent the signal of the former from becoming engulfed by the latter. While there was a slight degree of peak overlap, both species were clearly directly identifiable without the need for performing peak deconvolution and/or further peak analysis. The individual linewidths of 75 Hz and 90 Hz for methane and ethane respectively adsorbed in β-zeolite compared well with their single component counterparts, introduced in chapter 5.
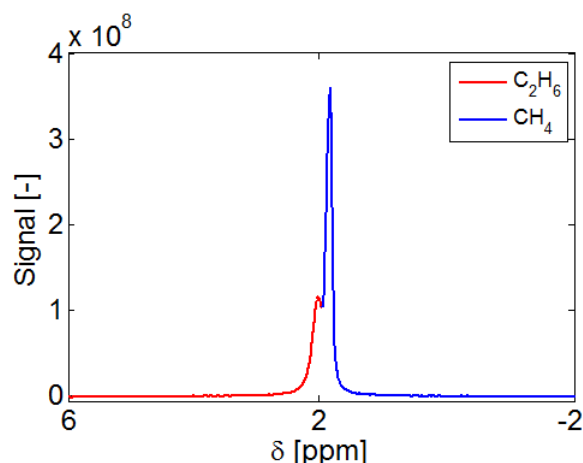
Figure 6.4: Binary ^{1}H spectrum of 0.17 bar CH_4 and 0.04 bar C_2H_6 adsorbed in β-zeolite.

Three separate binary methane-ethane samples co-adsorbed in β-zeolite, sufficiently differing in adsorbed pressures, were selected for PFG NMR analysis. It was possible to obtain the different relaxation times and self-diffusion coefficients of both species in each instance, by integrating over the full width of the peaks and fitting the data to two-component fits in each instance. The spectral attenuation profile from the diffusometry experiment is shown in figure 6.5 and illustrates that methane (blue) typically attenuated at 0.2 T m^{-1} in each instance, compared to 3.6 T m^{-1} for ethane (red). The echo attenuation plots in figure 6.6 show two-component molecular displacement behaviour, whereby the more mobile species, methane, attenuates more quickly than ethane.

Figure 6.6 also shows that the x-coordinates, which give an indication of the order of magnitude of the long-range diffusion coefficients, of the methane echo attenuation are typically two orders of magnitude lower than ethane in β-zeolite in the binary system. This means that the long-range diffusion coefficients of methane were faster than that of ethane, which was expected. The differences in the long-range diffusion coefficients can be explained by the gas sorption isotherms, shown in chapter 5. Since ethane adsorbed more strongly to the zeolite surface, its long-range diffusion coefficient was slowed down by adsorption to a greater extent and as such it was less mobile. Methane in contrast was able to move in between the zeolite's unit cells with a greater degree of freedom. This was the case since it was an even poorer sorbate molecule which was easily displaced by larger and more strongly adsorbing molecules. Therefore, its long-range diffusion coefficient was not slowed down by adsorption by comparison. Hence, increasing the hydrocarbon chain length resulted in

reduced molecular mobility due to both enhanced steric and sorption effects, which is well established in the literature (Bell 1994).
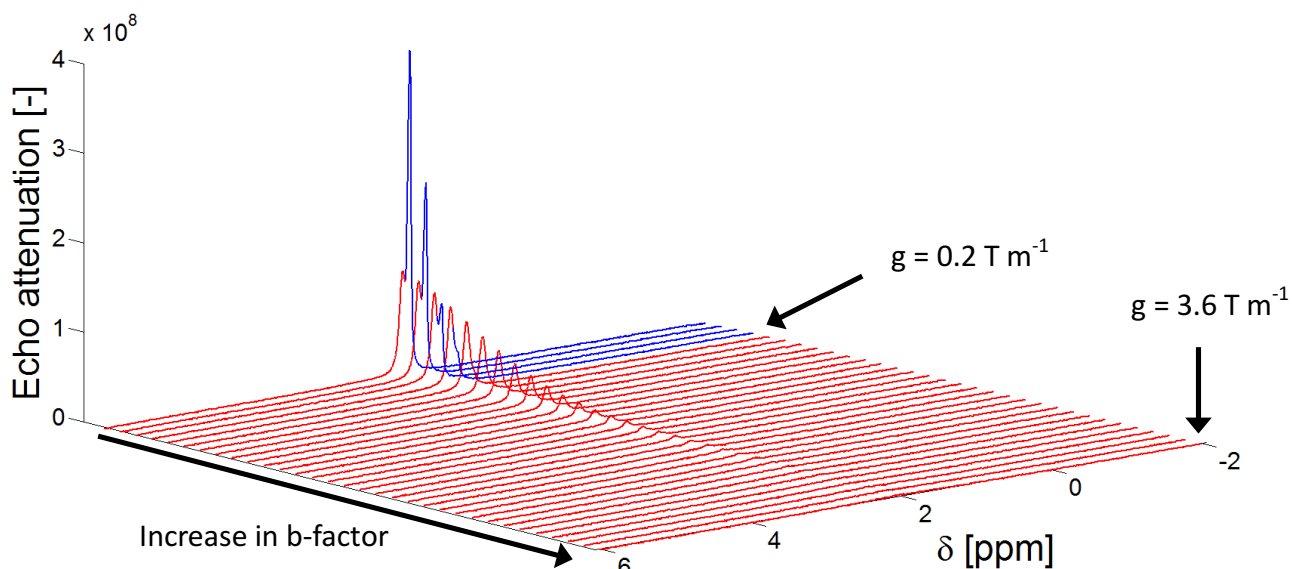

Figure 6.5: Spectral attenuation of β–zeolite imbibed in 0.17 bar methane (blue) and 0.04 bar ethane (red) with increasing b-factor values in a PFG NMR experiment. δ = 0.25 ms, Δ = 100 ms and g = 0.001 - 3.6 T m^{-1}.

In cases such as this, where there is competitive adsorption between two species with different sorption properties confined in a porous material, the preferential adsorption of one molecule over another can have a significant impact on the self-diffusion coefficients of both species. Therefore, this stresses the importance of incorporating adsorption into molecular displacement studies, experimental or simulation centric, which characterise self-diffusion coefficients as emphasised in chapter 5. Similar to the results shown in chapter 5, the long-range and intra-diffusion coefficients of both species decreased with increasing pressure. The intra-diffusion coefficients were determined using the solely PFG NMR based method introduced in the aforementioned chapter. The Root Mean Squared Displacements (*RMSD*s), ranging from 41 - 210 μm, exceeded the crystallite size of the zeolite. Therefore, an increase in the long-range diffusion coefficients was observed in both species with decreasing pressure, as molecular mobility as a function of loading was dictated by the inter-particle populations. With increasing pressure, the calculated intra-diffusion coefficients of ethane decreased to a greater extent in comparison to its long-range counterpart. This implies that increased adsorption in the zeolite's geometry dampened molecular displacements with increasing molecular loading. The *RMSD*s stemming from the intra-diffusion coefficients of

ethane also exceeded the crystallite geometry. However, the inter-particle weighting effect was countered to an extent by molecular adsorption, since ethane had a greater affinity towards the zeolite surface, in comparison to methane.
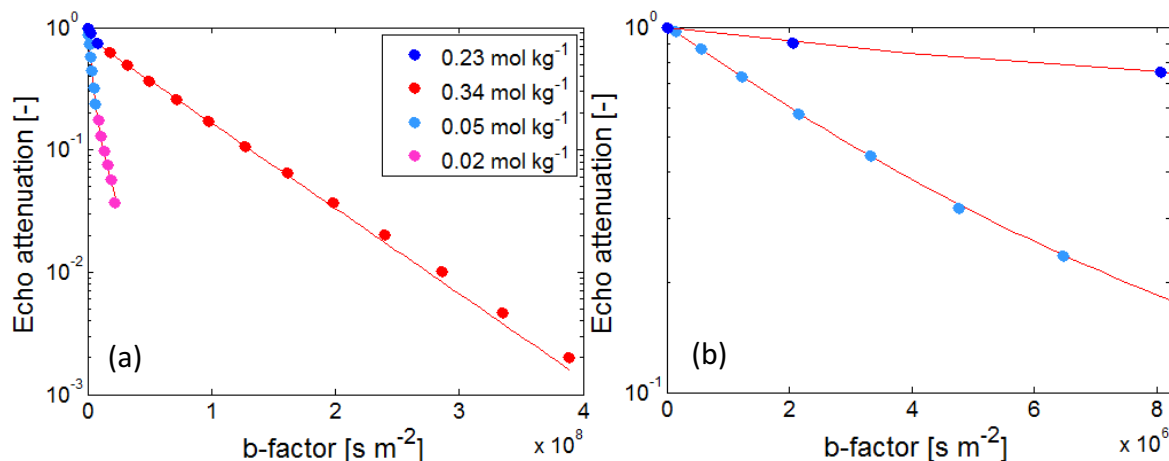

Figure 6.6: Long-range diffusion echo attenuation plot of: (a) binary methane-ethane adsorbed in β-zeolite and (b) focusing on the CH_4 attenuation. Loadings of each species are represented as follows: cool colours = methane, warm colours = ethane. δ = 0.25 ms, Δ = 100 ms and g = 0.001 - 0.78 T m^{-1}.

This was not the case with methane, which was the poorer sorbate molecule, as both the long-range and intra-diffusion coefficients did not vary significantly with molecular loading. This is because methane was displaced by ethane and therefore it was not impeded by adsorption. Reductions in the long-range and intra-diffusion coefficients of methane were observed due to a decrease in the mean free path for diffusion, which was caused by the presence of the adsorbed ethane molecules. Thus, the presence of methane did not influence the molecular displacements of ethane, whilst the presence of ethane affected the molecular displacements of methane. Figure 6.7 shows the changes in the intra-diffusion coefficients of methane and ethane co-adsorbed in β-zeolite as a function of molecular loading, with a summary shown in table 5.
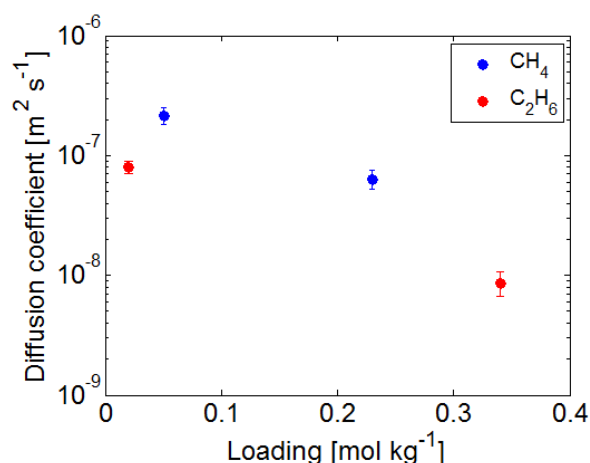
Figure 6.7: Intra-diffusion coefficients of CH_4 and C_2H_6 co-adsorbed in β-zeolite.

Table 5: Summary of the pressures, loadings and long-range and intra-diffusion coefficients of binary methane and ethane mixtures co-adsorbed in β-zeolite. As a comparison, the bulk gas phase CH_4 and C_2H_6 self-diffusion coefficients range from 10^{-6} - 10^{-5} m^2 s^{-1}.

Binary system	Pressure [mbar]	Loading [mol kg^{-1}]	D_{long} [m^2 s^{-1}]	D_{intra} [m^2 s^{-1}]
CH_4	421	0.23	$1.1 \pm 0.002 \times 10^{-7}$	$6.4 \pm 0.18 \times 10^{-8}$
C_2H_6	331	0.34^a	$1.6 \pm 0.040 \times 10^{-8}$	$8.6 \pm 0.22 \times 10^{-9}$
CH_4	86	0.05	$3.6 \pm 0.030 \times 10^{-7}$	$2.2 \pm 0.16 \times 10^{-7}$
C_2H_6	20	0.02	$9.8 \pm 0.020 \times 10^{-8}$	$8.0 \pm 0.12 \times 10^{-8}$

a.   *corresponds to 1 molecules per cavity*

The intra-diffusion coefficients of binary ethane (1.5 molecule per cavity) and ethylene (1 molecule per cavity) in NaX, with a crystallite size of 60 μm, at 293 K were reported in the literature as $4.6 \pm 0.9 \times 10^{-9}$ m^2 s^{-1} and $1.3 \pm 0.3 \times 10^{-9}$ m^2 s^{-1} respectively (Hong and Kärger 1991). Due to significant line broadening, the signals from both species were reconstructed in the PFG NMR experiment to characterise the two components separately. The ^{1}H resonance frequency was reported at 90 MHz, the maximum gradient amplitude used was 2.8 T m^{-1}, with a gradient pulse width ranging from 0.1 - 0.6 ms and an observation time ranging from 2 - 15 ms. The intra-diffusion coefficients reported in the literature were lower than those reported in this thesis, since the former involved higher molecular loadings. With that in mind, the intra-diffusion coefficients appear to be sensible in comparison.

6.4.2. Binary ^{1}H methane-propane diffusion above and in β-zeolite beds

Similar to the gas phase methane-ethane mixture, gas phase methane-propane mixtures were separated in pulse acquisition, diffusometry and relaxometry experiments with comparable ease. Figures 6.8 and 6.9 show an example of a binary gas phase methane-propane spectrum and an echo attenuation plot for 0.11 bar methane and 0.03 bar propane.
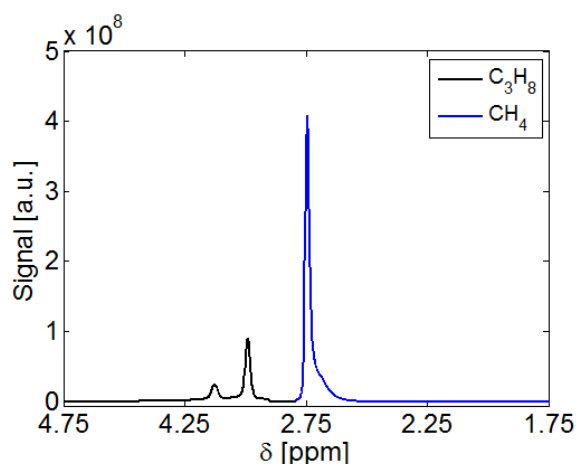
Figure 6.8: Binary ^{1}H spectrum of 0.11 bar CH_4 and 0.03 bar C_3H_8 above a β-zeolite bed.

From the PFG NMR experiments, the self-diffusion coefficient for CH_4 was 3.7×10^{-6} m^2 s^{-1} and 1.7×10^{-6} m^2 s^{-1} for C_3H_8.
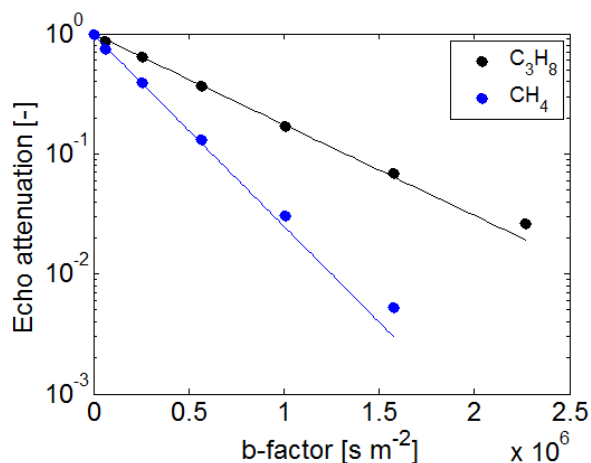
Figure 6.9: Echo attenuation plot of binary 0.11 bar CH_4 and 0.03 bar C_3H_8 above a β-zeolite bed. δ = 0.25 ms, Δ = 4 ms and g = 0.001 - 0.7 T m^{-1}.

However, as shown in figure 6.10, it was not possible to separate the adsorbed phase methane and propane peaks by their chemical shifts in the pulse acquisition experiments in the same manner as the co-adsorbed methane-ethane mixtures. This was due to significant

peak overlap, as the linewidth of propane (853 Hz) was significantly broader than that of ethane (582 Hz), at a similar loading of approximately 0.26 mol kg^{-1}.
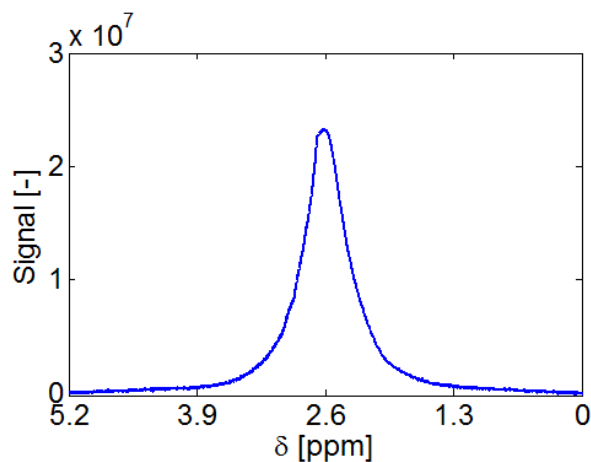
Figure 6.10: Unresolvable ^{1}H spectrum of binary methane-propane co-adsorbed in β-zeolite.

The same trends were observed for the long-range diffusometry experiments, whereby the more strongly adsorbing component, propane, had a slower self-diffusion coefficient in comparison to the weaker sorbate, methane. Figure 6.11 shows the echo attenuation plots for the binary methane-propane mixtures co-adsorbed in β-zeolite, with a summary of the long-range diffusion coefficients shown in table 6.
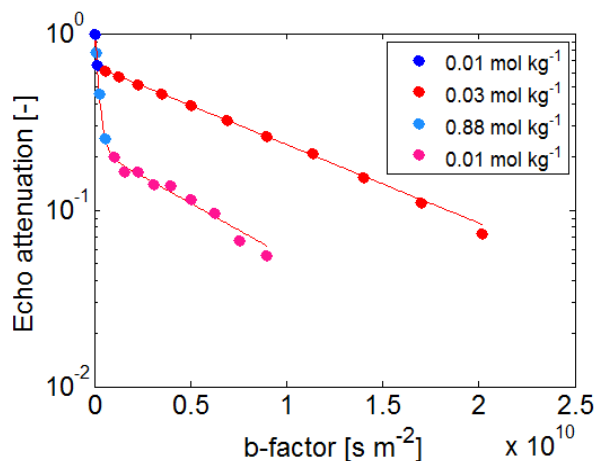
Figure 6.11: Long-range diffusion echo attenuation plots of binary methane-propane co-adsorbed in β-zeolite. The adsorbed loadings of each species are represented as follows: cool colours = methane, warm colours = propane. δ = 0.25 ms, Δ = 100 ms and g = 0.001 - 6.2 T m^{-1}.

Table 6 - Summary of adsorbed loadings and long-range diffusion coefficients of binary methane-propane mixtures co-adsorbed in β-zeolite. As a comparison, the bulk gas phase CH_4 and C_3H_8 diffusion coefficients range from 10^{-7} - 10^{-5} m^2 s^{-1}.

| Binary system	Pressure [mbar]	Loading [mol kg^{-1}]	D_{long} [m^2 s^{-1}]
CH_4	20.6	0.01	$1.0 \pm 0.01 \times 10^{-6}$
C_3H_8	28.2	0.03	$1.1 \pm 0.02 \times 10^{-10}$
CH_4	1600.5	0.88	$3.1 \pm 0.01 \times 10^{-9}$
C_3H_8	12.3	0.01	$1.7 \pm 0.10 \times 10^{-10}$

6.5. ^{1}H and ^{2}H NMR in porous materials

As discussed in chapters 4 and 5, guest molecules adsorbed in both large and small pore zeolites, regardless of their phase or affinity to the solid material surface, suffer from short T_2 times, ranging from hundreds of microseconds to a few milliseconds. Additionally, the T_2^* relaxation times of these guest molecules in small pore zeolites are as short as 40 μs. The consequence of this is that SNRs are typically rather poor in PFG NMR experiments. Therefore, examples of the typical requirements for such room temperature measurements conducted at a fixed field strength include using a large volume of sample and/or a large number of scans. The former is limited by the design pressure of the standard NMR tube, since the gas pressure above the bed cannot exceed 1.6 bar. This is because the zeolite bed will typically occupy approximately 20% of the total tube height in each instance, which limits the amount adsorbed on the zeolite bed during the sample preparation stage. Additionally, using a larger amount of zeolite powder volume does not solve this problem, since the zeolite bed height that is used, approximately 12 mm in height, occupies the full window of the active region of the r.f. coil. Additionally, introducing more zeolite powder into the tube will in turn reduce the volume of the unoccupied space above the bed. This therefore reduces the maximum allowable gas pressure in this region even further, which subsequently limits the adsorption pressure once again. A proposed solution to this is to use an NMR active nucleus such as deuterium which has been shown to possess a longer T_2 and T_2^* relaxation times. Bulk H_2O

and D_2O were compared in the literature, as it is thought that the molecular tumbling relaxation mechanisms of these liquids are similar to one another (Callaghan 1993).

The main objective of this study is to investigate whether longer T_2 relaxation times of the deuterated isotopes of the species discussed in this thesis can be observed and thus improve SNRs and reduce experimental acquisition times. This will enable longer echo times and longer gradient pulse durations to be selected in future PFG NMR experiments, to achieve increased signal attenuation. This is of particular relevance in cases where hardware limitations prevent complete signal attenuation to be observed, as is the case with ammonia adsorbed in small pore chabazite structures, which will be described in chapter 7. As shown in chapter 5, weakly adsorbing ^{1}H gaseous guest molecules confined in large pore zeolites are capable of attenuating completely within the measurement's capabilities and possess T_2 relaxation times which do not place a significant strain on the measurement hardware. Therefore, the investigation of such deuterated analogues is not required for such gaseous systems.

Protonated guest molecules were compared with their deuterated counterparts at similar loadings to observe differences in T_1 and T_2 relaxation times. The rationale for selecting these nuclei can be explained by the differences in their gyromagnetic ratios, and the associated equations related to spectral linewidths, relaxation times and magnetic susceptibility:

$$\frac{1}{T_2} = \frac{1}{T_2^*} + \gamma B_0 \qquad\qquad 6.2$$

$$\Delta v = \frac{1}{\pi T_2^*} \qquad\qquad 6.3$$

where γ is the gyromagnetic ratio [rad s^{-1} T^{-1}], B_0 is the magnetic field strength [T] and Δv is the spectral linewidth [Hz]. Thus, when subjected to identical magnetic fields, nuclei with smaller gyromagnetic ratios are expected to have longer T_2 and T_2^* relaxation time constants compared to nuclei with larger gyromagnetic ratios. The gyromagnetic ratio of the ^{2}H nucleus is approximately 6.5 times smaller than the ^{1}H nucleus: 0.41×10^8 rad s^{-1} T^{-1} compared to 2.68×10^8 rad s^{-1} T^{-1}. Hence, once the samples are placed in a magnet with a field strength of 7.1 T, the detection frequency is 46.4 MHz for the ^{2}H nucleus and 300 MHz for the ^{1}H nucleus, as introduced in chapter 2.

On the one hand, replacing conventional, protonated liquid reactants with deuterated solvents may be discouraged in some transient industrial operations which attempt to characterise diffusion limited steps in real-world chemical reactions. This is due to the differences in the physical properties of isotopic molecules. Another drawback to using deuterated guest molecules on an industrial scale is associated with material costs, which are significantly higher in comparison to protonated feedstock.

Whilst in some cases a short T_2 relaxation time implies that the sample is also likely to have a short T_1 relaxation time, although there are some exceptions to this, rapid signal averaging may be performed in such instances. One of the main aims of this project is to transfer this technique to lower magnetic field industrial spectrometers, which will be introduced in chapter 8. Therefore, this aspect is particularly desirable as lengthy experimental time frames are not preferable for off-line measurements.

6.5.1. Results and discussion

Preliminary tests were conducted using H_2O and D_2O in mesoporous alumina pellets. This system was selected due to the simplicity associated with the sample preparation stage, and the material's uniform pore hierarchy.

Pulse acquisition, T_1 inversion recovery and T_2 CPMG experiments were conducted with both nuclei. Each experiment was repeated three times. As shown in figure 6.12, the linewidth of the deuterated guest molecule was narrower by approximately a factor of seven, compared to the protonated guest molecule. Whilst this factor was slightly larger than the ratio of the gyromagnetic ratios of the nuclei studied, it was within experimental error.
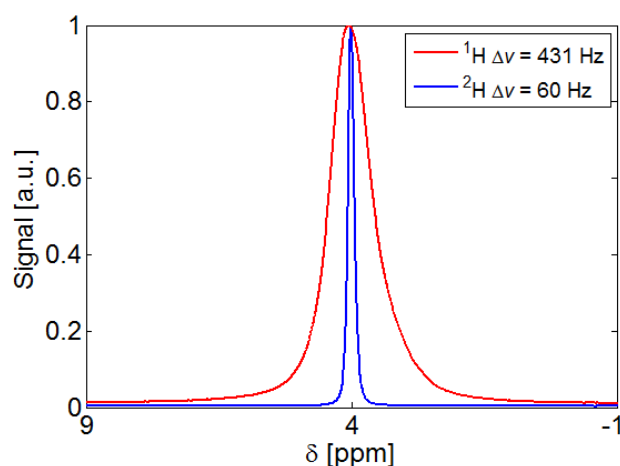
Figure 6.12: Comparing the linewidths of (referenced) ^1H and (unreferenced) ^2H spectra of water.

The T_1 and T_2 relaxation times also followed the trend described in the literature, as summarised in table 7 (Callaghan 1993):

Table 7 - Summary of linewidths and relaxation times of both nuclei.

Liquid in alumina pellets	Linewidth [Hz]	T_1 [ms]	T_2 [ms]	T_2^* [ms]
H_2O	431	1565 ± 1	6 ± 1	0.12
D_2O	60	473 ± 1	32 ± 1	0.84

Therefore, since the results for this model system were promising, guest molecules and porous materials of interest to Johnson Matthey were compared with their deuterated isotopes in a bid to observe similar improvements:

i.   Bulk CH_4 and CD_4 (1000 mbar of each isotope).

ii. CH_4 and CD_4 in chabazite (91 and 85 mbar of each isotope respectively).

It has been shown that the sorption profiles of gaseous protonated and deuterated molecules in microporous materials are similar to one another. Hence, adsorption and/or surface interactions were assumed to be similar for both isotopes used in this thesis (Kawamura *et al*. 2008; Chu *et al*. 2015). There was a slight difference in the pressures of the adsorbed methane analogues in chabazite, due small differences in sample tube heights. The relaxation times of both protonated and deuterated species, along with their respective probability distributions, are represented in the form of 2D T_1-T_2 plots. The data for these plots were obtained by simultaneously performing T_1 inversion recovery and T_2 CPMG measurements, as introduced in chapter 2. These plots are used only as a means to qualitatively display the relaxation times

of the two gases by showing differences in relaxation times, rather than drawing any meaningful comparisons between the proportions by which these times vary. In addition, these plots are not used to compare molecular interaction behaviour with the zeolite surface, which has been proposed in the literature for alternative porous materials (D'Agostino *et al*. 2014). It has been reported that the relaxation mechanisms for protonated and deuterated gases are different to one another: spin-rotation for CH_4 and quadrupolar relaxation for CD_4 (Breitmaier 1975; Ernst *et al*. 1987; Wagner *et al*. 1990). Therefore, the rationalisations for the degrees to which the relaxation times varied are not analysed. The T_1 relaxation times of the deuterated species were greater than their protonated counterparts, which is an opposing trend compared to the model system. This is thought to arise from the aforementioned differences in intra-molecular relaxation mechanisms. Quadrupolar relaxation mechanisms are not discussed in this thesis but the interested reader is forwarded to the work of Spiess (1980) and Jameson (1991).

Regarding bulk CH_4 and CD_4, increases were seen in the CD_4 T_2 relaxation times by a factor of 4. In addition, the correlation plots are positioned on the diagonal and therefore T_1 was approximately equal to T_2 in both instances, as shown in figure 6.13. A ^{1}H T_2 relaxation time of 126 ms implies that adequate SNRs and signal attenuation may be observed in PFG NMR experiments. However, bulk methane was selected to observe the manner in which it behaved in a bulk system and adsorbed in a heterogeneous system by comparison. Significantly larger probability distributions were observed for CD_4 compared to CH_4. This is due to the lower gyromagnetic ratio of the ^{2}H nucleus, which resulted in a lower SNR in comparison to the ^{1}H measurements.
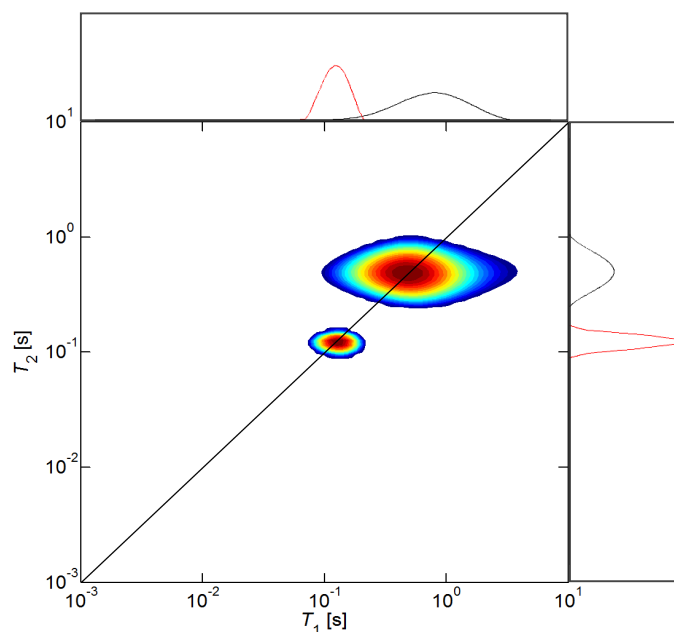
Figure 6.13: T_1-T_2 plot and probability distributions of: (red) 1000 mbar bulk CH_4 and (black) 1000 mbar CD_4. Two separate data sets are shown on a common plot for clarity and comparison.

Regarding CH_4 and CD_4 in chabazite, a more significant increase in the T_2 relaxation time of the deuterated sample was observed as shown in figure 6.14, this time by a factor of 12: 47 ms compared to 4 ms. The T_1 relaxation time increased by a factor of 7. However, this slight increase will nonetheless enable signal averaging within acceptable limits to be performed.
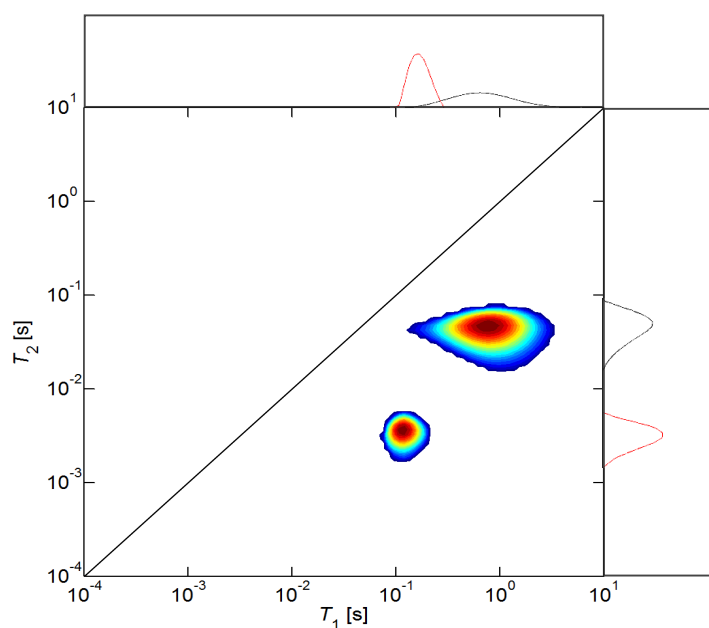

Figure 6.14: T_1-T_2 plot and probability distributions of: (red) 91 mbar CH_4 in chabazite and (black) 85 mbar CD_4 in chabazite. Two separate data sets are shown on a common plot for clarity and comparison.

Both the deuterated bulk methane and deuterated methane in chabazite analogues showed an increase in their respective T_2 relaxation times when compared with their protonated counterparts. Therefore, the intended aim of this study was met to a reasonable degree of confidence. The measured relaxation times of the bulk and heterogeneous systems are summarised in table 8.

Table 8 - Summary of relaxation times of bulk and heterogeneous methane systems.

Sample	T_1 [ms]	T_2 [ms]
1000 mbar bulk CD$_4$	503	494
1000 mbar bulk CH$_4$	127	126
91 mbar CD$_4$ in chabazite	867	47
85 mbar CH$_4$ in chabazite	119	4

6.6. Conclusions

Light olefins served as excellent candidates for studying the molecular displacement behaviour of binary systems both in the bulk gas and adsorbed phase in β-zeolite. Binary, methane-ethane mixtures also enabled excellent chemical shift resolution to be observed using conventional "pulse acquire" NMR spectroscopy. The long-range and intra-diffusion coefficients of methane were faster than those of ethane and were in reasonable agreement with their single component counterparts shown in chapter 5. It was not possible to achieve adequate chemical shift resolution in the binary methane-propane systems, due to these adsorbed molecules possessing shorter T_2 and T_2^* relaxation times, which caused excessive spectral line broadening.

The use of gaseous deuterated guest molecules confined in (micro) porous materials in diffusometry experiments presented an intriguing avenue for analysing the molecular motion of molecules with short relaxation times for both single and two-component systems. This is because improvements in T_2 relaxation times were observed in comparison to their protonated analogues of equivalent pressures. Future studies may involve the use of strongly adsorbing deuterated species such as ammonia adsorbed in small pore geometries. Alternatively, the relaxation and diffusion behaviour of aromatic compounds in large pore

structures may be investigated. This is because such molecules are also known for possessing small self-diffusion coefficients and short relaxation times as discussed in the literature (Jobic *et al*. 2001). Low temperature studies may also be conducted to analyse the line shapes of spectra which are susceptible to peak splitting, to characterise jump diffusion mechanisms and associated activation energies in zeolites (Gonçalves *et al*. 1995). This enables comparisons to be drawn between such intra-crystalline displacements and those that are outlined in chapter 5.

6.7. References

Acosta, R.H., Agulles-Pedrós, L., Komin, S., Sebastiani, D., Spiess, H.W., Blümler, P., (2006). Diffusion in binary gas mixtures studied by NMR of hyperpolarized gases and molecular dynamics simulations. Phys. Chem. Chem. Phys. 8: 4182-4188.

Breitmaier, E., Spohn, K.H., Berger, S., (1975). ^{13}C spin-lattice relaxation times and the mobility of organic molecules in solution. Angew. Chem. Internat. Edit. Vol. 14. No. 3.

Callaghan, P., (1993). *Principles of nuclear magnetic resonance microscopy*. Clarendon Press.

Chu, X.Z., Cheng, Z.P., Zhao, Y.J., Xu, J.M., Li, M.S., Zhou, L., Lee, C.H., (2015). Adsorption dynamics of hydrogen and deuterium in a carbon molecular sieve. Sep. Purif. Technol. 146: 168-175.

D'Agostino, C., Mitchell, J., Mantle, M.D., Gladden, L.F., (2014). Interpretation of NMR relaxation as a tool for characterising the adsorption strength of liquids inside porous materials. Chem. Eur. J. 20: 13009-13015.

Ernst, R.R., Bodenhausen, G., Wokaun, A., (1987). *Principles of nuclear magnetic resonance in one and two dimensions*. Clarendon press.

Gonçalves, J. A., Portsmouth, R.L., Alexander, P., Gladden, L.F., (1995). Intercage and intracage transport of aromatics in zeolites NaY, HY and USY studied by ^{2}H NMR. J. Phys. Chem. 99: 3317-3325.

Hong, W., Kärger, J., Pfeifer, H., (1991). J. Am. Chem. Soc. 113: 4812-4815.

Jameson, C. J., (1991). Gas-phase NMR spectroscopy. Chem. Rev. 91: 1375-1395.

Jobic, H., Bée, M., Méthivier, A., Combet, J., (2001). Influence of the cation composition on the dynamics of xylenes in X-type zeolites. Microporous Mesoporous Mater. 42: 135-155.

Kawamura, Y., Onishi, Y., Okuno, K., Yamanishi, T., (2008). Adsorption capacity of hydrogen isotopes on mordenite. Fusion. Eng. Des. 83: 655-660.

Morris, K., F., Johnson, C., S., (1992). Diffusion-ordered two dimensional nuclear magnetic resonance spectroscopy. J. Am. Chem. Soc. 114: 3139-3141.

Morris, G.A., Barjat, H., (1997). *Methods for structure elucidation by high resolution NMR*. Elsevier.

Pampel, A., Fernandez, M., Freude, D., Kärger, J., (2005). New options for measuring molecular diffusion in zeolites by MAS PFG NMR. Chem. Phys. Lett. 407: 53-57.

Pampel, A., Engelke, F, Galvosas, P., Krause, C., Stallmach, F., Michel, D., Kärger, J., (2006). Selective multi-component diffusion measurement in zeolites by pulsed field gradient NMR. Microporous Mesoporous Mater. 90: 271-277.

Snurr, R.Q., Kärger, J., (1997). Molecular simulations and NMR measurements of binary diffusion in zeolites. J. Phys. Chem. B. 101: 6469-6473.

Sørland, G.H., (2014). *Dynamic Pulsed Field Gradient NMR*. Springer.

Spiess, H.W., (1980). Deuteron spin alignment: A probe for studying ultraslow motions in solids and solid polymers. J. Chem. Phys. 72: 6755-6762.

Stilbs, P., (1987). Fourier transform pulsed-gradient spin-echo studies of molecular diffusion. Prog. Nucl. Mag. Res. Sp. 19: 1-45.

Swan, I., Reid, M., Howe, P.W.A., Connell, M.A., Nilsson, M., Moore, M.A., Morris, G.A., (2015). Sample convection in liquid-state NMR: why it is always with us, and what we can do about it. J. Magn. Reson. 252: 120-129.

Tian, P., Wei, Y., Ye, M., Liu, Z., (2015). Methanol to Olefins (MTO): from fundamentals to commercialisation. ACS Catal. 5: 1922-1938.

Wagner, R.S., Armstrong, R.L., McCourt, F.R., (1990). Proton and deuteron magnetic resonance study of the HD-He potential energy surface. J. Chem. Phys. 92: 5907.

Chapter 7

Single component self-diffusion in small pore chabazite structures

7.1. Introduction

This chapter describes the use of the modified Pulsed Field Gradient Nuclear Magnetic Resonance (PFG NMR) pulse sequence introduced in chapter 4. The pulse sequence is used to study the self-diffusion of both weakly and strongly adsorbing molecules, in a small pore chabazite structure and its phosphorylated analogue: SAPO-34. Similarities are seen in the molecular displacement behaviours for both sorbate molecules as a function of loading up to a certain point, whereby the self-diffusion coefficients increase with increasing molecular loading for the majority of the pressure ranges studied.

The main aim of this chapter is to use PFG NMR to determine the suitability of these small pore chabazite structures for characterising the self-diffusion of small molecules: methane, ethane and ammonia. These molecules possess sorption properties which are of relevance to Johnson Matthey's industrial processes such as Selective Catalytic Reduction (SCR). To date, the transport behaviour of ammonia in chabazite structures characterised using PFG NMR has not been reported in the literature, to the author's knowledge. Gas sorption isotherms were also conducted in these systems for methane, ethane and ammonia to observe differences in saturation pressures, to draw parallels between guest molecule saturation and self-diffusion patterns.

The self-diffusion coefficients of the systems discussed in this chapter were all less than 2×10^{-10} m^2 s^{-1}. Additionally, the associated Root Mean Squared Displacements ($RMSD$s) were all significantly smaller than the crystallite size of the pure chabazite structure (11.3 μm) and SAPO-34 (29.3 μm). Therefore, intra-diffusion coefficients were directly obtained for each sample from the PFG NMR data (and were thus not calculated), as the molecular displacements were confined to single zeolite crystallites. As a result, no molecular exchange occurred in the zeolite bed during the observation times used in this thesis, as the guest molecules did not exit the zeolite crystallites. The $RMSD$s were calculated using Einstein's relation:

$$RMSD = \sqrt{2D\Delta} \qquad\qquad 7.1$$

where D is the self-diffusion coefficient [m^2 s^{-1}] and Δ is the observation time [s] in the PFG NMR experiment.

Another aim of the work discussed in this chapter is to characterise the molecular motion of sorbate molecules with different affinities to microporous zeolites to investigate the resulting effects of molecular loading on displacement lengths. Due to the geometry of small pore chabazite structures, diatomic gaseous molecules are generally selected to study adsorption and molecular displacement behaviour as reported in the literature (Hedin *et al*. 2008). This is fortuitous since these small (NMR active) molecules are of particular interest from a research and industrial perspective as it pertains to this thesis. However, some non-diatomic molecules such as water, methanol, ammonia and ethane are also small enough to enter the zeolite's geometry.

7.2. Background

Chabazite (CHA) zeolite frameworks exhibit anisotropic geometries with cage structures, each possessing a volume of 316.4 Å^3, separated by pore 'windows' which range from 3.77 - 4.23 Å in diameter (Krishna 2012). The molecular weight of the zeolite framework is 4326 g mol^{-1}, and was used to determine the guest molecule loading in each adsorbed phase sample, using the method illustrated in chapter 4.
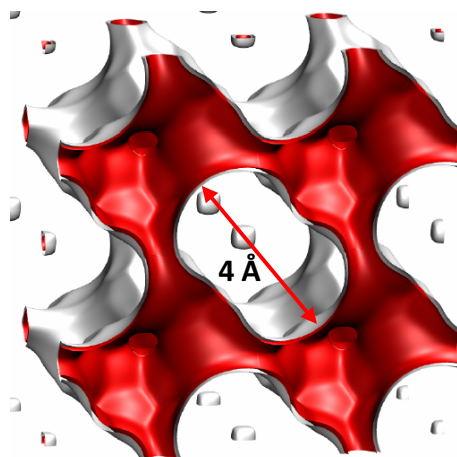
Figure 7.1: Simulated 3D structure of a CHA framework (Krishna 2012).

Literature studies have shown that conventional chabazite is used in industrial operations such as dehydration, Selective Catalytic Reduction (SCR) and air purification/separation processes (Shang *et al*. 2012; Wang *et al*. 2017). Its phosphorylated analogue, SAPO-34, is also extensively used in chemical reactions such as Methanol-to-Olefin (MTO) processes. This material has shown particularly enhanced selectivity to light olefin products whilst limiting the formation of long chain hydrocarbons and aromatics, in comparison to alternative, large(r) pore structures. However, given that the pore size is smaller in such cage structures, it is more susceptible to conventional catalyst deactivation processes such as coking, as pore mouth blocking and the accumulation of hydrocarbon intermediates restricts the geometric space (Keil 1999).

The guest molecules described in this chapter are similar to the guest molecules confined in the large pore β-zeolite structures which were discussed in chapter 5. Therefore, significantly smaller self-diffusion coefficients are expected for these guest molecules in the small pore chabazite geometry, as it is a smaller zeolite structure. The result of obtaining small self-diffusion coefficients in PFG NMR diffusometry experiments is that short length-scales are probed within the geometry in which the molecules are confined.

The zeolites discussed in this chapter, which belong to the same framework, possess large crystallite sizes: 11.3 μm and 29.3 μm for pure chabazite and SAPO-34 respectively. For a displacement length which is less than the size of the zeolite geometry, whereby the crystallite size is used as a reference as it is representative of the interconnected cage structures, a random walk model of molecular displacements is typically observed. In

addition, a Gaussian probability distribution of molecular displacements is expected, as the pathway(s) of the molecules are not dependent on one another and have an equal likelihood of being affected by inter-molecular collisions and (potential) internal resistance(s) within the unit cell of the zeolite (Grebenkov 2007). Therefore, in such instances where the molecules do not sufficiently travel a far enough distance to exit the crystallite, intra-diffusion coefficients are characterised, whereby this is the critical parameter of interest, as it is generally an accurate representation of the way in which molecules intrinsically behave in a confined zeolite geometry.

In instances where displacement lengths exceed the zeolite crystallite size, the inter-particle regions have a profound effect on governing the diffusion regime in the system (McDaniel *et al.* 1996). This results in the introduction of a weighted average with respect to characterising the dominant diffusion regime, as opposed to solely relying on the presence of molecules inside the crystallite, of which examples were illustrated in chapter 5. The longest T_1 relaxation time observed for the systems discussed in this chapter was 100 ms. Therefore, the observation time could not be sufficiently increased as to observe molecular displacements which were larger than the zeolite's crystallite. In addition, using higher temperatures to yield faster intra-diffusion coefficients was not practical from a safety perspective.

7.3. Methods and materials

7.3.1. Adsorbed phase PFG NMR experiments

All PFG NMR experiments were performed using a Bruker BioSpin DMX spectrometer operating at a ^{1}H resonance frequency of 300.13 MHz with a 5 mm radiofrequency (r.f.) coil fitted to a PFG probe head, which was placed inside a cryo-magnet. All measurements were taken at 294 K, with a precision of ± 1 K. In each instance, 0.05 g and 0.11 g of the chabazite and SAPO-34 powders were used respectively. The modified version of the APGStE pulse sequence introduced in chapter 4, was used in each PFG NMR experiment. All error bars were obtained by repeating each measurement three times on the same sample. Table 1 shows a summary of the PFG NMR parameters used for the adsorbed phase region in the sealed tube.

Table 1: Summary of the PFG NMR parameters for the gas and adsorbed phase regions in the sealed tube.

PFG NMR parameters	Adsorbed phase in bed
Observation time [ms]	10 - 100
Gradient strength [T m^{-1}]	0.05 - 10
Gradient pulse duration [ms]	0.4 - 2.4
Gradient ramp time [ms]	0.15
90° pulse [μs]	13
Recycle time [s]	0.5
Number of scans [-]	2048
Number of points [-]	25

Data obtained from the PFG NMR experiments discussed in this chapter were fitted to the single component exponential decay model introduced in chapter 4 and can be expressed as (Sørland *et al.* 1997):

$$\Psi = \sum_{i=n}^{n} p_i \, exp\left[-\gamma^2\delta^2 D_i\left(\Delta + \frac{3}{2}\tau - \frac{\delta}{3}\right)g^2\right] + \left(\Delta + \tau - \frac{\delta}{3}\right)f^2(\Delta + \tau)gf$$
$$+ \, \delta(\delta_1 - \delta_2)\tau(f + g)G_0 + \frac{4}{3}\tau^3{G_0}^2$$

                                   7.2

where Ψ is the echo attenuation [a.u.], γ is the ^{1}H gyromagnetic ratio [rad s^{-1} T^{-1}], g is the gradient strength with an amplitude ratio of 1 [T m^{-1}], f is the gradient strength with an amplitude ratio of 1 [T m^{-1}], δ is the gradient pulse width [s], G_0 is the constant, background gradient which is present in the sample [T m^{-1}] and Δ is the effective observation time [s]. The solid lines in the PFG plots in this chapter are fitting the data to equation 7.2. As mentioned in chapter 4, the delay times either side of the gradient pulses, δ_1 and δ_2, were set to 50 and 201.25 μs respectively, in a bid to minimise the overall echo time in the pulse sequence (Sun *et al.* 2003). The echo times of the PFG NMR experiments discussed in this chapter did not exceed 7 ms. Since an additional element of asymmetry in terms of the pulse sequence delay

times was introduced, the cross-magnetisation term arising due to background field gradients was considered. The mean background signal of the last three PFG NMR data points was subtracted from the total echo attenuation.

All samples discussed in this chapter possessed short T_1 relaxation times which did not exceed 100 ms, due to the level of confinement in this ultra-small pore structure. The use of a recycle time, T_R, as short as $3 \times T_1$ in conventional PFG NMR experiments is widely accepted, as quantitative signal intensities are not required to obtain self-diffusion coefficients, since each spectral intensity (or area) is normalised to the initial, maximum peak intensity/area. Doing so also enables the number of scans to be increased to enhance the Signal-to-Noise Ratio (SNR) associated with each measurement, whilst dealing with experimental time frames which are within acceptable limits. However, a T_R of $5 \times T_1$ was used in each PFG NMR experiment, since high gradient strengths were used to achieve complete echo attenuation, as molecules were diffusing at rates which were less than 2×10^{-10} m^2 s^{-1}. Therefore, a longer than necessary T_R was used as a precautionary measure to protect the r.f. coil used in the experiments, to allow sufficient time for the thermal energy induced by the (gradient) pulses to dissipate prior to acquiring the following data point in $\boldsymbol{q}$-space.

7.3.2. Chemicals and zeolites

The 11.3 μm chabazite and 29.3 μm SAPO-34 were supplied by Johnson Matthey, whereby the latter was originally acquired from Tosoh Corporation, Japan. The purity and origin of the gases used (CH_4, C_2H_6 and NH_3) were shown in chapter 4, table 1.

7.4. Characterisation methods

7.4.1. Scanning Electron Microscopy (SEM) of chabazite structures

The SEM image of the SAPO-34 structure used in this thesis, displayed in figure 7.2, shows the presence of cubic to prism particle shapes and had a mean particle diameter of 29.3 μm. Crystallite twinning was observed throughout the solid structure, which had small (10 - 100 nm) particles on the outer surface. X-ray Photoelectron Spectroscopy (XPS) studies confirmed

the presence of silica, alumina, and phosphate molecules (whereby this particular microporous material derives its name from its elemental content). The zeolite was used in the H-form. X-ray Diffraction (XRD) studies also confirmed that the crystalline structure was that of SAPO-34. The presence of crystallite imperfections, as well as non-acidic silanol groups, may serve as additional resistance barriers to reaction and molecular transport processes. This may influence the interpretation of molecular displacement behaviour(s), as it can accentuate surface contributions which add to this resistance (Yarulina *et al*. 2016). The pure chabazite structure used possessed a crystallite size of 11.3 µm and exhibited a hydrophilic surface, as shown in section 7.4.2.

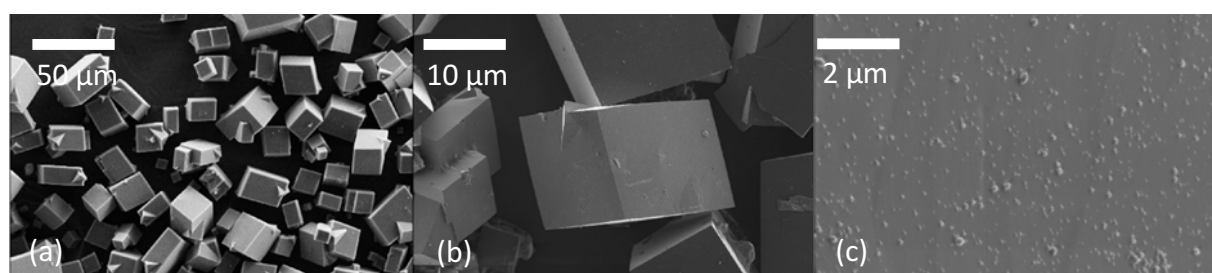

Figure 7.2: SEM image of 29 µm SAPO-34 used in this study: (a) Wide angle view of the cubic particles, (b) zoomed in view of the surface of the cubic particles, (c) zoomed in view of the surface.

7.4.2. Moisture removal in sample preparation

Elemental analysis performed on the chabazite materials using X-ray Photoelectron Spectroscopy (XPS) showed that the zeolites possessed a high surface alumina content. A (Si/Al) ratio of 2 for the chabazite structures gave rise to a highly hydrophilic surface, which is a conventional (microporous) zeolite property (Piera *et al*. 1998). As a result, the sample was particularly adept at adsorbing moisture from the atmosphere. The presence of alumina means that the materials possessed a high concentration of acid sites, which by their inherent nature are predisposed to chemisorbing with polar molecules such as water.

Figure 7.3 shows the sample pre-treatment results from an experiment conducted using a Hiden Isochema Intelligent Gravimetric Analyser (IGA) at Johnson Matthey's Technology Centre (JMTC) in Sonning Common, United Kingdom, to determine the amount of moisture lost from the sample at high temperature and low pressure. The zeolite was heated at a rate of 10 K/min and then held at 573 K and less than 1×10^{-7} mbar for 13 hours. The mass lost corresponded to a significant amount: approximately 15 % of the initial zeolite sample mass.

Therefore, prior to each PFG NMR experiment, the samples were dehydrated for 24 hours at 573 K under vacuum, before dosing with the desired guest molecules.
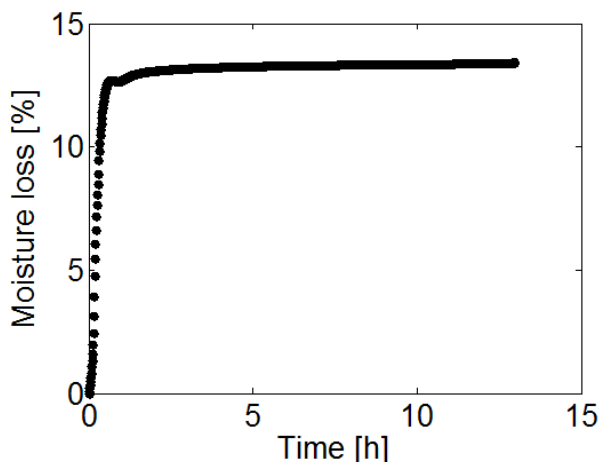

Figure 7.3: IGA dehydration profile of chabazite at 573 K and 9.5×10^{-8} mbar.

7.4.3. Nitrogen sorption isotherm

The nitrogen sorption isotherms were conducted at the Johnson Matthey Technology Centre (JMTC) at 77 K, using a Micromeritics 3Flex surface characterisation analyser. An example of a nitrogen sorption isotherm in a chabazite structure is shown in figure 7.4 and elucidates that the level of mesoporosity which existed in the structures corresponded to less than 2% of the total porosity. Since this is a negligible proportion, any contributions from the mesopore region are excluded in terms of the PFG NMR data interpretation, as it pertains to assigning relaxation constants and self-diffusion coefficients to different macroscopic regions within the zeolite.
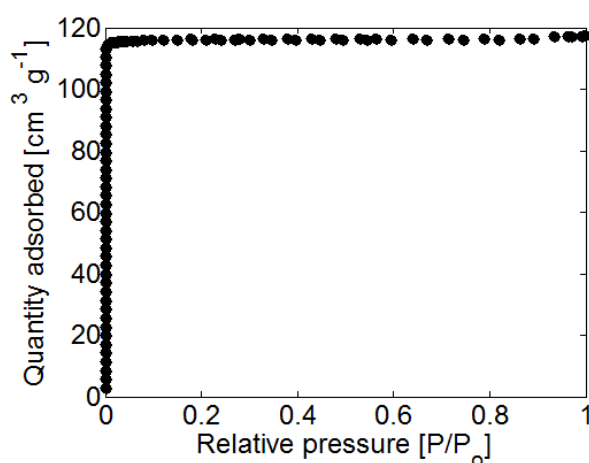

Figure 7.4: N_2 in chabazite adsorption-desorption isotherm at 77 K.

7.4.4. Gas sorption isotherms

All gas sorption experiments were carried out using approximately 0.08 g of chabazite and SAPO-34 at 294 K. The hydrocarbon molecule sorption experiments were carried out on the aforementioned IGA instrument and ammonia sorption was carried out using a Quantachrome manometric physisorption analysis instrument. The sorption pressures used for methane, ethane and ammonia ranged from 0 to 1.8 bar, 0 to 0.2 bar and 0 to 1.3 bar respectively. These sorption pressures could not be exceeded due to safety concerns associated with the pipework connecting the gas cylinders to the adsorption instruments. As shown in table 2, the adsorption pressures of the guest molecules adsorbed in the chabazite structures during the sample preparation stage prior to the PFG NMR experiment did not exceed 1.5 bar. Therefore, all gas sorption isotherms were extrapolated using a Langmuir model shown by equation 7.3, to the point at which the sorption curve plateaued, to gauge the differences in saturation pressures, and hence surface affinities, for the different guest molecules used. Incidentally, the chabazite and SAPO-34 powders adsorbed nearly identical amounts of hydrocarbon gas and as such only an example of the former is shown.

$$m_g = \frac{v_m K P}{1 + K P}$$

7.3

where m_g is the quantity of the adsorbed gas [mg], v_m is the molecular monolayer quantity [mg], K is an adsorption equilibrium constant [-] and P is the sorption pressure [Pa].
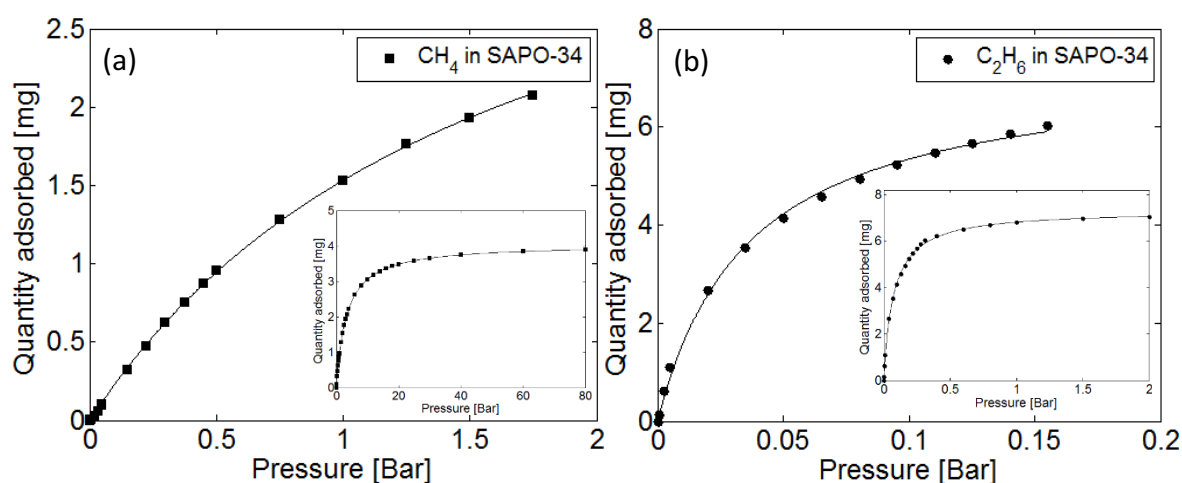

Figure 7.5: (a) CH4 and (b) C2H6 sorption isotherms in chabazite structures at 294 K. Extrapolated isotherms (up to saturation) are embedded in each figure.

Literature studies have shown that some small pore (and other large pore) zeolites can often possess poor gas phase adsorption characteristics and therefore require significant pressures to reach adsorption saturation (Zhang *et al.* 2014; Li *et al.* 2015). However, as shown in figures 7.5 and 7.6 respectively, the extrapolated isotherms for ethane and ammonia exhibit considerably lower saturation pressures than methane, therefore chabazite is particularly adept at capturing such molecules within reasonable pressure ranges, and compares well with literature data (Barrer and Ibbitson 1944) under similar isothermal conditions. The saturation pressure of ethane was lower than that of ammonia as it is a larger molecule. The extrapolated saturation pressures for all guest molecules studied were higher than the maximum sample preparation pressures selected, prior to conducting the PFG NMR experiments. The implications of this behaviour on the self-diffusion coefficient varying as a function of loading are briefly discussed in section 7.5.
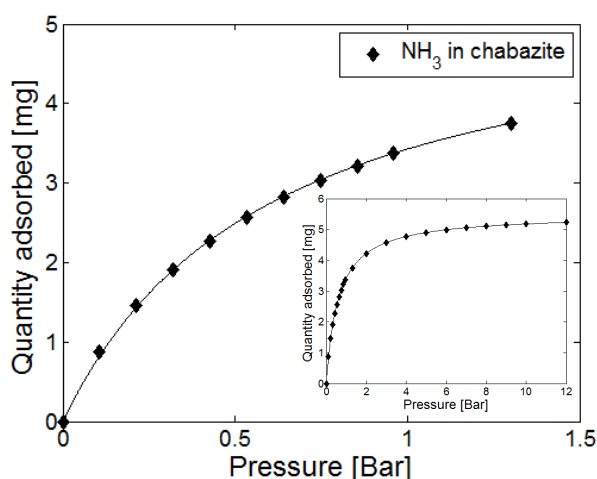
Figure 7.6: NH$_3$ sorption isotherm in a chabazite structure at 294 K with an embedded extrapolated isotherm (up to saturation).

7.5. PFG NMR results and discussion

7.5.1. Single component self-diffusion of methane, ethane and ammonia in chabazite structures

The guest molecules described in this chapter to study self-diffusion in chabazite structures are: methane, ethane and ammonia. Despite the differing sorption capabilities of these

molecules, the T_2 relaxation times were all less than 5 ms, and the spectral linewidths exceeded 1000 Hz in each instance. As a result, significant signal averaging was required in most PFG NMR experiments to achieve SNRs which were (at least) greater than 100.

Figure 7.7 shows that the intra-diffusion coefficients of single component methane and ethane adsorbed in SAPO-34 increase with increasing hydrocarbon loading, which defies conventional molecular displacement behaviour. The trend whereby increasing levels of confinement results in reduced self-diffusion coefficient of molecules adsorbed in zeolites has been well established in the literature (Kärger and Ruthven 1992; Bell 1994). This is observed due to an increase in molecular loading leading to the geometric dimensions of the zeolite becoming increasingly restricted, resulting in a reduction in the mean free path available for diffusion. The ethane in SAPO-34 echo attenuation profiles were plotted as a function of q-space, independent of observation time, as different observation times were used to achieve adequate signal attenuation. Various T_1 relaxation times enabled different observation times to be selected to achieve sufficient signal attenuation, as high gradient pulse amplitudes and durations were used in each instance.
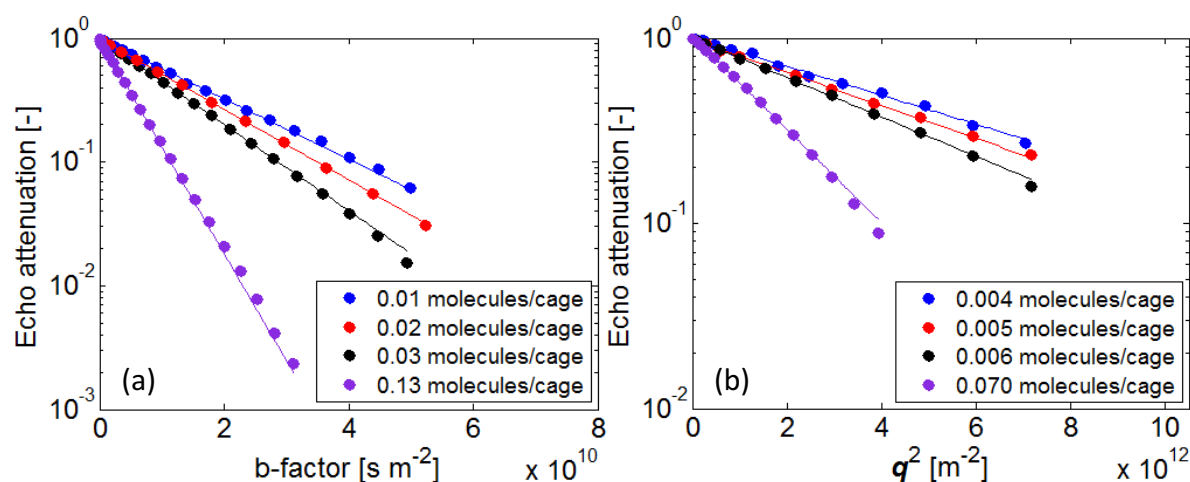
Figure 7.7: Conventional echo attenuation plot of (a) CH_4 adsorbed in SAPO-34 and (b) echo attenuation plot (independent of Δ) of C_2H_6 adsorbed in SAPO-34. δ = 2 ms, Δ = 20 - 100 ms and g = 0.05 - 8.4 T m^{-1}.

The same trends were observed for methane adsorbed in pure chabazite and are summarised, along with the methane and ethane results in SAPO-34, in figure 7.8. This behaviour was only observed in the zeolites discussed in this chapter, since the porous

materials discussed in chapters 5 and 6 had large(r) pores and did not possess constricting cage structures.
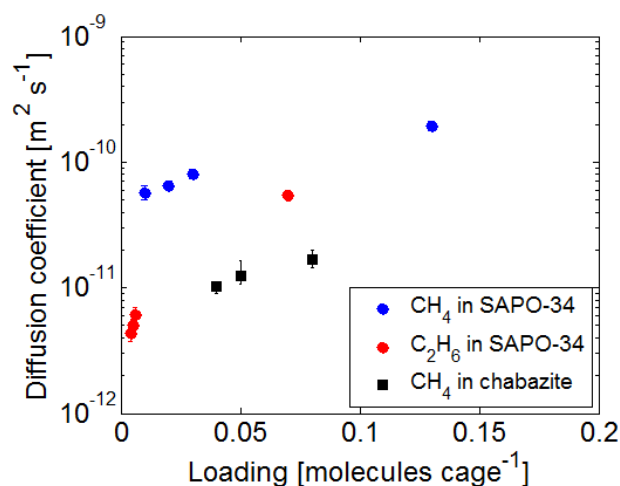

Figure 7.8: Summary of hydrocarbon intra-diffusion coefficients in chabazite frameworks *vs.* loading.

Hedin *et al*. (2008) reported similar trends whilst monitoring the diffusion of small and weakly adsorbing hydrocarbons in zeolite structures which are comparable in geometry to chabazite using PFG NMR, as illustrated in figure 7.9. Comparisons were also made with microporous zeolites with different geometric dimensions, and with increasing guest molecule hydrocarbon chain length. In those instances, conventional molecular displacement trends were observed, whereby the intra-diffusion coefficients were smaller in the smaller geometries, and faster for the smaller guest molecules. The molecular loadings reported in the literature study were higher than those used in this thesis and the significance of this is detailed in this section.
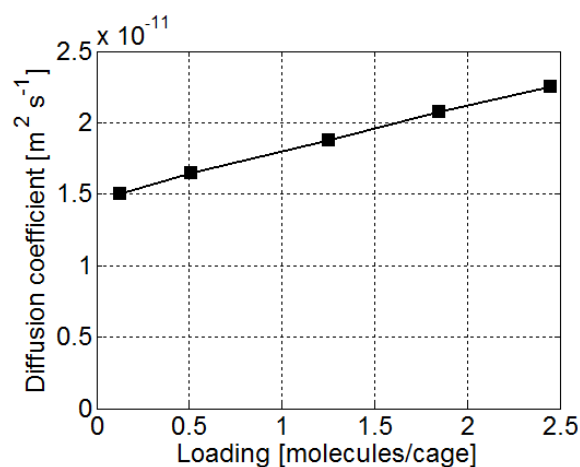

Figure 7.9: Literature study of ethane diffusivity in siliceous LTA *vs.* loading (re-plotted from Hedin *et al.* 2008). Δ = 2 - 15 ms, g = 0 - 12 T m^{-1} and T = 301 K.

Additionally, Geier *et al.* (2003) conducted PFG NMR experiments at 298 K to demonstrate that there was a strong concentration dependence of ammonia sorption in (medium pore sized) ZSM-5 structures, which possess a pore diameter of approximately 5.5 Å. An example of this trend is shown in figure 7.10. Therefore, since an identical trend was observed for both species, it implies that molecule-surface and molecule-molecule interactions have a significant influence on molecular transport. This relates to both strongly and weakly adsorbing guest molecules confined in small pore geometries.
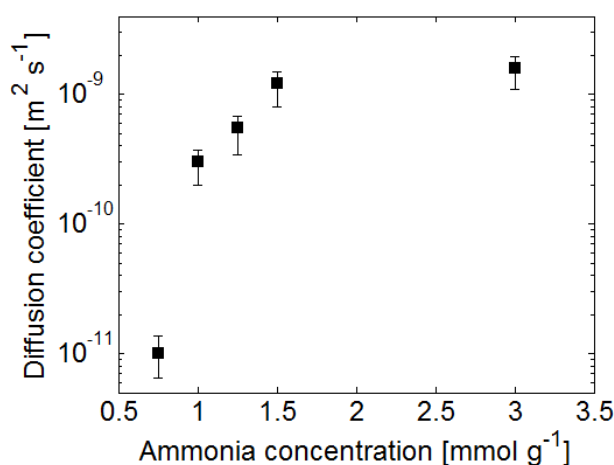

Figure 7.10: Literature study of ammonia diffusivity in ZSM-5 *vs.* concentration (re-plotted from Geier *et al.* (2003). In this study, g = 0.05 - 20 T m^{-1} and T = 298 K.

A Molecular Dynamics (MD) simulation study conducted by Beerdsen and Smit (2001) explains that it is not uncommon to observe an increase and a subsequent decrease in the diffusion with increasing molecular loading. Although such peculiar trends are only reported in instances whereby guest molecules are confined in cage-like structures and in geometries which typically do not exceed 6 Å, despite their affinity to the surface by which they are enveloped. This behaviour is thought to be observed due to a combination of surface interactions and repulsive molecule-molecule interactions. At low concentrations, molecules begin to occupy vacant acid sites which leads to surface coverage, whilst the centres of the zeolite cavities remain unoccupied. An increase in molecular loading results in an enhanced dominance of adjacent inter-molecular interactions. This is because cage structures and small pore structures are thought to promote the inter-molecular repulsion of identical molecules due to their proximity, as well as impeding molecular egress through the zeolite's unit cells at equilibrium. Therefore, an increase in loading results in an increase in the number of collisions that a molecule experiences, which subsequently speeds up the rate of molecular transport.

However, it was also reported that a return to normalcy is expected at a certain molecular loading, whereby the intra-diffusion coefficient decreases with an increase in the number of adsorbed molecules once saturation is approached. Therefore, as illustrated in figure 7.11 for an example of the simulated motion of methane in a small pore cage structured zeolite at 600 K, the intra-diffusion coefficients pass through a maximum and eventually decrease as a function of increasing loading.
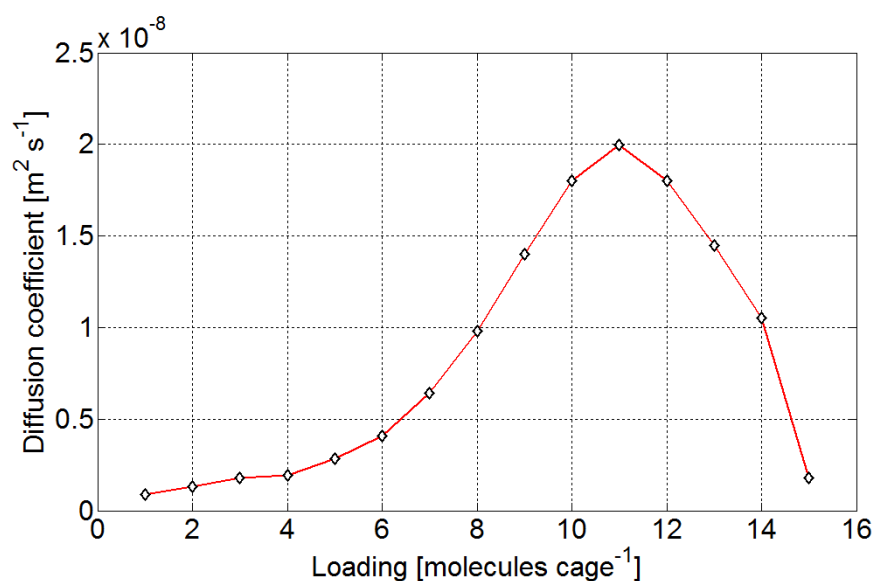

Figure 7.11: Literature MD study of methane diffusivity in LTA *vs*. loading at a temperature of 600 K (re-plotted from Beerdsen *et al.* 2004).

An alternative argument emphasising the impact of the zeolite surface has also been proposed, whereby it is thought that the presence of silanol artefacts on the internal zeolite framework could result in the trapping of guest molecules near the boundary layer, post-adsorption, (O'Malley *et al.* 2016).

However, by using ammonia as a guest molecule in pure chabazite, it was possible to observe both an increase and subsequent decrease in the intra-diffusion coefficients as a function of loading. It is plausible that this decrease was observed with ammonia as opposed to methane, since the saturation pressure of ammonia was significantly lower than that of methane. Therefore, any effects of approaching methane saturation could not be observed using the procedures outlined in this thesis. Whilst the saturation pressure of ethane was lower than that of ammonia in chabazite, the maximum adsorbed phase pressure in the flame sealed tube for ethane corresponded to 7% of the zeolite maximum cage capacity, as opposed to 13% for ammonia. Consequently, the effects of this phenomenon on self-diffusivity were

more noticeable for ammonia. Figure 7.12 shows the echo attenuations for ammonia adsorbed in chabazite, as well as a plot of the intra-diffusion coefficients as a function of molecular loading.
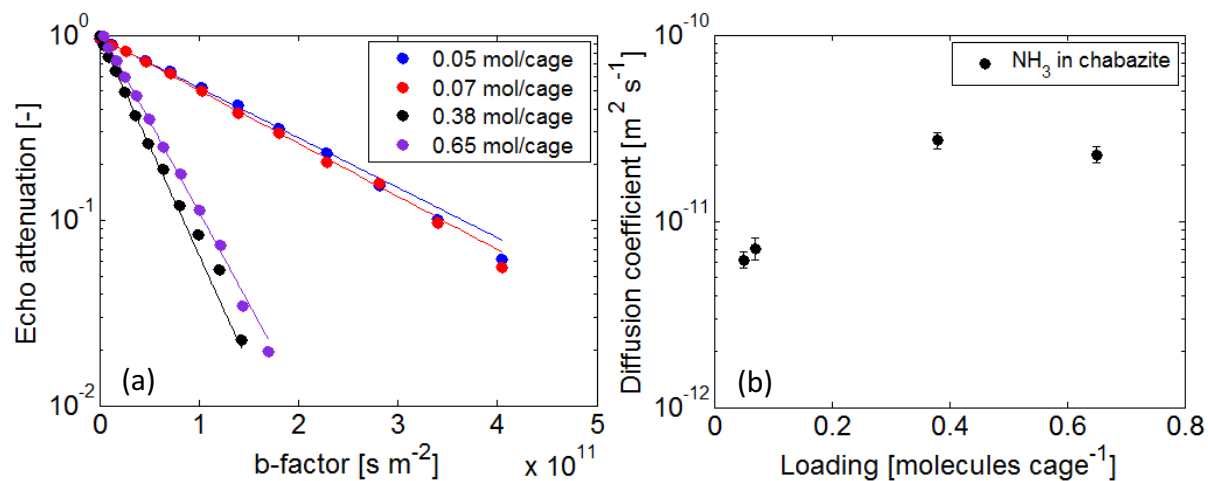

Figure 7.12: (a) Echo attenuation plots of ammonia adsorbed in chabazite, and (b) intra-diffusion coefficients as a function of loading. δ = 2.4 ms, Δ = 20 ms and g = 0.05 - 10 T m^{-1}.

It is plausible that this behaviour was observed in relatively low molecular loadings in chabazite, compared to higher loadings in ZSM-5 reported in the literature, as chabazite possesses a smaller internal geometry and thus requires fewer molecules to reach saturation (Li *et al*. 2007). It was not possible to further increase the adsorbed pressure of both the small hydrocarbons and ammonia used in this study from a safety standpoint, since the highest pressure used resulted in a gas phase pressure above the zeolite bed which was equivalent to the maximum design pressure of the 5 mm tubes. Additionally, it was not possible to conduct PFG NMR experiments involving ethane adsorbed in chabazite as the T_2 relaxation times were shorter than the shortest echo time of the modified APGStE pulse sequence. Therefore, no measurable signal was detected in the diffusometry experiments with the shortest allowable delay times in the PFG NMR pulse sequences.

However, by conducting variable temperature diffusometry experiments from 234 K - 294 K for single component methane and ammonia in SAPO-34, conventional kinetic-molecular displacement behaviour was observed whereby the intra-diffusion coefficients decreased with decreasing temperature. This is illustrated in figure 7.13, using 0.38 ammonia molecules per chabazite cage and 0.13 methane molecules per SAPO-34 cage as examples respectively. The error bars for the latter are within the size the marker.
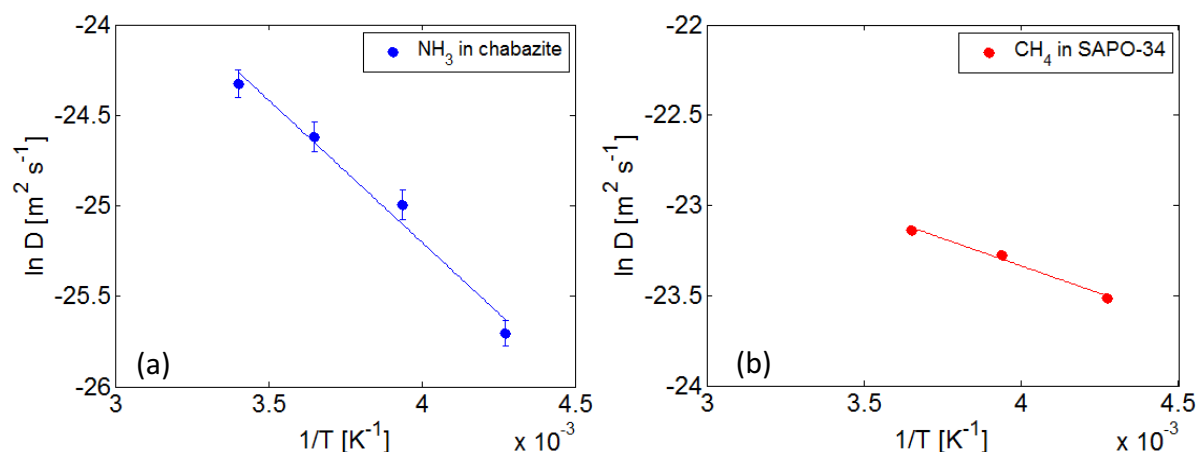
Figure 7.13: Arrhenius plots showing the natural log of the intra-diffusion coefficients of (a) 0.38 ammonia molecules per chabazite cage and (b) 0.13 methane molecules per SAPO-34 cage as a function of reciprocal temperature.

This behaviour implies that a thermal influence was a sufficient driving force for molecular transport through the cage structures and thus it was possible to overcome the energy barriers for transport in the zeolite geometry. The activation energies of diffusion, E_a, were 13.0 and 5.1 kJ mol^{-1} for the ammonia and methane respectively, which suggests that the enhanced adsorption of ammonia was a significant barrier to molecular mobility in comparison to methane. The E_a values were obtained from Arrhenius plots by using the Arrhenius equation:

$$D = exp\left(-\frac{E_a}{RT}\right) \qquad\qquad 7.4$$

Table 2: Summary of adsorbed pressures and molecular loadings of gaseous molecules adsorbed in chabazite structures.

System	Adsorbed phase pressure [mbar]	Adsorbed phase loading [molecules per cage]	Intra-diffusion coefficient [m^2 s^{-1}]
CH$_4$ in SAPO-34	175	0.13	$1.9 \pm 0.01 \times 10^{-10}$
	73	0.03	$8.0 \pm 0.01 \times 10^{-11}$
	56	0.02	$6.5 \pm 0.01 \times 10^{-11}$
	52	0.01	$5.7 \pm 0.02 \times 10^{-11}$
C$_2$H$_6$ in SAPO-34	146	0.070	$5.4 \pm 0.01 \times 10^{-11}$
	13	0.006	$6.2 \pm 0.10 \times 10^{-12}$
	10	0.005	$5.1 \pm 0.06 \times 10^{-12}$
	8	0.004	$4.3 \pm 0.10 \times 10^{-12}$
CH$_4$ in chabazite	172	0.08	$1.7 \pm 0.03 \times 10^{-11}$
	104	0.05	$1.2 \pm 0.40 \times 10^{-11}$
	91	0.04	$1.0 \pm 0.01 \times 10^{-11}$
NH$_3$ in chabazite	1519	0.65	$2.3 \pm 0.03 \times 10^{-11}$
	898	0.38	$2.7 \pm 0.01 \times 10^{-11}$
	155	0.07	$7.2 \pm 0.20 \times 10^{-12}$
	121	0.05	$6.2 \pm 0.10 \times 10^{-12}$

The maximum observed displacement lengths for each system are summarised in table 3 and shows that molecular transport was comfortably confined to single crystallites, thereby yielding intra-diffusion coefficients for all samples.

Table 3: Summary of the highest intra-diffusion coefficients and associated displacement lengths for each system studied. Chabazite crystallite size = 11.3 μm, SAPO-34 crystallite size = 29.3 μm.

System	D_{intra} [m^2 s^{-1}]	Observation time [ms]	RMSD [μm]
CH$_4$ in SAPO-34	1.9×10^{-10}	20	2.8
C$_2$H$_6$ in SAPO-34	5.4×10^{-11}	20	1.5
CH$_4$ in chabazite	1.7×10^{-11}	20	0.8
NH$_3$ in chabazite	2.7×10^{-11}	10	0.7

Quasi Elastic Neutron Scattering (QENS) studies to characterise the diffusion of ammonia in chabazite structures have been reported in the literature, where increases in self-diffusion coefficients were also observed as a function of molecular loading. The self-diffusion coefficients reported in the neutron scattering study discussed in the literature were typically an order of magnitude higher than those reported in this thesis. This was despite the fact that the molecular loadings reported in this thesis were significantly smaller, by up to an order of magnitude (O'Malley *et al*. 2016). However, this disparity is attributed to the reasons discussed in chapter 3, which stem from the differences in the length-scales over which the measurements were made for both techniques: Å - nm for QENS and μm for PFG NMR.

Ammonia adsorbed in SAPO-34 was also prepared in a bid to observe similar trends at lower pressures approaching saturation, in the hope that the presence of phosphorus would result in a stronger interaction between the (basic) sorbate molecule and the acidic surface of the zeolite. Therefore, it was anticipated that a more discernible decrease in the intra-diffusion coefficient would be observed with increasing loading. However, the adsorption of ammonia in this phosphorylated framework had a particularly potent effect, causing a significant amount of ammonia to enter the zeolite bed. The consequence of this is shown in figure 7.14, which shows a PFG NMR spectral attenuation plot with a signal attenuation of less than 14%. This, therefore, rendered ammonia essentially immobile in the SAPO-34 material, within the measurement capabilities of the spectrometer. Due to the sample possessing a short T_2 relaxation time, approximately 1 ms, significant constraints were placed on the maximum

echo time which could be selected. Additionally, a T_1 relaxation time of 13 ms did not allow any meaningful increases to be made with respect to enhanced signal attenuation, or probing longer molecular displacement length scales by increasing the observation time.

The sample was heated to 343 K in a bid to expedite the intra-diffusion process as to place it within the measurable range of the PFG NMR hardware capabilities. Additionally, the maximum allowable gradient pulse amplitude (10 T m^{-1}), duration and echo times, whereby these time variables are dictated by the T_2 relaxation time of the sample, were used to no avail. Therefore, the use of conventional PFG NMR techniques and hardware to characterise the molecular transport behaviour of NH$_3$ in highly acidic SAPO-34 materials is ill advised. However, PFG NMR probes can now be equipped with gradient sets which are capable of generating a maximum gradient strength of 28.5 T m^{-1}, which may help solve this problem. Additionally, potential solutions to circumvent this hurdle were proposed in chapter 6, with respect to using deuterated ammonia as a substitute guest molecule. However, the smaller gyromagnetic ratio of the ^{2}H nucleus in comparison to the ^{1}H nucleus means that there will be a reduction in the b-factor values in the PFG NMR experiment. Therefore, the trade-off between selecting suitable gradient strengths and gradient pulse durations to achieve adequate signal attenuation needs to be considered.
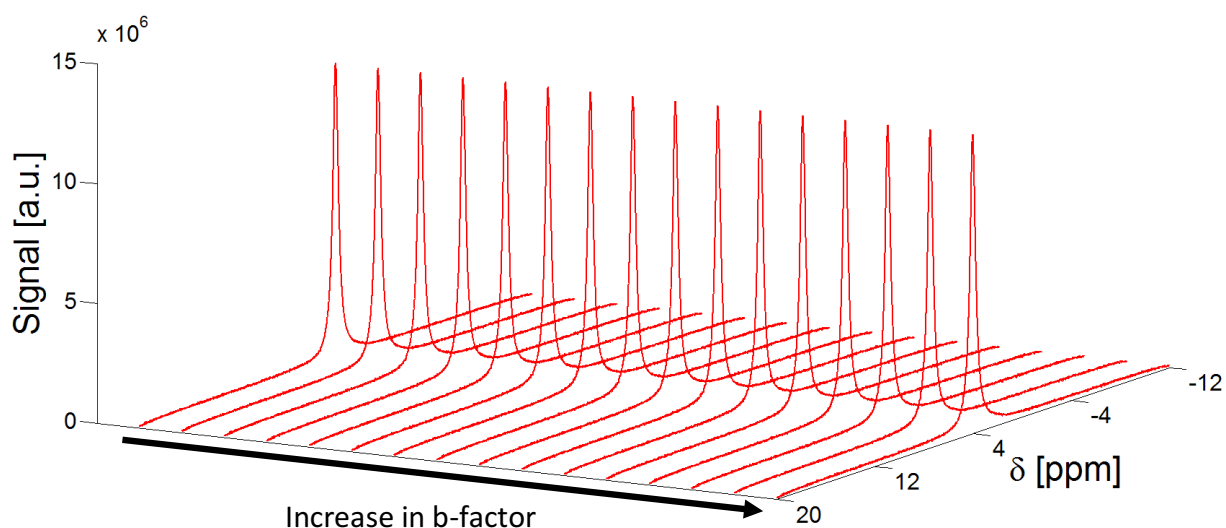

Figure 7.14: PFG NMR spectra for ammonia adsorbed in SAPO-34 at 343 K. δ = 0.4 ms, Δ = 20 ms and g = 0.05 - 10 T m^{-1}. Spectra are line broadened due to the low SNR of the sample.

This measurement limitation has important implications for industrial operations which rely on Selective Catalytic Reduction (SCR) processes using SAPO-34, which up until recently

included processes utilised by Johnson Matthey. The mobility of ammonia is essential, as it has a crucial role in transporting NO_x from the pore mouths to the caged windows of the zeolite, where it is converted to nitrogen and water, amongst other (benign) products. However, it has been shown that the presence of copper ions in the SAPO-34 framework may be used to enhance the selectivity of these desired products in SCR operations, at significantly elevated temperatures, exceeding 473 K (Gao *et al.* 2013).

7.6. Conclusions

PFG NMR was used to study the diffusion of ammonia and small hydrocarbon gases in chabazite structures at variable molecular loadings. In each instance, it was found that the intra-diffusion coefficients increased with increasing molecular loading which was in good agreement with PFG NMR and MD results published in the literature for similar materials. This peculiar trend is thought to be observed due to a combination of surface interactions and (repulsive) molecule-molecule interactions. At low concentrations, molecules began to occupy vacant acid sites which led to surface coverage, whilst the centres of the zeolite cavities remained unoccupied. An increase in molecular loading resulted in an enhanced dominance of adjacent inter-molecular interactions, as cage structures and small pore structures are thought to promote the repulsion of identical molecules due to their proximity. However, a decrease in diffusivity was observed at the highest loading of ammonia in chabazite. This compared well with theory proposed in the literature, whereby the intra-diffusion coefficients of guest molecules confined in alternative microporous zeolites were modelled using kinetic theory simulations. The *RMSDs* calculated in each system, in conjunction with the large zeolite crystallites used, resulted in the characterisation of intra-diffusion coefficients, with a Gaussian distribution of molecular displacements. This was supported by linear echo attenuation plots. The gas sorption isotherms showed that ethane and ammonia strongly adsorbed onto the chabazite surface, resulting in rapid pore filling, with methane approaching saturation at considerably higher pressures. Ammonia was found to be immobile in SAPO-34, due to the presence of phosphorous in the framework which served as a potent binding element.

7.7. References

Barrer, R.M., Ibbotson, D.A., (1944). Occlusion and hydrocarbons by chabazite and analcite. Trans. Faraday. Soc. 40: 195-206.

Beerdsen, E., Smit, B., Dubbeldam, D., (2004). Molecular simulation of loading dependent slow diffusion in confined systems. Phys. Rev. Lett. 93: 248301. 1-4.

Bell, A., (1994). *NMR Techniques in Catalysis.* CRC Press.

Gao, F., Walter, E.D., Washton, N.M., Szanyi, J., Peden, C.H.F., (2016). Synthesis and evaluation of Cu-SAPO-34 catalysts for ammonia selective catalytic reduction. 1. Aqueous solution ion exchange. ACS Catal. 3: 2083-2093.

Geier, O., Vasenkov, S., Freude, D., Kärger, J., (2003). PFG NMR observation of an extremely strong dependence of the ammonia self-diffusivity on its loading in H-ZSM-5. J. Catal. 213: 321-323.

Grebenkov, D.S., (2007). NMR survey of reflected Brownian motion. Rev. Mod. Phys. 79: 1077-1137.

Hedin, N., DeMartin, G.J., Roth, W.J., Strohmaier, K.G., Reyes, S.C., (2008). PFG NMR self-diffusion of small hydrocarbons in high silica DDR, CHA and LTA structures. Micropor. Mesopor. Mater. 109: 327-334.

Kärger, J., Ruthven, D., (1992). *Diffusion in zeolites and other microporous solids*. Wiley & Sons.

Keil, F.J., (1999). Methanol-to-hydrocarbons: process technology. Micropor. Mesopor. Mater. 29: 49-66.

Krishna, R., (2012). Diffusion in porous crystalline materials. Chem. Soc. Rev. 41: 3099-3118.

Li, S., Zong, Z., Zhou, S.J., Huang, Y., Song, Z., Feng, X., Zhou, R., Meyer, H.S., Yu, M., Carreon, M.A., (2015). SAPO-34 membranes for N_2/CH_4 separation: Preparation, characterisation, separation performance and economic evaluation. J. Membr. Sci. 487: 141-151.

McDaniel, P.L., Coe, C.G., Kärger, J., Moyer, J.D., (1996). Direct observation of N_2 self-diffusion in zeolitic adsorbents using ^{15}N PFG NMR. J. Phys. Chem. 100: 16263-16267.

O'Malley, A.J., Hitchcock, I., Sarwar, M., Silverwood, I.P., Hindocha, S., Catlow, R.A., York, A.P.E., Collier, P.J., (2016). Ammonia mobility in chabazite: insight into the diffusion component of the NH_3-SCR process. Phys. Chem. Chem. Phys. 17159-17168.

Shan, J., Li, G., Singh, R., Gu, Q., Nairn, K.M., Bastow, T.J., Medhekar, N., Doherty, C.M., Hill, A.J., Liu, J.Z., Webley, P.A., (2012). Discriminative separation of gases by a 'molecular trapdoor' mechanism in chabazite zeolites. J. Am. Chem. Soc. 134: 19246-19253.

Sørland, G.H., Hafskjold, B., Herstad, O., (1997). A Stimulated Echo Method for Diffusion Measurements in Heterogeneous Media Using Pulsed Field Gradients. J. Magn. Reson. 124: 172-176.

Sun, P.Z., Seland, J.G., Cory, D., (2003). Background gradient suppression in pulsed gradient stimulated echo measurements. J. Magn. Reson. 161: 168-173.

Yarulina, I., Goetze, J., Gücüyener, C., Thiel, L., Dikhtiarenko, A, Ruiz-Martinez, J., Weckhuysen, B.M., Gascon, J., Kapetijn, F., (2016). Methanol-to-olefins process over zeolite catalysts with DDR topology: effect of composition and structural defects on catalytic performance. Catal. Sci. Technol. 6: 2663-2678.

Wang, J., Zhao, H., Haller, G., Li, Y., (2017). Recent advances in the selective catalytic reduction of NO_x with NH_3 on Cu-chabazite catalysts. Appl. Catal. B. 202: 346-354.

Zhang, J., Burke, N., Zhang, S., Liu, K., Pervukhina, M., (2014). Thermodynamic analysis of molecular simulations of CO_2 and CH_4 adsorption in FAU zeolites. Chem. Eng. Sci. 113: 54-61.

Chapter 8

NMR relaxometry and diffusometry of gas and adsorbed phase molecules using a 43 MHz benchtop spectrometer

8.1. Introduction

This aim of this chapter is to demonstrate the suitability of a benchtop 43 MHz spectrometer with a maximum gradient strength of 0.16 T m^{-1}, which is based at the Johnson Matthey Technology Centre (JMTC), for conducting PFG NMR measurements. Whilst this instrument is typically designed for liquid phase NMR spectroscopy, the single and two-component adsorbed phase samples introduced in chapters 5 and 6 were used to perform this feasibility study. The instrument's capability with respect to characterising the relaxation and self-diffusion constants of bulk gases is also investigated. Transferring the techniques developed using a 300 MHz spectrometer to a lower field strength provides JMTC with the capability of using an in-house method for characterising molecular transport in porous materials. This enables off-line molecular displacement measurements to be made for complex and real-world systems in a matter of minutes. Hence, the need for outsourcing materials and equipment to external research centres which involve lengthy and expensive techniques (such as QENS) would be reduced. Benchtop NMR spectrometers are commercially available

at a fraction of the cost of superconducting magnets (≈ £60,000 *vs.* > £1,000,000) and they are portable due to their small size. Therefore, their use in industrial settings, which typically have magnetic equipment on site, is both preferable and novel since the characterisation of self-diffusion behaviour of gas molecules in zeolites has not been carried out in this manner to date.

Sufficient Signal-to-Noise Ratios (SNRs) were obtained in the relaxometry and diffusometry experiments for the samples analysed using the 43 MHz spectrometer. An example is shown where excellent chemical shift resolution was possible in the pulse acquisition experiment of the binary gas phase methane-ethane system shown in chapter 6. However, poorer resolution was obtained by contrast for the adsorbed phase binary methane-ethane mixture in which the ethane peak was less visible, and at a significantly lower signal intensity.

8.2. Background

It has been shown that low field NMR spectrometers are a powerful tool for the analysis of pore size distributions, time-dependent self-diffusion coefficients, relaxation behaviour and surface relaxivities of fluids confined in rock core systems with narrow pore sizes (Zhang *et al*. 2016). NMR spectrometers which are often of the order of 2 MHz or less in field strength are typically used in a bid to observe fewer internal field gradients in one and two-dimensional measurements (Leu *et al*. 2005; Washburn and Callaghan 2006). Internal gradients arise due to differences in magnetic susceptibility between guest molecules and their host porous media, which leads to field heterogeneities in pore geometries, which in many instances negatively influences the rate of decay of the transverse NMR signal (Hürlimann 1997). PFG NMR has previously been used in the literature using a 20 MHz spectrometer to study the diffusion of bulk water using a spin echo pulse sequence, where it was possible to approximately obtain a 10% attenuation in signal (Métais and Mariette 2003).

Performing NMR measurements at varying Larmor frequencies to characterise the longitudinal relaxation properties of bulk and heterogeneous systems is at the crux of techniques such as fast field cycling NMR (Korb 2001). Such techniques are capable of accurately characterising both the chemical and physical properties of biological systems,

rock cores and Magnetic Resonance Imaging (MRI) contrast agents, amongst other applications. This is achieved by rapidly cycling through a range magnetic field strengths to observe changes in the rotation rates of molecules such as proteins which display unconventional behaviour when contacted with liquid and solid interfaces (Steele *et al*. 2014). A typical example of the variation in the longitudinal relaxation time as a function of field strength, often referred to as an NMR dispersion profile, is shown in figure 8.1. In this example, the relaxation properties of water were compared with other aprotic solvents, namely acetone, to probe the structure and dynamics of these molecules at various surface interfaces within a mesoporous glass bead pack. It was found that significantly different NMR dispersion profiles were obtained for water and acetone, and this disparity was attributed to the different dynamics of these liquids at the pore surface, which gave rise to variations in surface mobility and molecular diffusion coefficients (Korb 2001).
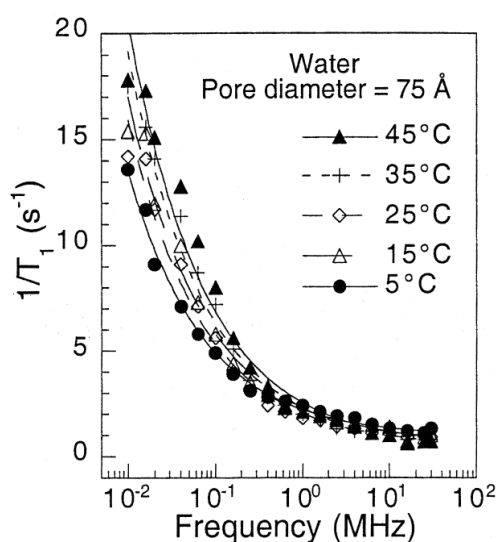

Figure 8.1: Example of an NMR dispersion profile of the longitudinal relaxation time of water adsorbed in mesoporous glass beads as a function of Larmor frequency (Korb 2001).

Utilising benchtop NMR spectrometers to study molecular displacements of molecules adsorbed in microporous zeolites is an intriguing concept, given the typically prohibitive parameters required for measurements in such systems. Consequently, high field superconducting magnets with high (pulsed) magnetic field strength capabilities are generally used to track the signal attenuation of molecules adsorbed in (micro) porous materials. The use of a benchtop NMR spectrometer to study the diffusion of gaseous guest molecules adsorbed in microporous zeolites has not been reported to date in the literature. Although

the use of fast field cycling NMR has been demonstrated in the literature to characterise the spin-lattice relaxation mechanisms of water molecules adsorbed in a hierarchical mesoporous zeolite, down to a field strength of 0.01 MHz. This variable temperature study characterised the relaxation properties of water to probe surface interaction strengths and to investigate the dependence of various acid sites on adsorption capacity and molecular exchange (Hsu *et al*. 2014).

8.3. Methods and materials

8.3.1. Inserting the flame sealed samples into the benchtop spectrometer

A Magritek 43 MHz benchtop spectrometer which has flow-through capabilities to study transient systems was used to conduct NMR spectroscopy, relaxometry and diffusometry experiments involving the zeolite materials introduced in previous chapters. Weakly adsorbing species confined in microporous zeolites were ideal candidates to study diffusion behaviour at low field strengths using PFG NMR, as weak gradient strengths were required on the high field spectrometer. The self-diffusion coefficients which were obtained were faster than that of bulk water, which the benchtop spectrometer was capable of measuring with consummate ease.

The same 5 mm hermetically flame sealed NMR tubes prepared for analysis on the 300 MHz spectrometer were used in all low field PFG NMR experiments reported in this chapter. The centre of the detection region in the benchtop spectrometer was located approximately 20 cm from the sample entry region (shown by the white circular disc in figure 8.2). Due to the height of the NMR tubes, which did not exceed 10 cm, Scotch$^®$ Magic™ tape was used to attach a cotton string to the top of the tubes. Subsequently, the tubes were lowered to the centre of the active region, and additional pieces of adhesive tape were used to secure the tubes in place to ensure that the adsorbed phase region was centred. By lowering the tubes further down, it was possible to analyse the gas phase region above the zeolite bed. The NMR tubes were retrieved post-experiment by removing the adhesive tape strips and by pulling on the cotton string.

Figure 8.2: Benchtop 43 MHz spectrometer in which a 5 mm tube is lowered into the centre and secured using strips of adhesive tape. Dimensions (in cm): 58 × 43 × 40.

8.3.2. Gas phase PFG NMR, T_1 and T_2 experiments

All PFG NMR experiments were performed at the JMTC using a benchtop Magritek Spinsolve spectrometer operating at a ^{1}H resonance frequency of 43 MHz. All measurements were taken at 299 K, with a precision of ± 0.1 K.

A conventional Pulsed Gradient Stimulated Echo (PGStE) pulse sequence introduced in chapter 2, was used in each PFG NMR experiment. Due to time constraints, the experiments were not repeated in order to estimate the experimental error. However, a coefficient of determination (R^2) which exceeded 0.98 was obtained in each instance. Tables 1 shows a summary of the diffusometry and relaxometry parameters used for the adsorbed phase region in the sealed tube respectively.

Table 1: Summary of the PFG NMR and relaxometry parameters for the gas and adsorbed phase regions in the sealed tube.

PFG NMR parameters	Value
Observation time [ms]	100
Gradient strength [T m^{-1}]	0.001 - 0.16
Gradient pulse duration [ms]	1 - 7
Gradient ramp time [ms]	0.25
90° pulse duration [µs]	8
Recycle time [s]	2
Number of scans [-]	128
Number of points [-]	16
Relaxometry parameters	**Value**
Maximum inversion time [s]	2 - 5
Echo time [µs]	100 - 500
90° pulse duration [µs]	8
Recycle time [s]	2
Number of scans [-]	16
Number of points [-]	21

The origin and purity of the materials described in this chapter were introduced in chapter 4, table 1.

8.4. Results and discussions

8.4.1. Gas phase NMR spectroscopy, relaxometry and diffusometry

The user interface of the Magritek Spinsolve data processing software displayed the NMR data in a manner similar to conventional raw data processing tools which accompany high field spectrometers, and updated the data points throughout the experiment.

An example of a pulse acquire spectrum for a binary gas phase methane-ethane mixture is shown in figure 8.3. Similar to the pulse acquisition spectrum obtained at 300 MHz, shown in chapter 6, excellent chemical shift resolution was achieved for the binary gas phase methane-ethane and methane-propane mixtures. This was due to the samples possessing T_2^* relaxation times which were of the order of milliseconds for both species, despite the reduction in magnetic field strength.
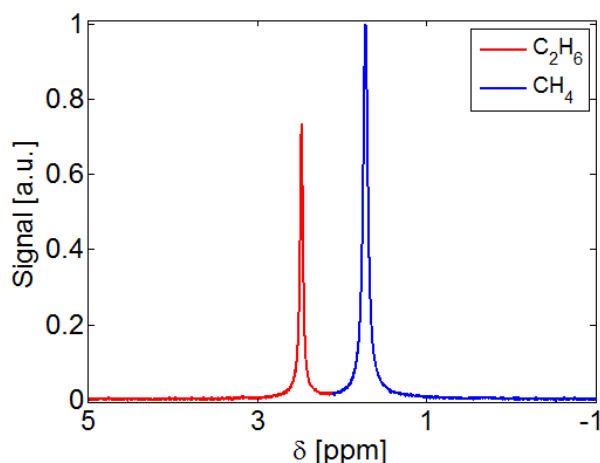

Figure 8.3: Binary ^{1}H spectrum of 0.54 bar CH_4 and 0.25 bar C_2H_6 above a β-zeolite bed.

Subsequently, individual diffusion coefficients and relaxation times were obtained by integrating separately across both peaks, as demonstrated in chapter 6. Figure 8.4 shows the typical T_1 inversion recovery and T_2 CPMG plots obtained for the gas phase samples using binary methane-ethane gas as an example, with gas pressure of 0.54 and 0.25 bar respectively. The relaxation times increased with increasing pressure for both bulk phase species, which compares well with literature data for longitudinal relaxation time constants as a function of pressure (Jameson *et al*. 1991; Woelk *et al*. 1994; Stallmach *et al*. 2015). This is thought to be due to an increase in molecular collisions, which results in an increase in spin-

rotation exchange, thereby resulting in a slower relaxation process (Kuethe *et al.* 2007). The T_1 and T_2 relaxation time constants for the bulk gases at low field were shorter than their high field (300 MHz) counterparts, for reasons which will be explained in section 8.4.2
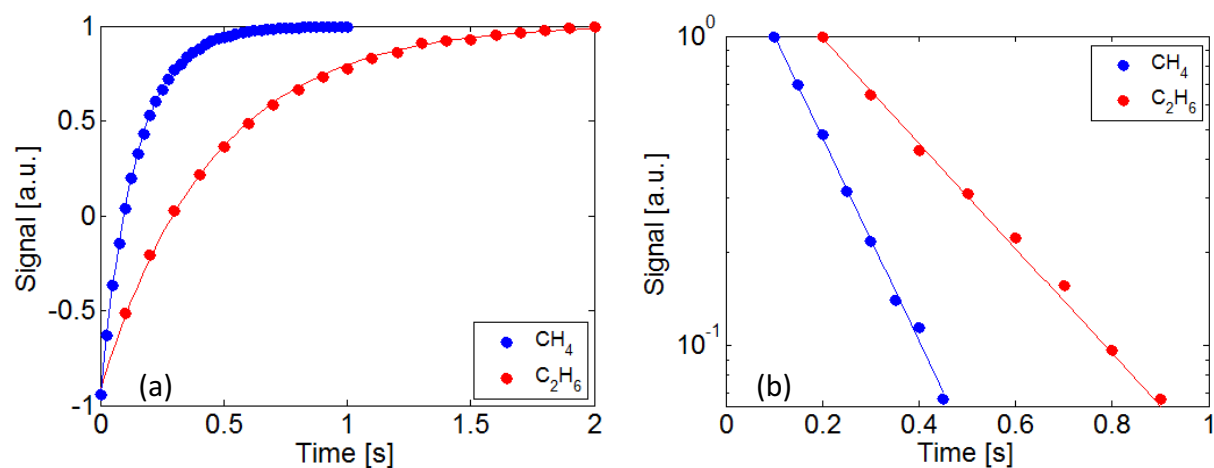

Figure 8.4: Examples of typical: (a) T_1 inversion recovery and (b) T_2 CPMG relaxation plots for bulk CH_4-C_2H_6 gas phase mixtures.

Figure 8.5 shows the typical echo attenuation plots obtained at 43 MHz for the gas phase samples using binary methane-propane gas as an example, with gas pressures of 0.11 and 0.03 bar respectively. In line with conventional kinetic and molecular displacement theory, the self-diffusion coefficients decreased with increasing pressure in each instance due to an increase in molecular mass which resulted in a reduction in thermal velocity. The diffusion coefficients of methane and propane were precise to within 10% of their high field counterparts shown in chapter 6. This disparity is attributed to the differences in experimental equilibrium temperatures: 299 K at 43 MHz *vs*. 294 K at 300 MHz.
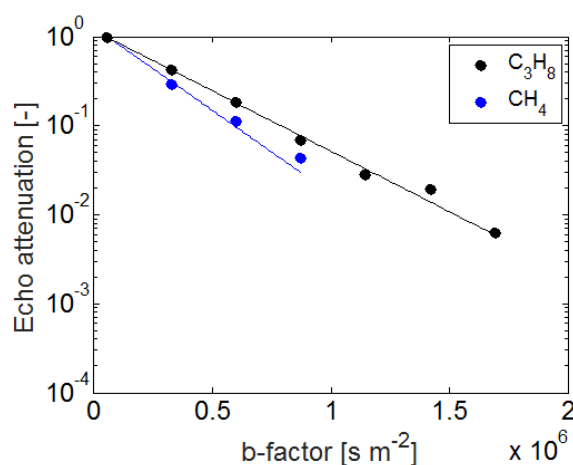

Figure 8.5: Echo attenuation plot of binary 0.11 bar CH_4 and 0.03 bar C_3H_8 above a β-zeolite bed. δ = 2 ms, Δ = 100 ms and g = 0.001 - 0.15 T m^{-1}.

Table 2 shows a summary of the single component and binary gas phase diffusometry and relaxometry results at 43 MHz.

Table 2: Summary of T_1 inversion recovery, T_2 CPMG and PGStE self-diffusion constants for the gas phase measurements at 43 MHz.

Sample	T_1 [ms]	T_2 [ms]	D [m^2 s^{-1}]
CH_4:250 mbar	34	32	1.2×10^{-5}
500 mbar	77	69	5.7×10^{-6}
1000 mbar	85	75	3.0×10^{-6}
C_2H_6: 100 mbar	90	55	2.0×10^{-5}
250 mbar	265	183	8.1×10^{-6}
500 mbar	471	321	4.7×10^{-6}
1000 mbar	579	400	2.3×10^{-6}
Binary CH_4-C_3H_8:110 mbar CH_4	107	91	4.3×10^{-6}
Binary CH_4-C_3H_8: 30 mbar C_3H_8	333	160	3.1×10^{-6}

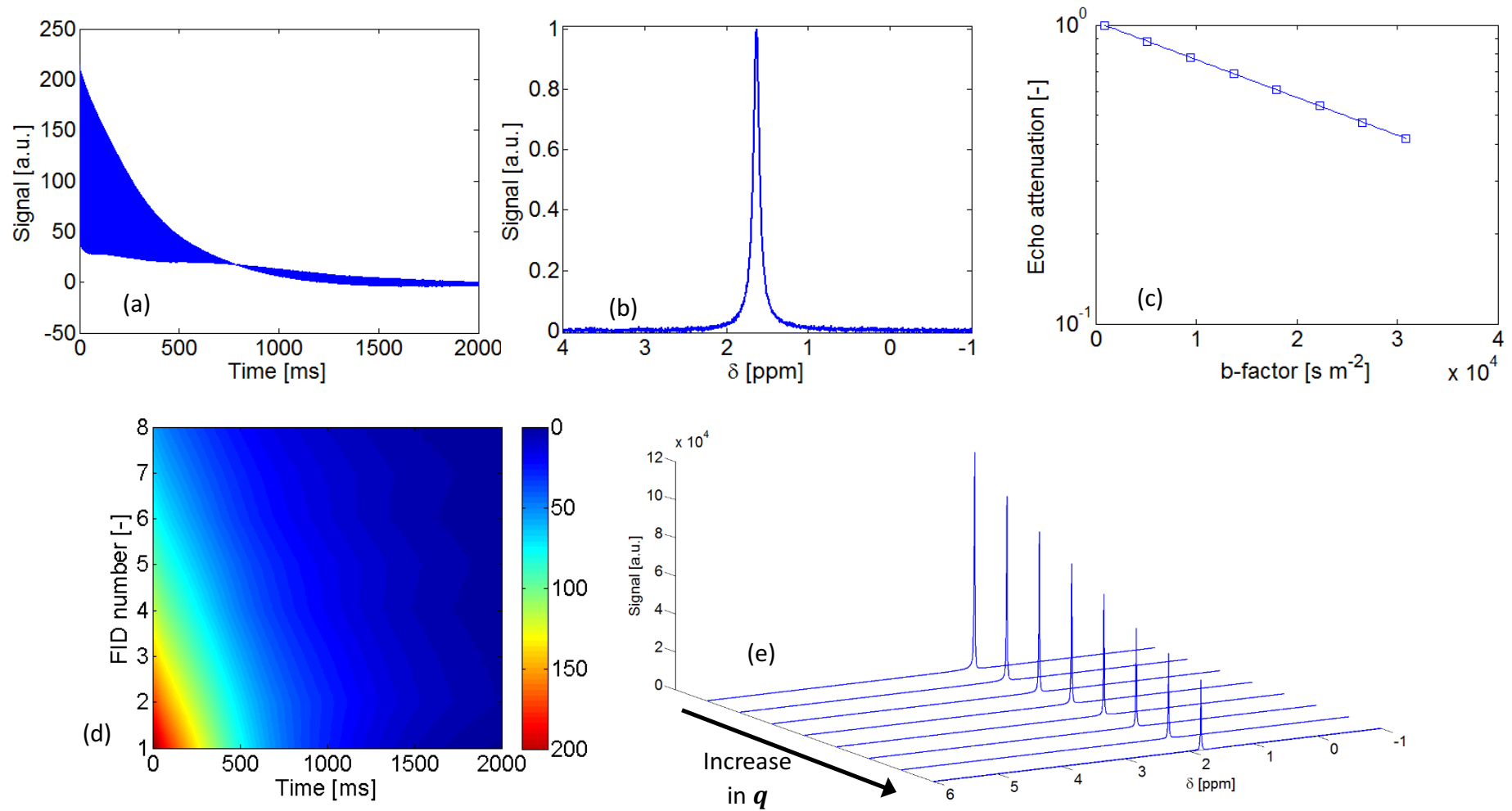Examples of the typical figures generated by this user interface from a PFG NMR experiment are displayed in figure 8.6.

Figure 8.6: Typical figures displayed by the Magritek Spinsolve software following a PFG NMR diffusometry experiment of 0.25 bar bulk CH_4: (a) Example of the real part of a Free Induction Decay (FID) set to a ^{1}H resonance frequency of 43 MHz, (b) frequency domain spectrum, (c) echo attenuation plot, (d) colour map of time domain FID profiles, (e) waterfall plot of (incomplete) spectral attenuation. 12,000 scans were used in this illustrative example. δ = 2 ms, Δ = 20 ms and g = 0.001 - 0.15 T m^{-1}.

8.4.2. Adsorbed phase NMR spectroscopy, relaxometry and diffusometry

Figure 8.7 shows a typical adsorbed phase spectrum obtained at 43 MHz, using CH_4 adsorbed in β-zeolite as an example. The spectral linewidths were narrower than those obtained under similar conditions at 300 MHz: 45 Hz *vs.* 75 Hz. This therefore implies that the T_2^* relaxation times of identical samples were longer at 43 MHz.
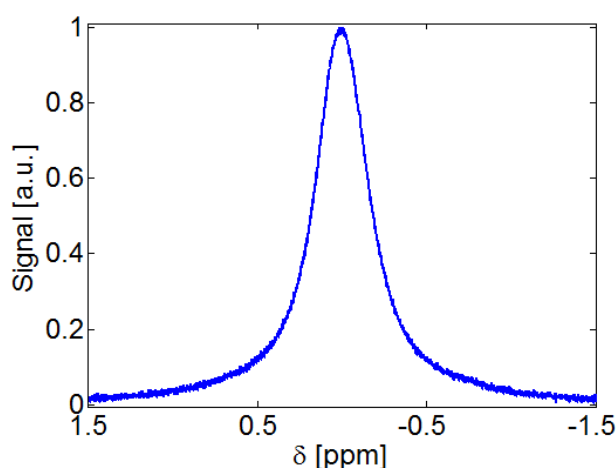

Figure 8.7: Pulse acquisition spectrum of 0.34 mol kg^{-1} of CH_4 adsorbed in β-zeolite at 43 MHz.

As shown in figure 8.8, the relaxation times of methane and ethane adsorbed in β-zeolite at the different field strengths displayed similar trends with varying pressures. Significant increases in the T_2 relaxation times of the adsorbed phase systems were observed at 43 MHz compared to 300 MHz.
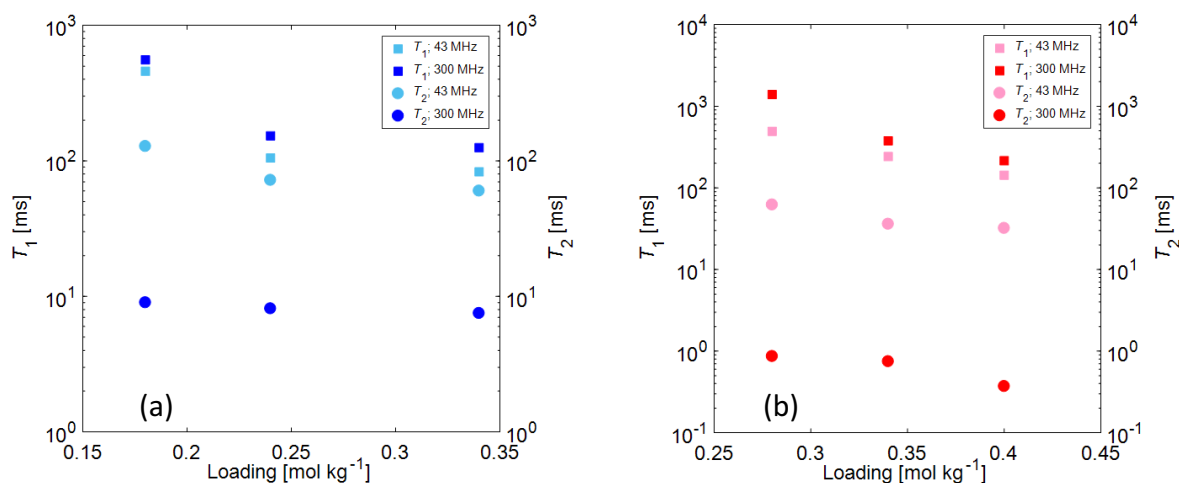

Figure 8.8: Comparison of the T_1 and T_2 relaxation times at different field strengths for (a) methane and (b) ethane adsorbed in β-zeolite.

The echo attenuation plots of single component methane and ethane resembled those obtained from the high field measurements with similar long-range coefficients, once operating temperature differences were accounted for. The only differences in the echo attenuation appearances were the values of the x- and y-coordinates, due to the maximum gradient limitations of the low field spectrometer. As shown in figure 8.8, the T_2 relaxation constants of the heterogeneous systems were longer at lower field strengths due to reductions in the effects of molecular diffusion on transverse signal decay. This therefore enabled longer gradient pulse durations to be selected to compensate for the shortcomings of the limited maximum gradient strengths. Figure 8.9 shows the echo attenuation plots of single component methane and ethane adsorbed in β-zeolite at various molecular loadings.
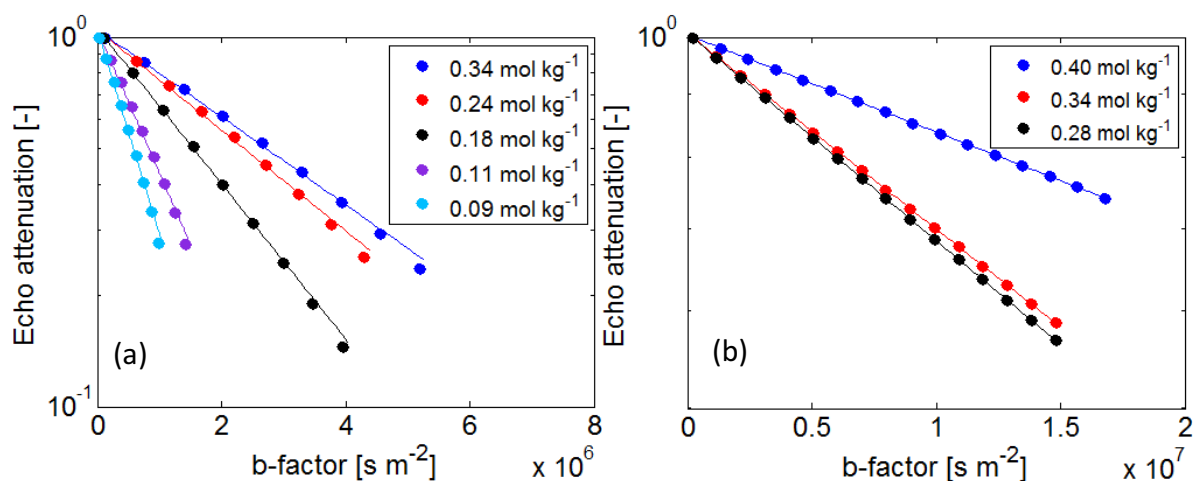

Figure 8.9: Echo attenuation plots of single component: (a) methane adsorbed in β-zeolite and (b) ethane adsorbed in β-zeolite. δ = 5 ms, Δ = 80 ms and g = 0.001 - 0.16 T m^{-1}.

Figure 8.10 shows a summary of the long-range diffusion coefficients of single component methane and ethane adsorbed in β-zeolite as a function of molecular loading.
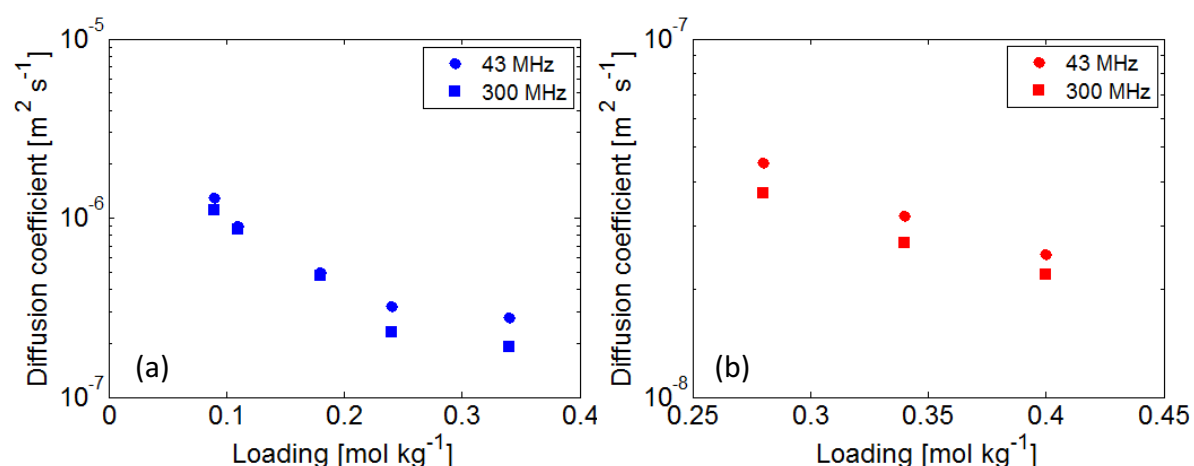
Figure 8.10: Field strength comparison of the long-range diffusion coefficients of (a) CH_4 and (b) C_2H_6 adsorbed in β-zeolite.

Table 3 shows a comparison of the relaxation constants and long-range diffusion coefficients of methane and ethane adsorbed in β-zeolite at both field strengths.

Table 3: Comparison of T_1, T_2 and long-range diffusion constants of methane and ethane adsorbed in β-zeolite at 43 MHz and 300 MHz.

Hydrocarbon loading [mol kg^{-1}]	T_1: 43 MHz [ms]	T_1: 300 MHz [ms]	T_2: 43 MHz [ms]	T_2: 300 MHz [ms]	D: 43 MHz [m^2 s^{-1}]	D: 300 MHz [m^2 s^{-1}]
CH_4: 0.09	-	642	-	12.0	1.3×10^{-6}	1.1×10^{-6}
0.11	-	611	-	11.2	9.0×10^{-7}	8.7×10^{-7}
0.18	458	557	128	9.0	5.0×10^{-7}	4.8×10^{-7}
0.25	105	153	72	8.1	3.2×10^{-7}	2.3×10^{-7}
0.34	83	125	60	7.5	2.8×10^{-7}	1.9×10^{-7}
C_2H_6: 0.28	493	1391	62	0.9	4.5×10^{-8}	3.7×10^{-8}
0.34	242	377	36	0.8	3.2×10^{-8}	2.7×10^{-8}
0.40	143	215	32	0.4	2.5×10^{-8}	2.2×10^{-8}

It has been shown that the rate at which molecules are subject to undergo longitudinal relaxation as a function of magnetic field strength may be characterised using a power law relationship (Berns *et al.* 2011):

$$R_1 = \frac{1}{T_1(\omega)} = A\omega^{-b} + C \qquad\qquad 8.1$$

where R_1 is the longitudinal relaxation rate, ω is the Larmor frequency and A, b and C are constants. Therefore, an increase in field strength results in longer spin-lattice relaxation times, although there are exceptions to this (Ramsey and Pound 1950). For both methane and ethane, the T_1 relaxation constants were slightly longer at 300 MHz. This is due to an increase in field strength resulting in a decrease in spectral density near the Larmor frequency, which lengthens the T_1 time constant. At lower field strengths, the rapid rate of molecular tumbling is close(r) to the Larmor frequency and therefore the T_1 time constant is shorter. This behaviour is not expected for unrestricted liquid phase molecules such as bulk water, which has a wide range of molecular tumbling rates, and is therefore not significantly affected by changes in field strength. As such, the T_1 relaxation times of bulk water at both field strengths were found to be similar, at approximately 2 s.

The T_2 relaxation constants of the adsorbed phase CH_4 and C_2H_6 on the other hand were longer at 43 MHz than at 300 MHz, as transverse signal decay due to molecular diffusion and associated internal gradients are more prominent at higher field strengths. This is due to increased susceptibility effects, which has a negative impact on spin-spin relaxation rates (Korb and Bryant 2002; Wilson and Hürlimann 2006). With respect to the adsorbed phase C_2H_6, a larger increase in the T_2 relaxation time was observed in comparison to CH_4: by a factor of 72 compared to a factor of 14 respectively. This is because C_2H_6 had a stronger interaction with the zeolite surface and was therefore more vulnerable to internal gradient and magnetic susceptibility effects. At both field strengths, the T_1 and T_2 relaxation times decreased with increasing pressure. This is due to an increase in the number of molecules present in the confined zeolite geometry, resulting in increased levels of restrictions to motion, which subsequently reduces the rate of molecular rotation (Levitt 2001).

The diffusometry experiments were conducted at 294 K at 300 MHz and 299K at 43 MHz. Hence, an observed maximum difference of up to 33% in the long-range diffusion coefficients for both species was within experimental error. The diffusivity is expected to be higher at 299 K, since conventional kinetic theory of weakly interacting sorbate species in large pore zeolites is applicable (Kärger *et al*. 1980).

As shown in figure 8.11, using binary methane-ethane in β-zeolite as an example, it was not possible to chemically resolve binary co-adsorbed species to the same degree of precision as their high field counterparts. The signal intensity of the ethane peak was considerably broader than that of methane, which resulted in significant peak overlap. However, whilst the chemical shift resolution was substantially worse than the high field strength result, it was nevertheless possible to distinguish both species from one another. Therefore, despite the aforementioned improvements observed in the T_2 relaxometry experiments, the effects of existing background gradients or magnetic susceptibility effects in these heterogeneous systems were nonetheless prevalent with a reduction in magnetic field strength.
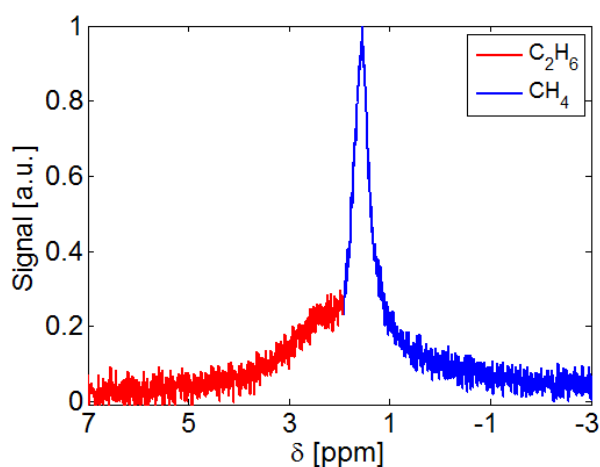

Figure 8.11: ^{1}H spectrum of 0.17 bar CH_4 and 0.04 bar C_2H_6 co-adsorbed in β-zeolite.

It was also possible to obtain individual long-range diffusion coefficients and relaxation times for both species. An example of an echo attenuation plot for 0.05 and 0.02 mol kg^{-1} of methane and ethane co-adsorbed in β-zeolite respectively is shown in figure 8.12. Signal attenuations and long-range diffusion coefficients which were comparable to those at higher field strengths were achieved. The long-range diffusion coefficient of ethane, 9.0×10^{-8} m^2 s^{-1}, and methane, 8.0×10^{-7} m^2 s^{-1}, at 43 MHz were of the same order of magnitude as the 300 MHz measurements: 8.9×10^{-8} m^2 s^{-1} and 3.6×10^{-7} m^2 s^{-1} for ethane and methane respectively. The former was nearly identical to its high field counterpart, whereas the latter was faster by a factor of two. This is partly attributed to differences in experimental temperatures: 299 K *vs*. 294 K.
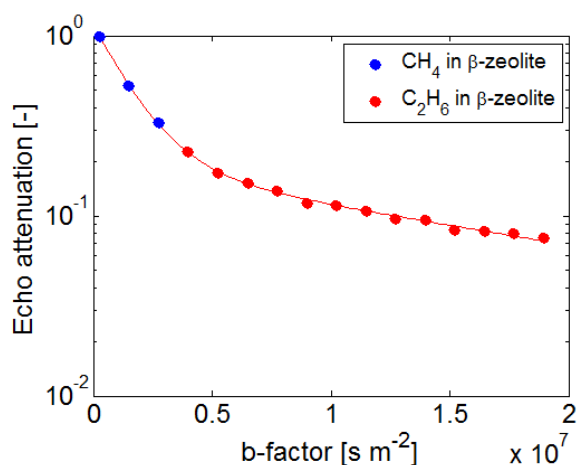
Figure 8.12: Echo attenuation plot of binary methane and ethane co-adsorbed in β-zeolite. The solid line is a two-component fit of the data (blue and red dots) to the Stejskal-Tanner equation. δ = 1 ms, Δ = 20 ms and g = 0.01 - 0.12 T m^{-1}.

With respect to the use of identical guest molecules adsorbed in small pore structures such as chabazite, it was possible to obtain a signal from the pulse acquisition experiment, in addition to performing relaxometry experiments to obtain T_1 and T_2 relaxation times. The relaxation times followed a trend which was similar to that observed in the large pore systems, whereby T_1 was longer at 300 MHz, 55 ms *vs*. 10 ms, and T_2 was longer at 43 MHz, 8 ms *vs*. 4 ms, using 0.06 ethane molecules per SAPO-34 cage as an example. However, it was not possible to successfully conduct a PFG NMR diffusometry experiment, since meaningful signal attenuation was not achieved. This is because the combination of a short T_2 relaxation time and weak maximum gradient strengths proved to be an insurmountable hurdle. This also applied to ammonia (strongly) adsorbed in mesoporous silica beads, although bulk ammonia PFG NMR measurements were carried out without any difficulties.

8.5. Conclusions

A low field benchtop spectrometer proved to be particularly successful at characterising the long-range diffusion coefficients of weakly adsorbing gas phase guest molecules, methane and ethane, adsorbed in a large pore β-zeolite. Although the loadings used in this thesis were relatively low in comparison to alternative techniques outlined in the literature, sufficient SNRs were nevertheless obtained within reasonable experimental time frames. The observed trends of relaxation rates varying as a function of loading and magnetic field strength were in good agreement with literature data.

Due to the difficulties faced with small pore and strongly adsorbing guest molecules, PFG NMR measurements at 43 MHz are best suited to sufficient concentrations of bulk gas, liquid and weakly adsorbing guest molecules in large pore microporous systems. This also applies to mesoporous systems, as the self-diffusion coefficients and relaxation times of molecules in these structures are typically higher by at least an order of magnitude in comparison to their microporous counterparts.

8.6. References

Berns, A.E., Bubici, S., De Pasquale, C., Alonzo, G., Conte, P., (2011). Applicability of solid state fast field cycling NMR relaxometry in understanding relaxation properties of leaves and leaf-litters. Org. Geochem. 42: 978-984.

Hürlimann, M.D., (1997). Effective gradients in porous media due to susceptibility differences. J. Magn. Reson. 131: 232-240.

Hsu, C.W., Chen, Y.W., Rana, B.S., Kumar, R., Sinha, A.K., Hwang, D.W., (2014). Dynamics of water in hierarchical mesoporous H-ZSM-5 by fast field cycling NMR relaxometry. J. Phys. Chem. C. 118: 20481-20487.

Jameson, C.J., Jameson, A.K., Smith, N.C., Hwang, J.K., Zia, T., (1991). ^{13}C and ^{1}H spin relaxation in CH_4 in the gas phase. J. Phys. Chem. 95: 1092-1098.

Kärger, J., Pfeifer, H., Rauscher, M., Walter, A., (1980). Self-diffusion of n-paraffins in NaX zeolite. J. Chem. Soc. Faraday. Trans. 1. 76: 717-737.

Korb, J.P., (2001). Surface dynamics of liquids in porous media. Magn. Reson. Im. 19: 363-368.

Korb, J.P., Bryant, R.G., (2002). Magnetic field dependence of proton spin-lattice relaxation times. Magn. Reson. Med. 48: 21-26.

Kuethe, D.O., Montaño, R., Pietrass, A., (2007). Measuring nanopore size from the spin-lattice relaxation of CF_4 gas. J. Magn. Reson. 186: 243-251.

Levitt, M., (2001). *Spin dynamics: Basics of nuclear magnetic resonance imaging.* John Wiley & Sons.

Leu, G., Fordham, E.J., Hürlimann, M.D., Frulla, P., (2005). Fixed and pulsed gradient diffusion methods in low-field core analysis. Magn. Reson. Im. 23: 305-309.

Métais, A., Mariette, F., (2003). Determination of water self-diffusion coefficients in complex food products by low field ^{1}H PFG-NMR: comparison between the standard spin-echo sequence and the T_1-weighted spin-echo sequence. J. Magn. Reson. 165: 265-275.

Nusser, W., Kimmich, R., Winter, F., (1988). Solid-state NMR study of protein/polypeptide backbone fluctuations interpreted by multiple trapping diffusion of dilating defects. J. Phys. Chem. 92: 6808-6814.

Ramsey, N.F., Pound, R.V., (1950). Nuclear audiofrequency spectroscopy by resonant heating of the nuclear spin system. Phys. Rev. Lett. 77: 278-279.

Stallmach, F., Pusch, A.K., Splith, T., Horch, C., Merker, S., (2015). NMR relaxation and diffusion studies of methane and carbon dioxide in nanoporous ZIF-8 and ZSM-58. Micropor. Mesopor. Mater. 205: 36-39.

Steele, R.M., Korb, J.P., Ferrante, G., Bubici, S., (2014). New applications and perspectives of fast field cycling NMR relaxometry. Magn. Reson. Chem. 54: 502-509.

Washburn, K.E., Callaghan, P.T., (2006). Tracking pore to pore exchange using relaxation exchange spectroscopy. Phys. Rev. Lett. 97: 175502-1-4.

Wilson, R.C., Hürlimann, M.D., (2006). Relationship between susceptibility induced field inhomogeneities, restricted diffusion and relaxation in sedimentary rocks. J. Magn. Reson. 183: 1-12.

Woelk, K., Rathke, J.W., Klingler, J., (1994). The toroid cavity nmr detector. J. Magn. Reson. Ser. A. 109: 137-146.

Zhang, Y., Xiao, L., Liao, G., Song, Y.Q., (2016). Direct correlation of diffusion and pore size distributions with low field NMR. J. Magn. Reson. 269: 196-202.

Chapter 9

Conclusions and future work

9.1. Conclusions and future work

The conclusions, accomplishments and proposed future work of the PFG NMR study of fluids adsorbed in microporous materials are summarised for each experimental chapter.

Chapter 4

A calibrated vacuum line was used to prepare all single and two-component samples used in the PFG NMR experiments presented in this thesis, using well established literature methods. The molecular loadings of the adsorbed phases were calculated using an NMR calibration by correlating the relaxation corrected bulk gas phase signal intensities to gas pressure. Reductions in echo times were made to the conventional APGStE pulse sequence to improve the SNRs of systems which possessed short T_2 relaxation times. Using unequal bipolar gradient amplitudes did not have a positive impact on the SNRs of the adsorbed phase systems. Therefore, equal gradient strengths opposing in polarity were used in each diffusometry experiment.

The maximum allowable sorption pressure in the sample preparation stage was limited to 2 bar, as the 5 mm tubes consisted of borosilicate, with a wall thickness of approximately 1.5 mm. Therefore, using exotic materials of construction such as sapphire, which is capable of withstanding pressures up to 400 bar, would enable the preparation of higher pressure samples. This will allow accurate comparisons to be made with existing (PFG NMR) literature

data. Due to the high melting point of sapphire crystals, approximately 2000 °C, it would not be possible to use conventional flame sealing methods to obtain hermetically sealed NMR sample tubes. However, this is not a deterrent since a range of flange fittings which enable a secure, air tight connection are commercially available. Subsequently, the problem of temperature induced adsorption-desorption would be bypassed, resulting in the adsorption of precise and controlled quantities of molecules by the zeolite bed. However, a customised vacuum manifold would need to be designed to accommodate these higher pressures, since the existing apparatus also consists of borosilicate.

Chapter 5

A solely PFG NMR based method was demonstrated to calculate the single component intra-crystalline diffusion coefficients of gas phase hydrocarbon guest molecules adsorbed in large pore β-zeolite materials from long-range diffusion coefficients typically observed in such systems. The parameters which characterise conventional "fast-exchange" regimes were obtained solely using NMR, without the requirement of gas sorption isotherm data to acquire the inter-particle parameters outlined in equation 5.8. Conventional molecular displacement behaviour was observed for each species, whereby the self-diffusion coefficients decreased with increasing molecular loading and increasing hydrocarbon chain length. Variable observations time experiments were conducted to characterise non-exchanging and various exchanging regimes. These regimes displayed a Gaussian and a non-Gaussian probability distributions of molecular displacements in the form of linear and curved echo attenuation plots respectively. Comparisons were also made between the long-range and intra-diffusion coefficients of methane adsorbed the aforementioned in large crystallite ("research grade") and small crystallite ("industrial grade") β-zeolite. The long-range and intra-crystalline diffusion coefficients in both grades of materials were in good agreement with one another.

Intra-diffusion coefficients were also directly obtained from PFG NMR data for liquid phase hydrocarbon guest molecules adsorbed in the large crystallite β-zeolite, since the measured *RMSD*s did not exceed 2 μm for each system. In general, the liquid phase molecules possessed

intra-diffusion coefficients which were up to three orders of magnitudes slower than the adsorbed gaseous molecules.

Chapter 6

The same PFG NMR protocols introduced in chapter 5 were applied to binary methane-ethane and methane-propane mixtures. Excellent chemical shift resolution was observed in all gas phase and adsorbed phase methane-ethane measurements. Poor resolution was obtained in the adsorbed phase methane-propane systems due to broad spectral linewidths, resulting in significant peak overlap which prevented the unique identification of both species in a pulse acquire experiment.

The effects of competitive adsorption were observed in the diffusometry experiments, as the diffusivity of the weaker sorbate molecule was significantly faster than the stronger sorbate molecule and was subsequently displaced in most instances. Therefore, this resulted in the stronger sorbates significantly influencing the molecular dynamics of the weaker sorbates.

^{1}H-^{2}H NMR spectroscopy and relaxometry experiments were conducted using H_2O and D_2O adsorbed in a model mesoporous alumina material under identical experimental conditions. Improvements were observed in the spectral linewidths and relaxation times for D_2O, due to the smaller gyromagnetic ratio of the ^{2}H nucleus in comparison to the ^{1}H nucleus. Subsequently, similar experiments were conducted involving CH_4 and CD_4 adsorbed phase in chabazite and in the bulk gas phase. Significant improvements were observed in the T_2 relaxation times of the deuterated isotopes, which presented an intriguing avenue for future work involving deuterated ammonia, which will be described in the summary of chapter 7. Additionally, the use of deuterated guest molecules enables variable temperature NMR to be performed. Therefore, the spectral line shapes, associated jump diffusion coefficients and activation energies of the systems presented in this thesis may be characterised to draw comparisons with intra-crystalline diffusion coefficients obtained using conventional PFG NMR.

Chapter 7

PFG NMR was used to study the molecular dynamics of weakly adsorbing methane and strongly adsorbing ethane and ammonia in a large crystallite pure chabazite structure and its phosphorylated analogue: SAPO-34. The intra-diffusion coefficients unconventionally increased with increasing molecular loading, up to a certain point, for all guest molecules due to the constricting cage structure of the chabazite framework. A decrease in the intra-diffusion coefficient of ammonia adsorbed in chabazite was eventually observed at the highest loading. The observed trends compared well with experimental and simulated literature data for similar molecules adsorbed in analogous structural geometries. The *RMSD*s obtained in each instance were smaller than the crystallite sizes of the zeolites and therefore intra-diffusion coefficients were characterised for all systems studied. Insufficient signal attenuation was observed for ammonia adsorbed in SAPO-34 in the diffusometry experiments using the maximum pulsed gradient amplitudes and durations, up to a temperature of 343 K. It was therefore deemed immobile under these conditions due to the presence of phosphorous in the zeolite framework resulting in a significantly potent acid-base surface-sorbate interaction.

As shown in chapter 6 in which water and methane were used as examples, replacing protonated guest molecules that are of industrial relevance with their deuterated analogues yielded promising results with respect to obtaining longer T_2 relaxation times. Deuterated ammonia therefore presents as a potential candidate for performing future diffusometry experiments. This is because the advantages of increased SNRs due to longer T_2 relaxation times presents the opportunity to study systems which cannot be characterised with ^{1}H PFG NMR. Additionally, future studies may involve performing case studies to investigate the effect(s) of precious metal content in zeolite structures on molecular displacements, as these additives are typically present in real world industrial zeolite frameworks.

Chapter 8

A benchtop 43 MHz spectrometer was used at the Johnson Matthey Technology Centre (JMTC) to conduct PFG NMR experiments of the single and two-component gas and adsorbed phase species discussed in chapters 5 and 6. Reductions were seen in the relaxation times of the bulk gas phases. However, significant increases were observed in the T_2 relaxation times of the adsorbed phases: by up to two orders of magnitude for both methane and ethane.

Excellent chemical shift resolution was possible for the binary gas phase methane-ethane systems, whereas poor resolution was obtained for the co-adsorbed methane-ethane and methane-propane systems. The long-range diffusion coefficients were in good agreement with their high field counterparts. It was not possible to successfully perform diffusometry experiments using these guest molecules adsorbed in small pore zeolites, as well as ammonia adsorbed in mesoporous silica beads. This was due to the short T_2 relaxation times of these samples and the gradient strength limitations of the benchtop spectrometer.

Appendix A

A.1 ASG2 NW16 Edwards active strain gauge calibration

The vacuum line and all connected glassware is evacuated prior to commencing the calibration experiment. Since the volumes of the manifold, the NMR tube and the arm which connects the two are known, a range of known pressures (0.025 - 1.3 bar) is introduced into the 5 mm tube, which is isolated from the evacuated manifold. The valve connecting the manifold to the vacuum line is subsequently closed and the pressure in the tube is exposed to the manifold, upon which the pressure is recorded by the gas independent ASG2 NW16 Edwards Active strain gauge attached to the manifold. The expected pressure in the manifold for each pressure increment is calculated using Boyle's law:

$$p_1 = \frac{p_2 v_2}{v_1} \qquad \text{A1}$$

where p_1 and v_1 are the pressure and volume in the manifold and p_2 and v_2 are the pressure and volume of the NMR tube. This calculated pressure is compared to that recorded by the gauge and, as shown in figure A1, a linear relationship is observed between both pressures. The experiments are repeated with the calibration bulb, with similar trends observed. Therefore, since excellent agreement is obtained in each instance, the suitability of the pressure gauge for gas phase calibrations and zeolite sample preparation is confirmed.
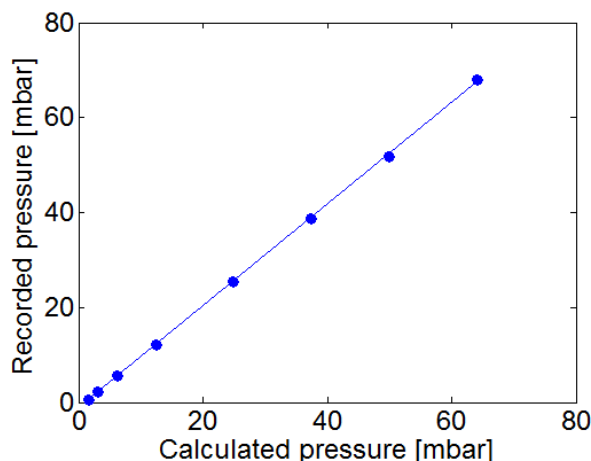
Figure A1: Example of a pressure gauge calibration plot using atmospheric air at 294 K.

A.2 Adsorbed phase loading calculation

Using a tube which contains C_3H_8 adsorbed in a 15 μm β-zeolite bed as an example, the method used to calculate the molecular loadings, in molecules per unit cell and moles per kg, using the NMR calibration plots introduced in chapter 4 is detailed in this section. The calibration plots are obtained by plotting the relaxation corrected signal of C_3H_8 *vs*. the known C_3H_8 pressure, which yields a straight line:
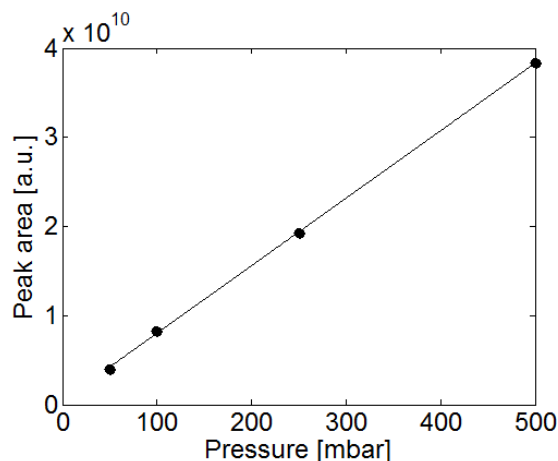

Figure A2: Bulk gas NMR calibration plot showing the relaxation corrected signal *vs*. tube pressure for C_3H_8.

The adsorbed phase region of C_3H_8 in the sample tube is then placed in the r.f. coil and the pulse acquisition experiment is performed using the same experimental and

shimming parameters used for the calibration experiments. This signal is then relaxation corrected:

$$Relaxtion\ corrected\ NMR\ signal = \frac{Uncorrected\ NMR\ signal}{exp^{-\left(\frac{2t}{2T}\right)}}$$ A2

where t is equal to half the echo time (0.50 ms) and T is equal to the T_2 time constant of the sample (0.93 ms).

$$Relaxtion\ corrected\ NMR\ signal = \frac{2.21 \times 10^{10}}{exp^{-\left(\frac{2 \times 0.50}{2 \times 0.93}\right)}}$$ A3

$$= 3.8 \times 10^{10}$$

The relaxation corrected signal of the propane sample therefore corresponds to an adsorbed pressure, P, of 494 mbar (which is equal to 49400 J m^{-3}).

The volume of the tube occupied by the zeolite bed when placed in the r.f. coil, V, is equal to 1.2×10^{-6} m^3. As mentioned in chapter 4, ideal gas behaviour is assumed, therefore the pressure is converted to a concentration, C, as follows:

$$C = \frac{P}{RT}$$

$$= \frac{49400}{8.314 \times 293}$$ A4

$$= 20.28\ mol\ m^{-3}$$

This is then multiplied by the volume occupied by the molecules in the tube to obtain the number of moles:

$$n = C \times V$$

$$= 20.28 \times 1.2 \times 10^{-6} \qquad \text{A5}$$

$$= 2.43 \times 10^{-5} \, mol$$

This is then converted to the number of molecules, N, by multiplication with Avogadro's number, N_A:

$$N = n \times N_A$$

$$= 2.43 \times 10^{-5} \times 6.02 \times 10^{23} \qquad \text{A6}$$

$$= 1.46 \times 10^{19}$$

The number of unit cells in the zeolite bed is determined using the mass of the zeolite powder, m, which is 0.1 g, the molecular weight of the zeolite, M_w, which is 3845 g mol^{-1} and N_A:

$$Number \ of \ unit \ cells = \frac{m}{M_w} \times N_A$$

$$= \frac{0.1}{3845} \times 6.02 \times 10^{23} \qquad \text{A7}$$

$$= 1.56 \times 10^{19}$$

Therefore, the number of molecules per unit cell is given by:

$$Number \ of \ molecules \ per \ unit \ cell = \frac{Number \ of \ molecules}{Number \ of \ unit \ cells} \qquad \text{A8}$$

$$= \frac{1.46 \times 10^{19}}{1.56 \times 10^{19}}$$

$$= 0.94$$

As mentioned in chapter 4, the number of molecules per unit cell may be multiplied by a geometric conversion factor, 0.26, to convert the units into mol kg^{-1}:

$$Adsorbed\ phase\ loading = 0.94 \times 0.26 \qquad\qquad A9$$

$$= 0.24\ mol\ kg^{-1}$$

A.3 PFG NMR Gaussian decay plot

Figure A3 shows the typical spectral attenuation plot with a Gaussian decay which is obtained in all PFG NMR samples, using CH$_4$ adsorbed in a 15 μm β-zeolite as an example:
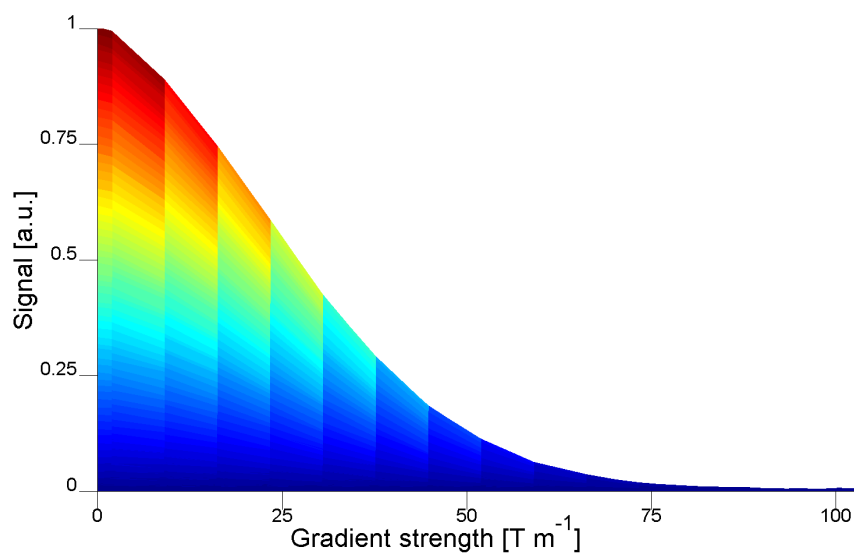

Figure A3: Example of a typical spectral attenuation plot which shows the Gaussian decay profile observed for all PFG NMR samples. The break lines correspond to each gradient strength increment.

A.4 Intra-diffusion calculation

The intra-diffusion coefficient and errors shown in chapters 5 and 6 are calculated as follows:

Table 1: Calculation of the zeolite and gas phase relaxation corrected signals using 0.09 mol kg^{-1} CH$_4$ adsorbed in a 15 µm β-zeolite crystallite as an example. Half the echo time, T, is set to 2.5 ms.

Sample region	Signal [a.u.]	T_2 weighting [a.u.]	Relaxation corrected signal, S [a.u.]
Gas phase	4.04×10^9	$= exp\left(-\dfrac{2 \times 2.5}{2 \times 4.62}\right)$ $= 0.58$	$S_{gas} = \dfrac{Gas\ signal}{T_2\ weighting}$ $= 6.95 \times 10^9$
Zeolite bed	5.02×10^{10}	$= exp\left(-\dfrac{2 \times 2.5}{2 \times 2.30}\right)$ $= 0.34$	$S_{zeolite} = \dfrac{Zeolite\ signal}{T_2\ weighting}$ 1.49×10^{11}

Table 2: Parameters obtained *via* PFG NMR for the calculation of intra-diffusion coefficients.

Parameter	Value	Comments
Mean D_{long} $[m^2\ s^{-1}]$	1.13×10^{-6}	−
Mean D_{gas} $[m^2\ s^{-1}]$	3.49×10^{-5}	−
Assumed tortuosity	1	−
D_{inter} $[m^2\ s^{-1}]$	3.49×10^{-5}	−
Zeolite bed height, h $[mm]$	12	−
Inner tube diameter, r $[mm]$	1.5	−
Sample space volume $[mL]$	0.085	Space occupied by zeolite bed in NMR tube $= \pi r^2 h$
Zeolite density $[g\ m^{-3}]$	1508558	−
Mass of zeolite $[g]$	0.09	−
Volume of zeolite $[mL]$	0.060	$= \dfrac{zeolite\ mass}{zeolite\ density} \times 10^6$
Zeolite volume: sample space volume ratio, ε $[-]$	0.704	Solid fraction in tube
Void space in zeolite bed region, ϕ $[-]$	0.296	$(1 - volume\ ratio)$

$$p_{inter} = \frac{S_{gas} \times \phi}{S_{zeolite}}$$

$$p_{inter} = \frac{6.95 \times 10^9 \times 0.296}{1.49 \times 10^{11}} \qquad \text{A10}$$

$$= 0.014$$

$$D_{intra} = \frac{\left(D_{long} - (p_{inter} D_{inter})\right)}{1 - p_{inter}}$$

$$= \frac{\left(1.13 \times 10^{-6} - (0.014 \times 3.49 \times 10^{-5})\right)}{1 - 0.014} \qquad \text{A11}$$

$$= 6.56 \times 10^{-7}\ m^2\ s^{-1}$$

A.5 Intra-diffusion error calculation

The error estimation, δx, is a result of a propagation of the errors in each measurement, which contains addition and multiplication terms. Wolfram Mathematica is used to obtain the partial derivatives of each multiplication and addition term using the following equations:

Multiplication rule

$$x = \frac{ab}{c}$$

$$\delta x = \sqrt{\left(\frac{\partial x}{\partial a}\partial a\right)^2 + \left(\frac{\partial x}{\partial b}\partial b\right)^2 + \left(\frac{\partial x}{\partial c}\partial c\right)^2}$$

$$\delta x = \sqrt{\frac{b^2}{c^2}\delta a^2 + \frac{a^2}{c^2}\delta b^2 + \frac{a^2 b^2}{c^4}\delta c^2}$$

$$\delta x = \sqrt{\frac{a^2 b^2}{c^2}\left(\frac{\delta a^2}{a^2} + \frac{\delta b^2}{b^2} + \frac{\delta c^2}{c^2}\right)}$$

A12

$$\delta x = \left(\frac{ab}{c}\right)\sqrt{\left(\frac{\delta a^2}{a^2} + \frac{\delta b^2}{b^2} + \frac{\delta c^2}{c^2}\right)}$$

$$\delta x = x\sqrt{\left(\frac{\delta a^2}{a^2} + \frac{\delta b^2}{b^2} + \frac{\delta c^2}{c^2}\right)}$$

Addition rule

$$x = 2a + b + c$$

$$\delta x = \sqrt{\left(\frac{\partial x}{\partial a}\partial a\right)^2 + \left(\frac{\partial x}{\partial b}\partial b\right)^2 + \left(\frac{\partial x}{\partial c}\partial c\right)^2}$$

A13

$$\delta x = \sqrt{(2\delta a)^2 + (\delta b)^2 + (\delta c)^2}$$

This simplifies to:

$$\delta x = \sqrt{\frac{1}{\left((a-1)b+c\right)^4} \times \left(\begin{array}{c} a_1^2 b^2 c^2 (d-e)^2 + (a-1)^2 b^2 c_1^2 (d-e)^2 + \\ (a-1)^2 b^2 d_1^2 \left((a-1)b+c\right)^2 + (a-1)^2 b_1^2 c^2 (d-e)^2 \\ +c^2 e_1^2 \left((a-1)b+c\right)^2 \end{array}\right)} \quad \text{A14}$$

Table 3: Parameters obtained *via* PFG NMR for the approximation of errors associated with the calculation of the intra-diffusion coefficients.

Parameter	Assigned parameter	Value
a	ϕ	0.296
b	S_{gas}	6.95×10^9
c	$S_{zeolite}$	1.49×10^{11}
d	D_{inter}	3.49×10^{-5}
e	$D_{long-range}$	1.13×10^{-6}
a_1	*Error in solid fraction estimate*	0.070
b_1	S_{gas} *standard deviation*	1.00×10^8
c_1	$S_{zeolite}$ *standard deviation*	7.28×10^8
d_1	D_{gas} *standard deviation*	4.71×10^{-9}
e_1	$D_{long-range}$ *standard deviation*	7.02×10^{-8}

$$\delta x = \sqrt{\frac{1}{\left((0.296-1)6.95 \times 10^9 + 1.49 \times 10^{11}\right)^4} \times \left(\begin{array}{c} 0.070^2 (6.95 \times 10^9)^2 (1.49 \times 10^{11})^2 (3.49 \times 10^{-5} - 1.13 \times 10^{-6})^2 + \\ (0.296-1)^2 (6.95 \times 10^9)^2 (7.28 \times 10^8)^2 (3.49 \times 10^{-5} - 1.13 \times 10^{-6})^2 + \\ (0.296-1)^2 (6.95 \times 10^9)^2 (4.71 \times 10^{-9})^2 \left((0.296-1)6.95 \times 10^9 + 1.49 \times 10^{11}\right)^2 \\ +(0.296-1)^2 (1.00 \times 10^8)^2 (1.49 \times 10^{11})^2 (3.49 \times 10^{-5} - 1.13 \times 10^{-6})^2 \\ +(1.49 \times 10^{-11})^2 (7.02 \times 10^{-8})^2 \left((0.296-1)6.95 \times 10^9 + 1.49 \times 10^{11}\right)^2 \end{array}\right)}$$

$$= 1.41 \times 10^{-7} \ m^2 \ s^{-1}$$

$$Error = \frac{1.41 \times 10^{-7}}{6.56 \times 10^{-7}} \times 100$$

$$= \pm \ 21\%$$

A.6 Effective mean free path calculation

The effective mean free path for a gas, λ, in the sealed 5 mm tube is calculated as follows:

$$\frac{1}{\lambda} = \frac{1}{d_{inter}} + \frac{1}{\lambda_{gas}}$$

A15

where d_{inter} is the effective diameter of the inter-crystalline space and λ_{gas} is the mean free path in the bulk gas phase. The latter is given by:

$$\lambda_{gas} = \frac{RT}{\sqrt{2}\pi d^2 N_A P}$$

A16

where R is the gas constant [J mol^{-1} K^{-1}], T is the temperature [K], d is the diameter of the diffusing species [m], N_A is Avogadro's number [mol^{-1}] and P is the pressure of the gas [J m^{-3}]. For a gas pressure of 150000 J m^{-3}:

$$\lambda_{gas} = \frac{8.314 \times 294}{\sqrt{2}\pi(4 \times 10^{-10})^2 \times 6.022 \times 10^{23} \times 150000}$$

$$= 3.81 \times 10^{-8}\ m$$

Assuming a d_{inter} which is of the same order of magnitude as the crystallite size, 10 μm, the effective mean free path is:

$$\lambda = \left(\frac{1}{1 \times 10^5} + \frac{1}{3.81 \times 10^{-8}}\right)^{-1}$$

$$\lambda = 3.80 \times 10^{-8}\ m$$

A.7 Examples of adsorbed and gas phase T_1 and T_2 plots

Figures A4 and A5 show typical examples of the T_1 and T_2 plots obtained for the adsorbed and gas phase samples used in this thesis for CH_4 and C_2H_6 respectively, to highlight the quality of the fits.
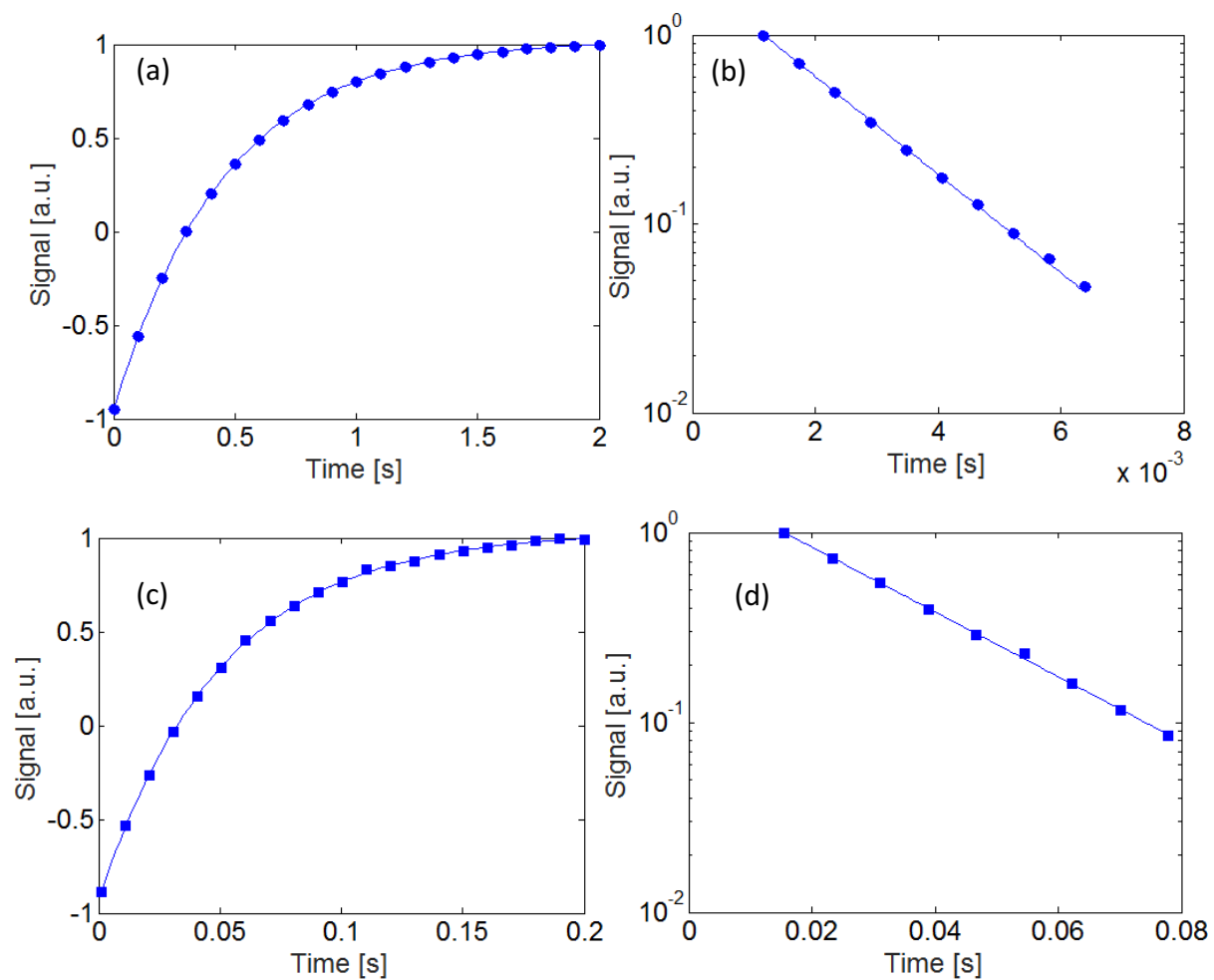
Figure A4: Example of T_1 and T_2 plots obtained from the (a, b) adsorbed phase region and the (c, d) gas phase above the zeolite bed, using CH_4 as an example.
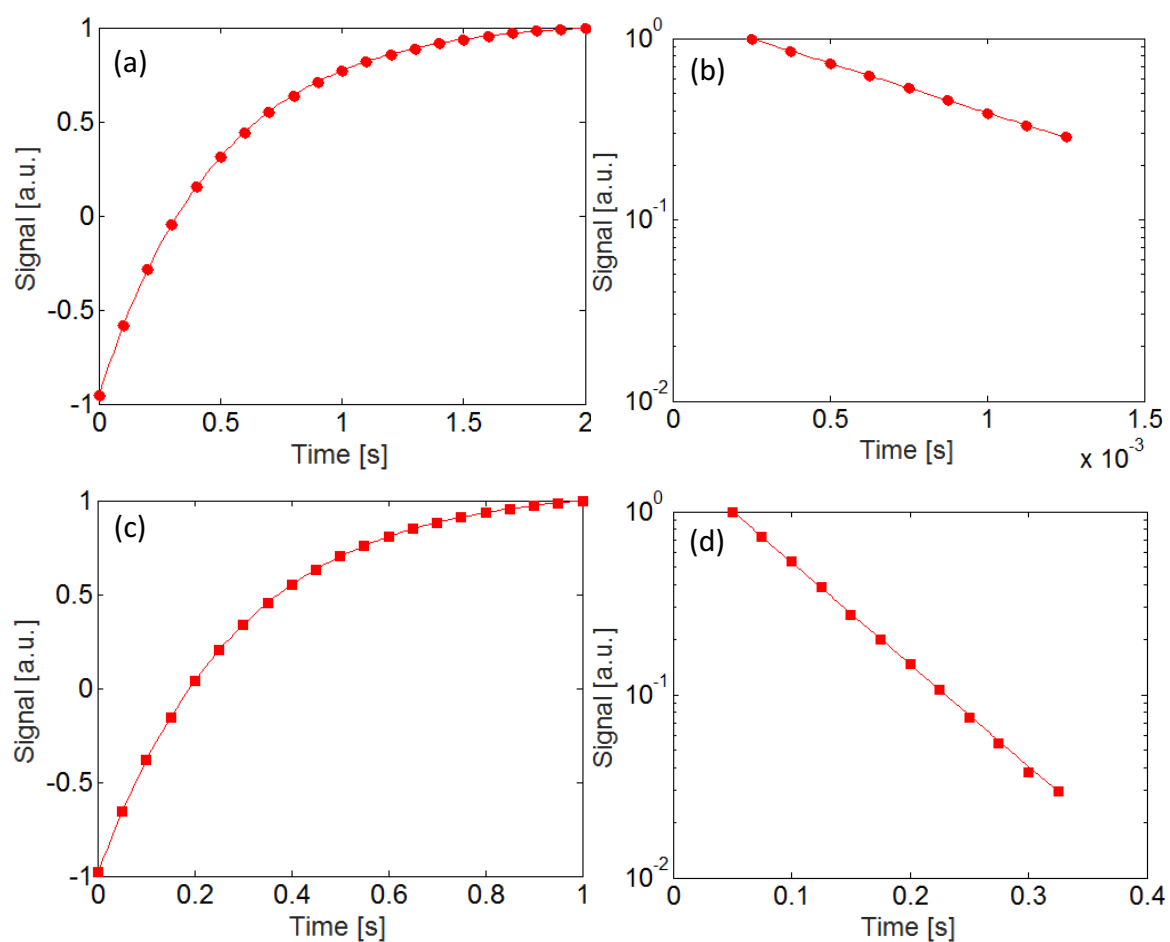
Figure A5: Example of T_1 and T_2 plots obtained from the (a, b) adsorbed phase region and the (c, d) gas phase above the zeolite bed, using C_2H_6 as an example.

Table 4: Summary of T_1 and T_2 values for CH_4 and C_2H_6 used in the D_{intra} calculations in chapter 5.

Hydrocarbon loading [mol kg^{-1}]	T_1: 300 MHz [ms]	T_2: 300 MHz [ms]
CH$_4$: 0.09	642	12.0
0.11	611	11.2
0.18	557	9.0
0.25	153	8.1
0.34	125	7.5
C$_2$H$_6$: 0.28	1391	0.9
0.34	377	0.8
0.40	215	0.4

A.8 Self-diffusion of gases

The wall collision frequency for gases, Z, per unit area is given by:

$$Z = \frac{1}{4}nv \qquad\qquad \text{A17}$$

where n is the number of molecules per unit volume, v.